ANL-07/30

Argonne NATIONAL LABORATORY

Development of Materials Resistant to Metal Dusting Degradation

Final Report

Nuclear Engineering Division

About Argonne National Laboratory

Argonne is a U.S. Department of Energy laboratory managed by UChicago Argonne, LLC under contract DE-AC02-06CH11357. The Laboratory's main facility is outside Chicago, at 9700 South Cass Avenue, Argonne, Illinois 60439. For information about Argonne, see www.anl.gov.

Availability of This Report

This report is available, at no cost, at http://www.osti.gov/bridge. It is also available on paper to the U.S. Department of Energy and its contractors, for a processing fee, from:

U.S. Department of Energy
Office of Scientific and Technical Information
P.O. Box 62
Oak Ridge, TN 37831-0062
phone (865) 576-8401
fax (865) 576-5728
reports@adonis.osti.gov

ANL-07/30

Development of Materials Resistant to Metal Dusting Degradation

Final Report

by
K. Natesan and Z. Zeng
Nuclear Engineering Division, Argonne National Laboratory

work supported at
Argonne National Laboratory
The U.S. Department of Energy
Office of Industrial Technologies
Project Manager: S. Dillich

October 2007

CONTENTS

FIGURES

TABLES

ABSTRACT

The deposition of carbon from carbonaceous gaseous environments is prevalent in many chemical and petrochemical processes such as, hydrogen-, ammonia-, and methanol-reforming systems, syngas production systems, and iron-ore reduction plants. One of the major consequences of carbon deposition is the degradation of structural materials by a phenomenon known as "metal dusting." There are two major issues of importance in metal dusting. First is formation of coke and subsequent deposition of coke on metallic structural components. Second is the initiation and subsequent propagation of metal dusting degradation of the structural alloy. In the past, we reported on the mechanism for metal dusting of Fe- and Ni-base alloys. In this report, we present metal dusting data on both Fe- and Ni-base alloys after exposure in high and atmospheric pressure environments that simulate the gas chemistry in operating hydrogen reformers.

We have also measured the progression of pits by measuring the depth as a function of exposure time for a variety of Fe- and Ni-base structural alloys. We have clearly established the role of transport of iron in forming a non-protective spinel phase in the initiation process and presence of carbon transfer channels in the oxide scale for the continued propagation of pits, by nano-beam X-ray analysis using the advance photon source (APS), Raman scattering, and SEM/EDX analysis. In this report, we have developed correlations between weight loss and pit progression rates and evaluated the effects of carbon activity, system pressure, and alloy chemistry, on weight loss and pit propagation. To develop pit propagation data for the alloys without incurring substantial time for the initiation of pits, especially for the Ni-base alloys that exhibit incubation times of thousands of hours, a pre-pitting method has been developed. The pre-pitted alloys exhibited pit propagation rates similar to those of materials tested without pre-pitting. We have also developed a substantial body of metal-dusting data on the performance of Fe- and Ni-base weldments. During the course of this project, we have developed new Ni-base and Cu-base alloys and tested them in simulated metal dusting environments at 1 atm and at high pressures. Results clearly showed superior performance of both classes of alloys in resisting metal dusting. We also developed an approach to mitigate metal dusting by performing an intermediate oxidation step for extending the life of alloys in which metal dusting has initiated and pits are in progression. Finally, we have analyzed several components that have failed in plants such as hydrogen plant, pilot plant reformer, and a gas boiler.

PROJECT DESCRIPTION

The current project, funded by the U.S. Department of Energy (DOE), Idaho Operations Office, involves research and development of materials and processing methods, in accordance with the Program Plan for the Industrial Materials for the Future (IMF) subprogram. Consistent with the mission of the DOE Energy Efficiency and Renewable Energy (EERE) Industrial Technologies Program (OIT), the mission of the IMF subprogram is to lead a national effort to research, design, engineer, and test new

and improved materials, as well as more profitable uses of existing materials, for the Industries of the Future (IOF).

Degradation of metallic structural components by metal dusting is a major concern in several IOFs. It is a major issue in plants for the production of hydrogen, ammonia synthesis processes, methanol-reformer systems, and syngas (H_2/CO mixtures) systems that are pertinent to chemical and petrochemical industries.[1-18] Metal dusting is experienced at high temperatures in oxidizing-carburizing environments that are prevalent in heat-treating industry. The gases used in heat-treating operations mix with oil residue on the work pieces to form gases that are kinetically favorable for metal dusting attack. Petroleum refineries experience metal dusting attack in processes that involve hydro-dealkylation and catalyst re-generation. In the steel sector, metal dusting is an issue in iron-making blast furnaces in steel plants and in processes, such as Nucor, that involve direct reduction of ores to form iron. Metal dusting also occurs with processes that handle carbon dioxide for cooling, the recycle-gas loop equipment of coal gasification units, fired heaters handling hydrocarbons at elevated temperatures, and metallic interconnects used in solid oxide fuel cells. Currently, the industrial sectors circumvent metal dusting attack by cooling the gas to temperatures low enough to avoid the problem but pay a penalty in the form of lower efficiency, wastage of energy, and decrease in product yield.

The current project is aimed at development of metallic alloys and surface engineering of commercial alloys to mitigate metal dusting degradation. The alloys have an improved corrosion resistance and also possess adequate mechanical properties at temperatures up to 816°C (1500°F). The project involves exposure of candidate alloys and surface-engineered materials to metal dusting environments that simulate the temperatures, pressures, and gas chemistry prevalent in hydrogen and ammonia reformers and in syngas systems. The project also develops a database on metal dusting degradation from the standpoint of incubation time, general corrosion, pitting attack, pitting rate, and size for the candidate alloys as a function of the process variables.

BACKGROUND

Carbon activity (a_C) reflects the potential of carbon to deposit from carbon-bearing gases. When a_C >1, carbon can deposit as a solid phase that is usually called “coke.“ In many industries, metallic alloys are used as structural components at elevated temperature in high carbon activity environment. For example, in hydrogen and syngas plants, methane and various other hydrocarbons are reformed or partially oxidized to produce hydrogen and carbon monoxide. When those carbon-bearing gases are catalyzed at elevated temperature, carbon will deposit on the surface of alloys that constitute vessels, gas-transfer pipes, and other equipment. Interactions between carbon and alloys lead to disintegration of the alloys into fine particles that can be carried away by the flowing gas. In the metal wastage process, pits form on the surface of alloys accompanied by the formation of a fine powder of carbide or pure metal and carbon dust. This metal wastage process, called “metal dusting,” is a much

more severe problem than regular carburization since the equipment or pipes will be totally destroyed after alloys become fine powder.

Three possible steps can contribute to degradation of material by metal dusting process. The first step is deposition of carbon from a multicomponent gas phase onto the surface of alloys. In typical carbonaceous environments, three potential reactions can lead to carbon deposition:

$$H_2 + CO = C + H_2O \qquad a_C = K \bullet P_{H2} \bullet P_{CO}/P_{H2O} \qquad (1)$$

$$2CO = C + CO_2 \qquad a_C = K \bullet P_{CO}^2/P_{CO2} \qquad (2)$$

$$CH_4 = C + 2H_2 \qquad a_C = K \bullet P_{CH4}/P_{H2}^2 \qquad (3)$$

The first reaction is the fastest and plays a major role in carbon deposition. High carbon activity is the driving force for the deposition. In the second step, carbon atoms dissolve and diffuse into the alloys. The second step is driven by the concentration gradient of carbon. In the third step, graphite particles develop and lead to the separation of metal grains and/or carbide particles. Even though the third step leads to catastrophic attack, the driving force for this step had not been clear for a long time.

For iron-base alloys, it was proposed that metal dusting occurs because of the following: (a) carbon deposits on the metal surface and dissolves in the metal, (b) Fe_3C forms as carbon diffuses into the iron and the metal becomes oversaturated, and (c) metastable Fe_3C decomposes to Fe and graphite.[5-8] According to this mechanism, the final product is graphite and iron. However, there is no conclusive evidence that the iron phase is present in every case of metal dusting.[9,10] It is not clear what drives the formation and decomposition of Fe_3C under the same conditions of temperature, pressure, and composition. Clearly, graphite crystallizes from a supersaturated solution. Nevertheless, it is doubtful that its crystallization also causes Fe_3C to decompose. The formation and decomposition of chemical bonds in the carbide phase require a sizable free energy change.

Recently, in research conducted at Argonne under the sponsorship of DOE/OIT, we proposed a new mechanism for metal dusting based on the crystallinity of carbon obtained by X-ray diffraction and Raman spectroscopy.[9,11-13] Metal dusting in iron-base alloys is considered to be a process of catalytic crystallization of carbon with participation by iron. The difference in the free energy of poorly crystallized carbon and well-crystallized graphite is a driving force for crystallization of carbon.[9] However, this process cannot occur at low temperature because the C-C bonds are too strong to allow movement of carbon atoms. Fe_3C and iron act as catalysts in the carbon crystallizing process in a manner that tends to improve the crystallinity of the carbon since Fe_3C and iron have a suitable lattice plane, which has diffraction parameters similar to those of graphite. This lattice plane works as a template for the crystallization of carbon. At the same time, fine iron or Fe_3C particles are liberated from the pure metal or alloys. Carbon filaments grow when carbon continues to diffuse through Fe_3C and precipitate at one preferred side of the particles. Although the driving force is small, it results in severe corrosion over the long term. This mechanism successfully explains not only

why the metal dusting products are carbon and Fe_3C instead of iron, but also why carbon filaments are accompanied in the metal dusting process. The mechanism of metal dusting for Ni-base alloys is similar to that for Fe-base alloys, although no Ni_3C is formed in the process. The lattice of nickel metal can also work as a template to aid the crystallization of carbon. Since metal dusting process involves catalytic crystallization instead of a regular chemical reaction, metal dusting should be defined as a metal wastage process instead of regular corrosion, although the outcome of metal dusting is similar to corrosion. This metal wastage process is unique and is, generally, not uniform but initiates as pits at several sites on the metal surface and eventually propagates into the substrate.

According to the new mechanism of metal dusting, two methods could be used to stop the driving force for carbon ingress and minimize metal dusting attack. First is to build a barrier to stop carbon diffusion into alloys. A perfect oxide scale can act as a protective layer on the alloy surface since the diffusion rate of carbon in oxide, especially at low temperatures, is almost zero. Therefore, alloys that can form a stable, defect-free oxide layer in the metal dusting environment would be desirable. The current project focuses on the phase composition of oxide scales on the surface of alloys, the effect of alloy composition on the metal dusting rate, and the effect of gas and alloy composition on phases that form in the oxide scale. Second, if carbon cannot find a suitable lattice plane in alloys, then the alloys may not act as a catalyst to aid in the crystallization of carbon and may not disintegrate in the catalytic carbon crystallization. Therefore, the approach in the current project is to use the mechanistic knowledge developed thus far in developing new alloys and surface engineering currently available alloys, so that they do not act as a catalyst to assist in the crystallization of carbon.

ECONOMIC BENEFIT

The economic benefit to the industrial sector can be significant, if the development of new alloys and surface engineering approaches proposed in this program succeeds. The following assumptions and calculations are made for the benefits that can be realized in the chemical and petrochemical sectors. Similar calculations can be performed for the petroleum, steel, and heat treatment sectors, but are not made in this report.

A typical hydrogen reformer recovers heat at ≈400°C rather than at 800°C and generates excess steam. This excess steam represents about 125 BTU/{standard cubic foot of hydrogen (scfh)}, which could be saved if 800°C heat could be used directly in hydrogen plants. In the year 2000, about 3.8 billion scfh/d was produced in the U.S. This value translates into 475 billion BTU/d that could be saved if the metal dusting issue were solved and the 800°C heat could be used directly. This value is equivalent to a saving of 475 million scf of natural gas per day. Realistically, if half this amount were saved, the savings for the U.S. hydrogen industry will be $1.4-3.8 million/day or $0.5-1.3 billion per year for the hydrogen industry alone. Since several additional hydrogen plants have been built since 2000, the savings would be even

greater. As the U.S. and the world moves toward a hydrogen economy, the production of hydrogen is expected to increase exponentially over time, and any improvement in the design and operation of the new plants will accelerate the economic benefit.

The gas-to-liquids (GTL) industry is in its infancy. One operating plant produces about 21,000 barrels of product per day (bpd) from 160 million standard cubic feet per day (MMscfd) of natural gas. GTL plants will operate with even lower steam/carbon ratio, with a potential for more severe metal dusting attack than in current reformer systems. Some estimates suggest that several 100,000-bpd plants will be built in the next ten years. This translates into 4,800 MMscfd of natural gas usage in year 10. Calculations show that a plant designed for high-temperature heat transfer can realize a 6% savings in natural gas. This amounts to 9.6 MMscfd of natural gas per plant or 274 MMscfd at year 10. The average over ten years would be a savings of natural gas of about 137 MMscfd. The cost of natural gas is variable in that some of it is now flared and considered of no value. There are known reserves of natural gas that will only come to the market if GTL becomes viable. Nonetheless, estimates indicate that overcoming the metal dusting problem would reduce the cost of a typical 100,000-bpd plant from $50 to $133 million per year.

Since the reformer industry is primarily based on conversion of fossil fuels (carbon-containing fuels) such as natural gas, methanol, and other hydrocarbons, any improvement in process efficiency, energy savings, and product yield can result in less consumption of hydrocarbon-containing feedstock for a given output. Since the generation of greenhouse gas (CO_2) emissions is directly related to the use of fossil fuel feedstock, the development and application of new materials (from this project) would lead to less consumption of C-containing feedstock for a given unit of product output, and this will reduce greenhouse gas emission.

OBJECTIVES

The primary objective of the current project is to mitigate metal dusting degradation of metallic structural alloys by (a) development of alternative structural alloys with improved corrosion resistance and with adequate mechanical properties at temperatures up to 816°C (1500°F) and (b) surface modification of currently available commercial Fe- and Ni-base structural alloys. The study conducted at Argonne in recent years has clearly established the mechanisms for metal dusting in Fe- and Ni-base alloys, and the results from this study form the basis for the ongoing project. The project involves laboratory testing of Fe- and Ni-base commercial alloys, weldments of these alloys, and newly developed materials to establish their metal dusting rates as a function of key process variables. The project also includes establishment of procedures for surface modification of candidate alloys to resist metal dusting.

The better performing alloys (based on the laboratory tests) are produced and evaluated in simulated metal dusting environments. In addition, a knowledge base on materials/wastage information is developed from an analysis of pit size, distribution, depth, and volume as a function of temperature, pressure, gas chemistry, and alloy chemistry for application in chemical and petrochemical industries.

STEERING GROUP AND MTI PROJECT MEETINGS

The organizations that are involved in the current project include the Materials Technology Institute (MTI) of the Chemical Process Industries, Air Products and Chemicals Inc., ConocoPhillips, Halder Topsoe, Air Liquide, DuPont Chemical Company, Haynes International, Special Metals, Spectrum Metals, Krupp VDM, and Sandvik Steel.

A list of Steering Committee meetings, MTI meetings, and Project Assessment meetings, in which the current project was discussed, is given below:

October, 18, 2004	Steering Committee meeting at Argonne National Laboratory
October, 18, 2004	MTI meeting at Houston, TX
February 22, 2005	MTI meeting, Tampa, FL
April 3-7, 2005	NACE meeting, Houston, TX
May 31-June 3, 2005	Industrial Technology Program Materials Project and Portfolio Review meeting, Chicago, IL
June 6-8, 2005	MTI meeting, Kansas City, MO
October 24, 2005	Steering Group and MTI meetings, Pittsburgh, PA
February 20-23, 2006	MTI meeting, Orlando, FL
June 5-8, 2006	MTI meeting, St. Louis, MO
October 23-26, 2006	MTI meeting, Dallas, TX
February 26 – March 1, 2007	MTI meeting, Galveston, TX
June 4-7, 2007	MTI meeting, Minneapolis, MN
October 22-25, 2007	MTI meeting, Hilton Head, SC

PROJECT TASKS

The project research focused on the following tasks:

- Procure materials, fabricate specimens, and perform metal dusting experiments with off-the-shelf Ni-base alloys in simulated reformer effluent gas chemistry at temperatures in the range 450-700°C at both atmospheric and at high pressures..

- Use nano-beam X-ray analysis, Raman scattering, scanning electron microscopy and other techniques to study the initiation of metal dusting and understand the process of carbon diffusion through oxide scale.

- Develop surface engineered specimens of Ni-base alloys, such as alumina, chromia, and/or silica surface layers, and evaluate their susceptibility to coking,

carbon deposition, and metal dusting attack in simulated reformer effluent chemistry at atmospheric and high pressures.

- Fabricate Fe- and Ni-base alloy weldments and evaluate their performance in metal dusting environments.
- Develop a pre-pitting procedure to study pit growth kinetics after an incubation period.
- Develop and fabricate alternative alloys with adequate mechanical strength and prepare specimens for exposure in metal dusting experiments.
- Develop procedures that are feasible in plant operation to mitigate metal dusting degradation.

1. GAS CHEMISTRY AND CARBON ACTIVITY

Gaseous environments that are prevalent in chemical process industries were characterized by computer modeling of gas-phase reactions under both equilibrium and nonequilibrium conditions.[9,10,14,15] To evaluate the role of gas composition on the metal dusting rate of alloys, specimens were exposed to gas mixtures (see Table 1.1) of varying composition that encompassed the environments that are anticipated in industrial processes. In all, we have used 21 gas compositions in our experimental program. Figure 1.1 shows these compositions in terms of CO/CO_2 and H_2O/H_2 ratios.

The carbon activities were calculated for different gas mixtures as a function of temperature at atmospheric pressure (14.7 psia) and at plant system pressures. The carbon deposition process can be influenced by two possible reactions:

$$CO\ (g) + H_2\ (g) = C + H_2O\ (g) \quad (1)$$

$$2CO\ (g) = C + CO_2\ (g) \quad (2)$$

Since the gas composition is maintained fairly constant during the passage through the waste-heat boiler, either Reaction 1 or Reaction 2 may dictate the carbon activity in the stream at different temperatures. If Reaction 1 determines carbon activity, it will be directly proportional to H_2 and CO partial pressures and inversely proportional to H_2O partial pressure. On the other hand, if Reaction 2 determines carbon activity, then it will be directly proportional to the square of the CO partial pressure and inversely proportional to CO_2 partial pressure. In addition, if gas phase equilibrium does prevail, albeit at high temperatures and/or for long residence times, then the calculated carbon activity value will be the same (i.e., irrespective of Reaction 1 or 2) since, thermodynamically, the gas composition will adjust to give the most stable (lowest free energy) composition. Therefore, carbon activity was calculated as a function of temperature from 496°C (925°F) to the maximum test temperature and for 1 atm to the maximum test pressure for various gas mixtures based on Reaction 1, Reaction 2, and thermodynamic equilibrium.

Carbon activities were calculated for several of the gas mixtures and their impact on metal dusting was reported earlier.[13] Carbon activity calculated using Reactions 1 and 2 decreases with increasing temperature but increases with an increase in system pressure. Carbon activities of gases 1 to 17 have been reported earlier.[13] Figures 1.2 to 1.5 show the carbon activity as a function of temperature for gas mixtures 18, 19, and 21. Gas compositions 2, 4-6, 8-11, 13-18, 20, and 21 have been used in several metal dusting experiments and their compositions are listed in Sec. 2.7.

Table 1.1 Chemical composition (in mole %) of gas mixtures used in the metal dusting study.

Gas	H_2	CO	CO_2	H_2O	CH_4	N_2
1	43.8	7.2	5.7	39.2	4.1	-
2	52	18	5.6	23	1.1	-
2b	66.2	23	7.1	2.3	1.4	-
3	36.3	8.4	5.6	35	0.2	15
4	74.2	17.5	8.3	0	-	-
5	72.2	17.6	8.3	2.0	-	-
6	77.2	12.7	10.1	0	-	-
7	25.3	70	4	0.01	-	-
8	71.4	11.3	17.4	0	-	-
9	71	11.7	17.3	0	-	-
10	53.4	18.4	5.7	22.5	-	-
11	79.5	18.2	-	2.3	-	-
12	75.4	6.2	18.4	-	-	-
13	71.0	2.6	26.4	-	-	-
14	40	45	5	10	-	-
15	20	65	5	10	-	-
16	40	25	25	10	-	-
17	20	74.5	5	0.5	-	-
18	54.6	23.2	4	18.2	-	-
19	47.4	15.5	6.2	30.9	-	-
20	40.5	19.9	-	-	0.5	39.6
20b	40.2	19.8	0.2	0.1	0.5	39.3
21	65.1	30	0.9	4	-	-

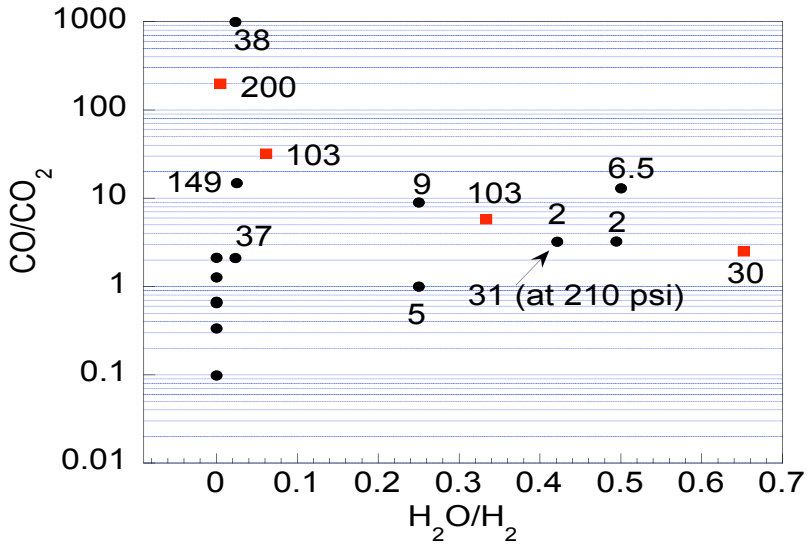

Figure 1.1. Chemical composition and carbon activity for gas mixtures used in metal dusting study. Carbon activity was calculated from the reaction CO (g) + H_2 (g) = C + H_2O (g) at 593°C. The number in the parenthesis indicates the carbon activity of the gas mixture.

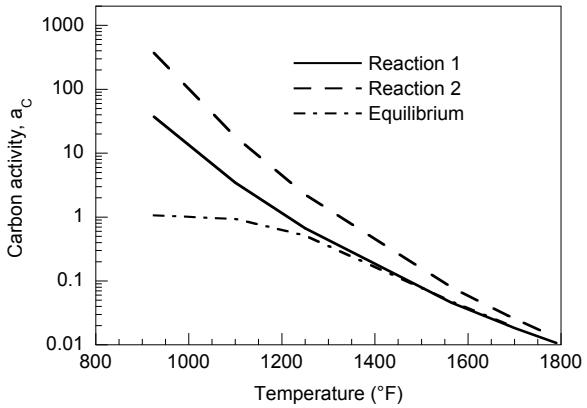

Figure 1.2. Carbon activity of Gas 18 as function of temperature at 1 atm.

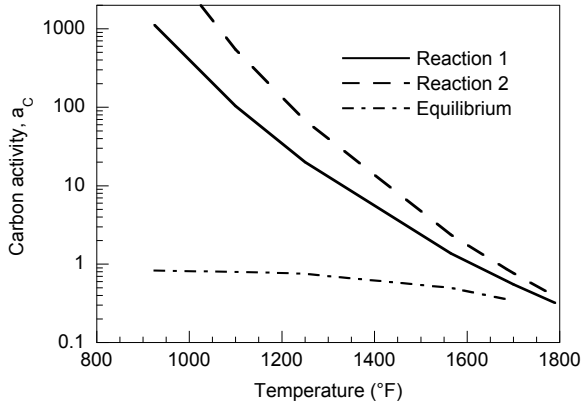

Figure 1.3 Carbon activity of Gas 18 as function of temperature at 30 atm.

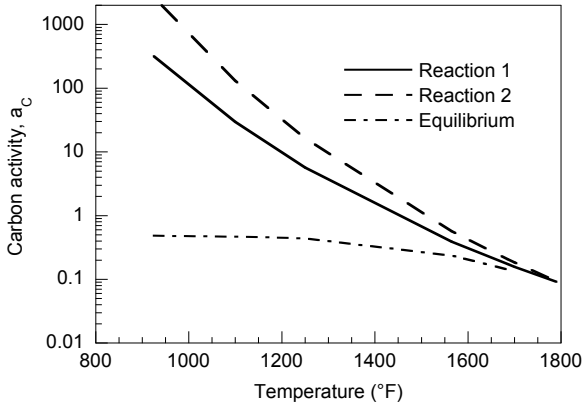

Figure 1.4. Carbon activities of Gas 19 as function of temperature at 25 atm.

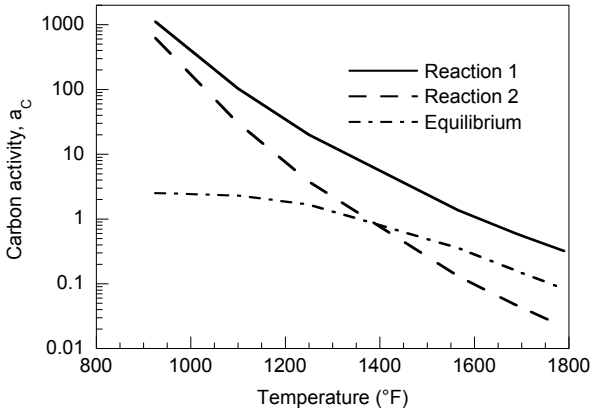

Figure 1.5. Carbon activities of Gas 21 as function of temperature at 1 atm.

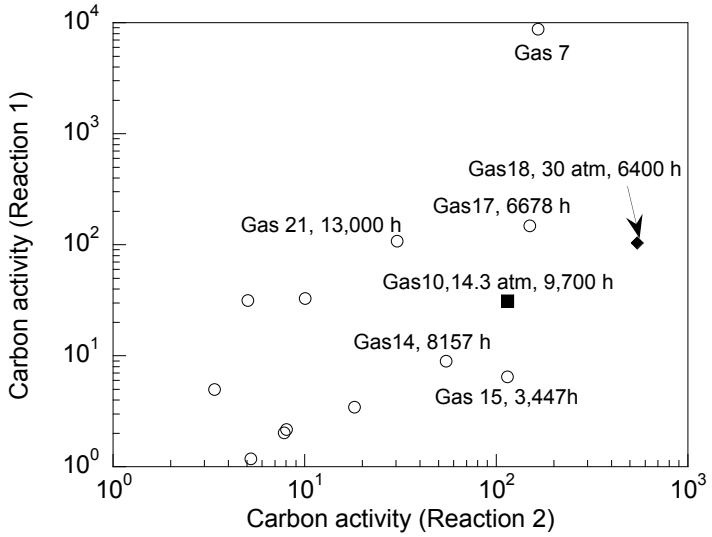

Figure 1.6. Calculated carbon activities from Reactions 1 and 2 at 593°C for gas mixtures used in several long-term experiments.

2. EXPERIMENTAL PROGRAM

2.1 Description of Reactor Systems

Five experimental systems were used in the metal dusting experiments.[13,14] Two existing systems at ANL were modified to accommodate the requirements of the program. Each of the modified systems consisted of a horizontal, tubular, high-temperature furnace capable of operation up to 900°C. The reaction chamber, with gas inlet/outlet fittings, was fabricated from quartz and positioned within the furnace chamber. The ends of the reaction chamber had specially designed flanges with O-ring seals. A chromel-alumel thermocouple, inserted from one end of the reaction chamber, was used to monitor the specimen temperature. Specimens were suspended from quartz rods held on the top of a high-purity alumina boat. The specimens and the boat were positioned in the constant-temperature section of the reaction chamber. High-purity gases such as CO, CO_2, CH_4, and H_2 were procured and piped into the reaction chamber through flow meters to obtain the desired composition. In some experiments, H_2 gas was bubbled through a water bath to saturate the H_2 with water prior to entering the reaction chamber. Upon completion of the experiments, the specimens and the carbon accumulated on the specimens and in the boat were removed for detailed microstructural, X-ray, and Raman analysis.

While the two systems described above enabled study of the key variables in metal dusting research, additional facilities were needed for long-term testing of metallic alloys, surface-engineered materials, and coatings. For this purpose, three new systems were designed and assembled in a metal dusting research laboratory. Figure 2.1 shows a schematic diagram for the three test facilities set up for metal dusting experiments. The three environmental exposure test fixtures were positioned horizontally on a laboratory bench top in a staggered linear arrangement with a common gas supply. Each test fixture consisted of a quartz retort chamber (74-cm length, 5-cm OD, 0.32-cm thick), which was centered in a 30-cm-diameter resistive heating furnace. A Barber-Coleman Model 560 three-mode controller was used to control the furnace temperature. Type 316 stainless steel (SS) flange caps with an O-ring seal were used to close the ends of the quartz retort tube. The flange caps provided port fittings for the gas flow, steam/vapor preheater, and ceramic thermowells used for measurements of specimen temperature. Figure 2.2 shows a schematic diagram for the furnace assembly and gas flow arrangement used for the metal experiments.

The gas that flowed through the retort chamber had various ratios of H_2, CH_4, CO, CO_2, and steam/water vapor. Laboratory-grade compressed gases were supplied from AGA Gas Co. in industry standard 1A size (136 atm and 4.3 m^3 internal volume) cylinders. Each gas was piped to the reaction chamber through a low-pressure manifold line that is fed from a two-stage, gas-pressure-reducing regulator with a flash arrestor and a solenoid shut-off valve. The solenoid valves were controlled by a gas-leak detection system manufactured by International Sensor Technology Co. Overhead sensors that are selective to H_2, CH_4, and CO gases were used to detect gas leaks. In

the event of a leak detected above a user-selected threshold by any of the sensed gases, the detection system closed the solenoid valves for all gases.

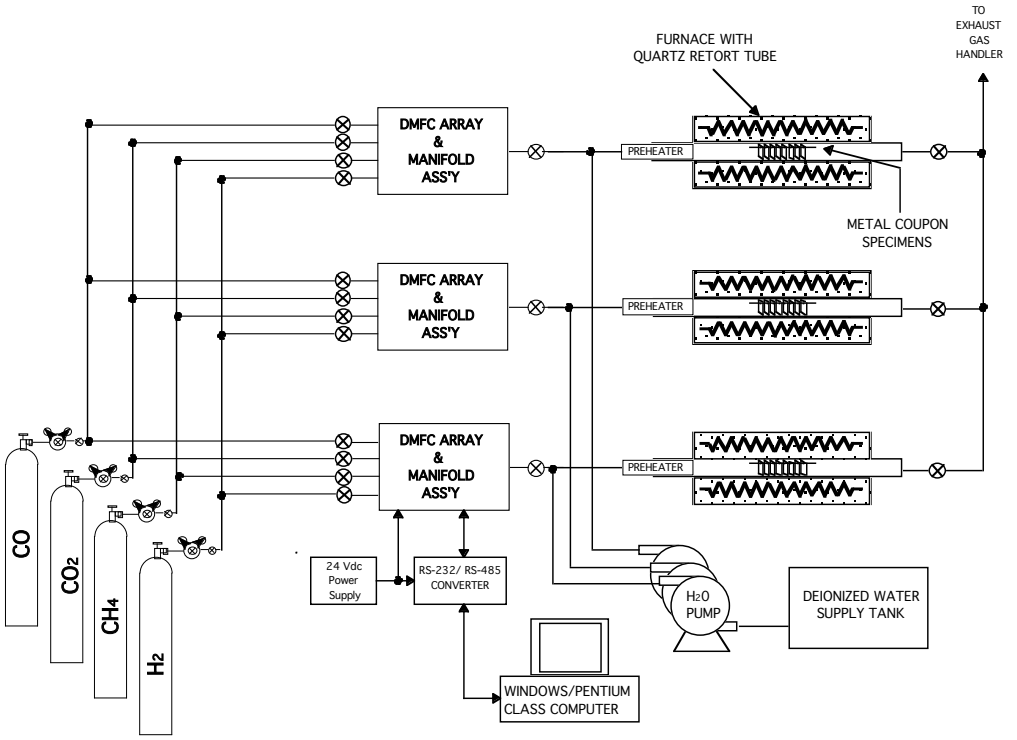

Figure 2.1 Schematic of three atmospheric test facilities used for metal dusting experiments.

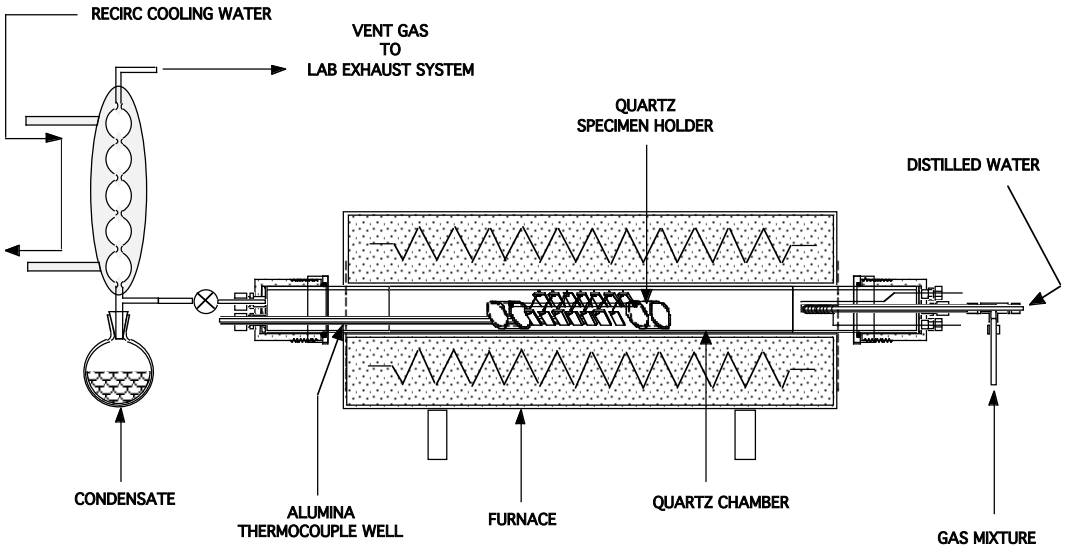

Figure 2.2. Schematic of furnace assembly and gas flow arrangement used for metal dusting experiments.

Gases from the low-pressure manifold lines were supplied to respective Brooks model 5850S digital mass flow control (DMFC) valves. Figure 2.3 shows a schematic diagram of the steam and gas flow scheme used. The output from each mass flow controller combined into a central manifold tube that connects to the steam/vapor preheater assembly at the input cover flange for the retort tube. The steam/vapor preheater had a coaxial-design mixing chamber enabling the water vapor to be entrained by the flowing gas mixture prior to passing the preheat element. The gas mixture flow rate was typically 200-400 cm^3/min (STP), and the water flow rate was 1-5 cm^3/h. The preheat temperature was maintained with a Love Controls Model 16A three-mode process controller. Distilled water was supplied to the preheat mixing chamber by a Watson-Marlow Model MPL micro-metering pump that was fed from a 20-L polycarbonate carboy. The micro-metering pump was based on peristaltic action, and the flow rate was adjusted by varying the rotational speed of the roller cam and/or the diameter of the flexible tubing. The gas-steam mixture flowed past the alloy test specimens to the exit port at the rear flange cap. After the gas-steam mixture exited the retort, it was passed through a chilled water pyrex condenser to collect water vapor for future measurement, while the remaining gas mixture was vented to a room exhaust vent handler.

Alloy test specimens were mounted on a quartz specimen tree (see Fig. 2.4) that was centered in the heat zone of the retort chamber. Metal-dusting experiments were conducted under isothermal conditions at temperatures between 427 and 704°C (800 and 1300°F). A chromel-alumel thermocouple controlled the furnace temperature. The test temperature and the precision of its control are important to the reproducibility and usefulness of the results. An indicating controller calibrated for the control thermocouple maintained the furnace temperature. Specimen temperature was monitored with a second, sheathed chromel-alumel thermocouple inserted into the reaction chamber in the vicinity of the specimens. The outputs of the monitoring and control thermocouples were calibrated over the temperature range of interest, so that if the monitoring thermocouple became inoperative due to corrosion, the control thermocouple was used during continuation of the test. The multicomponent gas environment for the metal dusting program consisted of CO, CO_2, H_2, CH_4, and H_2O. The actual composition of the gas mixture had a wide enough range to establish carbon activity of ≈0.5 to ≈100 at the temperatures and pressures of interest. The exposure time periods in different experiments ranged between 5 and 1000 h, depending on the objective of the test.

Figure 2.5 shows a system that was built to conduct experiments at system pressures up to 40.8 atm (600 psi). The system consisted of a horizontal, tubular, high-temperature furnace capable of operation up to 900°C. The reaction chamber, with gas inlet/outlet fittings, fabricated from alumina and/or quartz was positioned within a pressure vessel made of a high-temperature heat-resistant alloy (16-mm ID, 50-mm OD, 500-mm long). A chromel-alumel thermocouple was inserted into the pressure

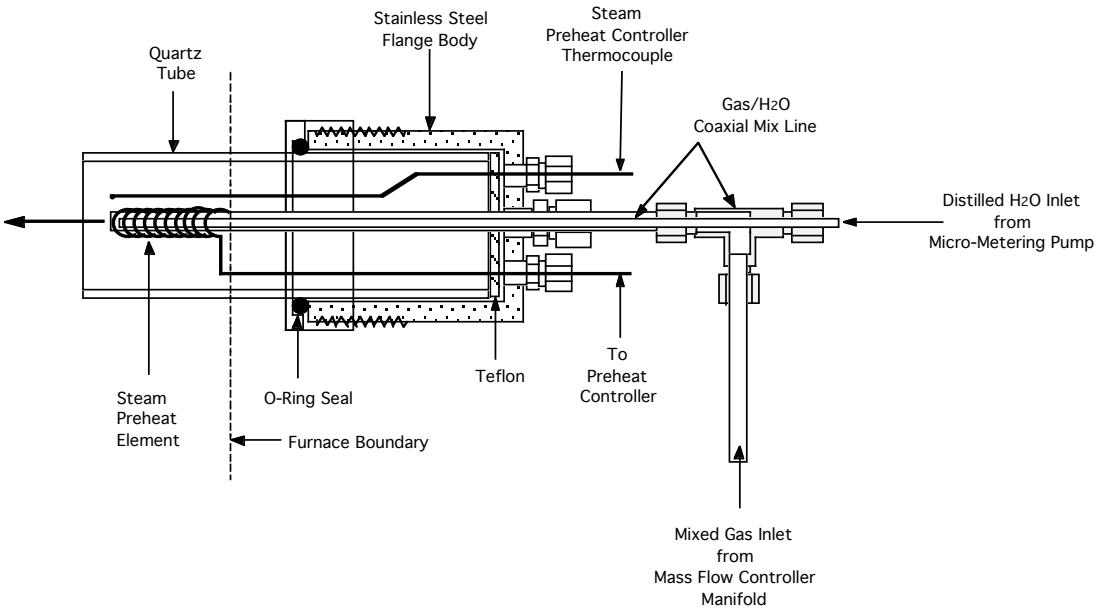

Figure 2.3. Schematic of steam and gas flow scheme used for metal dusting experiments.

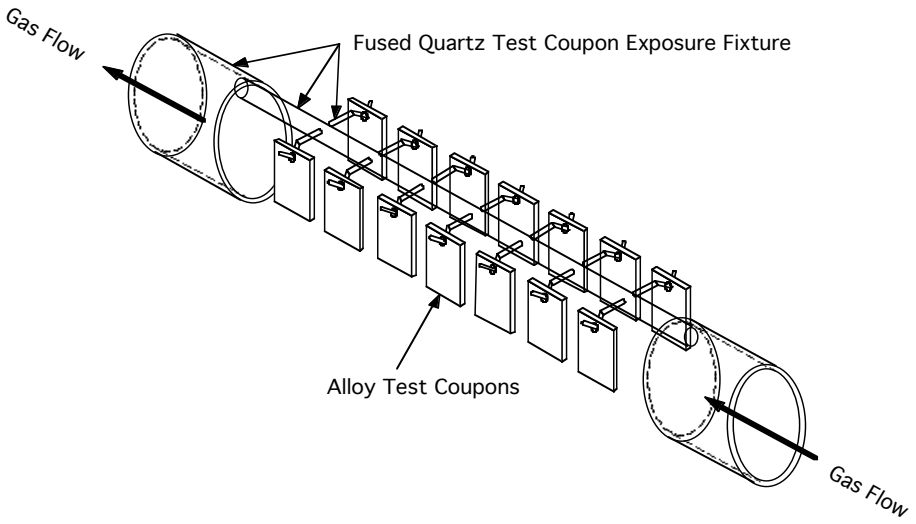

Figure 2.4. Schematic of quartz specimen holder and test coupon arrangement used for metal dusting experiments.

vessel to monitor the specimen temperature. Specimens were suspended from an alumina rod and were positioned in the constant-temperature section of the tubular furnace. High-purity gases such as CO, CO_2, CH_4, and H_2, were piped into the reaction chamber through flow meters to obtain the desired composition. To include steam in the exposure environment, water was pumped from a water pump, converted to steam, pressurized, and inserted along with the gas mixture. The effluent from the reactor

chamber was condensed to remove the water prior to exhaust. Figure 2.6 shows a magnified view of the high-pressure parts of the system described in Fig. 2.5.

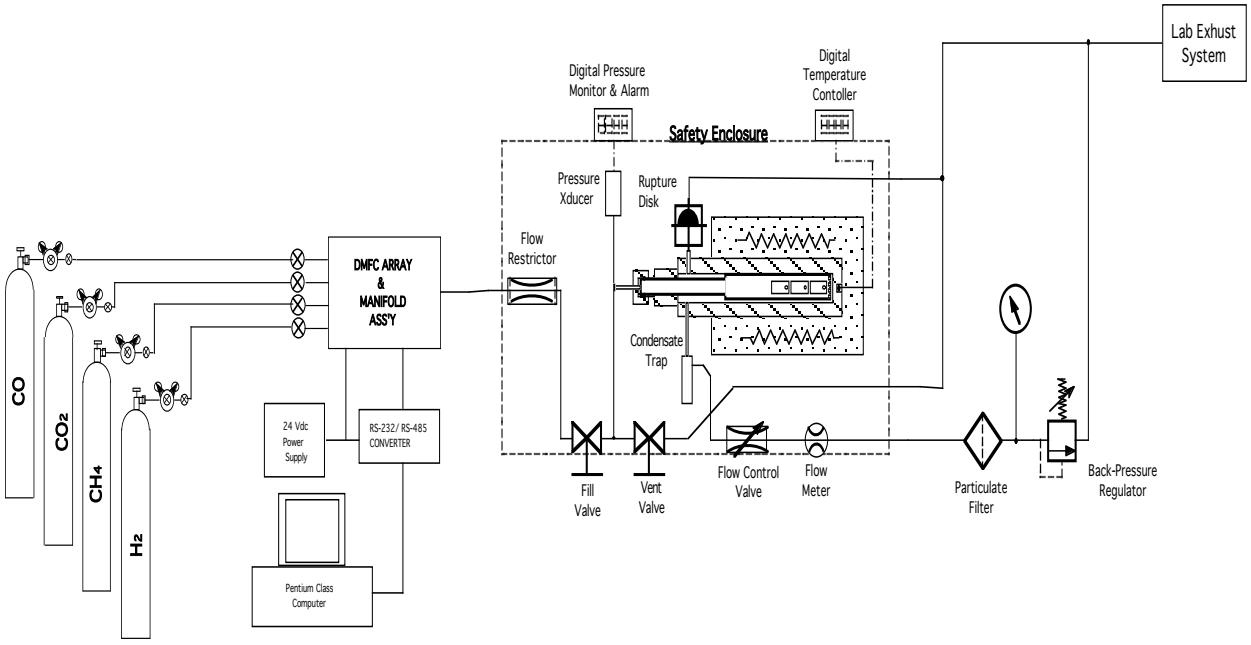

Figure 2.5. Schematic of high-pressure, high-temperature system for metal dusting experiments.

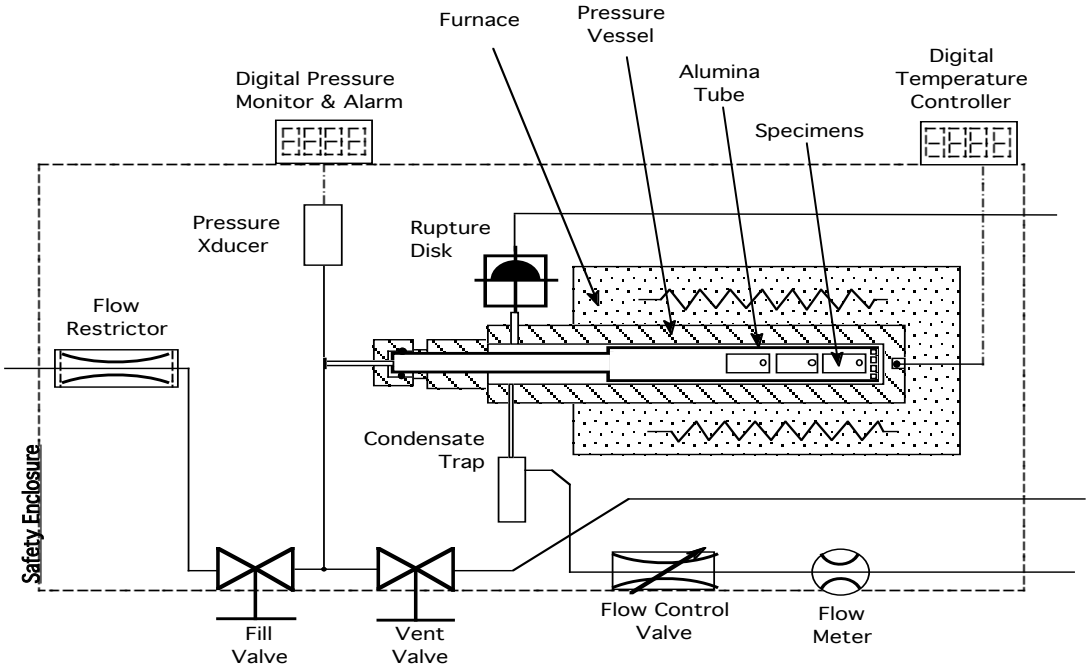

Figure 2.6. Magnified view of high-pressure region of the system shown in Fig. 2.5.

2.2 Surface Profiler to Measure Depth of Metal Dusting Pits

In several recent steering committee meetings, extensive discussions were held on the importance of key variables in understanding the metal dusting degradation of metallic structural materials. In addition, discussions on the posttest analysis of specimens identified the necessity of understanding the pit nucleation and growth (in particular, the pit geometry including diameter, depth, and shape), distribution, and density as a function of process variables such as temperature, gas chemistry, system pressure, and exposure time.

Later in 2005, we procured a surface profiler unit with a capability to measure the depth of pits in a nondestructive fashion so that we could measure and correlate the pit depth as a function of time after repeated exposures of a given specimen to the metal dusting environment. The surface profiler, procured from ADE Phase Shift, is equipped with a MicroXAM surface measurement system comprising a non-contact optical profiler. The surface roughness (and pit depth) of the alloys was measured by using a white light beam. Figure 2.7 shows a schematic of the profilometer system. Table 2.1 shows a listing of operational and performance specifications for the unit. The profilometer can measure pit depth up to 10 mm with a resolution of 0.92 μm. The measurement area is ≈0.8 x 0.6 mm^2 for a single scanning. However, the equipment can theoretically measure the entire area of the sample by stitching each small piece together with MapVue AE software. Figure 2.8 shows pits on a metallic specimen and typical size (diameter and depth) measurements made using the profiler.

Table 2.1 Specification for MicroXAM surface profiler

Objective magnification	**50X**	**20X**	**10X**	**5X**	**2.5X**
Numerical aperture	0.55	0.40	0.30	0.13	0.075
Measurement area (μm)	165x125	413x313	827x626	1654x1253	3308x2506
Spatial sapling (μm)	0.22x0.26	0.55x0.65	1.1x1.3	2.2x2.6	4.4x5.2
Optical resolution @ 550 nm (μm)	0.50	0.69	0.92	2.12	3.67
Working distance (mm)	3.4	4.7	7.4	9.3	10.3
Depth of focus @ 550 nm (μm)	1.16	2.19	3.89	20.72	62.25
Degress of maximum surface slope (EX mode)	22.6	9.5	4.8	2.4	1.2
Performance					
RMS repeatability (standard mode: 1nm		Lateral surface sampling: 0.11 to 8.8 μm			
RMS repeatability (standard mode: 1nm		Field of view: .084 x .063 mm @ 100X			
RMS repeatability (standard mode: 1nm		Maximum slope: 40 to 3.2 degrees			
Vertical scan range: 30, 100, or 5000 μm		Reflectivity: 1 to 100%			
Data acquisition time: up to 7.2 μm/s					

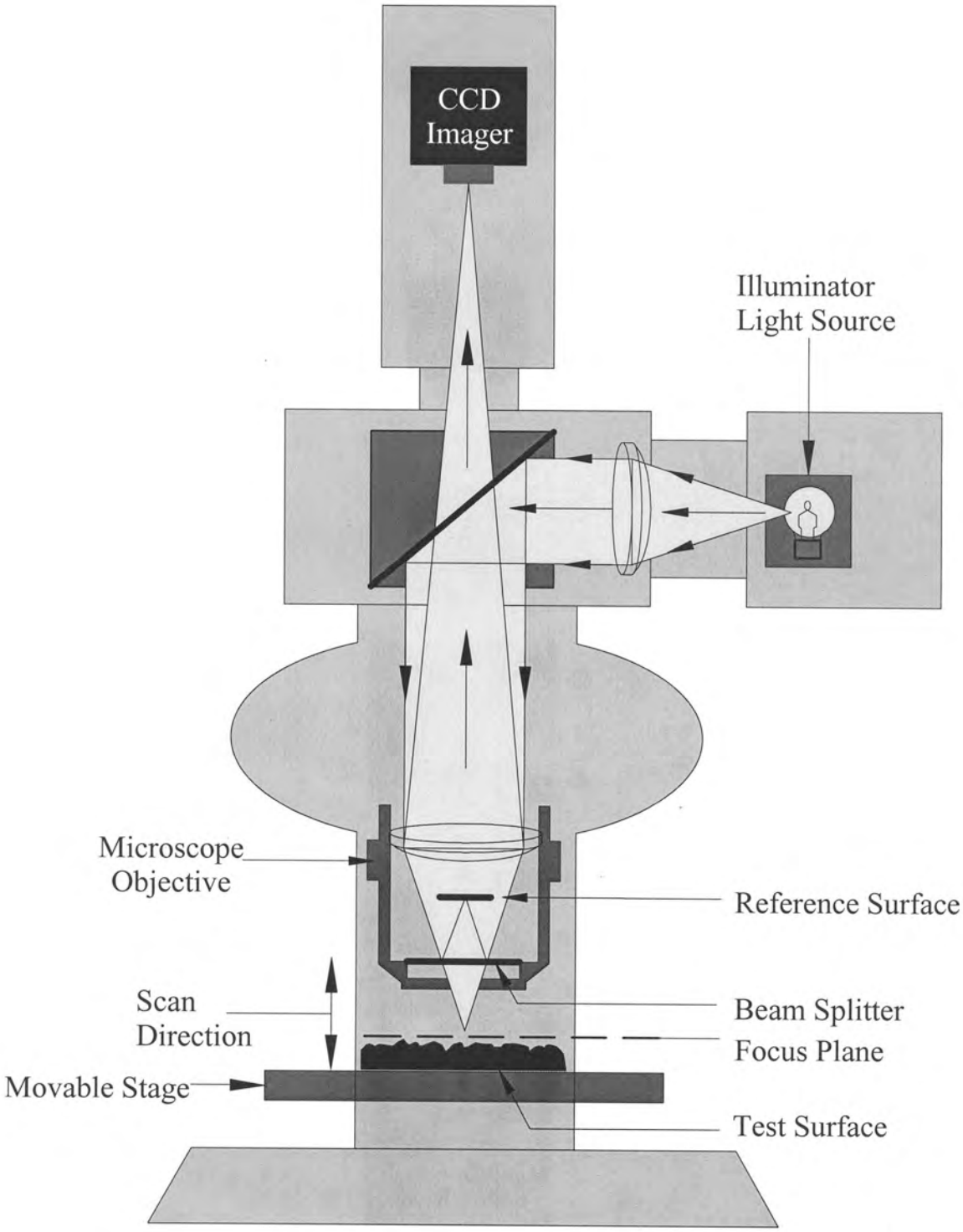

Figure 2.7. Schematic of MicroXAM surface profiler.

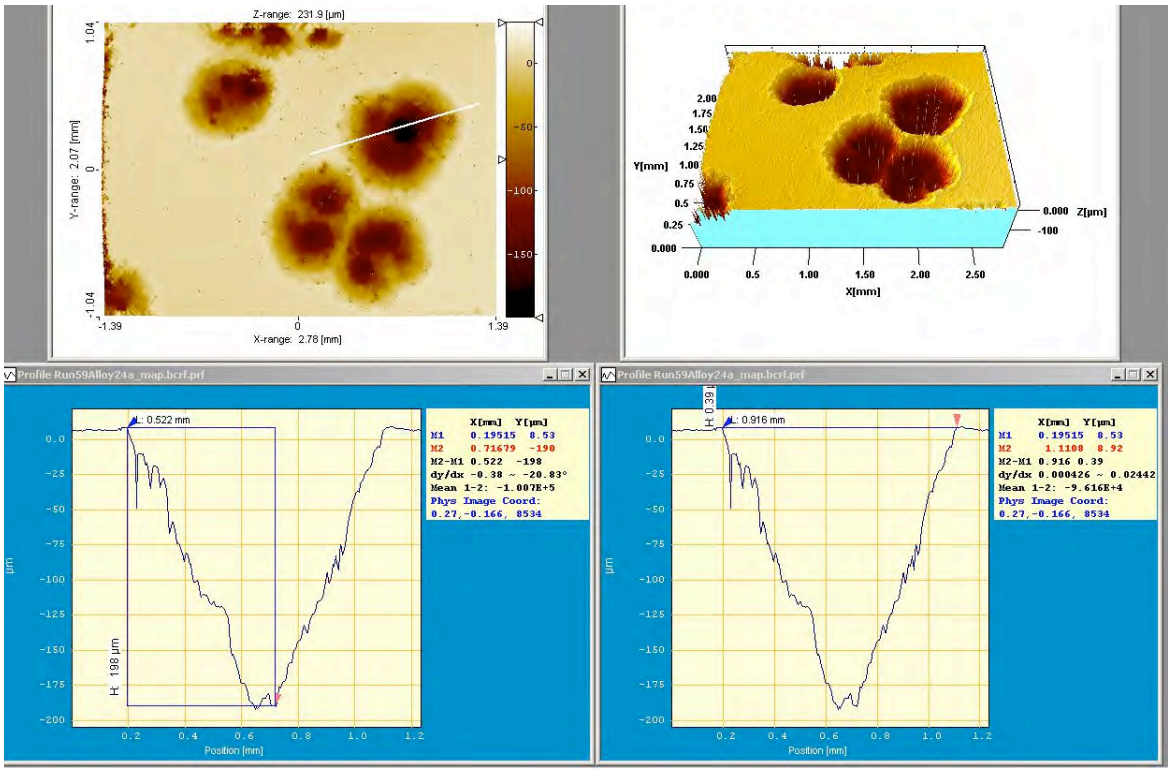

Figure 2.8. Example of a profile map measured by MicroXAM surface profiler.

2.3 X-ray Micro-beam Studies

Understanding the chemical composition, chemical state, and the crystallographic phase of each sub layer in the oxide scale is essential to establish the underlying processes that lead to metal dusting initiation and propagation. Also, a detailed knowledge of the degradation pathway can help develop strategies to slowdown or prevent the dusting corrosion. Given the micron and submicron size of the oxide scales and their sub layers, this is beyond the reach of many conventional analysis techniques, such as regular XRF and XRD. The size of a pit at an early stage is <1 µm and the thickness of the sub layers in the oxide scale is <0.8 µm, therefore, use of a submicron X-ray microprobe is mandatory for the success of proposed study. The combination of high flux and small spot size available at Advanced Photon Source (APS with 7GeV) undulator beamline enabled us to study spatially resolved crystallographic phases and chemical states of the oxide scales in metal dusting corrosion pits. We used X-ray microbeam fluorescence spectroscopy and diffraction to address the metal dusting corrosion.

Experiments were performed at the 2ID-D beamline of the APS at Argonne National Laboratory. Using zone plate diffraction gratings, the X-ray nanoprobe in the experimental station produces a monochromatic X-ray beam of size 200x300 nm with a photon flux of $5x10^9$ photons/s with an X-ray energy band width (dE/E) of 0.01%. The focal plane of the zone plate optics was adjusted so that the minimum spot size was obtained at the surface of the specimen. Figure 2.9 shows the scattering and data

acquisition geometry for the synchrotron radiation experiments: the beam upon incident on the region of interest on the specimen, the scattering intensity in a section of reciprocal space is captured by a flat, two-dimensional detector (CCD camera). Samples for the synchrotron radiation experiments were prepared in a similar manner as for the cross-section analysis in scanning electron microscopy. The beam energy was 8.5 KeV. The position of the oxide-metal interface was determined by monitoring the Fe-fluorescence counts as the sample was translated across the beam.

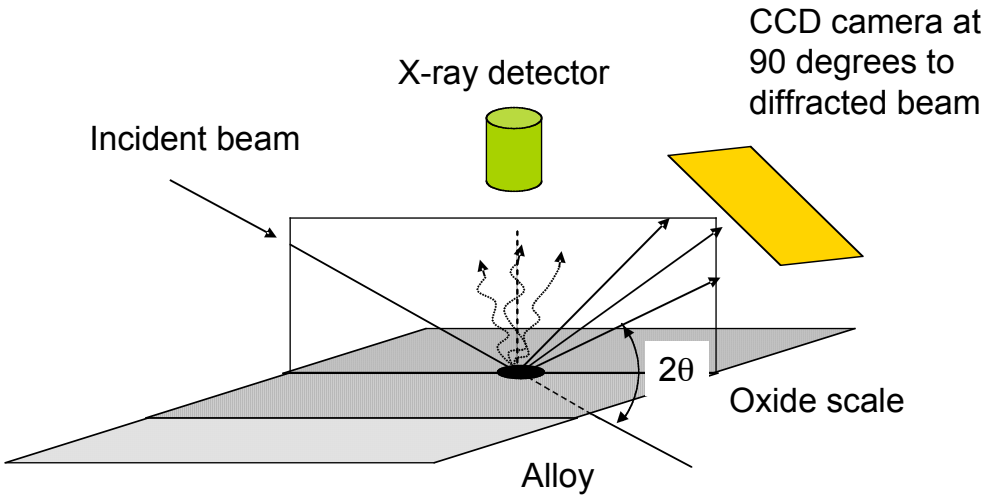

Figure 2.9. Schematic showing the geometry of data acquisition system at the synchrotron beamline.

2.4 Materials

The test program included a number of Fe- and Ni-base alloys, predominantly those commercially available, selected on the basis of Steering Committee discussions. Table 2.2 lists the nominal chemical compositions of the alloys selected for evaluation in the program. Heat analysis of all the alloys, provided by the alloy supplier, was maintained at Argonne National Laboratory. In addition, several surface-engineered alloy specimens (including surface coatings) were evaluated in the program. Only wrought alloys were evaluated.

The Fe-base alloys included a low-Cr ferritic steel (T22), an intermediate-Cr ferritic steel (T91), and several high-Cr ferritic and austenitic steels and other alloys. The Cr content of the latter alloys ranged between 17.3 and 28.0 wt.%. The Ni content of the high-Cr alloys ranged between 9.3 and 36.6 wt.%, except for ferritic alloys, which contained no/low nickel. Several of the Fe-base alloys contained a third element such as Al or Si, which has a high affinity for O. For example, MA956 and APMT contains 4.5 and 4.9 wt.% Al, respectively. Alloys 153MA, 253MA, and 353MA contain Si in a range of 1.3-1.6 wt.%, whereas Alloy 38815 contains 5.8 wt.% Si.

Generally, the Ni-base alloys had a much more complex chemical composition since they contained Cr (in a range of 15.4-28.8 wt.%) and several other elements, such

as, Mo (Alloys 617 and 625), Al (601, 617, 602CA, 214, and 693), and Si (45TM and HR 160). Further, several alloys contained Nb, W, and Co, which can also influence the oxidation behavior of the alloys and their resistance to metal dusting attack.

In addition to commercial Fe- and Ni-base alloys, several alloys were selected for fabricating weldments for evaluation in metal dusting environments. Table 2.3 lists the weldment alloys, filler metals, and supplier organizations. Six Ni-base alloys and four Fe-base alloys were used for the fabrication of weld specimens. Weldments of Type 347 and 310 stainless steels were prepared by electron beam (e-beam) and gas tungsten arc weld (GTAW) approaches.

Table 2.2 Chemical composition (in wt.%) of alloys selected for evaluation.

Material	C	Cr	Ni	Mn	Si	Mo	Al	Fe	Other
Fe-base alloys									
T22	0.20	2.3	–	0.6	0.5	1.0	-	Bal	–
T91	0.08	8.6	0.1	0.5	0.4	1.0	-	Bal	N 0.05, Nb 0.07, V 0.2
153MA	0.05	18.4	9.5	0.6	1.4	0.2	-	Bal	N 0.15, Ce 0.04
253MA	0.09	20.9	10.9	0.6	1.6	0.3	-	Bal	N 0.19, Ce 0.04
353MA	0.05	24.4	34.7	1.4	1.3	0.1	-	Bal	N 0.18, V 0.06
321L	0.02	17.4	9.3	1.8	0.5	-	-	Bal	N 0.02, Ti 0.3
310	0.03	25.5	19.5	1.7	0.7	-	-	Bal	-
800	0.08	20.1	31.7	1.0	0.2	0.3	0.4	Bal	Ti 0.31
803	0.08	25.6	36.6	0.9	0.7	0.2	0.5	34.6	Ti 0.6
38815	0.01	13.9	15.3	0.6	5.8	1.0	0.13	Bal	-
MA956	-	20.0	-	-	-	-	4.5	Bal	Ti 0.5, Y_2O_3 0.6
321	0.04	17.3	10.3	1.2	0.4	-	-	Bal	Ti 0.4, N 0.01
APMT	0.04	21.7	-	0.1	0.6	2.8	4.9	Bal	-
4C54	0.17	26.7	0.3	0.7	0.5	-	-	Bal	N 0.19
330	0.05	19	35	1.5	1.3	-	-	Bal	
430	0.08	16.5	-	0.5	0.5	-	-	Bal	
EBrite	0.01	28	0.5	0.4	0.4	-	-	Bal	
RA85H	0.20	18.5	14.5	0.8	3.5	-	1.0	Bal	
Crofer	0.03	22	0.8	0.5	-	-	0.5	Bal	La 0.2, Ti 0.2, Cu 0.5
Ni-base alloys									
600	0.04	15.4	Bal	0.2	0.1	-	-	9.7	-
601	0.03	21.9	61.8	0.2	0.2	0.1	1.4	14.5	Ti 0.3, Nb 0.1
690	0.01	27.2	61.4	0.2	0.1	0.1	0.2	10.2	Ti 0.3
617	0.08	21.6	53.6	0.1	0.1	9.5	1.2	0.9	Co 12.5, Ti 0.3
625	0.05	21.5	Bal	0.3	0.3	9.0	0.2	2.5	Nb 3.7, Ti 0.2
602CA	0.19	25.1	62.6	0.1	0.1	-	2.3	9.3	Ti 0.13, Zr 0.19, Y 0.1
214	0.04	15.9	Bal	0.2	0.1	0.5	3.7	2.5	Zr 0.01, Y 0.006
230	0.11	21.7	60.4	0.5	0.4	1.4	0.3	1.2	W 14, La 0.015
45TM	0.08	27.4	46.4	0.4	2.7	-	-	26.7	RE 0.07
HR 160	0.05	28.0	Bal	0.5	2.8	0.1	0.2	4.0	Co 30.0
693	0.02	28.8	Bal	0.2	-	0.1	3.3	5.8	Nb 0.7, Ti 0.4, Zr 0.03
333	0.05	25	45	1.5	1.0	3	-	18	Co 3, W 3
HR120	0.05	25	37	0.7	0.6	2.5	0.1	33	Co 3, W 2.5, N 0.2

Table 2.3 List of weldment details.

Weldment designation	Base alloy	Filler metal/Welding procedure	Supplier organization
Ni-base alloy weldments			
W1	602CA	S 6025/GTAW	Krupp VDM
W2	230	230W/GTAW	Haynes International
W3	HR160	HR160/GTAW	Haynes International
W5	690	FM52/GTAW	Special Metals
W6	693	53MD/GTAW	Special Metals
W7	601	601/GTAW	Special Metals
Fe-base alloy weldments			
W4	803	617/GTAW	Special Metals
W8	347	No filler, e-beam	Argonne National Laboratory
W9	310	No filler, e-beam	Argonne National Laboratory
W10	353MA	353MA/GTAW	Outokumpu
W11	310	ER310/ GTAW	Allegheny Ludlum
W12	347	347/GTAW	Allegheny Ludlum

2.5 Specimen Preparation

The samples were flat coupons with approximate dimensions of 12 x 20 x 1 to 2 mm. They were sheared slightly oversize, and their edges were milled to remove cut edges and reduce the coupons to final size. A standard surface finish was used for all alloy specimens. The finish involved a final wet grinding with 400-grit SiC paper. The surface-engineered specimens were used in the as-fabricated condition. In the tests to evaluate the effect of surface preparation on metal dusting, specimen surfaces were prepared by electropolishing, mill annealing, shot peening, etc. Stenciling or electric engraving at the corner of the coupons identified all of the specimens. Prior to testing, specimens were thoroughly degreased in clean acetone, rinsed in water, and dried. The specimen dimensions were measured to ±0.02 mm, and the total exposed surface area, including edges, was calculated. The specimens were weighed to an accuracy of 0.1 mg. All the weldments were tested in the as-welded condition.

2.6 Post-exposure Analysis of Specimens

Several analytical approaches and techniques were used to evaluate the tested specimens. These included specimen weight in as-exposed and cleaned conditions, pitting size and density (pits per unit area of surface), pit depth (average depth over significant number of pits), and substrate penetration as determined by metallographic examination. After the specimens were weighed in the as-exposed condition, deposits

on the specimens were mechanically removed with a soft brush, and the deposit material was analyzed for metal content, if warranted. The brushed specimens were cleaned ultrasonically to remove residual deposits and then washed in water and dried. Subsequently, the specimens were weighed, and the weight gain/loss was noted. The cleaned specimens were examined for surface pits by optical microscopy. This procedure allowed determination of the number of pits present in different regions of the specimen and the pit density. In addition, the sizes of several pits were measured and averaged to establish an average pit size. Surface profiler measurements were made to determine the pit size, including depth. This non-destructive approach in characterizing the pits enabled monitoring the pit growth as a function of exposure time.

At the end of a given run, several of the cleaned specimens (after weighing and pit measurement) were cut and mounted on the cut faces for metallographic polishing and examination in the as-polished condition (with chemical etching, if needed) by optical and/or scanning electron microscopy. Pit depth and substrate penetration thickness were measured in all the exposed specimens. The remaining good metal was calculated as the difference between the original thickness and the thickness unaffected by substrate penetration after exposure.

Raman spectra were excited with 60 mW of 476-nm radiation from a Kr-ion laser. The scattered light was analyzed with a triple Jobin-Yvon grating spectrometer. All of our spectra were acquired in 300 sec at room temperature.

2.7 Metal Dusting Experiments

Table 2.4 lists the experimental conditions used for the various metal dusting runs. The list includes the test temperature, system pressure, gas chemistry, exposure time, alloys tested, and the purpose for conducting these experiments. The specimens from Runs 1-32 were extensively analyzed, and the results were discussed in an earlier report and in several publications.[9,11-19] Several conclusions were drawn from that study:

- One of the major consequences of carbon deposition is the degradation of structural materials by a phenomenon known as “metal dusting.” There are two major issues of importance in metal dusting. First is the formation of carbon from the gas mixture and subsequent deposition of carbon on metallic materials. Second is the initiation of metal dusting in the alloy and subsequent propagation of the degradation. The first is influenced by the a_C in the gas mixture and the availability of the catalytic surface for carbon-producing reactions to proceed. There may be a threshold in a_C (>>1) for carbon deposition. Metal dusting of the alloy in the reformer environments is determined by a competition between the oxide scale development and access of the virgin metal surface to the carbon deposit.

- A new metal dusting mechanism was proposed in this study. Mechanisms for degradation of both Fe- and Ni-base alloys are related to the catalytic crystallization of carbon that deposits from the gaseous environment. The only difference is that iron carbide acts as a catalyst in Fe-base alloys, whereas nickel metal instead of

nickel carbide (which is thermodynamically not stable) acts as a catalyst in Ni-base alloys. To achieve good crystallinity, carbon dissolves, diffuses through the alloy, and precipitates at defects of iron carbide or nickel metal. The accumulation of carbon leads to separation of carbide or nickel grains into nano-size particles. The free energy difference between poorly and well crystalline carbon is the driving force for both metal dusting and the growth of carbon nano-filaments. We believe that the proposed mechanism can explain more of the experimental observations made regarding Fe- and Ni-base alloys subjected to metal dusting degradation.

- Tests were conducted on several alloys at 482, 593, and 704°C. The metal dusting rate at 593°C was the highest. However, further study was needed to establish the temperature dependence of metal-dusting rates in different alloys and to relate the metal wastage rates to the carbon activity in the exposure environment, including system pressure and temperature.

- The local nature of dusting (initiated by pits on the alloy surface) on structural alloys showed that defects in the oxide scales play a large role in initiation. Oxide scaling may not occur if a_C is >>1 and/or if the H_2O content in the environment is very low. Laboratory experiments have clearly indicated the effect of gas chemistry (in particular, H_2O content) in the scaling, carbon deposition, and dusting initiation. The environment in reformers is high enough in pO_2 that a Cr-rich alloy can develop a chromia scale (given enough exposure time) before carbon deposition. The presence of an oxide scale may not prevent metal dusting but can delay its initiation, thereby slowing the overall attack.

- Raman spectra showed the existence of spinel, Cr_2O_3, and disordered chromium oxide in the scale grown on high-chromium Fe-base alloys. All three phases act, to different degrees, as protective layers to prevent alloys from metal dusting corrosion. The spinel phase is not as stable as Cr_2O_3 and could be reduced by the deposited carbon, and metal dusting corrosion would initiate from these locations.

- The phase composition of the oxide scale is important in metal dusting corrosion. Cr_2O_3 is a better phase than spinel to resist metal dusting since spinel can be reduced. If alloys can generate more Cr_2O_3 phase and less spinel phase on the alloy surface, their ability to resist metal dusting will increase. Therefore, alloys with more Cr and less Fe content performed well in a carburizing atmosphere. The phase composition of the oxide scale changes with exposure time: spinel phase content increases and chromium oxide phase content decreases. Therefore, alloys are easily attacked by metal dusting after long time exposure since spinel phase content increases.

- Metal dusting degradation involves two steps, namely, incubation and propagation. The incubation period is determined by the carbon activity in the gas phase, alloy chemistry, system pressure, and probably the exposure temperature. For the same exposure conditions, the incubation period for the onset of metal dusting is significantly greater for the Ni-base alloys than that for Fe-base alloys.

- Higher carbon activity may lead to higher metal loss rate, since higher carbon activity provides higher driving force to form highly disordered carbon on the metal surface.

- High system pressure not only increases the carbon activity but also seems to accelerate the carbon transport into the alloy and to reduce the incubation time for onset of metal dusting.

- Both aluminum and silicon additions increased the ability of alloys to resist metal dusting. However, silicon addition failed to protect alloys from metal dusting at high pressure, although it was beneficial at 1-atm pressure tests. High Cr content in alloys is necessary but not sufficient to resist metal dusting. Iron content (especially in Ni-base) in the alloy is detrimental and should be maintained as low as possible to extend the life of the alloy. Cobalt addition is not beneficial in resisting metal dusting.

- MA956, APMT, and 4C54 are the best three Fe-base alloys to resist metal dusting. Two of the three alloys contain Al (4.5% in MA956 and 4.9% in APMT). Alloy 4C54 contains a high Cr level of 26.7%.

- Ni-base alloys performed better than Fe-base alloys when exposed to similar atmospheres. Among the Ni-base materials, Alloy 693 was the best, which can be attributed to its high Cr and Al contents. Alloy 602CA was good in most of the tests, but it was attacked in high-carbon-activity Gas 17.

- Surface modification (by preoxidation and/or coatings) and alternative materials were examined at ANL to alleviate the metal dusting problem. The advantage of oxide coatings is that they can minimize carbon-producing reactions (by reducing the availability of catalytic surface) and can also act as a barrier to minimize carbon ingress and pitting of the substrate alloy. Test results showed a beneficial effect, but long-term tests are needed to substantiate the results.

- We have examined in-situ development of oxide scales as a means to prevent or minimize metal dusting attack. Test results showed that the performance of pre-oxidized samples was worse than the samples without pre-oxidation. More spinel phase was found on the surface of alloys that were pre-oxidized. The spinel phase, especially if it contained a high Fe content, was detrimental and led to an increase in metal dusting corrosion.

During the course of the current project, we have developed a substantial body of information on both Fe- and Ni-base alloys upon exposures to gas mixtures that encompass a wide range of compositions and carbon activity. Data were also developed on the long-term performance of the alloys in environments that simulate the reformer effluent at atmospheric and high pressures. Since the initiation time for the Ni-base alloys is fairly large, we have developed pre-pitting approaches to shorten the initiation period and expedite the study of pit propagation and growth in these alloys. Furthermore, we have developed methods to mitigate metal dusting by intermediate

oxidation of the partially metal dusted alloys. During the past three years, we have also developed several Ni- and Cu-base alloys, the compositions of which were based on our fundamental understanding of metal dusting initiation and propagation. These alloys were fabricated into coupons and tested in simulated metal dusting environments, and their performance were compared with that of other commercial alloys. Information on various aspects of the project is presented in subsequent sections of this report.

Table 2.4. Experimental conditions for laboratory runs.

Run Number	Experimental conditions	Gas mixture #	Objective
1	593°C, 1 atm, 48 h	6	Program start
2	593°C, 1 atm, 100 h	4	No water
3	593°C, 1 atm, 100 h	5	2 vol.% H_2O
4	704°C, 1 atm, 100 h	4	Effect of temperature, H_2O
5	704°C, 1 atm, 100 h	5	"
6	593°C, 1 atm, 5 h	5	Effect of time, H_2O
7	593°C, 1 atm, 5 h	4	"
8	593°C, 1 atm, 72 h	4	Ceramics only (no catalysis)
9	593°C, 1 atm, 72 h	5	"
10	593°C, 1 atm, 90 h	4	New system validation
11	593°C, 1 atm, 115 h	4	Fe specimen only
12	593°C, 1 atm, 115 h	Gas 4+H_2O	Fe specimen only
13	593°C, 1 atm, 100 h	Gas 4+H_2O	Ni specimen only
14	593°C, 1 atm, 100 h	4	Ni specimen only
15	593°C, 1 atm, 1000 h	2	Fe-base alloys
16	593°C, 1 atm, 1000 h	2	Ni-base alloys
17	482°C, 1 atm, 100 h	2	Fe specimen only
18	482°C, 1 atm, 100 h	2	Ni specimen only
19	593°C, 1 atm, 1000 h	Gas 2, low H_2O	Fe-base alloys
20	482°C, 1 atm, 1000 h	2	Fe-base alloys
21	482°C, 1 atm, 1000 h	2	Ni-base alloys
22	704°C, 1 atm, 98 h	High CO Gas	Fe, T91, 304
23	704°C, 1 atm, 98 h	"	Ni, Ni-base alloys
24	704°C, 1 atm, 102 h	No water	Ni, Ni-base alloys
25	593°C, 1 atm, 1000 h	2	Fe-base alloys, preoxidized at 750°C in air
26	593°C, 1 atm, 1000 h	2	Ni-base alloys, preoxidized at 750°C in air
27	593°C, 1 atm, 142 h	2	Pack diffusion coatings/Fe-base alloys
28	593°C, 1 atm, 300 h	2b	Fe-base, preoxidized in 75% CO-25% CO_2 at 900°C for 200 h
29	593°C, 1 atm, 300 h	2b	Ni-base, preoxidized in 75% CO-25% CO_2 at 900°C for 200 h
30	593°C, 1 atm, 1040 h	2	Aluminized coating
31	593°C, 1 atm, 300 h	2b	Fe-base, preoxidized in 98% H_2-2% H_2O at 900°C for 200 h

32	593°C, 1 atm, 300 h	2b	Ni-base, preoxidized in 98% H_2-2% H_2O at 900°C for 200 h
33	593°C, 1 atm, 163 h	4	Cu coated Fe, Ni, 800
34	593°C, 1 atm	4	Cu clad rod of Fe
35	593°C, 1 atm, 784 h	4	Cu clad Fe
36	593°C, 1 atm, 288 h	4	Glidcop alloy
37a	593°C, 1 atm, 120 h	4	Cu clad Fe
37b	593°C, 1 atm, 120 h	4	Cu clad Fe, reversed gas flow
37c	593°C, 1 atm, 552 h	4	Cu clad Fe, continuation of 37b
38HP	593°C, 40.8 atm, 90 h	8	Fe base
39HP	593°C, 40.8 atm, 100 h	8	Fe base
40	593°C, 1 atm, 119 h	9	Fe base
41HP	593°C, 27.2 atm, 100 h	8	Fe base
41R	593°C, 27.2 atm, 140 h	8	Fe base
42HP	593°C, 14.3 atm, 100 h	8	Fe base
43HP	593°C, 40.8 atm, 100 h	13	Fe base
44	593°C, 1 atm, 122 h	4	Fe and Ni base
45	593°C, 1 atm, 300 h	4	Fe and Ni base
46	593°C, 1 atm, 300 h	4	Fe and Ni base
47	593°C, 1 atm, 300 h	4	Fe and Ni base
48	593°C, 1 atm, 122 h	13	Fe and Ni base
49HP	593°C, 14.3 atm, 1131 h	10	Fe base
50HP	593°C, 14.3 atm, 100 h	10	Ni base
51HP	593°C, 40.8 atm, 113 h	10	Ni base
52HP	593°C, 40.8 atm, 680 h	10	Fe base
53	593°C, 1 atm, 8438 h	11	Fe base
54	593°C, 1 atm, 7,589 h	11	Ni base
55	593°C, 1 atm, 6678 h	17	Ni base
56	593°C, 1 atm, 8157 h	14	Ni base
57	593°C, 1 atm, 3447 h	15	Ni base
58	593°C, 1 atm	16	Ni base
59HP	593°C, 14.3 atm, 9700 h	10	Ni base
60	593°C, 1 atm, 246 h	10	Ni base
61	593°C, 1 atm, 13,842 h	21	Ni base
62	815°C, 1 atm, 5716 h	20	Heat treat alloys
63	593°C, 1 atm, 9109 h	21	Ni-base alloy weldments
64HP	593°C, 30 atm, 3500 h	18	Ni base – pre pit alloys
65	593°C, 1 atm, 1136 h	21	Fe-base weldments
66	593°C, 1 atm, 2136 h	20	Fe and Ni base

3. PRE-PITTING EXPERIMENT

Alloys are generally protected by thin oxide scales, which form when they are exposed to metal dusting environments. As defects develop in the oxide scale, locally, pits start to form due to carbon ingress, and the pits continue to grow at several isolated locations on the oxide surface.[20-29] The metal dusting process involves two steps: onset of initiation and propagation, the latter being more important since the metallic components in service are expected to last years and the rate of attack plays a large role in establishing the component service life. However, even the not-so-resistant Ni-base alloy can have an incubation time of the order of a few thousand hours; therefore, it is desirable to expedite the initiation step for the Ni-base alloys and to conduct propagation tests in the laboratory over long time periods in environments that simulate process conditions.

For this reason, we initiated a program to develop pre-pitting approaches. In several instances, the pits seem to develop along the edges of specimens and eventually grow over the surface. Figure 3.1 shows pits that developed in Alloy 800 and Type 321 stainless steel upon exposure to the metal dusting environment. Most pits appeared at the edge of Alloy 321, and the pits of Alloy 800 coalesced to larger areas at the edge. While carbon diffusion is retarded by the oxide scale on the flat surface, more defects are expected at the sharp edge, as shown in Fig. 3.2.

Since the Fe-base alloys, generally, exhibit shorter initiation time than the Ni-base alloys, we used Alloy 800 and Fe-9Cr-1Mo steel as surrogates to evaluate our experimental approach for pre-pitting. At least two methods are able to break the oxide scale without a long incubation time and to initiate pitting. First is a mechanical, and the second is chemical. We focus on the mechanical method in this report. If this method is successful, we can apply it to Ni-base alloys that have a long incubation time.

Surfaces of Alloy 800 and 9Cr-1Mo steel were scratched by an engraver with a carbide-tipped point. Figure 3.3 shows the sample before exposure in a metal dusting experiment. Both alloys were exposed to a flowing carburizing atmosphere consisting of 72.2% H_2-8.3% CO_2-17.6% CO-1.96% H_2O at 593°C. After each exposure period, the specimens were examined with a scanning electron microscope. Any adhering coke was removed with an ultrasonic bath and acetone.

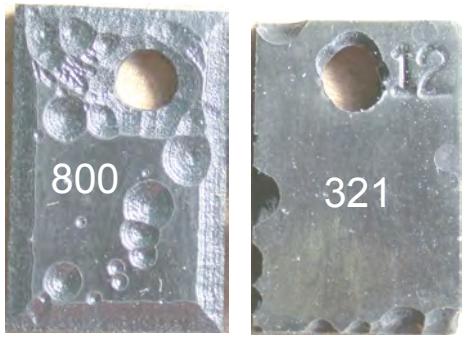

Figure 3.1. Metal dusting pits on the edges of Alloy 800 and Type 321 stainless steel.

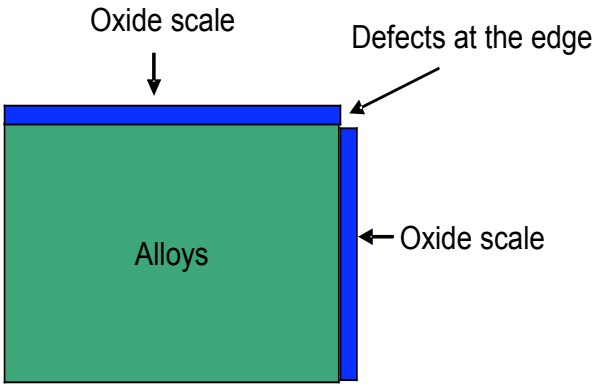

Figure 3.2. Schematic of scale cracking at the corner of the alloy.

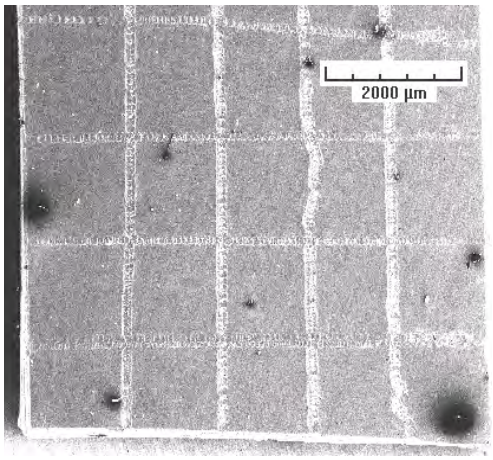

Figure 3.3. Alloy 800 scratched by an engraver with carbide-tipped point.

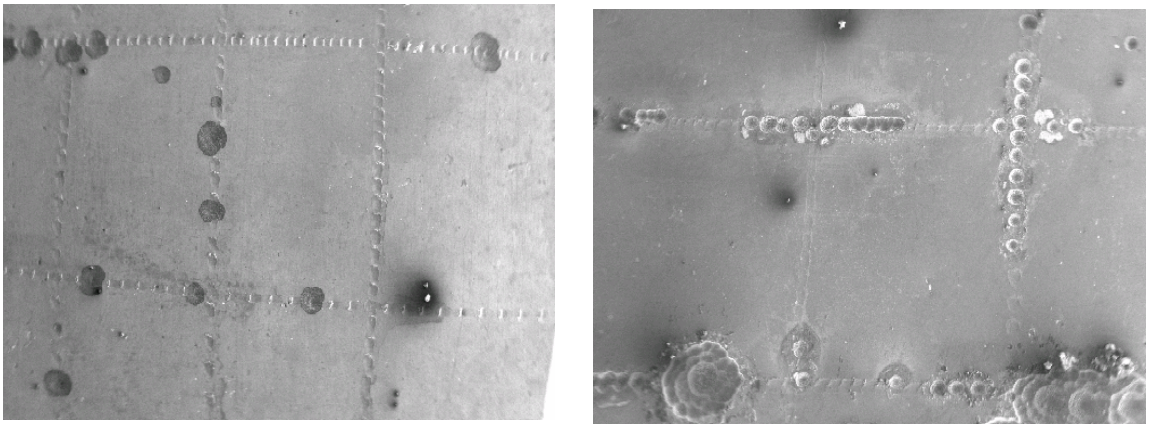

Area 1

Area 2

Figure 3.4. Metal dusting pits on Alloy 800 after 6-day exposure to a flowing carburizing atmosphere consisting of 72.2% H_2-8.3% CO_2-17.6% CO-1.96% H_2O at 593°C.

Metal dusting pits appeared along the scratched area on the surface of Alloy 800. At area 1 in Fig. 3.4, only one pit appeared at the non-scratched area. The other 12 pits appeared along the scratched lines. In area 2 in Fig. 3.4, 38 pits appeared along the

scratched lines, and only one pit appeared at the non-scratched area. With 9Cr-1Mo steel, metal dusting pits also appeared at the scratched areas. Small pits (Fig. 3.5) grew to large pits (Fig. 3.6) and finally coalesced to area wide degradation (Fig. 3.7). These results indicate that pitting can be initiated by a mechanical scratching approach. They also suggest that the alloy surface should not have scratch-like defects, since those regions can act as pit-initiation sites when exposed in the metal dusting environment.

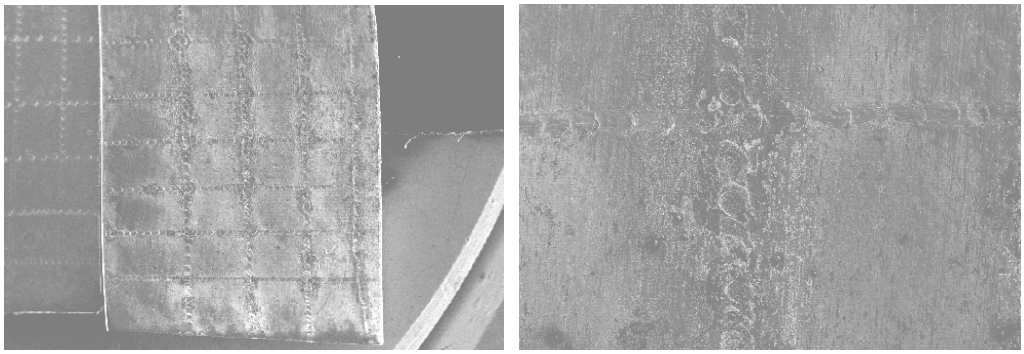

10 X 50X

Figure 3.5. Metal dusting pits on Alloy 9Cr-1Mo after 2-day exposure to a flowing carburizing atmosphere consisting of 72.2% H_2-8.3% CO_2-17.6% CO-1.96% H_2O at 593°C.

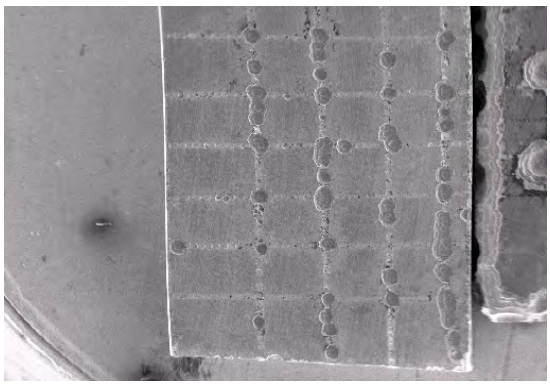

Figure 3.6. Metal dusting pits on Alloy 9Cr-1Mo after 4-day exposure to a flowing carburizing atmosphere consisting of 72.2% H_2-8.3% CO_2-17.6% CO-1.96% H_2O at 593°C.

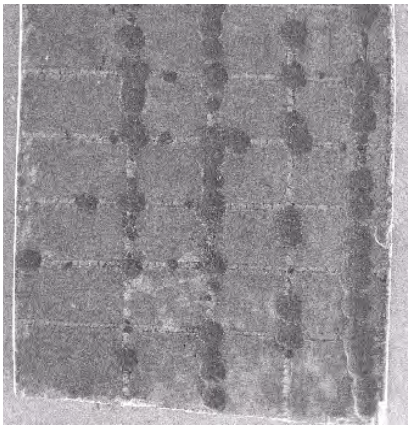

Figure 3.7. Metal dusting pits on Alloy 9Cr-1Mo after 6-day exposure to a flowing carburizing atmosphere consisting of 72.2% H_2-8.3% CO_2-17.6% CO-1.96% H_2O at 593°C.

To understand the effect of scratches on the metal dusting corrosion, we scanned the scratched area with energy-dispersive X-ray (EDX) analysis. However, EDX could not locate small channels (Fig. 3.8) for carbon transfer. One possible reason is that the channel is not a straight line perpendicular to the alloy surface. Electrons go straight down to the oxide scale in the EDX experiment. The composition difference between the channels of carbon transfer and the oxide scale could not be distinguished by EDX because the signals from the channels were masked by signals from the oxide scale. One possible method to locate these channels of carbon transfer is to measure the electrical resistance on the surface. Oxides such as chromium oxide and spinel are insulators at room temperature, but Ni and Fe_3C are good conductors. If there is a channel consisting of Ni metal or Fe_3C, its electrical resistance will be much smaller than that of oxide scale.

The procedure for detecting the low-resistance area on the surface of alloys is to deposit metal (such as copper) particles by an electrochemical method. Figure 3.9 shows a device in which copper is deposited on the alloys by immersing them in the $CuSO_4$ solution and applying a voltage across the electrodes. The areas with low resistance will have deposits of copper particles because current can pass through them. Deposited copper particles thus act as an indicator to locate the carbon transfer channels. Such areas can be identified under a microscope and probably indicate regions of active degradation via metal dusting.

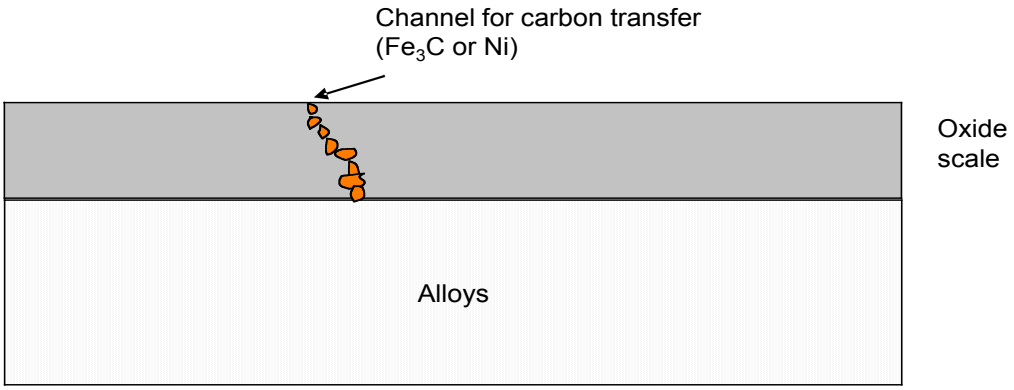

Figure 3.8. Model of possible carbon transferring channel.

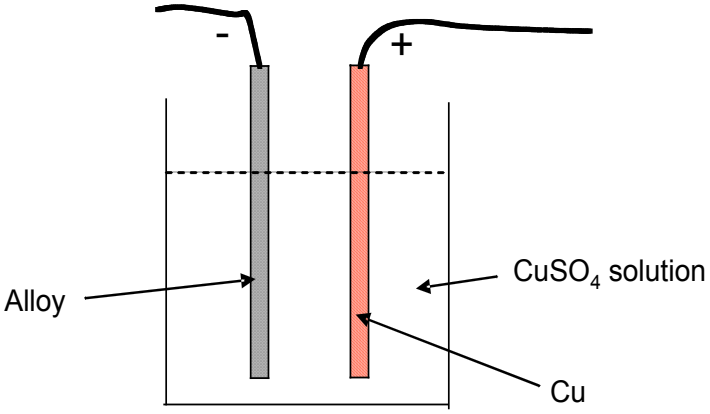

Figure 3.9. Device for electrochemical deposition of copper.

Figures 3.10 and 3.11 show alloy surfaces from copper indicator experiment. Copper accumulated at the scratched regions in both Alloy 800 and 9Cr-1Mo, indicating the susceptibility of these locations to metal dusting. If there is a metal dusting pit, most of the copper accumulates at the pit (Fig. 3.12).

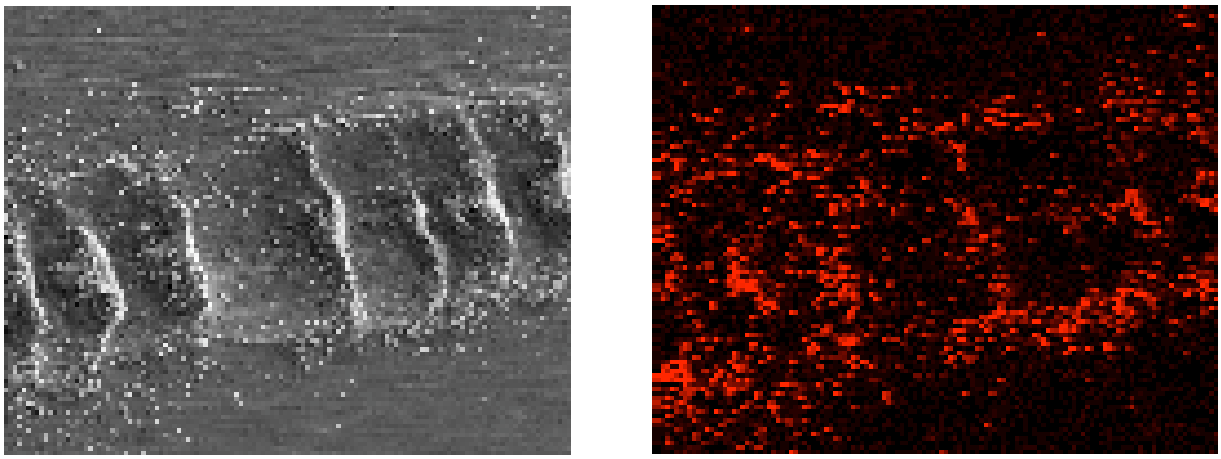

Figure 3.10. Left: SEM micrograph of Alloy 800 after exposure to a carburizing atmosphere. The surface was scratched by an engraver prior to exposure. Right: Copper electrochemically deposited on the Alloy 800 surface. The copper enhancement (in scratched areas) indicates regions susceptible to metal dusting.

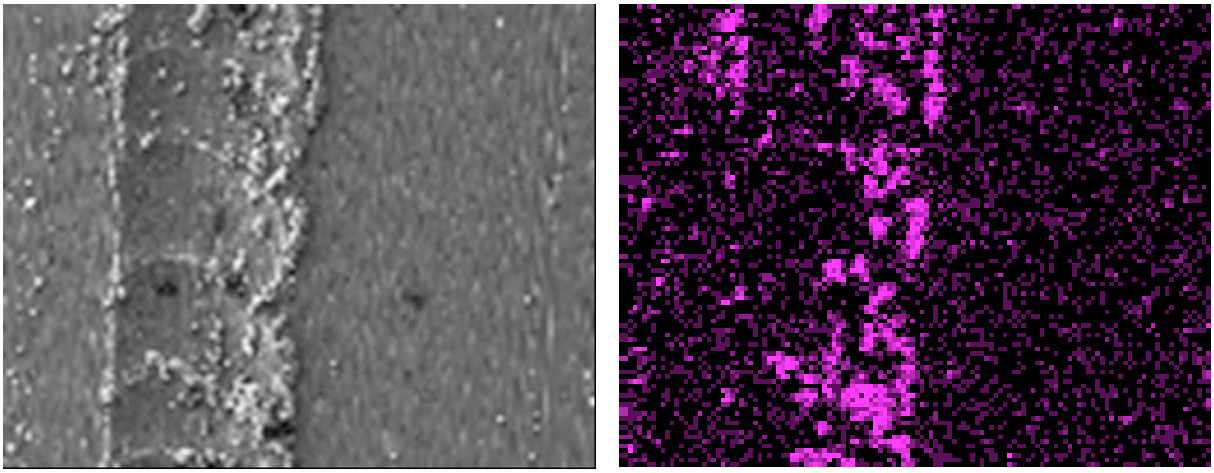

Figure 3.11. Left: SEM micrograph of Alloy 9Cr-1Mo after exposure to a carburizing atmosphere. The surface was scratched by an engraver prior to exposure. Right: Copper was electrochemically deposited on the Alloy 9Cr-1Mo surface. The copper enhancement (in scratched areas) indicates regions susceptible to metal dusting.

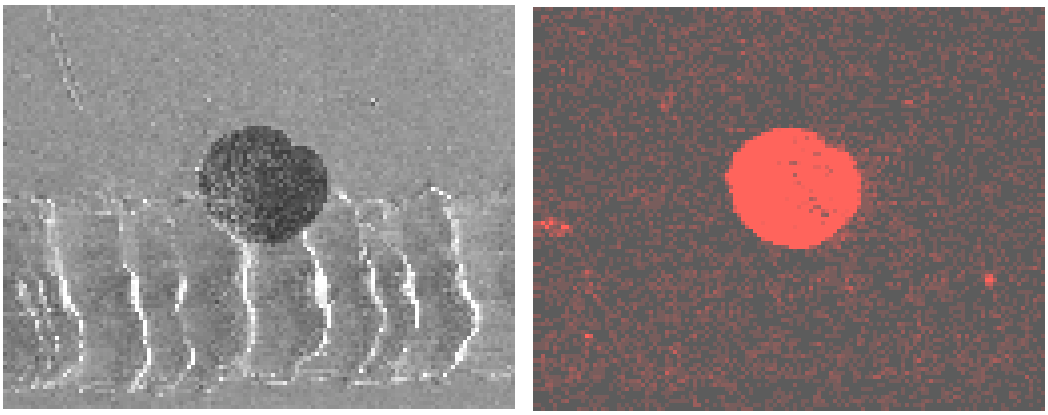

Figure 3.12. Left: SEM micrograph of Alloy 800 after exposure to a carburizing atmosphere. The surface was scratched by an engraver prior to exposure. A single pit was observed along the scratch line. Right: Copper electrochemically deposited on the surface of Alloy 800.

Similar pre-pitting experiments were conducted with Ni-base alloys that were scratched with a diamond tip. The effect of temperature on the pit growth of Ni-based alloys was studied. We found that the temperature effect differed with alloy composition. The behavior of Alloy 601 was similar at 593 and 704ºC. SEM photomicrographs show that the pit diameter in Alloy 601 after exposure to a carburizing gas mixture at 593ºC for 500 h is close to that exposed at 704ºC (Fig. 3.13). However, the pit depths were different. Figure 3.14 shows the pit depths, measured by the surface profiler, in Alloy 601 exposed at the two temperatures. The pit depths were 27.2 and 61.8 μm at 593 and 704°C, respectively, after 500-h exposure to a carburizing gas consisting of 50% H_2 and 50% CO.

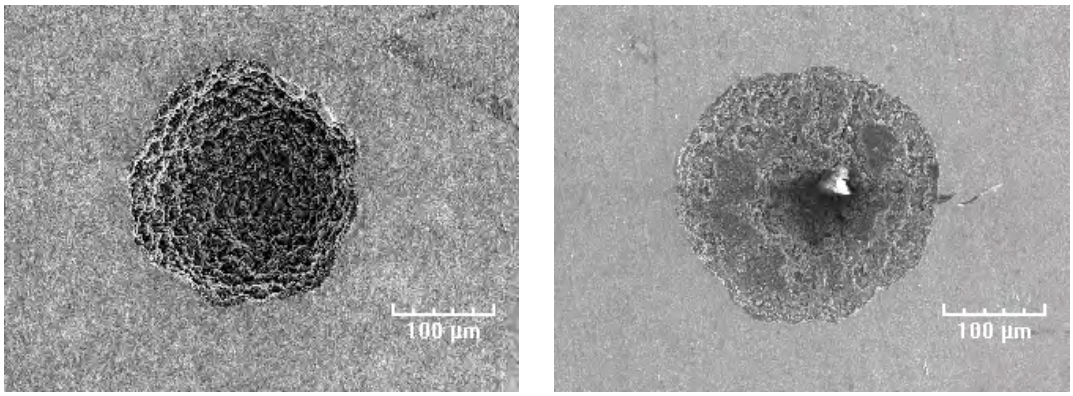

Alloy 601 tested at 704ºC Alloy 601 tested at 593ºC

Figure 3.13. SEM micrographs of Alloy 601 after 500-h exposure to a carburizing gas consisting of 50% H_2 and 50% CO at 704 and 593ºC.

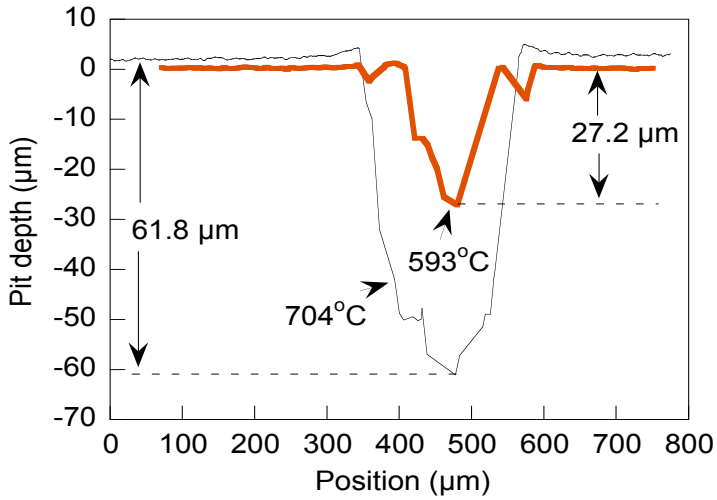

Figure 3.14. Surface profile of Alloy 601 after 500-h exposure to a carburizing gas consisting of 50% H_2 and 50% CO at 593 and 704ºC.

Pits developed faster on Alloy 617 at 593ºC than at 704ºC. Figure 3.15 shows that only two small pits appeared on Alloy 617 when the sample was exposed to a carburizing gas at 704ºC, whereas the pit density on the alloy However, pit density on Alloy 617 exposed to the same gas at 593ºC was as high as 250 pits/cm^2. The pits were shallow at both 593 and 704ºC, but the pit propagation rate was higher at 704ºC than at 593ºC.

The behavior of Alloy 602CA was different from that of Alloy 617. Figure 3.16 shows deep pit (≈73 μm) that formed in Alloy 602CA after 500-h exposure to a carburizing gas at 704ºC. However, when this alloy was tested at 593ºC, no real pit was observed, but some material grew out of the surface of Alloy 602CA (Fig. 3.17), which may be the early stage of a pit growth. Alloy 214 developed big and deep pits at 704ºC (Fig. 3.18), but the pit density was much higher at 593ºC than at 704ºC.

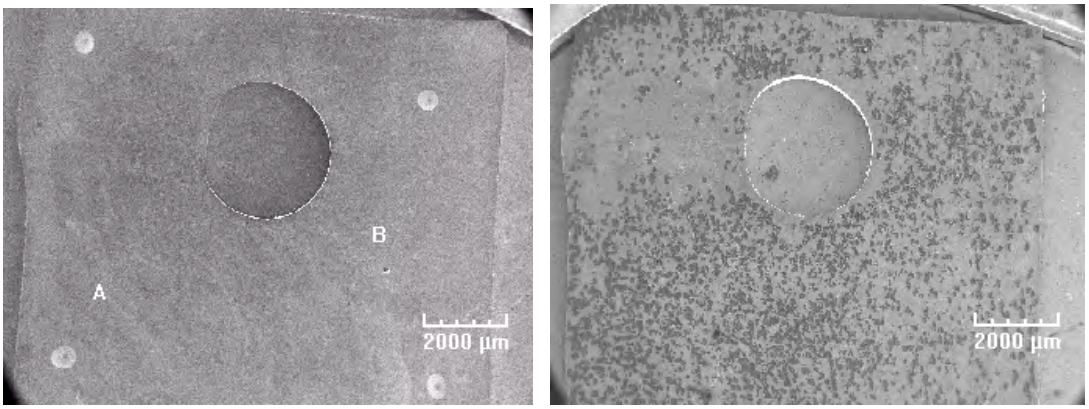

Alloy 617 tested at 704ºC Alloy 617 tested at 593ºC

Figure 3.15. SEM photomicrographs of Alloy 617 after 500-h exposure to a carburizing gas consisting of 50% H_2 and 50% CO at 704 and 593ºC.

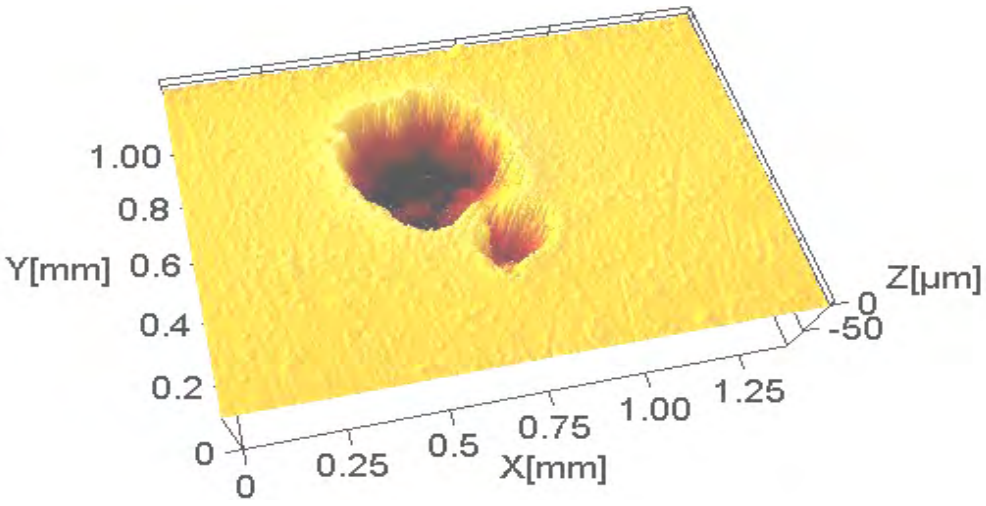

Figure 3.16. Profile map of Alloy 602CA exposed to a carburizing gas consisting of 50% H_2-50% CO at 704ºC for 500 h.

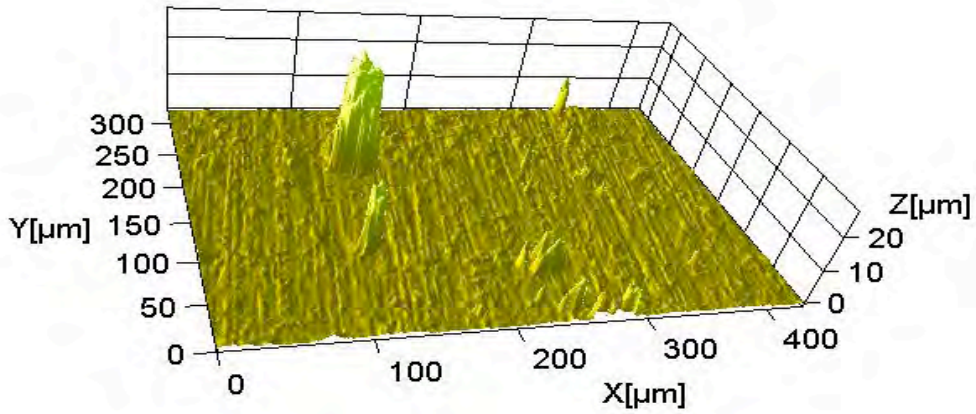

Figure 3.17. Profile map of Alloy 602CA exposed to a carburizing gas consisting of 50% H_2-50% CO at 593ºC for 500 h.

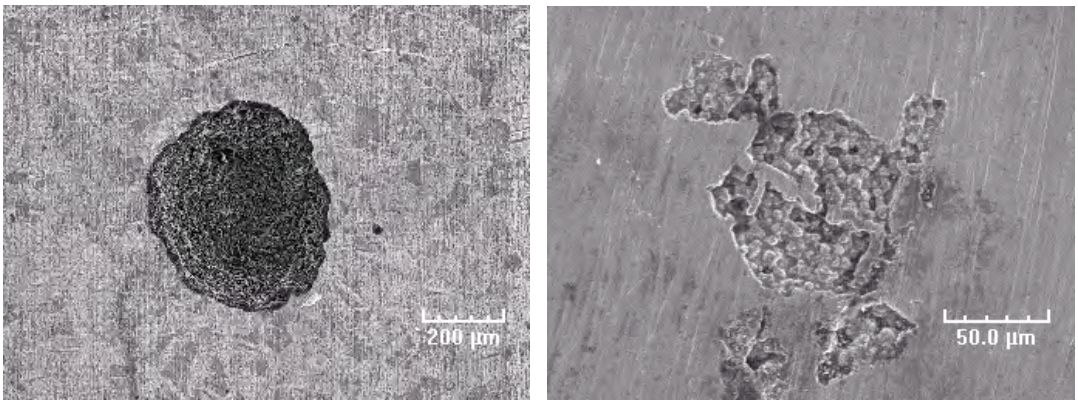

Alloy 214 tested at 704ºC Alloy 214 tested at 593ºC

Figure 3.18. SEM photomicrographs of Alloy 214 exposed to a carburizing gas consisting of 50% H_2-50% CO at 593 and 704ºC for 500 h.

Figure 3.19 shows a macrophotograph of the surfaces of pre-pitted alloys. To examine the pit growth rate of these pre-pitted alloys in a metal dusting environment, pit progression was measured for these alloys as a function of exposure time by monitoring the size of the same pits at various exposure times. Figures 3.20 and 3.21 show the pit depth data obtained by surface profiler measurements. For Alloys 601 and 617, the pit growth rates of pre-pitted specimens were similar to the non-pre-pitted (virgin) specimens. This result indicates that we can expedite the pit nucleation (without waiting for the pit to develop, especially for alloys with long incubation times) and study the growth kinetics by using pre-pitted specimens.

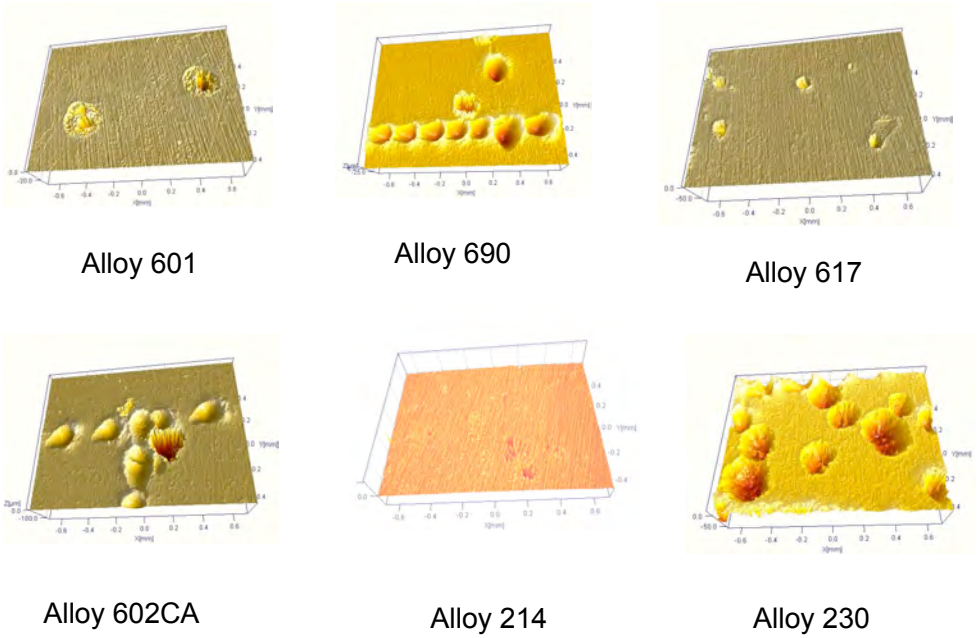

Figure 3.19. Pits, developed by a pre-pitting approach, on several nickel-base alloys.

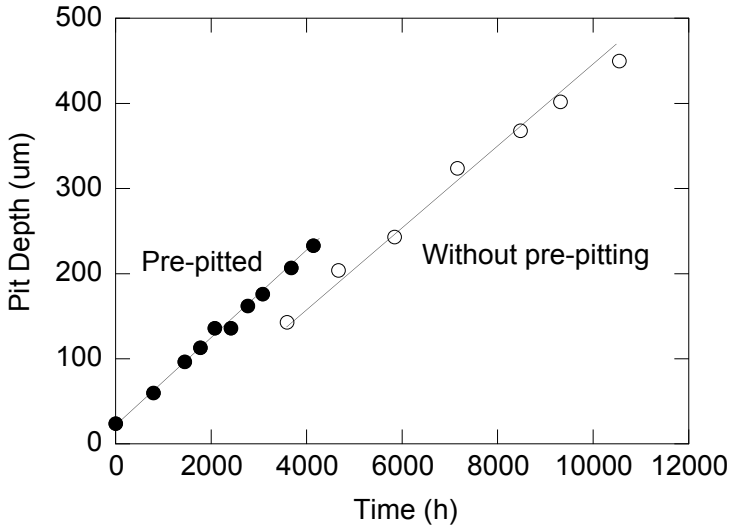

Figure 3.20. Comparison of Pit growth rate for virgin and pre-pitted Alloy 601 after exposure to Gas 21 (a_C=104) at 593°C, 1 atm.

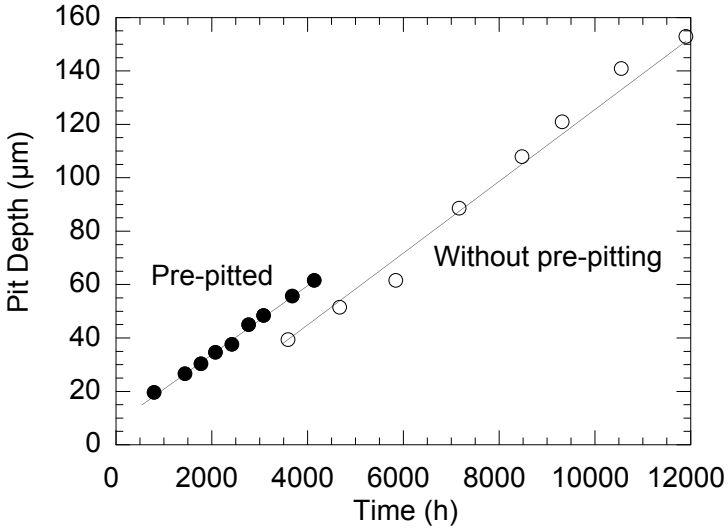

Figure 3.21. Comparison of Pit growth rate for virgin and pre-pitted Alloy 617 after exposure to Gas 21 (a_C=104) at 593°C, 1 atm.

4. PERFORMANCE OF NiCKEL-BASE ALLOYS

We reported earlier that Ni-base alloys exhibit better resistance to metal dusting attack than Fe-base alloys, and indicated that differences in the lattice mismatch in catalytic crystallization of carbon may be one reason.[10,11] The misfit between the Ni and graphite lattice (3.6%) is much greater than that between Fe_3C and graphite (0.28%).[12] The lattice of Fe_3C almost perfectly matches the lattice of graphite, indicating that carbon atoms move easier from Fe_3C to graphite than it does in nickel. Therefore, the energy barrier for the precipitation of carbon on the surface of Ni is higher than that needed for precipitation on the surface of Fe_3C. This condition leads to a lower carbon precipitation rate, smaller crystallite size, and lower metal dusting rate in Ni. The observed crystallite size of coke on Ni was smaller than that on Fe. This difference suggests that Fe_3C is better than Ni in serving as a template for the catalytic crystallization of carbon and may explain why the metal dusting rate of Fe and Fe-base alloys is higher than that of Ni and Ni-base alloys. The other factor that can affect the metal dusting rate is the chemical and mechanical integrity of the oxide layer that develops on the surface of alloys. In this report, we present results from a study of the effect of alloy chemistry and phase composition of oxides present on the surface of Ni-base alloys on metal dusting rate. We also examined the metal dusting rate of several Ni-base alloys to establish the materials that are most resistant to metal dusting corrosion.

4.1 Weight Loss Data for Ni-Base Alloys at Carbon Activity of 31

Metal dusting attack, as measured by weight loss, was observed on Ni-base alloys when tested for 9700 h in the same gas environment at 593°C and 14.3 atm (see Fig. 4.1). However, the weight loss rates for Alloys 693 and 602CA were very low. Both alloys contain Al and have high Cr and low Fe content. The weight loss rate for Alloy 45TM was the highest among the Ni-base alloys used in the study, although the Cr content in this alloy is fairly high. The Fe content in Alloy 45TM is also the highest among these alloys. The weight loss rate of Alloy 601 was also high; the Fe content of this alloy is the second highest among the alloys tested. Results indicate that addition of Fe to the Ni-base alloys leads to a substantial decrease in incubation time for the onset of metal dusting. When the Fe content in the alloy is >10 wt.%, the alloy is readily attacked, as evidenced by numerous pits on the exposed surfaces of the alloy specimens.

The weight loss rate for the Co-containing Alloy 617 is the second highest among these alloys. Addition of Mo to this alloy did not improve its resistance to metal dusting corrosion. The other Co-containing Alloy, HR160, also exhibited metal dusting degradation, although it contained 28% Cr. Therefore, addition of Co to alloys is also not beneficial to metal dusting resistance. The Cr content in Alloy 214 is the lowest among these alloys, and its weight loss rate was also high, although it contained Al. High Cr content in alloys seems essential but not entirely sufficient for preventing metal dusting corrosion in Ni-base alloys.

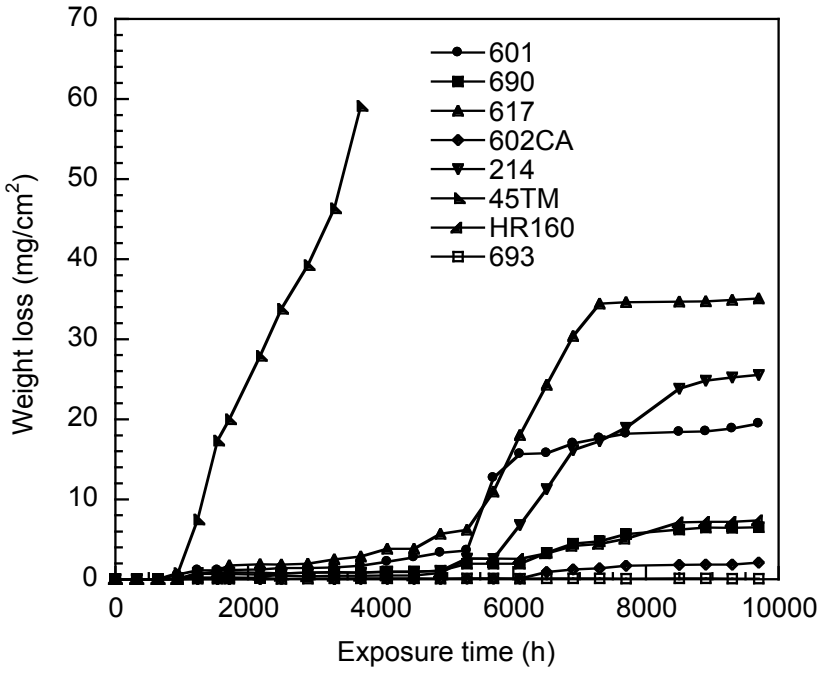

Figure 4.1. Weight loss data for Ni-base alloys that were exposed in Gas 10 at 593°C and 14.3 atm (210 psi).

Even though the weight loss data developed for various alloys are useful in the evaluation and ranking of the alloys according to their susceptibility to metal dusting, such data may only indicate the protective capacity of the surface oxide scale and, furthermore, may represent only an average behavior for the alloy in a given exposure environment and temperature. Because corrosion damage of the alloy occurs by nucleation of pits on the surface and their growth inward, it is essential that we develop an understanding of the morphology of pits (size, distribution, depth, etc.) on the alloy surface and of the maximum growth rate of the pits to evaluate the ultimate damage leading to component failure under a given set of exposure (process) conditions.

4.2 Characterization of Pits on Ni-Base Alloys at Carbon Activity of 31

In Run 59HP, we exposed several Ni-base alloys to Gas 10 at 593°C and 14.3 atm for a total time of 9700 h. During the course of the experiment, we retrieved the specimens periodically and took SEM photomicrographs of various surface regions to characterize and monitor the growth of pits as a function of exposure time. Lacking the capability to measure the pit depth during that period, we concentrated on measuring changes in the diameter of several pits on the surface of each alloy.

No metal dusting attack was observed on Ni-base alloys in the relatively short exposure time of 246 h at 1-atm pressure (Table 4.1). However, pits appeared on Alloys 601, 690, 617, and 214 when exposed in the same gas at 593°C and 14.3 atm. Similar results were obtained when specimens were tested at 40.8 atm. Table 4.2 gives the pit characteristics after 9700 h. The results show that the ratio of pit depth to pit

diameter for Alloy HR160 is the smallest among the alloys tested. This alloy corroded by forming shallow pits. The ratio of pit depth to pit diameter for Alloy 693 was the largest among these alloys, but the absolute value of pit diameter in this alloy was substantially smaller than that in other alloys.

Table 4.1. Surface Characteristics of alloys after 246-h exposure at 1, 14.3, and 40.8 atm and 593°C.

Alloy	1 atm	14.3 atm	40.8 atm
601	Clean surface	Pits	Pits
690	Clean surface	Pits	Pits
617	Clean surface	Pits	Pits
602CA	Clean surface	Clean surface	Clean surface
214	Clean surface	Pits	Pits
45TM	Clean surface	Clean surface	Clean surface
HR160	Clean surface	Clean surface	Clean surface

Table 4.2. Maximum pit size and weight loss for alloys after 9700-h exposure in Run 59HP.

Alloy.	Weight loss (mg/cm^2)	Pit depth (μm)	Pit diameter (μm)	Ratio of pit depth to pit diameter
601	19.5	110	450	0.244
690	6.5	147	440	0.334
617	35.1	201	887	0.227
602CA	2.1	96	374	0.256
214	25.6	-[a]	-[a]	-[a]
45TM[b]	59.1	141	600	0.235
HR160	7.3	13	210	0.062
693	0.1	37	99	0.374

[a]Specimen uniformly corroded.
[b]Exposed for only 3,300 h.

Figure 4.2 shows a comparison of the surfaces of several alloys after exposure at 593°C and pressures of 1 and 14.3 atm. The carbon activity in the gas in the latter case is 14 times higher than at 1 atm, which can decrease the incubation time for the initiation of metal dusting pits on the alloy surface.

Figure 4.3 shows SEM photomicrographs of the pit morphology observed on Alloy 601 for exposure times in the range of 6900 and 9300 h. The figures show that numerous pits form in Alloy 601 and undergo significant growth as a function of exposure time. Figure 4.4 shows the SEM photomicrographs of pit morphology for Alloy 690 for exposure times in the range of 2900 and 9300 h. The compositional difference between Alloys 601 and 690 is that the latter contains 27.2 wt.% Cr versus 21.9 wt.% in 601. However, Alloy 601 contains 1.4 wt.% Al, which is supposed to be beneficial in resisting metal dusting. Nonetheless, the pit density in Alloy 601 was significantly larger than in Alloy 690. Figure 4.5 shows photomicrographs of pit morphology in Alloy 617.

Figure 4.6 shows photomicrographs of pit development in Alloy 602CA, which contains ≈2.7 wt.% Al. The alloy showed very few pits for the same exposure time as Alloys 601, 690, and 617, and the growth rate of the pits was also less than those of the other three alloys. Figure 4.7 shows the pit morphology in Alloy 45TM. The pit density in this alloy was large, as was the pit growth rate; as a result, the exposure of this alloy was shortened to 3300 h.

Figure 4.8 shows the pit morphology in Alloy HR160. This alloy contained 28 wt.% Cr, 30 wt.% Co, and 2.8 wt.% Si, but the pit density seemed large under exposure conditions of Run 59HP. Figure 4.9 shows the pit morphology in Alloy 214, which contained only 15.9 wt.% Cr but had 3.7 wt.% Al. The alloy had numerous pits on the surface, and the pits seemed to coalesce, with the result that the attack was more uniform than that resulting from local pit formation. Alloy 693 was most resistant to metal dusting among the alloys tested, and no pits of significant size were detected over ≈8000 h. After 9300-h exposure, the alloy exhibited a number of small pits as shown in Fig. 4.10. The pit diameter ranged between 100 and 150 μm after 9300 h exposure.

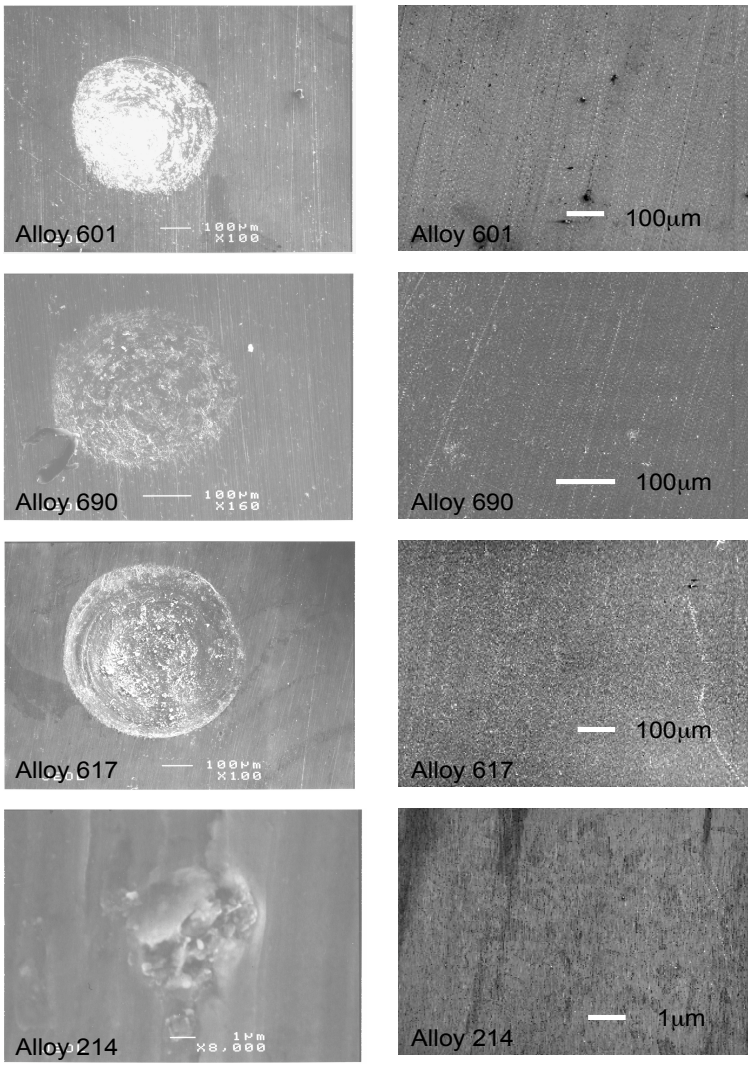

Figure 4.2. SEM photo-micrographs of surfaces of several Ni-base alloys after exposure to metal dusting environment. Left: exposed at 14.3 atm and 593°C for 160 h; metal dusting pits were observed. Right: exposed at 1 atm and 593°C for 240 h; surfaces of alloys are smooth and no metal dusting pits appear.

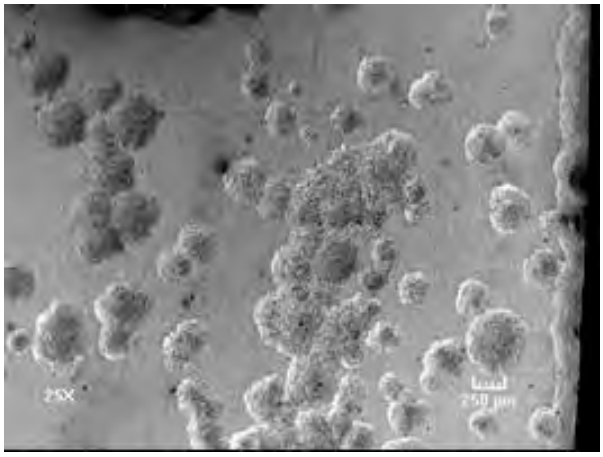

6900 h

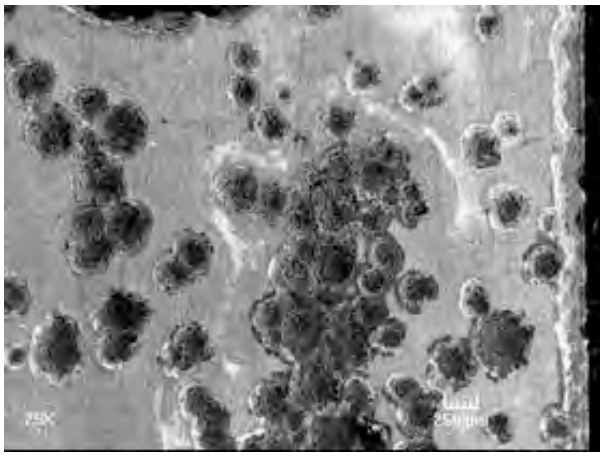

7300 h

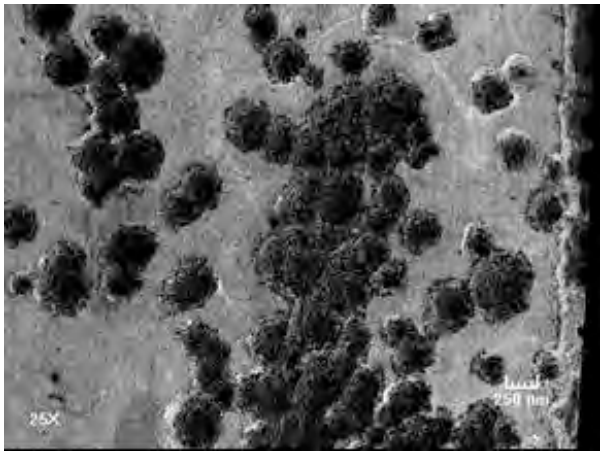

7700 h

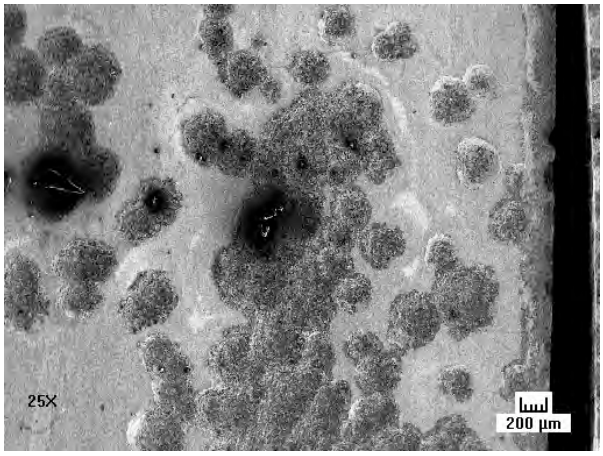

8100 h

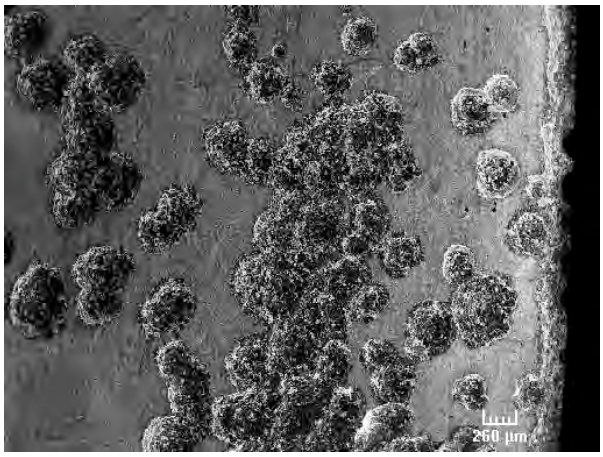

8500 h

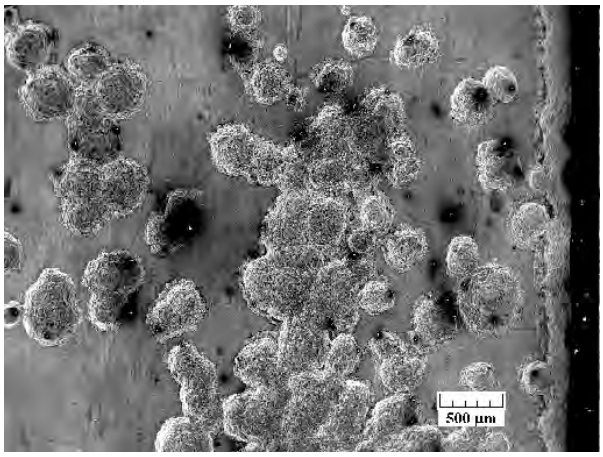

9300 h

Figure 4.3. Pit morphology as a function of time for Alloy 601 exposed to Gas 10 at 593°C and 14.3 atm (210 psi).

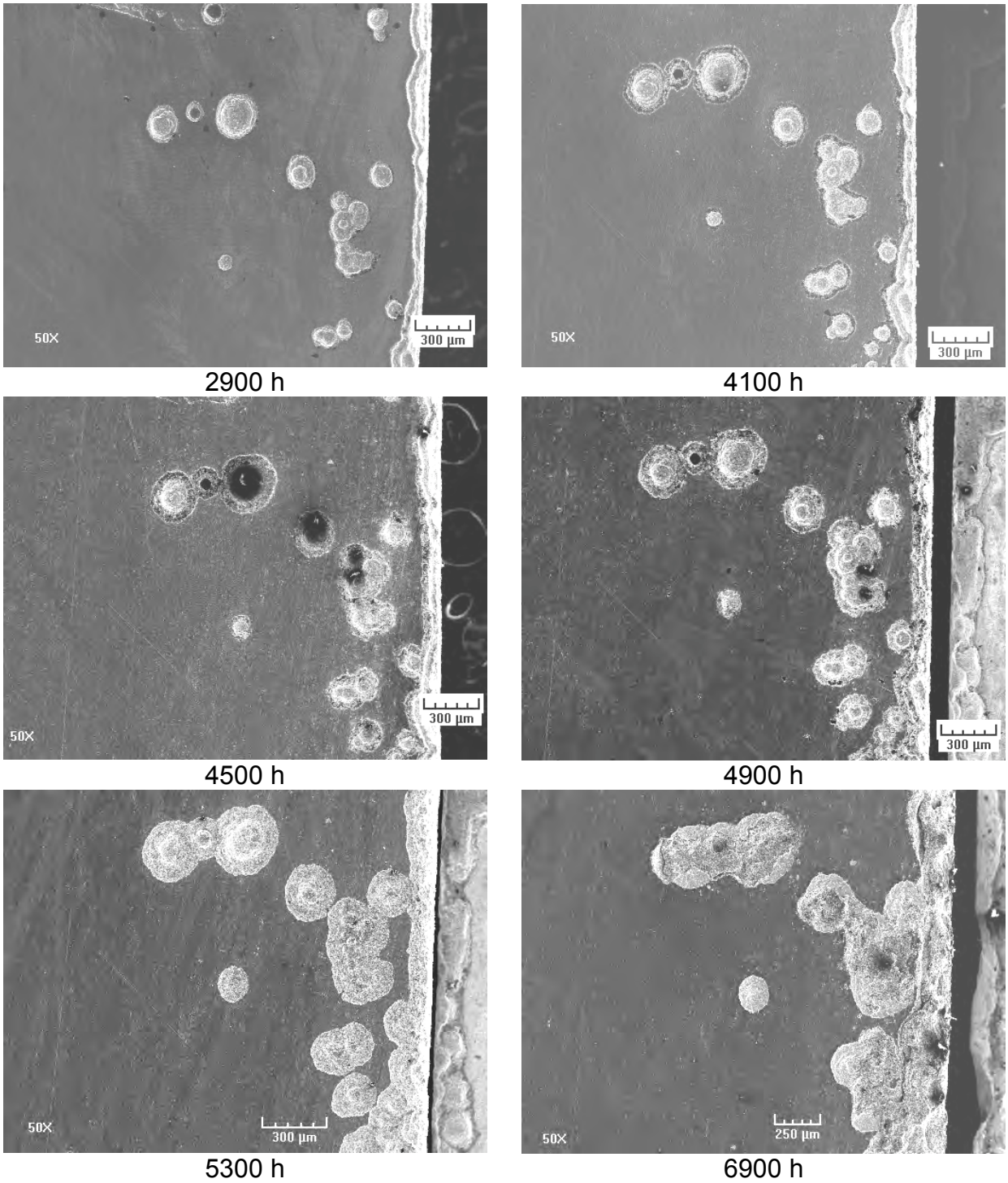

Figure 4.4. Pit morphology as a function of time for Alloy 690 exposed to Gas 10 at 593°C and 14.3 atm (210 psi).

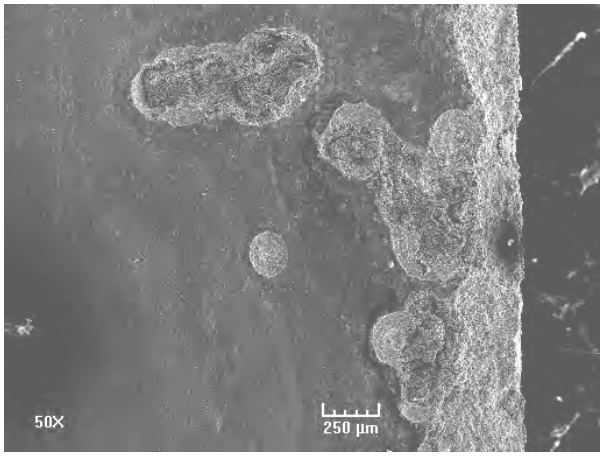

7300 h

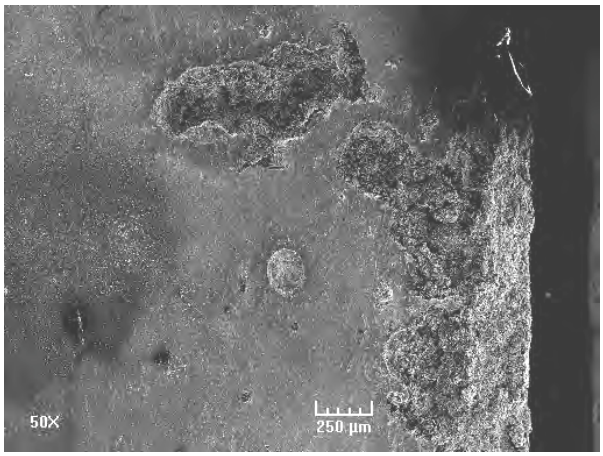

7700 h

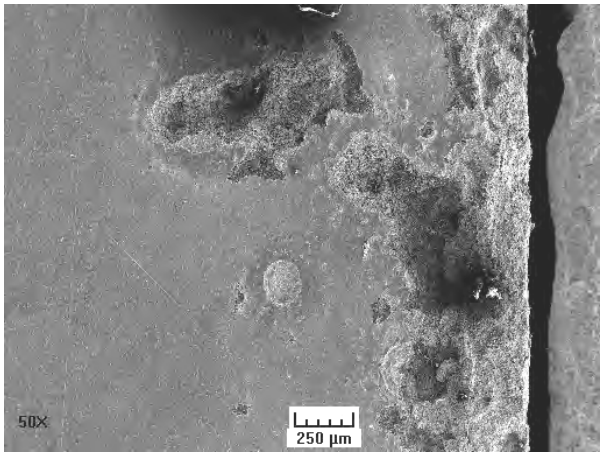

8100 h

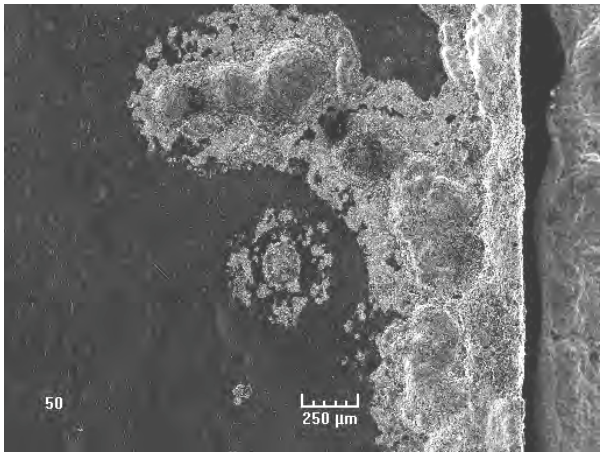

8500 h

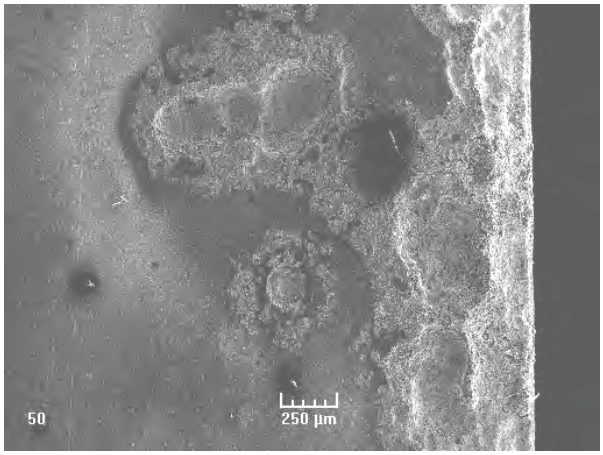

8900 h

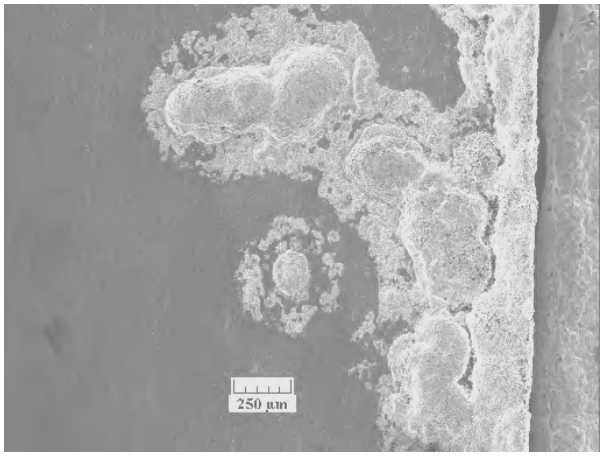

9300 h

(Figure 4.4 continued.) Pit morphology as a function of time for Alloy 690 exposed to Gas 10 at 593°C and 14.3 atm (210 psi).

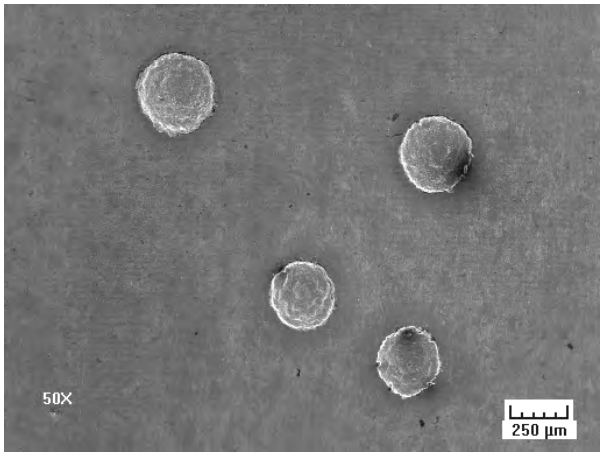

2900 h

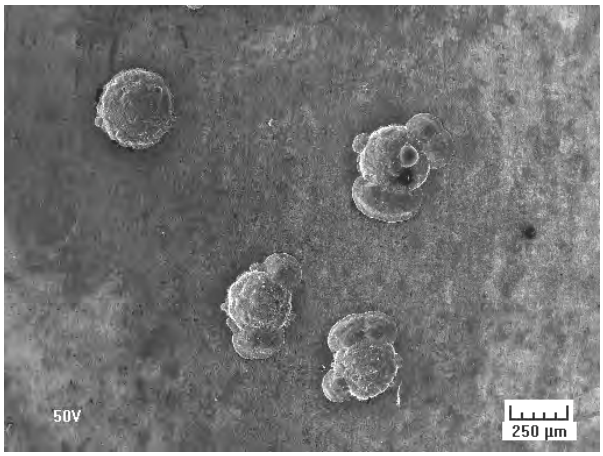

4100 h

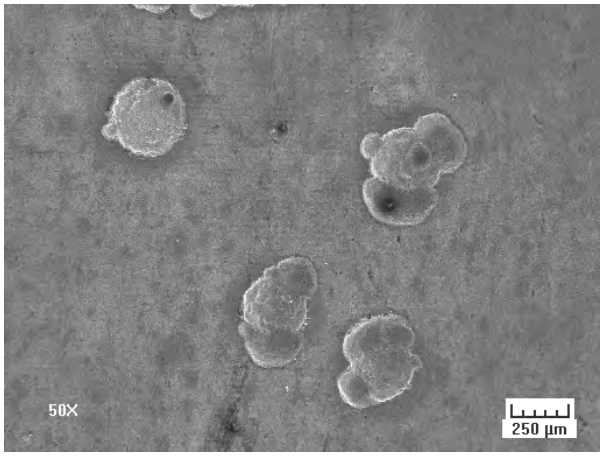

4500 h

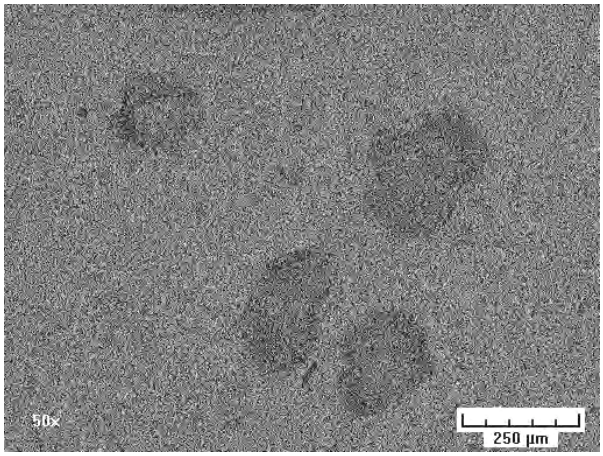

4900 h

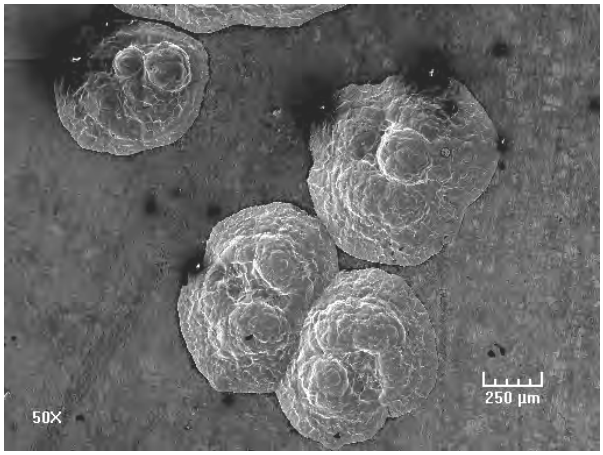

5300 h

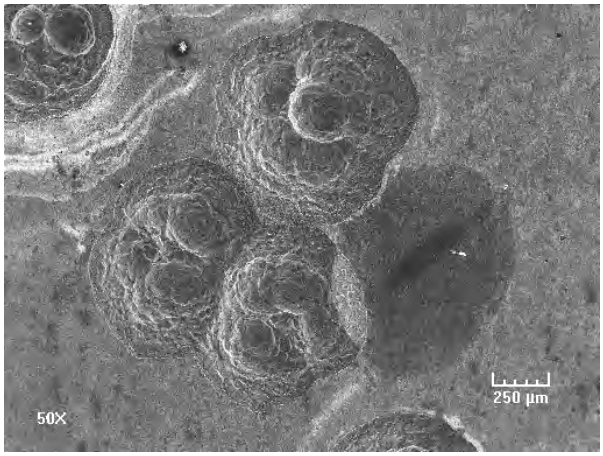

6900 h

Figure 4.5. Pit morphology as a function of time for Alloy 617 exposed to Gas 10 at 593°C and 14.3 atm (210 psi).

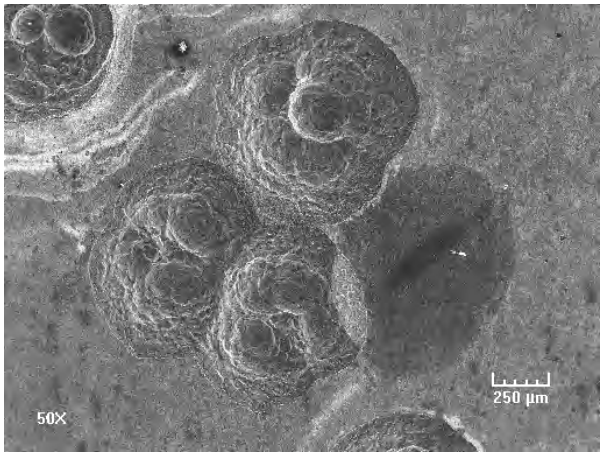

7300 h

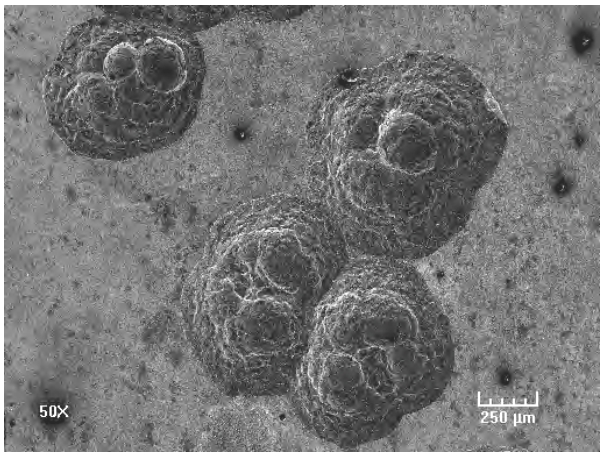

7700 h

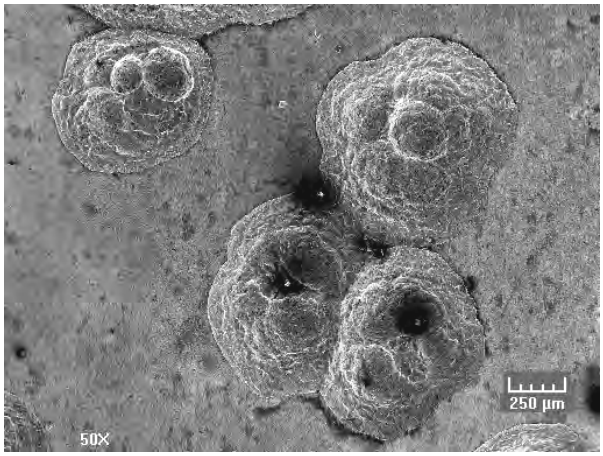

8100 h

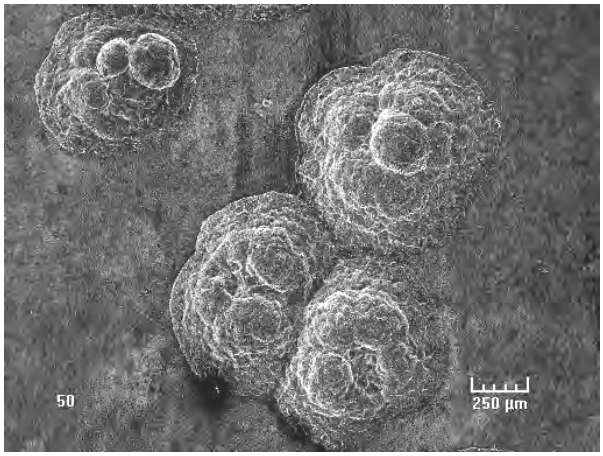

8500 h

8900 h

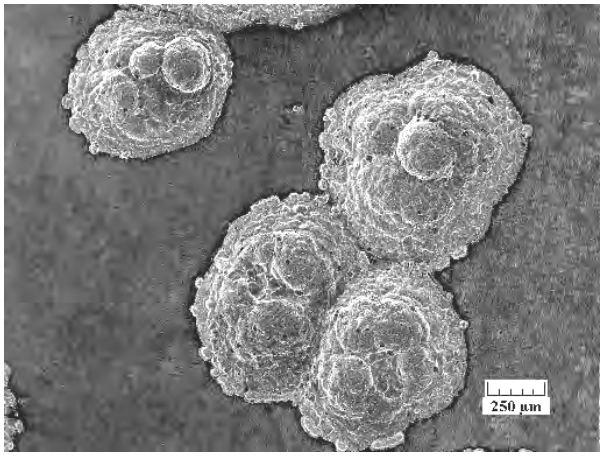

9300 h

(Figure 4.5 continued.) Pit morphology as a function of time for Alloy 617 exposed to Gas 10 at 593°C and 14.3 atm (210 psi).

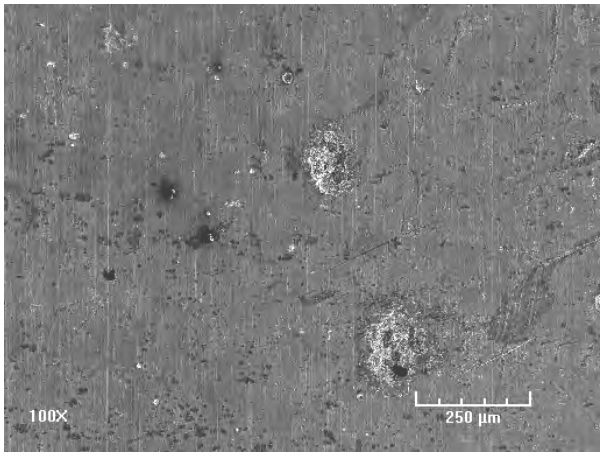

6900 h

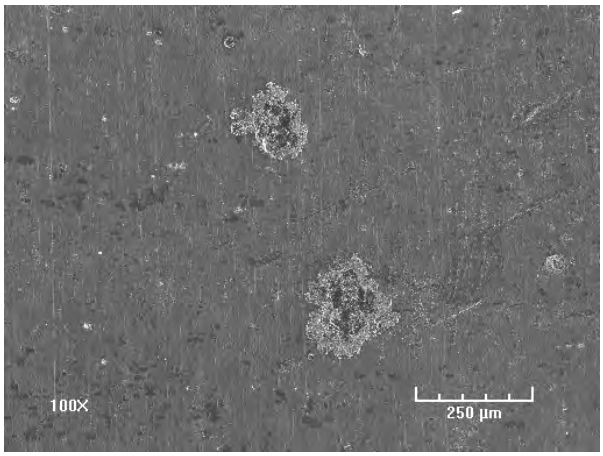

7300 h

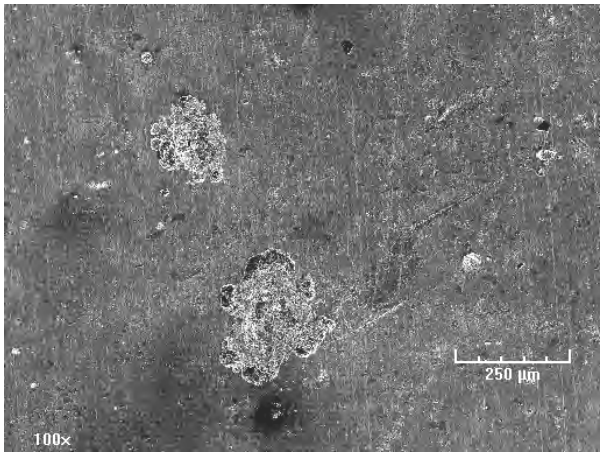

7700 h

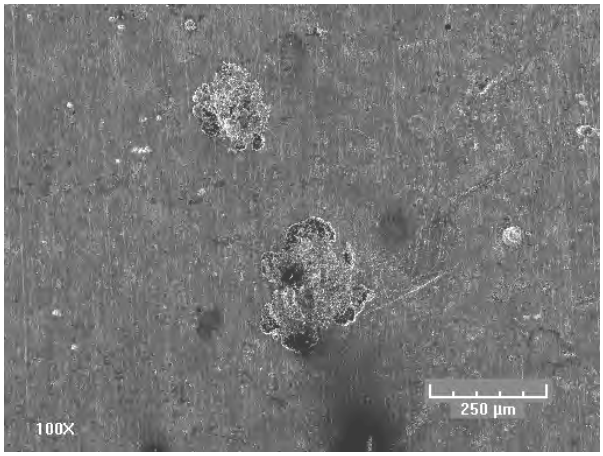

8100 h

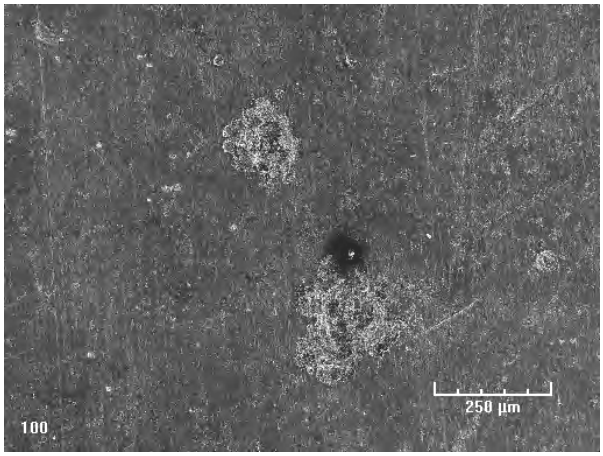

8900 h

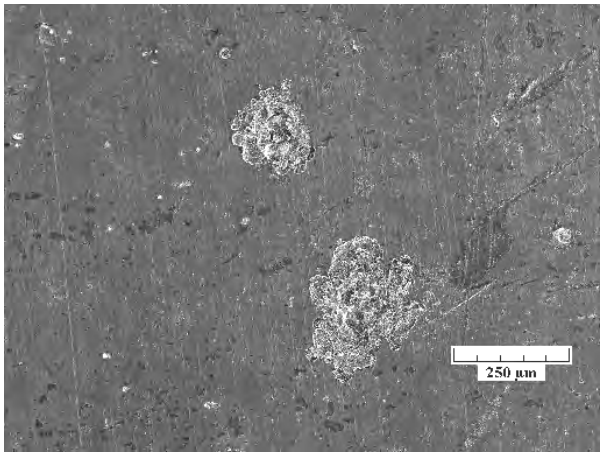

9300 h

Figure 4.6. Pit morphology as a function of time for Alloy 602CA exposed to Gas 10 at 593°C and 14.3 atm (210 psi).

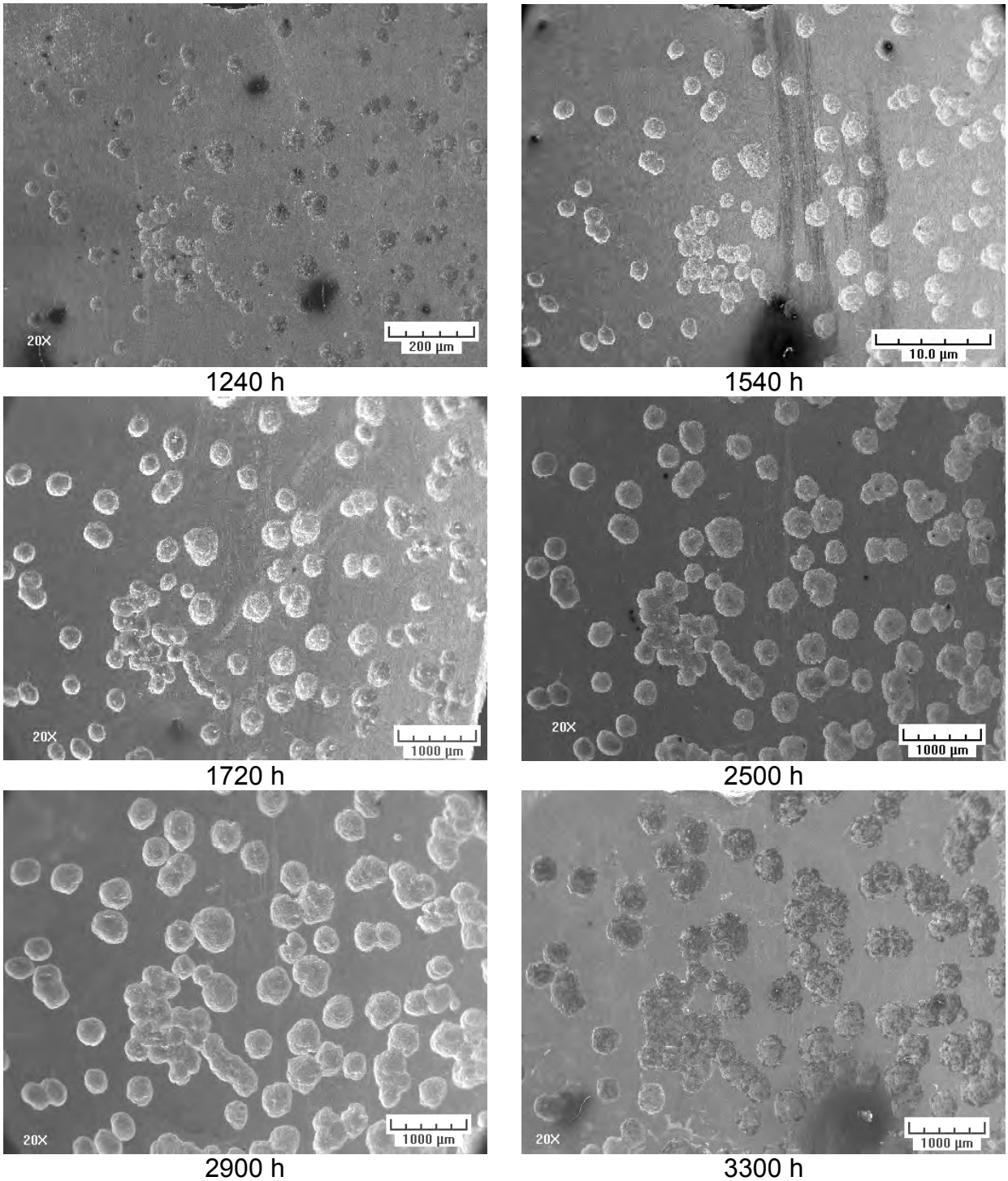

Figure 4.7. Pit morphology as a function of time for Alloy 45TM exposed to Gas 10 at 593°C and 14.3 atm (210 psi).

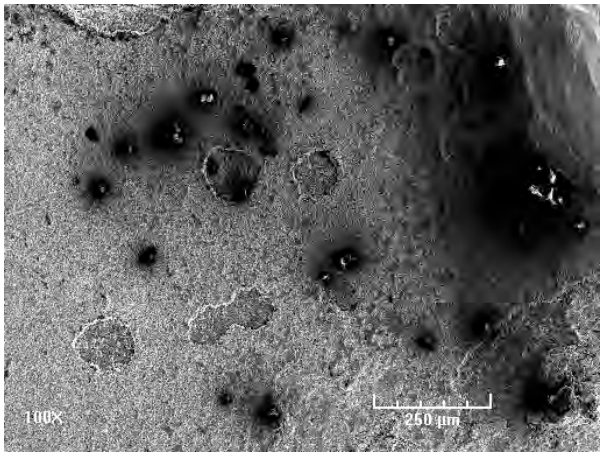

6900 h

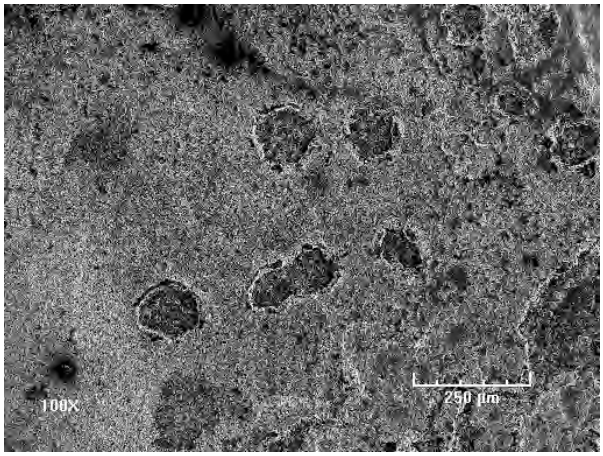

7300 h

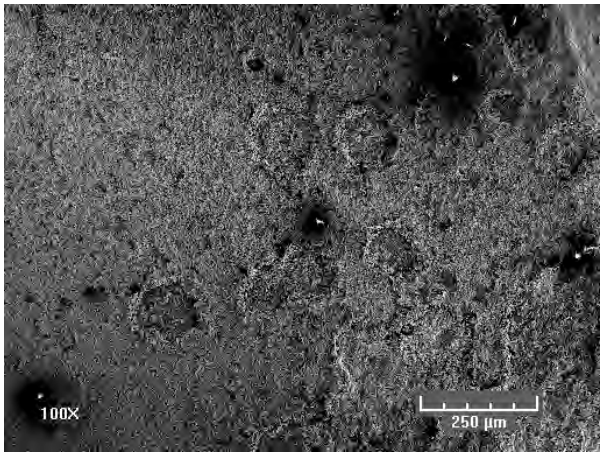

8100 h

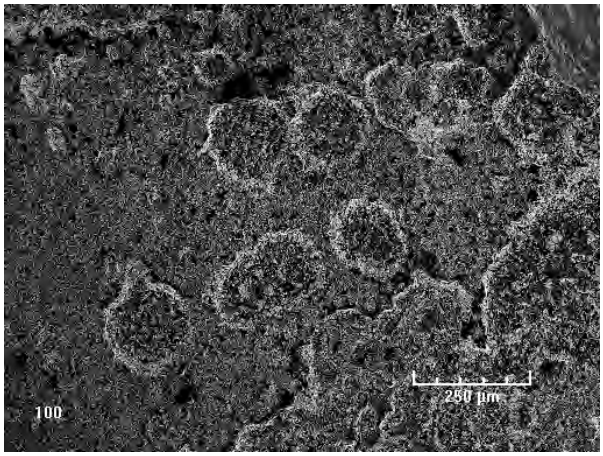

8500 h

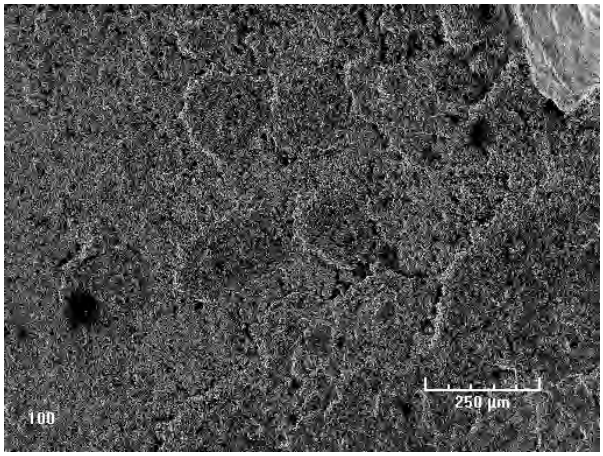

8900 h

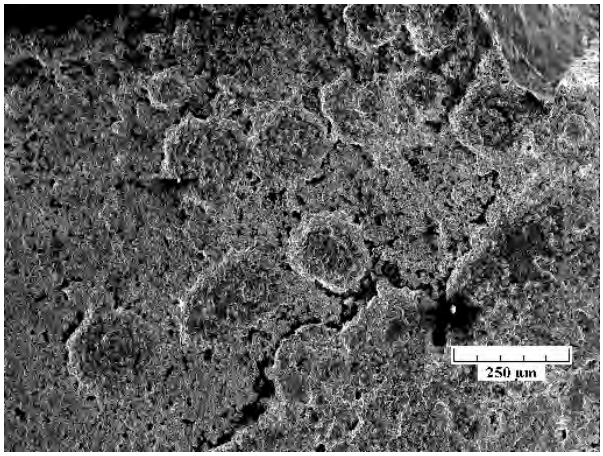

9300 h

Figure 4.8. Pit morphology as a function of time for Alloy HR160 exposed to Gas 10 at 593°C and 14.3 atm (210 psi).

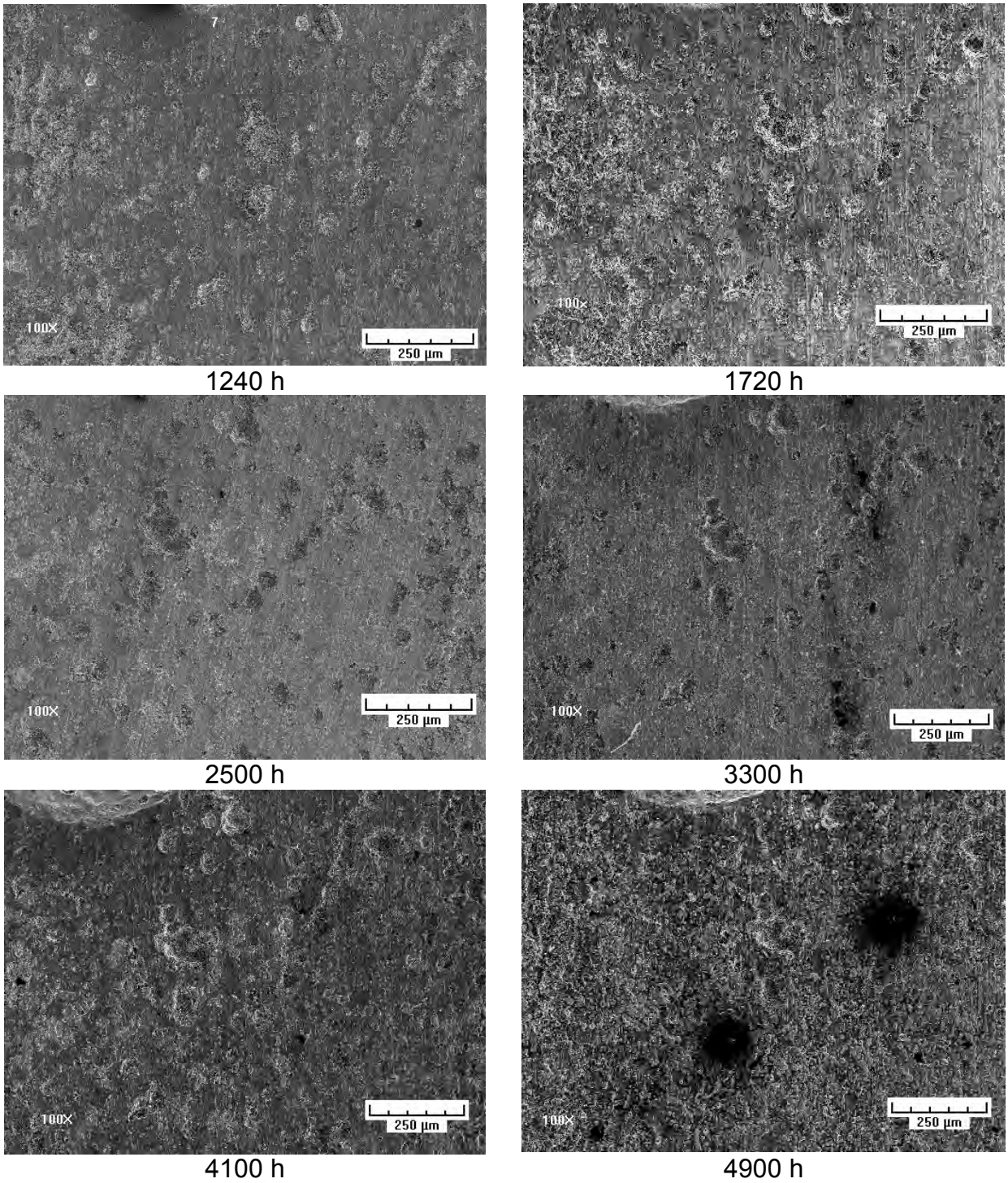

Figure 4.9. Pit morphology as a function of time for Alloy 214 exposed to Gas 10 at 593°C and 14.3 atm (210 psi).

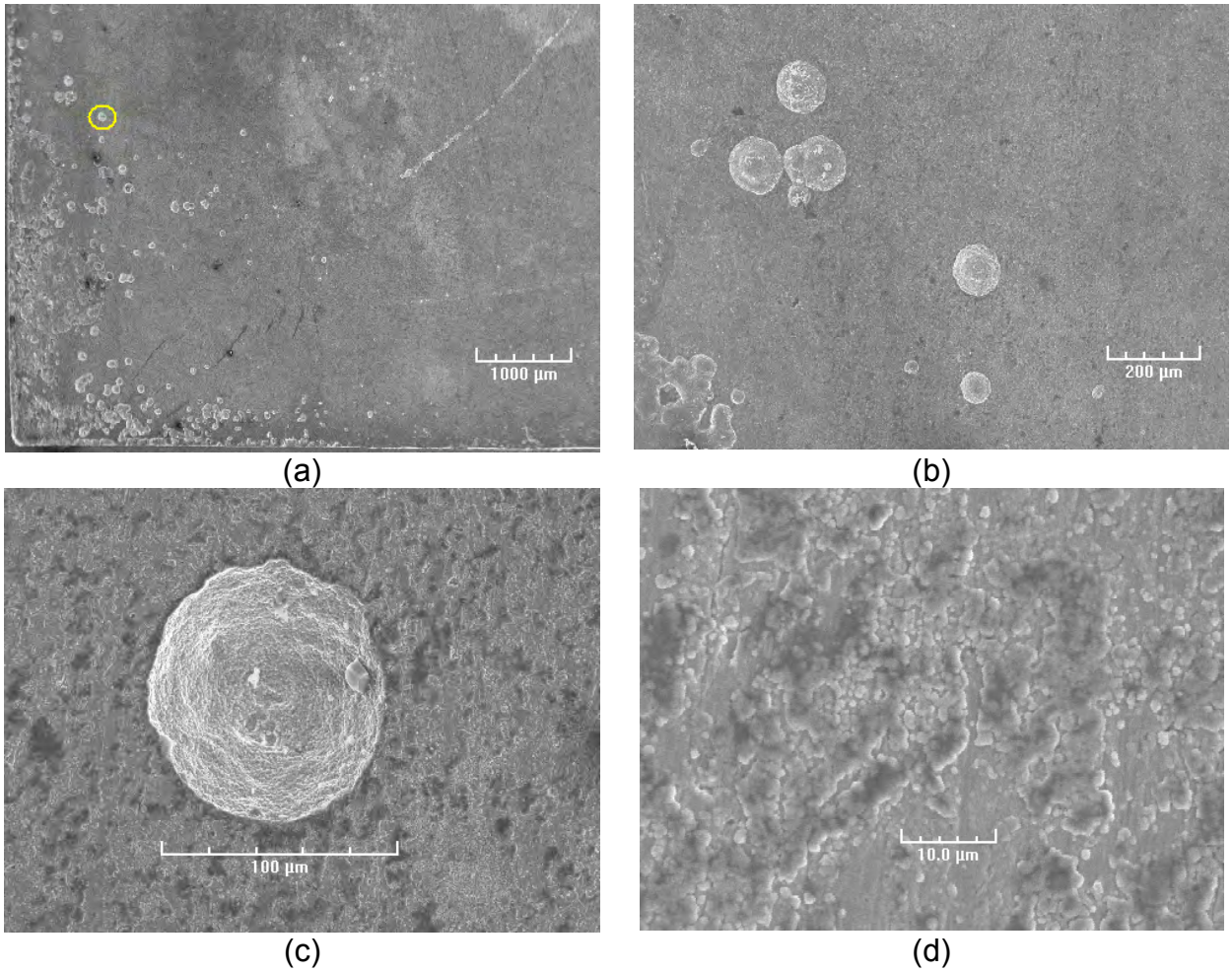

Figure 4.10. Pit morphology for Alloy 693 after 9300-h exposure to Gas 10 at 593°C and 14.3 atm (210 psi).

4.3 Pit Diameter and Pit Density in Ni-Base Alloys

To determine the growth rate for the pits and the pit density (as a function of pit size), a fixed area of surface of each specimen was examined as a function of exposure time. All the specimens were exposed to Gas 10 at 593°C and 14.3 atm (210 psi). The pit diameter and number of pits of different diameter ranges were measured by optical and scanning electron microscopy. Figures 4.11 to 4.17 show the distribution of different size pits for seven alloys. It is evident that the medium-size pits (over the exposure time of 9700 h in the present test) are most common. Furthermore, the larger pits increase in numbers with exposure time, but the smaller pits decrease. This decrease indicates that the nucleation of new pits is not prevalent under the test conditions used. Also, the increased oxide thickness (with exposure time) seems beneficial in preventing/minimizing carbon transport inwards and Fe transport outwards, thereby reducing the formation of Fe-containing spinel phase.

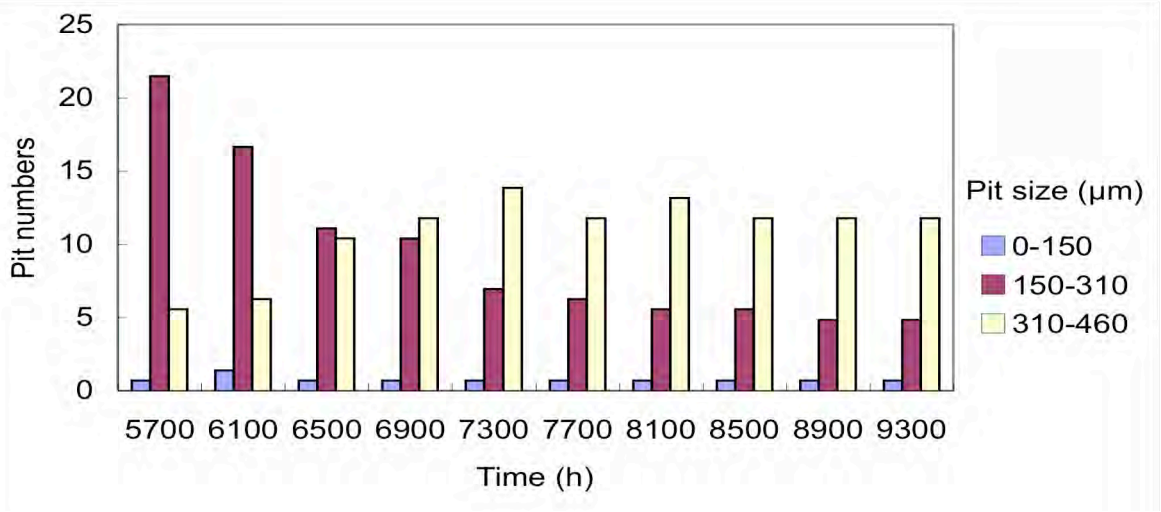

Figure 4.11. Pit diameter and density for Alloy 601 as a function of exposure time in Gas 10 at 593°C and 14.3 atm (210 psi).

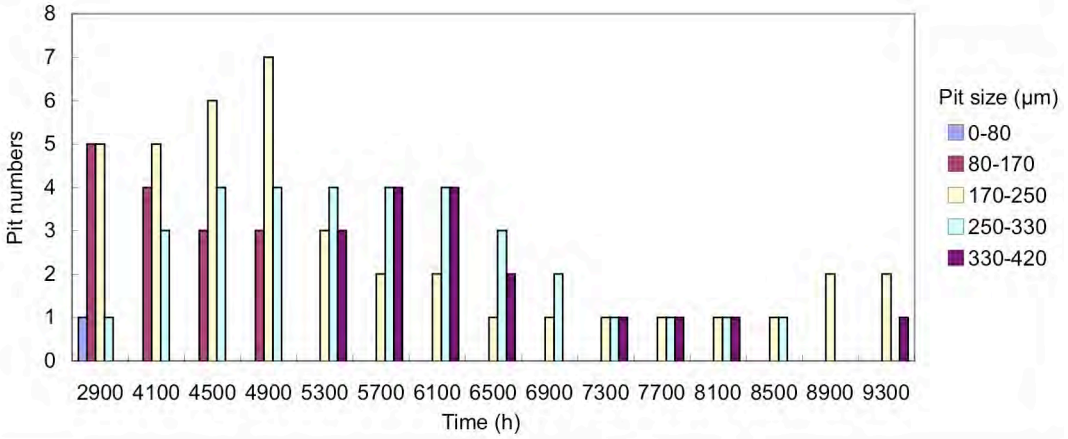

Figure 4.12. Pit diameter and density for Alloy 690 as a function of exposure time in Gas 10 at 593°C and 14.3 atm (210 psi).

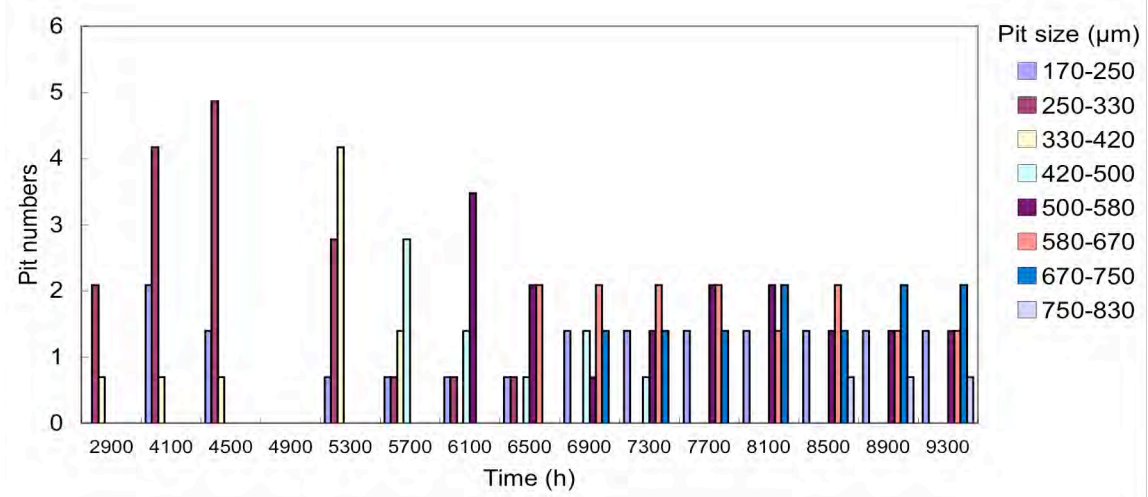

Figure 4.13. Pit diameter and density for Alloy 617 as a function of exposure time in Gas 10 at 593°C and 14.3 atm (210 psi).

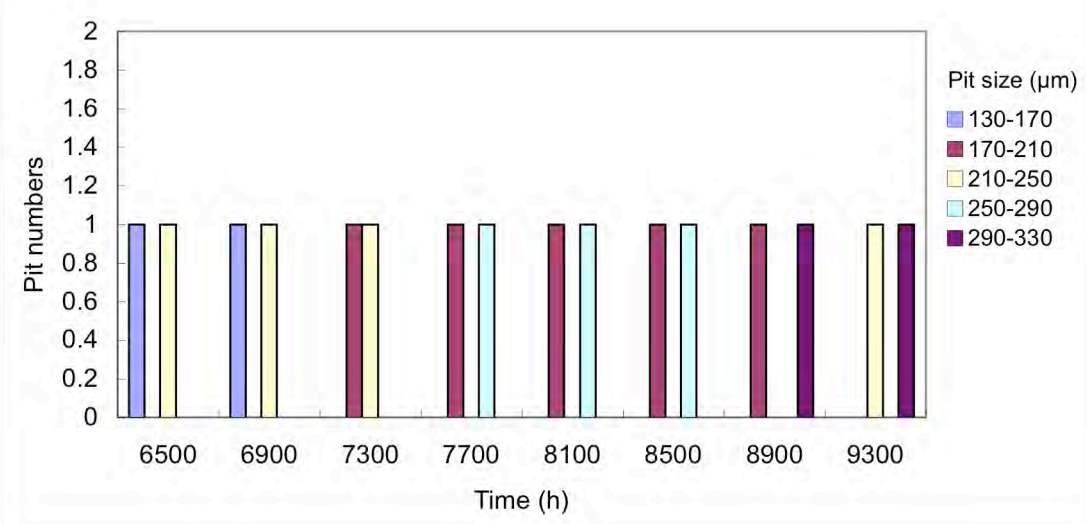

Figure 4.14. Pit diameter and density for Alloy 602CA as a function of exposure time in Gas 10 at 593°C and 14.3 atm (210 psi).

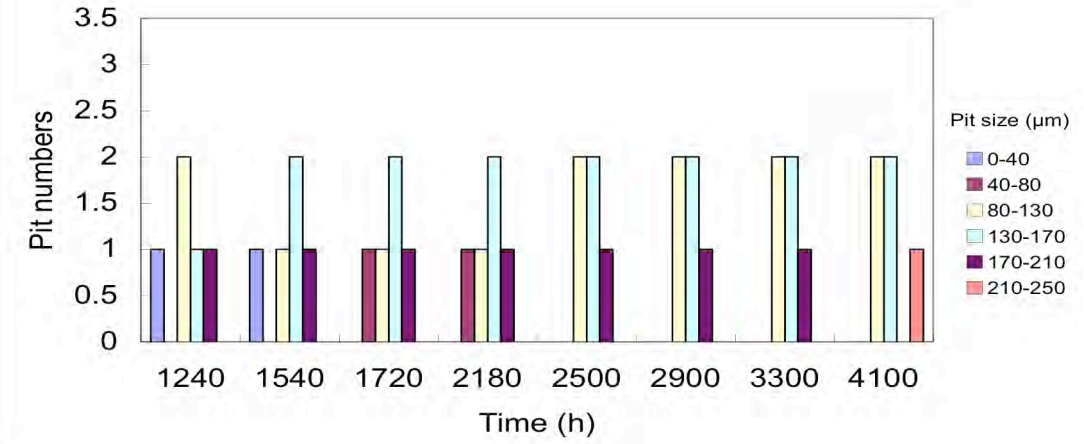

Figure 4.15. Pit diameter and density for Alloy 214 as a function of exposure time in Gas 10 at 593°C and 14.3 atm (210 psi).

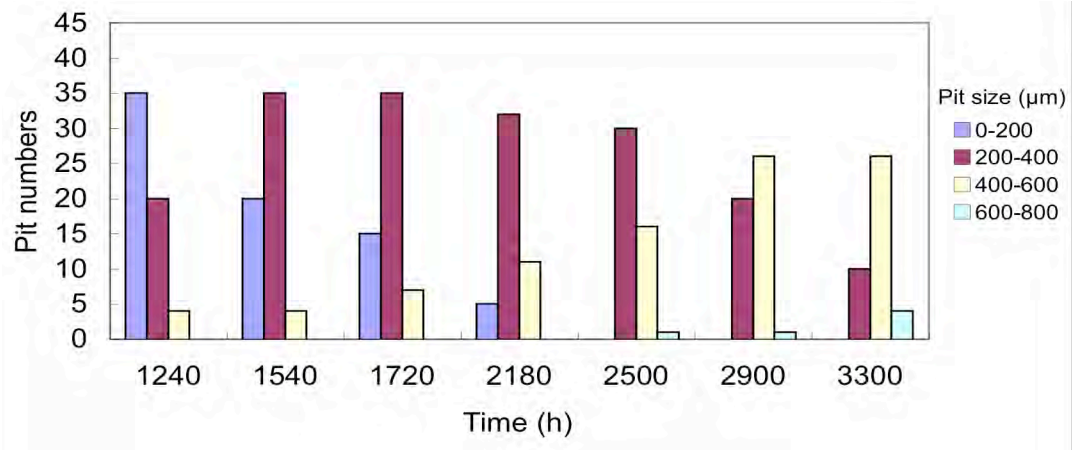

Figure 4.16. Pit diameter and density for Alloy 45TM as a function of exposure time in Gas 10 at 593°C and 14.3 atm (210 psi).

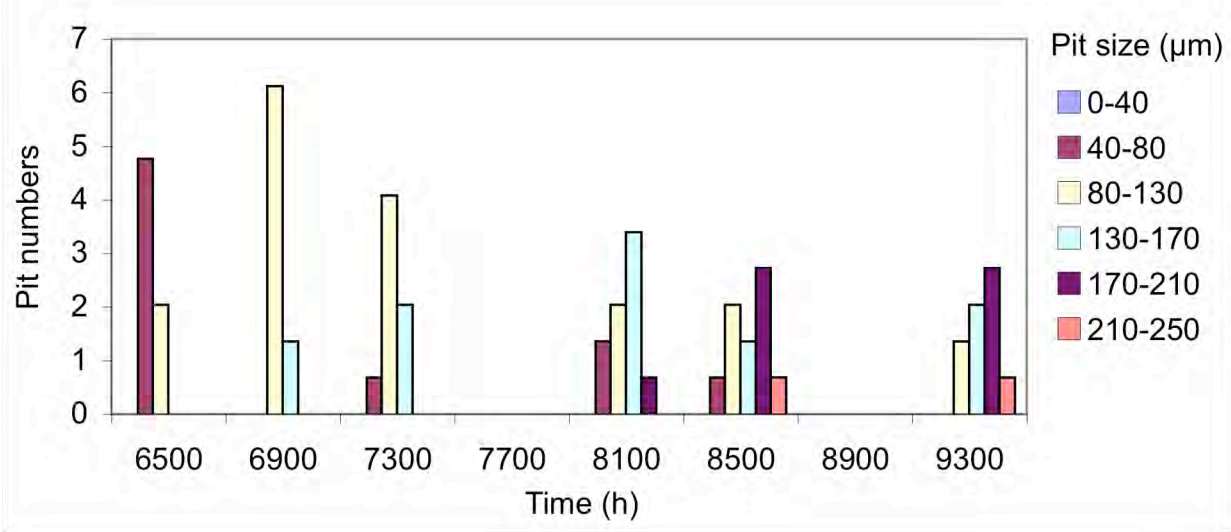

Figure 4.17. Pit diameter and density for Alloy HR160 as a function of exposure time in Gas 10 at 593°C and 14.3 atm (210 psi).

At the end of the 9700 h exposure, we procured and installed a surface profiler that could provide a 3-dimensional (3-D) view of the pits in various specimens and measure the depth of pits at various locations on the specimens. Most of the alloys from Run 59HP exhibited discrete pitting except Alloy 214, which showed numerous pits approaching uniform corrosion (indicated by a rough surface). Both pitting and uniform corrosion were observed on Alloy HR160. Figure 4.18 shows a 3-D map of various specimens after 9700-h exposure (in Gas 10) in Run 59HP. Table 4.3 shows the pit depths on these alloys. The pit diameter/depth ratios are different amount these alloys. HR160 shows the largest pit diameter/depth ratio because of its more uniform corrosion. The pit depth of Alloy 214 could not be measured because the surface of the alloy exhibited essentially uniform corrosion.

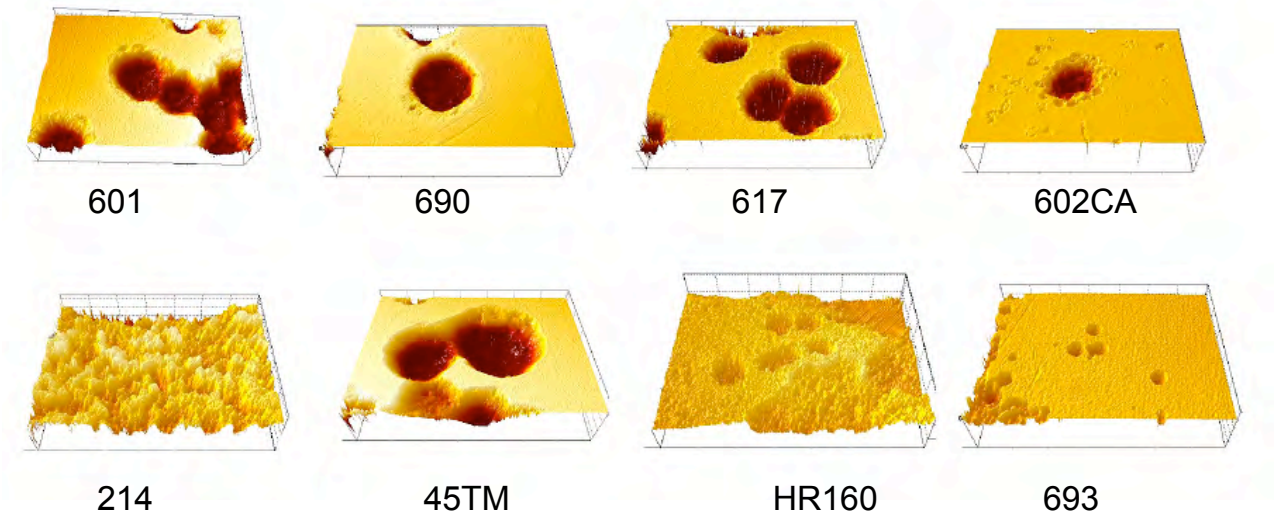

Figure 4.18. 3-D profile map of Ni-base alloys after 9700-h exposure in Gas 10 at 593°C and 14.3 atm (210 psi).

Table 4.3. Pit characteristics in alloys exposed to metal dusting environment

Pit characteristics	Alloy designation						
	601	690	617	602CA	45TM	HR160	693
Pit diameter (μm)	357	447	894	382	947	189	120
Pit depth (μm)	141	145	200	95	175	21	43
Pit diameter to depth	2.5	3.1	4.5	4.0	5.4	9.0	2.8

4.4. Correlation between Pit Growth Rate and Weight Loss

We have measured the dimension of a single pit (for each alloy) as a function of exposure time and correlated the pit size data with measured weight change for the corresponding alloys. Figure 4.19 shows the measured pit size and weight change for all the alloys used in the present study. The plots, for most of the alloys, indicate a good correlation between the growths in size of an arbitrarily selected pit on the surface of the alloy with the measured weight change. The data also show an "S" shaped behavior for both the pit growth and weight change, indicating an incubation time for the pit to develop and grow. Furthermore, the absolute increase in pit size as a function of exposure time is different for different alloys. For example, the pit size increases from 200 to 450 μm as the exposure time increases from 4,000 to 9,300 h for Alloy 601. The corresponding increases for Alloy 690 are 70 to 200 μm for a time increase from 2900 to 9300 h. Similar information for other alloys can be obtained from the curves shown in Fig. 4.19.

The behavior of Alloy 214 is somewhat different from that of others, because it shows a poor correlation between the size increase of a single pit with its weight change. The reason for this poor correlation is that this alloy contains a low (15.9 wt.%) concentration of Cr and a high (3.7 wt.%) concentration of Al and develops a large number of small pits. The nucleation and growth of a large number of small pits with low growth rates are reflected in the weight loss but not in the growth rate of an individual pit. The alloy exhibited more uniform coverage of pits after ≈3000 h of exposure, and we could not measure the size of an individual pit. Alloy 45TM exhibited an extremely rapid growth rate for the pit (380 to 600 μm during 1400 to 3400 h), and its exposure was terminated after 3800 h. The cause for this rapid increase in pit growth can be attributed to the higher (26.7 wt.%) content of Fe in the alloy.

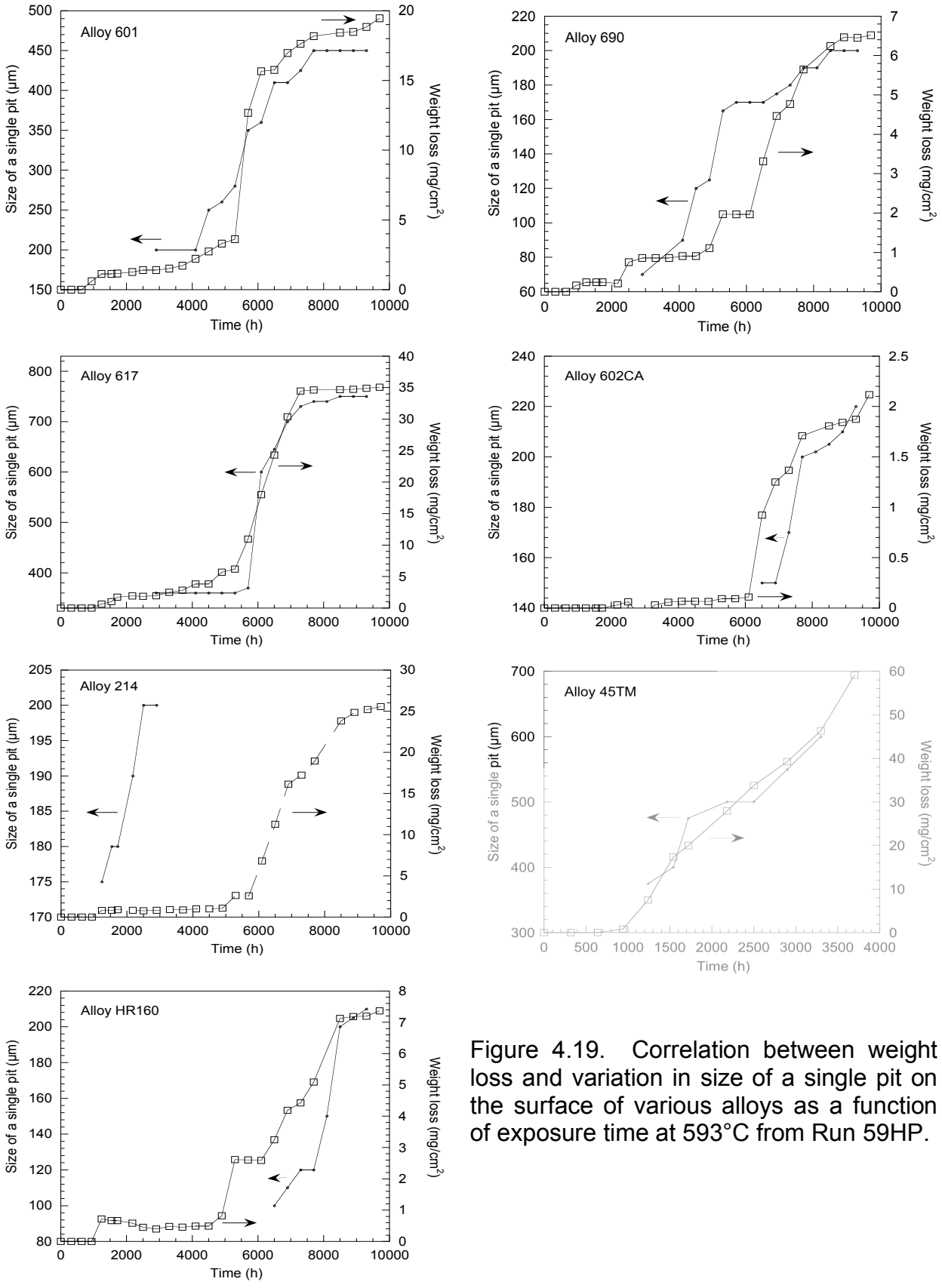

Figure 4.19. Correlation between weight loss and variation in size of a single pit on the surface of various alloys as a function of exposure time at 593°C from Run 59HP.

4.5 Effect of System Pressure on Metal Dusting Corrosion of Ni-base Alloys

To evaluate the role of system pressure in the initiation and propagation of metal dusting pits on various Ni-base alloys, we conducted experiments at atmospheric pressure with a gas composition adjusted to yield the same carbon activity of 31 as the high-pressure Run 59HP [14.3 atm (210 psi)]. Specimens of various alloys were exposed to Gas 11 (79.5% H_2, 18.2% CO, and 2.3% H_2O) at 1 atm for 7589 h. The specimens from the run at atmospheric pressure were also retrieved periodically, cleaned, and weighed to determine the weight loss as a function of exposure time.

Figure 4.20 shows weight loss data obtained for various alloys exposed at system pressures of 1 and 14.3 atm, but at the same carbon activity of ≈31 and the same temperature of 593°C. The results indicate that all the tested alloys showed a sharp decrease in initiation time for metal dusting degradation at higher system pressure. All alloys exhibited negligible weight loss after testing for as long as 7600 h at 1 atm. This indicates that testing at 1 atm system pressure does not initiate metal dusting attack, especially in Ni-base alloys, in the time frame of experiments generally conducted in a laboratory set up. On the other hand, performing the tests at a higher pressure (at the same carbon activity) decreases the initiation time for metal dusting and the time for onset of pitting seems to be alloy dependent.

Both Alloys 610 and 617 contain ≈22 wt.% Cr but the weight loss is higher by a factor of two in Alloy 617 primarily due to the presence of 12.5 wt.% Co that behaves similar to Fe from the oxidation standpoint. Similarly, Alloy HR160 with an even higher Co content of 30 wt.% showed more uniform shallow pits (more akin to uniform corrosion) and the weight loss was less. Alloys 690 and 45TM contain ≈27 wt.% Cr, but the weight loss in 45TM is a factor of 10 higher than in Alloy 690, primarily due to 27 wt.% Fe in 45TM alloy. The presence of Al in Alloys 602CA (2.7 wt.%) and 693 (3.3 wt.%) seems to sharply decrease the weight loss when tested in the same environment as other Ni-base alloys.

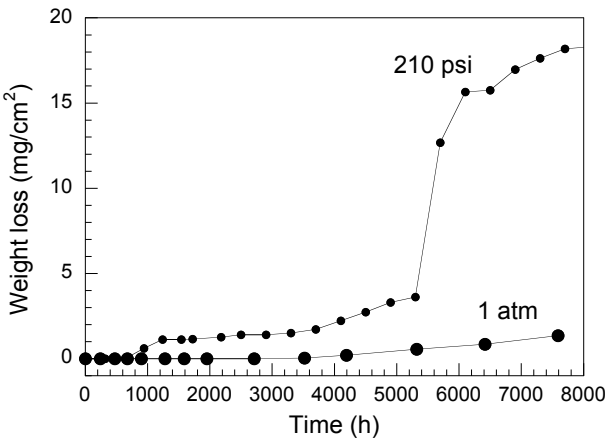

Alloy 601

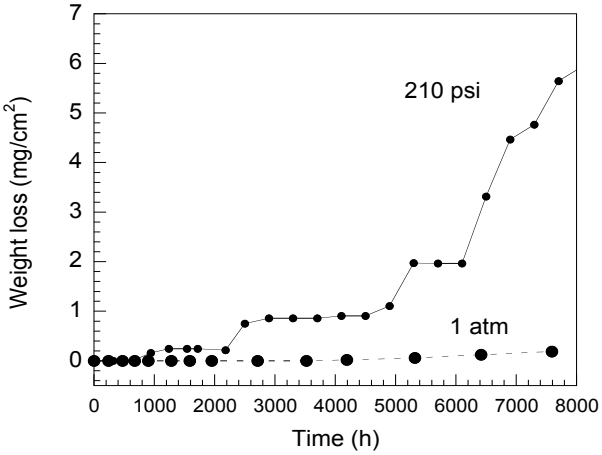

Alloy 690

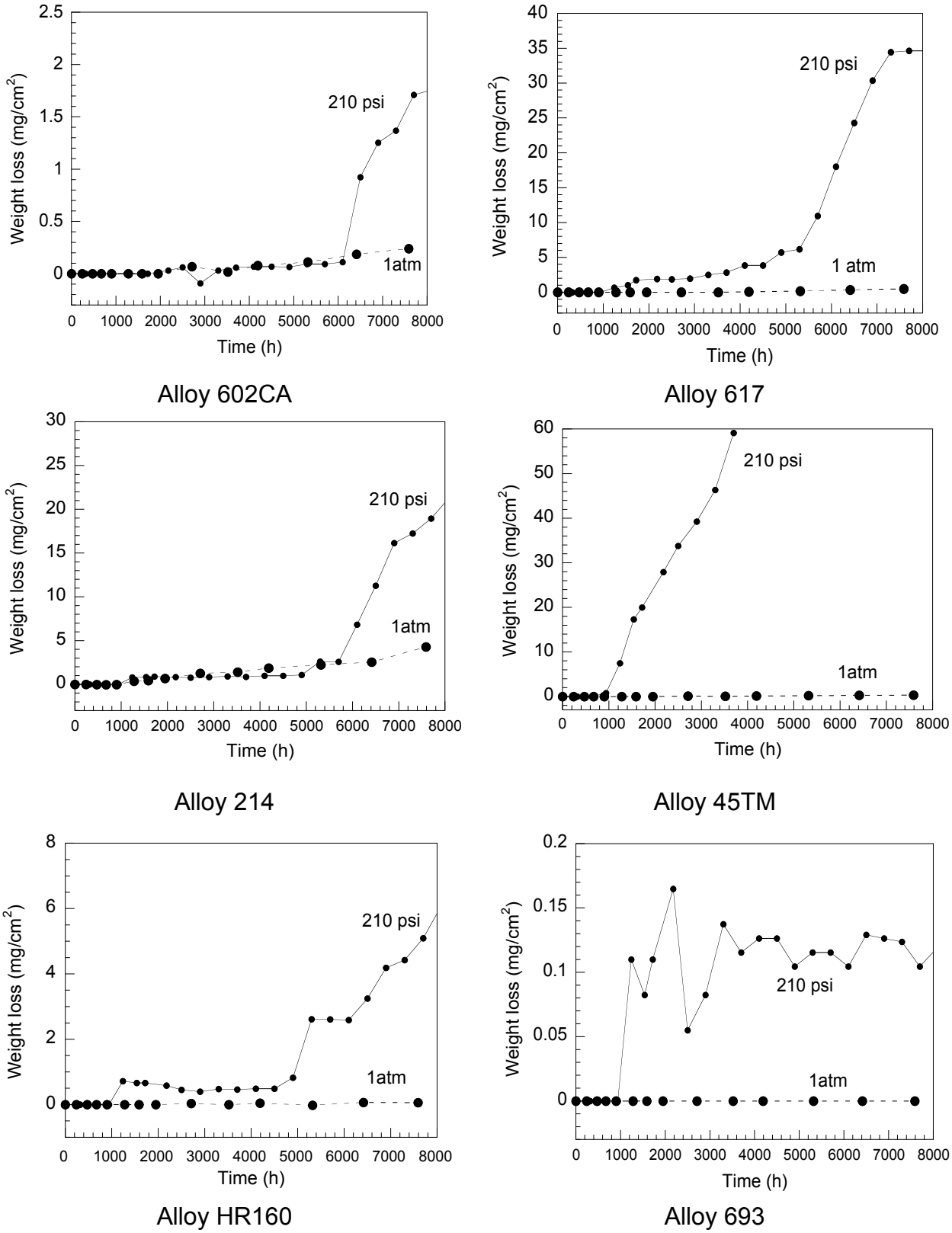

Figure 4.20. Weight loss for Ni-base alloys at system pressures of 1 and 14.3 atm, at carbon activity of ≈31, and temperature of 593°C.

We also conducted another pair of experiments at a carbon activity ≈104. Run 64HP was conducted in Gas 18 at 30 atm (441psi) and 593°C. Experiments at 1 atm pressure was conducted with a gas composition (Gas 21) adjusted to yield the same carbon activity of 104 as the high-pressure Run 64HP (30 atm). Specimens of various alloys were exposed to Gas 21 at 1 atm for 13,842 h.

Figure 4.21 shows weight loss data for various alloys exposed at system pressures of 1 and 30 atm, but at the same carbon activity of ≈104 and the same temperature of 593°C. The results are similar to the experiment at 14.3 atm with a carbon activity ≈ 31. All the tested alloys showed a sharp decrease in initiation time for metal dusting degradation at higher system pressure.

Figure 4.22 shows a comparison of the weight loss rates at 593°C for several Ni-base alloys exposed at 30 atm with a carbon activity ≈104 and for those exposed at 14.3 atm with a carbon activity ≈31. The combination of higher system pressure and higher carbon activity leads to a decrease in time for the initiation of metal dusting attack. Once the attack initiates, the specimens lose weight fairly rapidly under both conditions. The extent of the weight loss is alloy dependent influenced by the chemical composition and the stability/integrity of the oxide scales that develop during exposure.

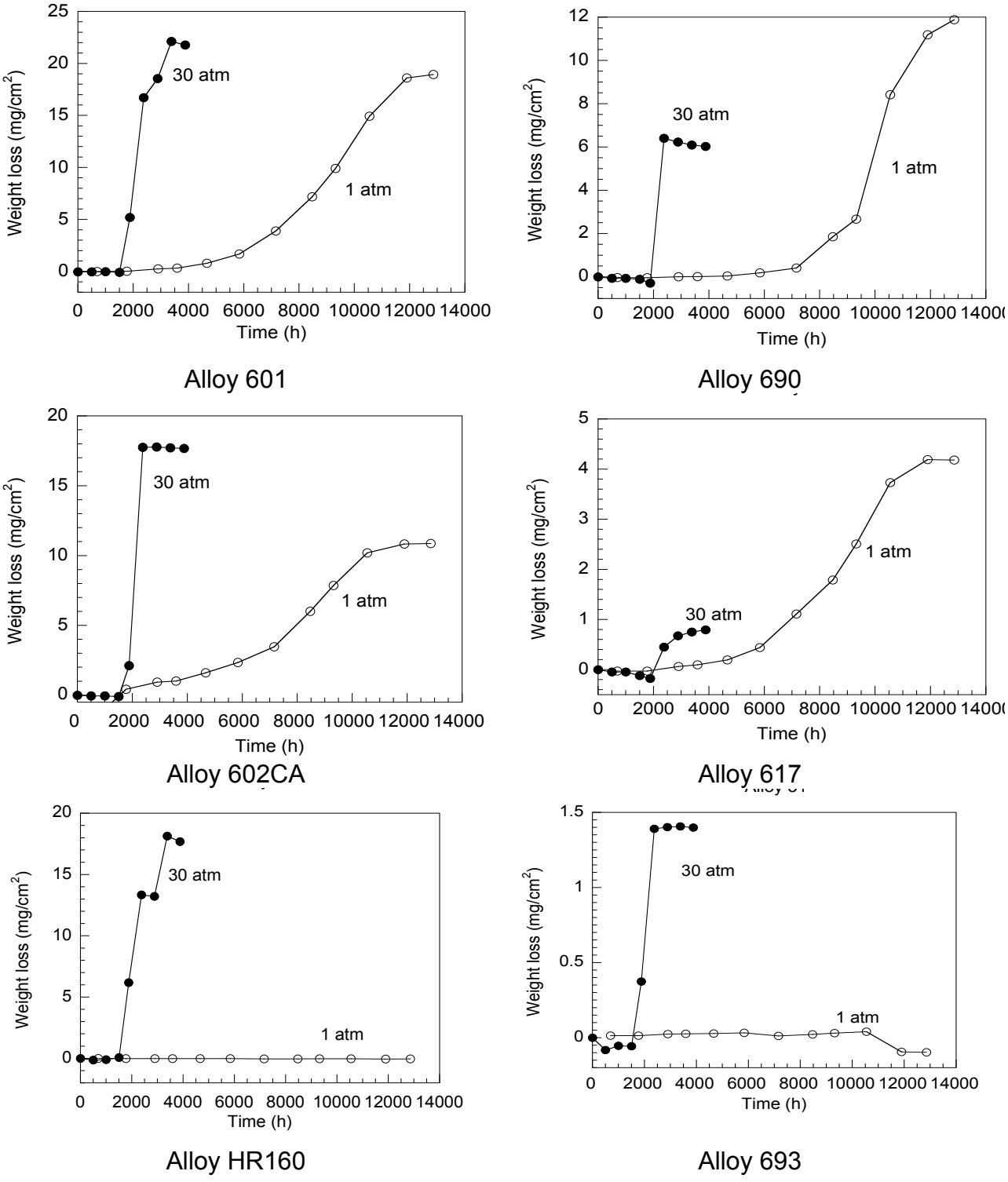

Figure 4.21. Weight loss for Ni-base alloys at system pressures of 1 and 30 atm, a carbon activity of ≈104, and temperature of 593°C.

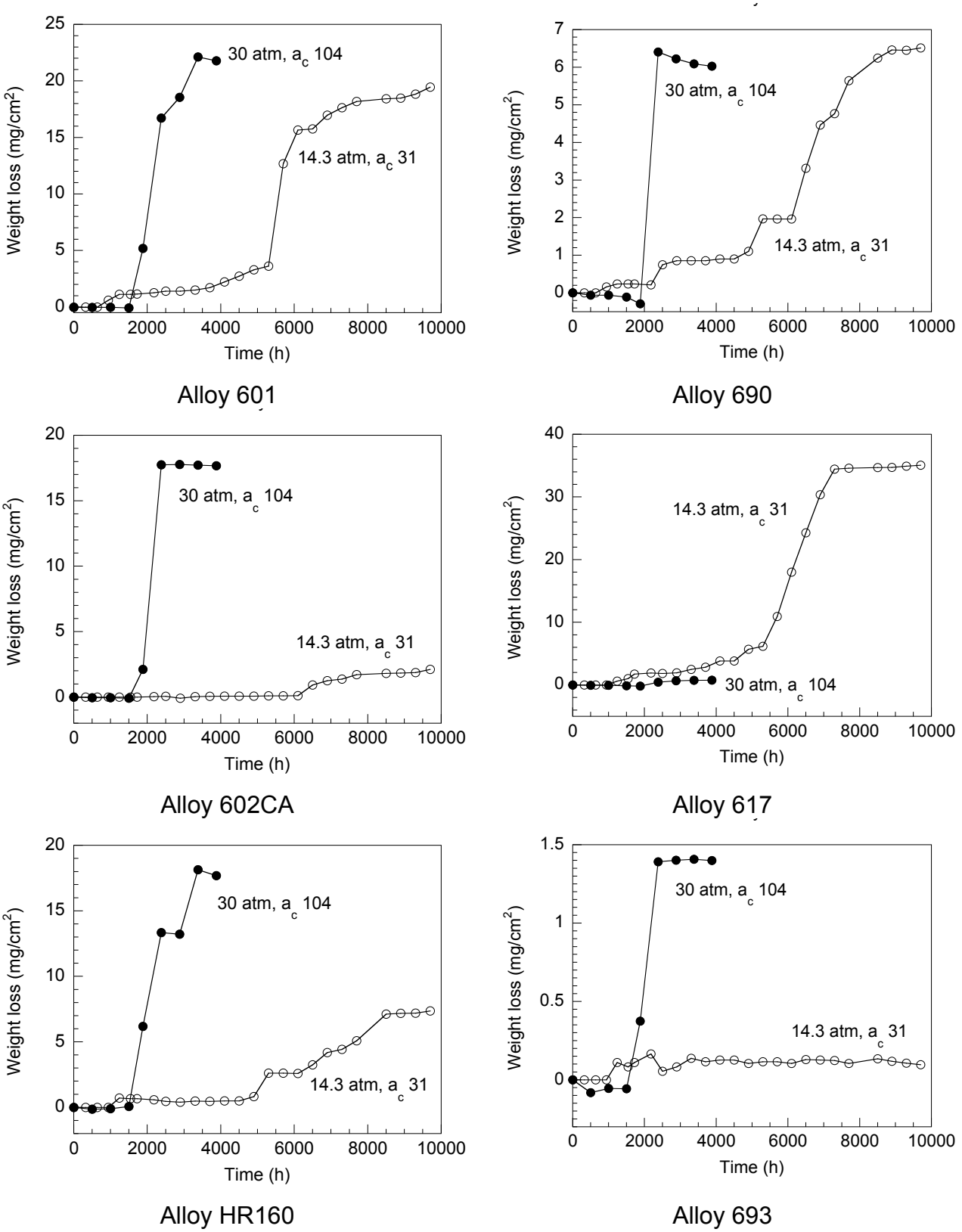

Figure 4.22. Weight loss for Ni-base alloys at system pressures of 14.3 (a_C 31) and 30 atm (a_C 104) and temperature of 593°C.

4.6. Metal Dusting in Heat-Treat Environment

Metal dusting is experienced at high temperatures in oxidizing-carburizing environments that are prevalent in heat-treat industry. The environment prevalent in heat-treat applications contain gases generated from oil residue on the work pieces that are kinetically favorable for metal dusting attack. We exposed 20 alloys at 1 atm and 815 and 593°C in Gas 20 (with carbon activity >>200 at 815 and 593°C, respectively), which had a composition that simulated the environment in heat-treat industry. Only EBrite alloy was attacked at 815°C after 5716 h exposure, as shown in Figure 4.23.

Figures 4.24 and 4.25 show the macrophotographs of several commercial and ANL-developed alloys, respectively, after 2136-h exposure at 1 atm, 593°C in Gas 20. All the ANL-developed alloys and RA85H (which contains 3.5 wt.% Si) performed well and no pitting was observed. EBrite was attacked heavily and the pit density in Alloy HR120 was high. Corrosion attack initiated along the edges of specimens in Alloys 321 and Crofer.

Figure 4.23. Macro-photograph of alloys after 5716-h exposure to Gas 20 at 815°C.

Figure 4.24. Macro-photographs of several alloys after 2136 h exposure to Gas 20 at 593°C.

Figure 4.25. Macrophotograph of ANL-developed alloys after 2136-h exposure to Gas 20 at 593°C.

Figure 4.26 shows the weight loss data for several commercial alloys after exposure in Gas 20 at 593°C. The weight loss of Alloy HR120 is the highest among these alloys because of its high pit density (see photograph in Fig. 4.24). Alloys 321 and Crofer also corroded rapidly. Figure 4.27, a magnified view of data in Fig. 4.26, shows that almost all these commercial alloys lost weight except Alloys RA85H and 601. Alloy 321 developed the deepest pits among these alloys (see Fig. 4.28). Pit sizes in Alloy HR120 and Crofer were also large, although the chromium content in Alloy HR120 (25 wt.%) is high. We did not measure the pit depth of Alloy 430 because a pit has developed through the thickness (of 460 μm) within 960 h. Although the pits on Alloy 430 developed fast, its pit density was low. Therefore, the weight loss of this specimen is low (see Fig. 4.27).

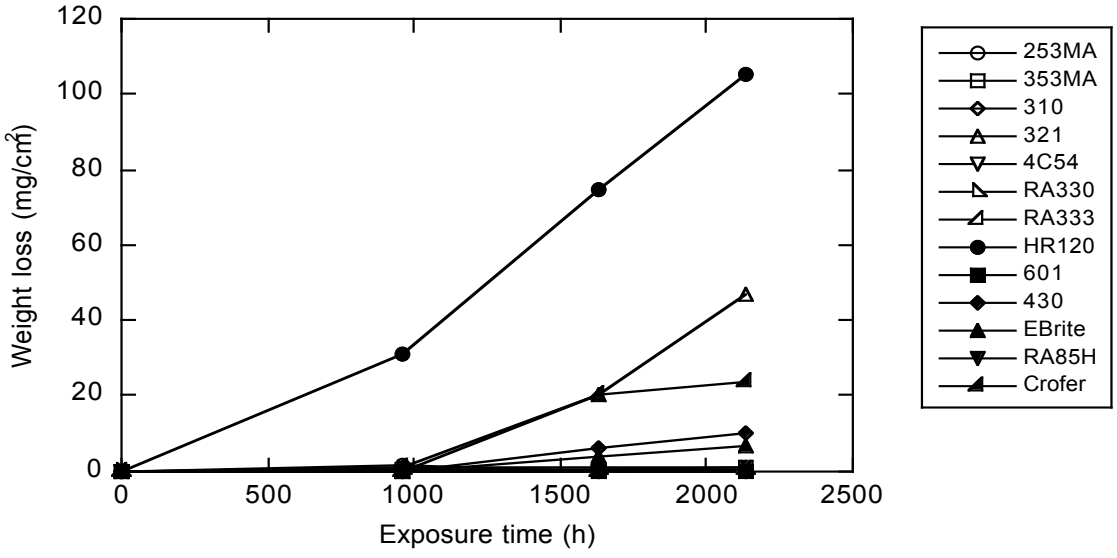

Figure 4.26. Weight loss data for commercial alloys after exposure in Gas 20 at 593°C, 1 atm.

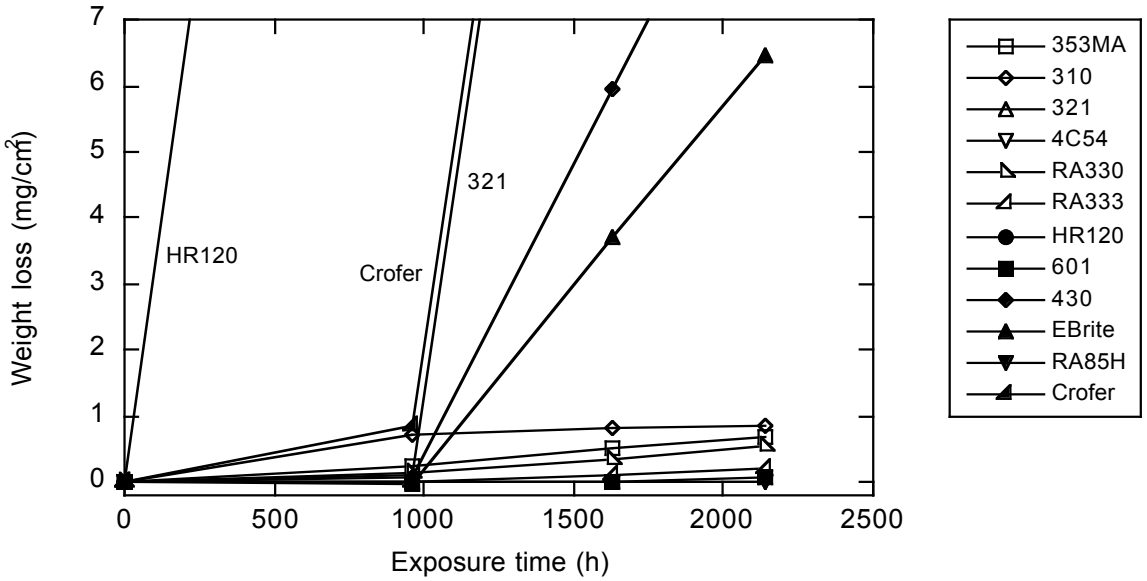

Figure 4.27. Magnified view of data in Fig. 4.26.

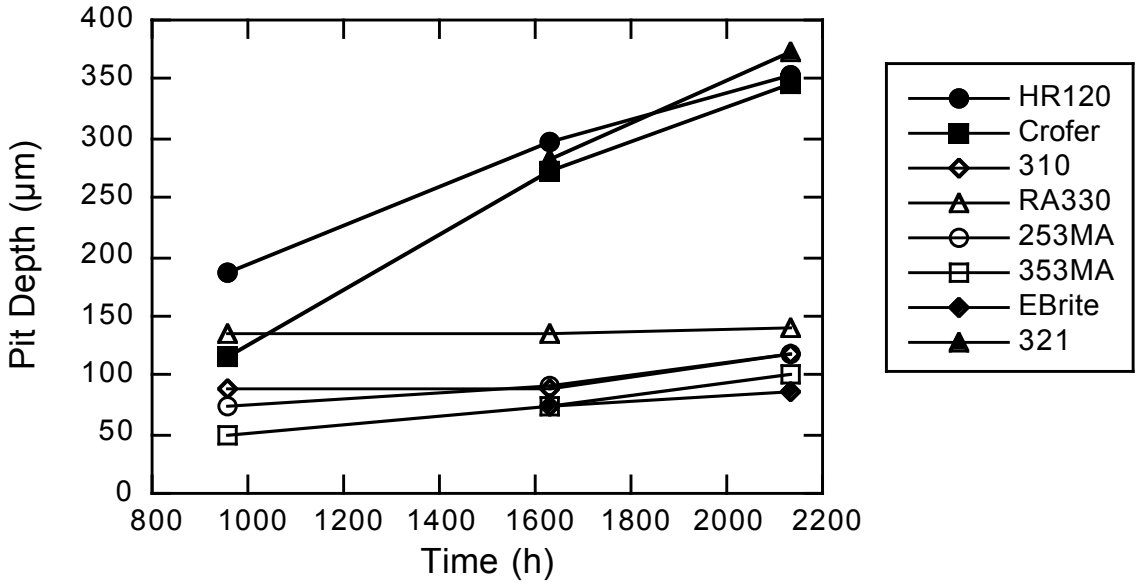

Figure 4.28. Pit depth for commercial alloys after exposure in Gas 20 at 593°C, 1 atm.

4.7. Effect of Alloy Composition on Metal Dusting

Figure 4.29 shows the weight loss data for several Ni-base alloys after exposure in Gas 21 (65.1% H_2, 30% CO, 0.94% H_2O, 4% CO_2) with a carbon activity of 104 at 593°C and 1 atm (Run 61). The weight loss rate of Alloys 214, 600, and 45TM is high in this gas environment. Alloys 602CA, 601, 617, and 690 also lost weight. Metal dusting pits were observed on Alloy 625, although its weight loss was small. However, Alloys 230, HR160, and 693 were not attacked by metal dusting even after 13842-h exposure to the carburizing gas. The chromium content is low in both Alloys 214 and 45TM. Although Alloy 214 contains 3.7% wt.% Al, it was readily attacked indicating that the

chromium content in the alloys has to be >20 wt.% to resist metal dusting corrosion. The iron content in 45TM is the highest among these alloys and it also corroded at a high rate.

Several of these alloys also exhibited significant pitting attack. The growth rate of pit depth in Alloy 45TM is the highest among the alloys although the Cr content in Alloy 45TM is much higher than that in Alloy 601. Its weight loss rate is also the fastest. High iron content in this alloy may be responsible for its worse performance in metal dusting environment. Aluminum addition in Alloy 617 and 602CA seems to decrease the pit growth rate.

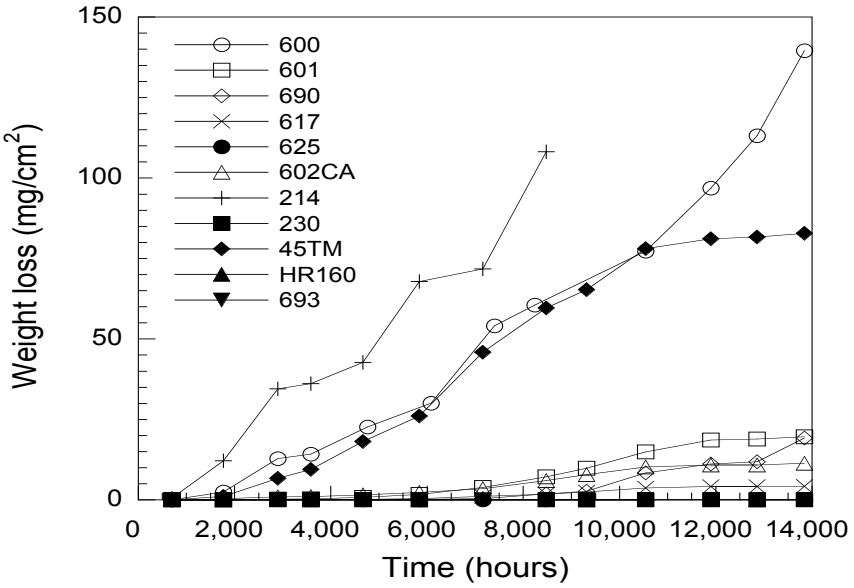

(a)

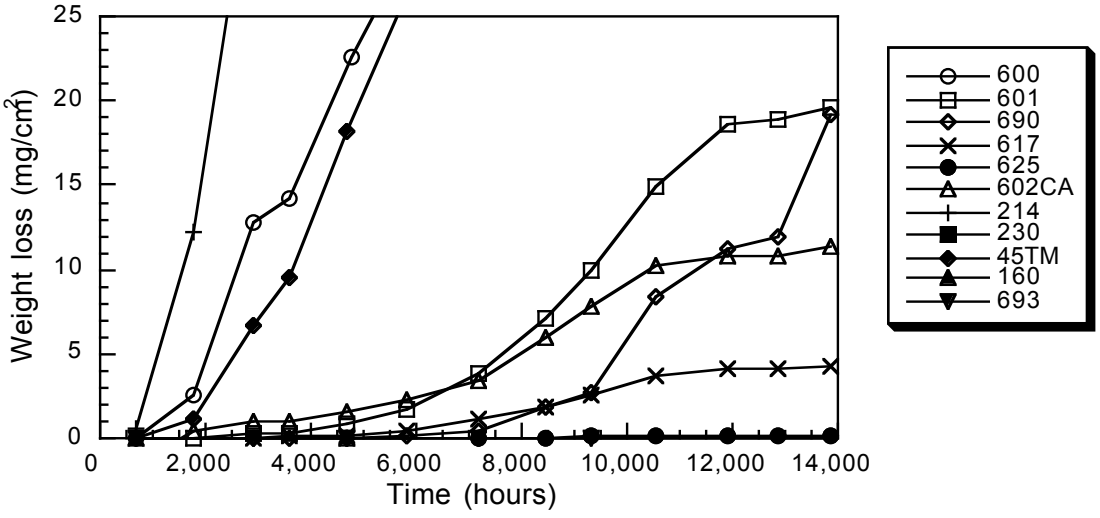

(b)

Figure 4.29. (a) Weight loss data for several Ni-based alloys after exposure in Gas 21 (65.1% H_2, 30% CO, 0.94% H_2O, 4% CO_2) with a carbon activity of 104 at 593°C and 1 atm. (b) Magnified view.

The pit-depth data, from Fig. 4.30, were fitted by straight lines and the correlations were used to calculate the through-wall penetration time as a function of wall thickness for pipes of different alloys. Figure 4.31 shows a plot of the penetration time versus wall thickness. The through-wall penetration time for Alloy 625 is the longest among the seven Ni-base alloys that were tested.

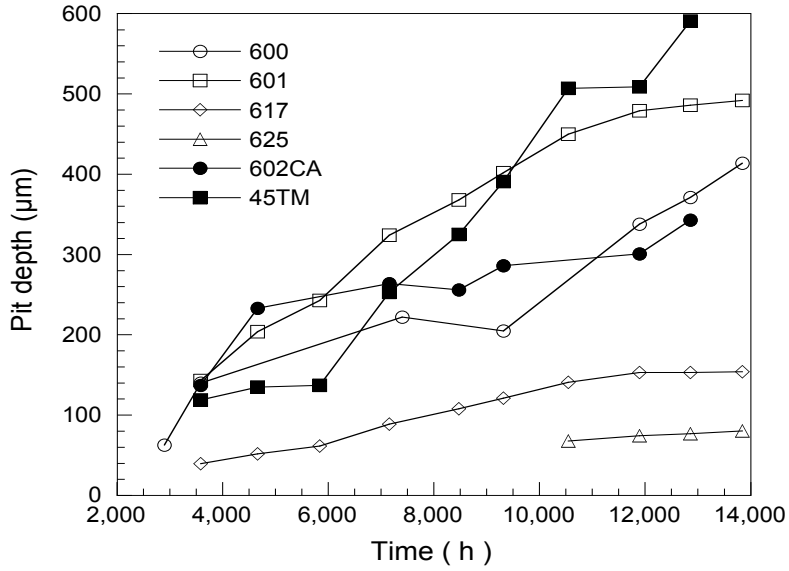

Figure 4.30. Pit depth as a function of time for several Ni-base alloys exposed to a gas mixture with a carbon activity of 104 at 593°C and 1 atm (Run 61).

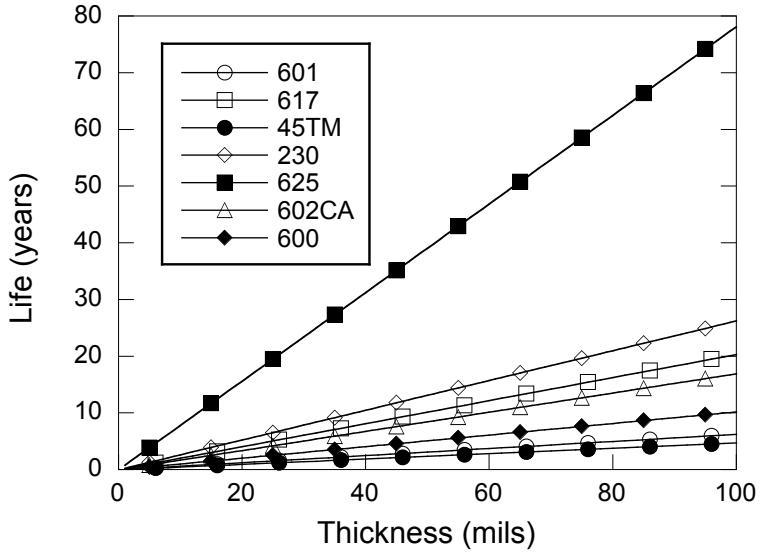

Figure 4.31. Time for through-wall penetration for Alloys 600, 601, 602CA, 625, 617, 45TM and 230 as a function of wall thickness, after exposure at 593°C, 1 atm in a gas mixture with a carbon activity of 104.

4.8. Effect of Carbon Activity on Metal Dusting

A comparison of the effect of carbon activity on metal dusting degradation can be made from the data developed in Runs 54 and 61, both of which were conducted at 593°C and 1 atm. The gas chemistry in the two runs was adjusted to establish carbon activity of 31 (Run 54 with Gas 11) and 104 (Run 61 with Gas 21). In both runs, the specimens from were retrieved periodically, cleaned, and weighed to determine the weight loss as a function of exposure time. Measurements of pit depths were also made using the surface profiler.

A comparison of the effect of carbon activity on the weight loss at 593°C, 1 atm is shown in Figure 4.32. All the tested alloys showed a decrease in initiation time upon exposure to the higher carbon activity environment. Furthermore, for any given alloy the weight loss rate was higher at the higher carbon activity. At present, a direct comparison of the weight loss rates at the two levels of carbon activity is not possible since the weight loss at the lower carbon activity has not reached steady state value during the 7400-h exposure.

Figure 4.33 shows a comparison of the maximum pit depths that were measured in various specimens exposed in the two runs. The data indicate that the specimens exposed in Run 54 has smaller pit depths than those exposed in Run 61, even though the exposure time and temperature were similar in both runs. This is a reflection of the effect of carbon activity (in the exposure environment) on the time to (incubation time) initiate metal dusting. For example, alloys such as 602CA and 45TM exhibited virtually no pits after exposure in Run 54 whereas the same alloys had maximum pit depths of 261 and 268 μm, respectively, after exposure in Run 61.

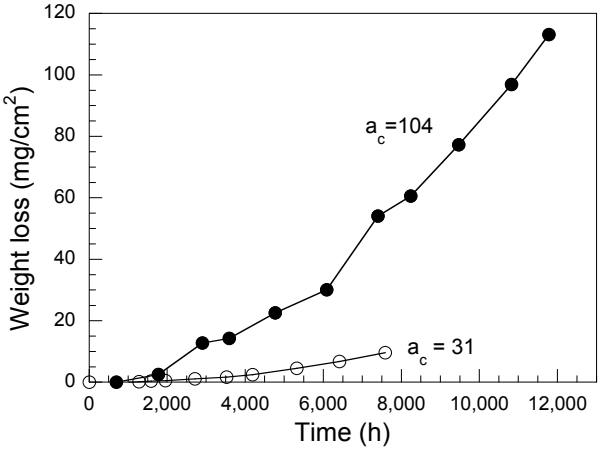

Alloy 600

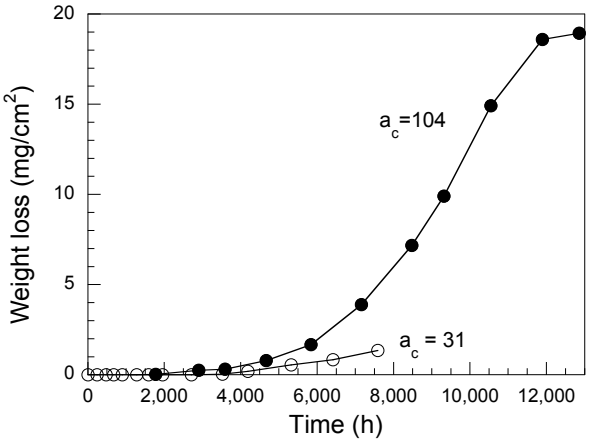

Alloy 601

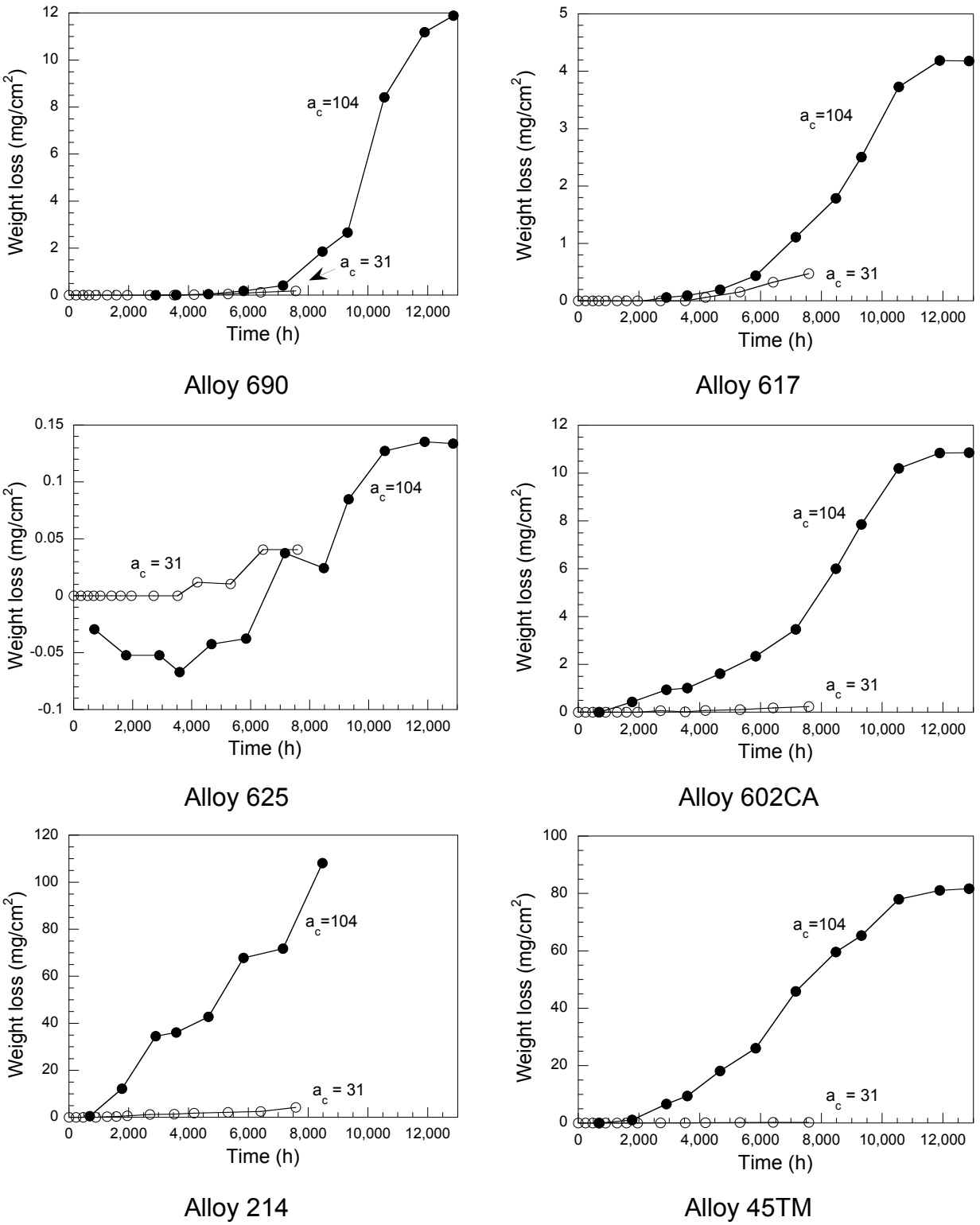

Figure 4.32. Weight loss data for Ni-base alloys exposed at carbon activity of 31 and 104, 593°C, and 1 atm.

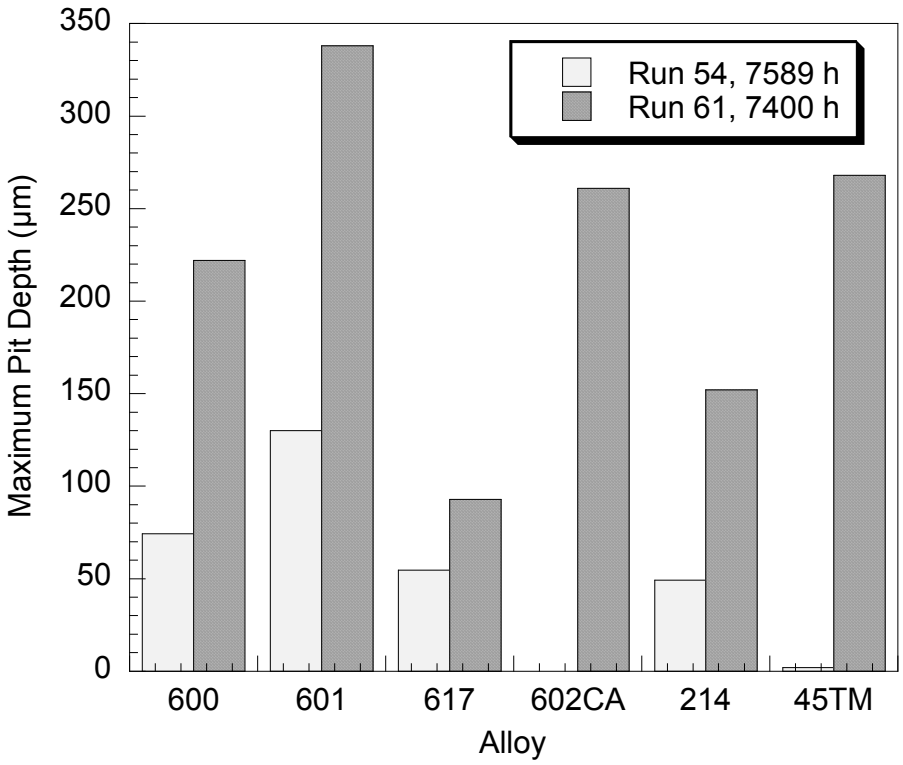

Figure 4.33. A comparison maximum pit depths that were measured in several Ni-base alloys, after exposure in Runs 54 and 61.

5. APPROACH TO MITIGATE METAL DUSTING CORROSION

In recent years, we studied the mechanism for metal dusting degradation in simulated hydrogen reformer environments and established the causes for the initiation of pits in both Fe- and Ni-base alloys.[12,17] The information that we developed on the performance of various alloys led us to model the process for the formation of a metal dusting pit. Two major factors can affect the formation of metal dusting pits. First is the rate of carbon diffusion into alloys. If alloys do not develop a protective oxide layer to resist carbon diffusion, the carbon that has diffused into and accumulated in alloys will lead to metal dusting corrosion. Second is the rate of the formation of oxide scale. If alloys can form a continuous oxide scale on their surface, carbon diffusion through the oxide scale is slowed, and carbon accumulation in the alloy diminishes. In general, metal dusting environments contain both oxygen and carbon, and the process that dominates is dictated by several factors, such as temperature, pressure, alloy composition, and gas chemistry.

Generally, the hydrogen reformer environment contains sufficient steam to establish oxygen partial pressures that are conducive to the formation of chromia and/or spinel phases in the oxide scale that develops on Fe- and Ni-base alloys. Therefore, most areas of an alloy surface are protected from metal dusting corrosion. The process can continue only in those areas amenable to with carbon ingress.[19] Figure 5.1 shows an enlarged channel for transferring carbon. The channel consists of Fe_3C or Ni particles.

At low oxygen partial pressure (pO_2), oxygen cannot oxidize Fe_3C and Ni. Carbon diffuses through the channels into the alloys at a relatively high rate. If oxygen can also diffuse through these channels, an oxide scale may form underneath the channel because Cr can form Cr_2O_3 at a much lower pO_2 than the oxides of Fe and Ni. The oxide scale underneath the channel will eventually stop or minimize the diffusion of carbon into the alloys, and metal dusting will cease. However, because the oxygen atom is much larger than the carbon atom, and the diffusion rate of oxygen is not high enough to form a continuous chromium oxide layer, carbon can continue to diffuse into the alloys and lead to metal dusting corrosion. The Fe_3C and Ni particles act as filters to allow carbon diffusion but prevent oxygen diffusion. A self-healing mechanism may not work in this situation, and a metal dusting pit will finally form. Although chromium can still react with oxygen at the pit area, a continuous oxide scale may not form. Many carbon transfer channels form deep roots into alloys (see Fig. 5.2), and the process of metal dusting does not stop after the pits develop. However, if we temporarily remove CO and CO_2 from the exposure atmosphere, the diffusion of carbon will cease, whereas diffusion of oxygen can continue. Therefore, a continuous oxide scale could develop underneath the carbon transfer channel without interference from carbon, thereby blocking the channel for further transport of carbon. Results from the following experiments show that this approach retards the growth of metal dusting pits.

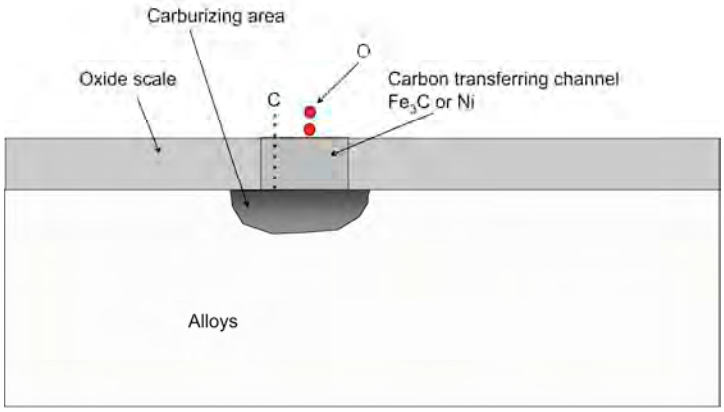

Figure 5.1. Schematic of a model for initiation of a metal dusting pit.

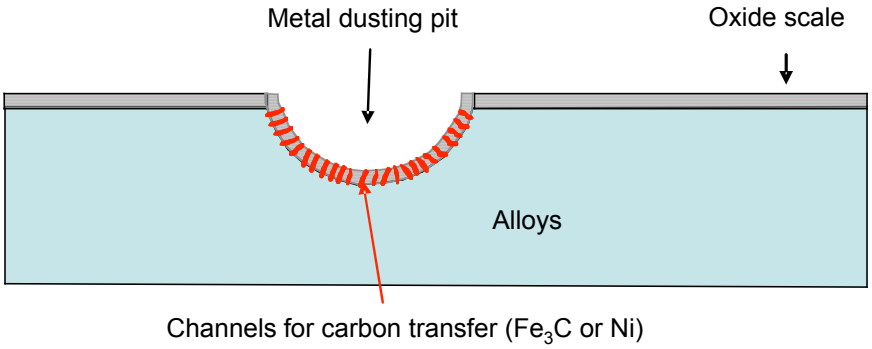

Figure 5.2. Schematic of carbon transfer channels in a pit.

5.1 Mitigation of Metal Dusting in Fe-base Alloys

To examine this intermediate oxidation (in the absence of carbonaceous gases) approach to mitigate metal dusting attack, Alloy 800 specimens were selected for the study. The specimens were exposed for 5 days to a gas mixture consisting of 72.2% H_2-8.3% CO_2-17.6% CO-1.96% H_2O (Gas 5) at 593°C. Metal dusting pits of 100-200 μm in diameter were observed (see Fig. 5.3). The pit surface was rough due to the deposited carbon particles in the pit. Subsequently, the specimen was exposed at 593°C for 2 days to a gas mixture of H_2-2% H_2O, which has similar water content to Gas 5 but no carbon containing species.

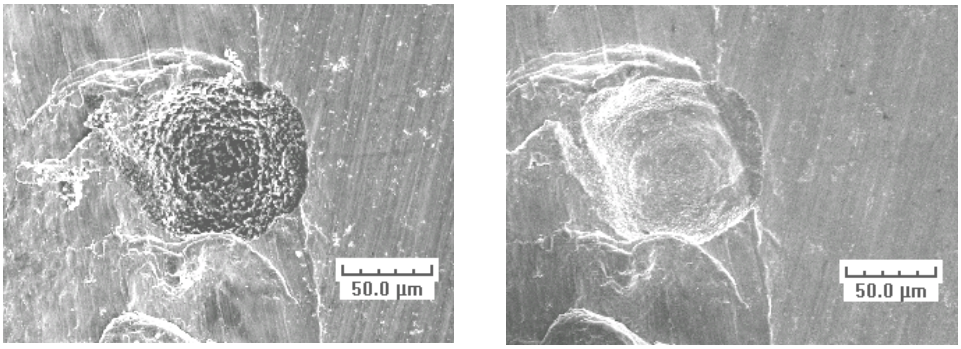

Figure 5.3. Left: Pit on Alloy 800 after 5-day exposure to a carburizing gas at 593ºC. Right: The specimen after further exposure in H_2-2% H_2O at 593ºC for 2 days.

The pit surface became smooth after exposure to the H_2-2% H_2O environment, because carbon particles in and around the pit were removed by oxidation. The pit area was slightly oxidized by the gas with oxygen partial pressure similar to that of Gas 5. The sample was again exposed to Gas 5 for 4 days at 593°C. The pit size remained the same as before exposure (Fig. 5.4, left). No further metal dusting attack occurred at this pit, even when this specimen was exposed to Gas 5 for 6 days (Fig. 5.4, right) after intermediate oxidation in the H_2-2%H_2O gas mixture. Similar observations were made on the effects of intermediate oxidation on other pits on the Alloy 800 surface.

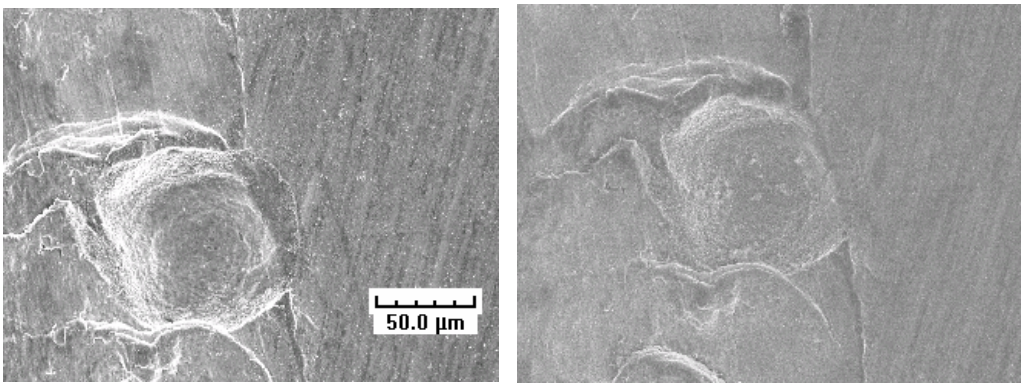

Figure 5.4. The specimen shown in Fig. 5.3 after exposure to 72.2% H_2-8.3% CO_2-17.6% CO-1.96% H_2O at 593ºC for (left) 4 days and (right) 6 days.

Figures 5.5 and 5.6 show a second metal dusting pit on Alloy 800 that exhibited behavior similar to that of the pit in Fig. 5.3. Figure 5.7 shows the behavior of a third pit on the surface of the same specimen of Alloy 800. In the case of the third pit, the oxide was not protective enough to resist metal dusting, and a small pit could be observed after 4 days exposure of the oxidized specimen [Fig. 5.7(c)]. These observations can be explained by the model shown in Fig. 5.8.

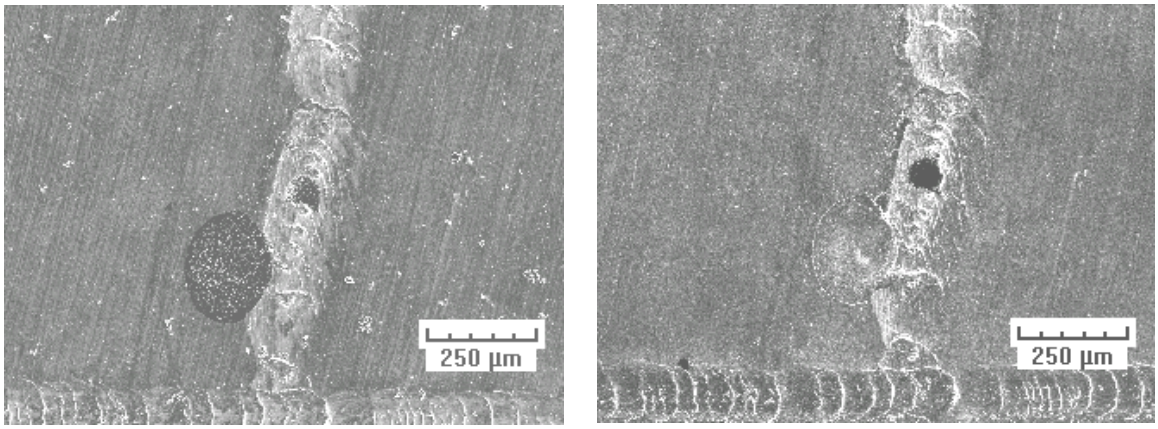

(a) (b)

Figure 5.5. (a) Another metal dusting pit on Alloy 800 after exposure to carburizing atmosphere consisting of 72.2% H_2-8.3% CO_2-17.6% CO-1.96% H_2O at 593ºC for 5 days. (b) The specimen after further treatment by exposure to a gas consisting of H_2-2% H_2O at 593ºC for 2 days.

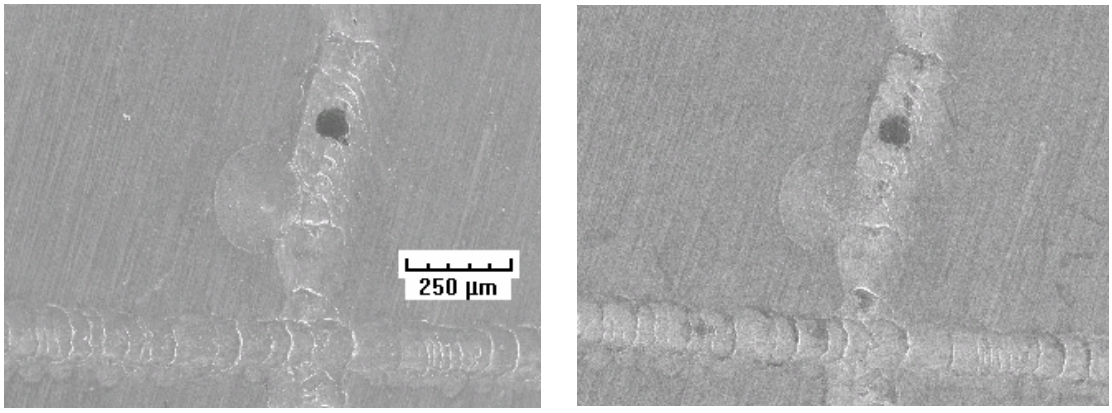

(a) (b)

Figure 5.6. Specimen, shown in Fig. 5.4, after further exposure to the carburizing atmosphere for (a) 4 days and (b) 6 days.

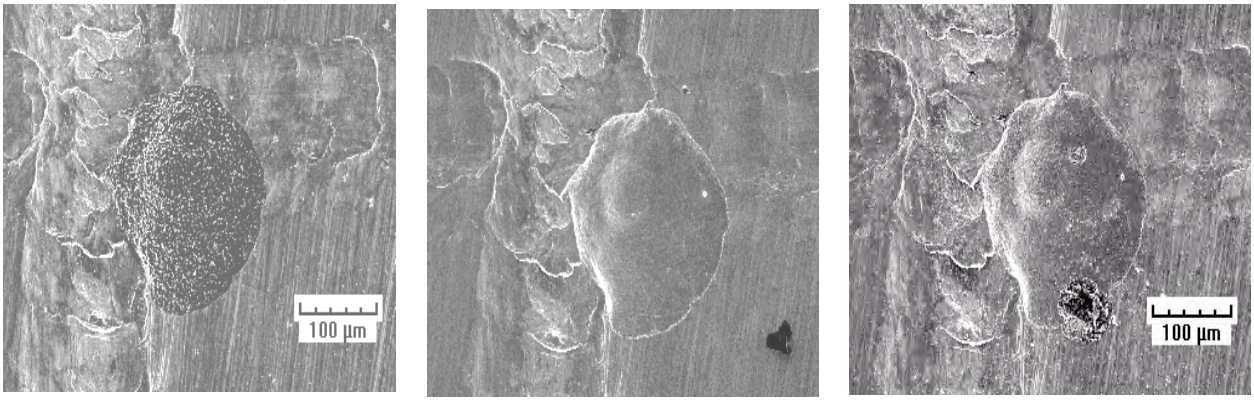

(a) (b) (c)

Figure 5.7. (a) Third pit on Alloy 800 after exposure to carburizing atmosphere consisting of 72.2% H_2-8.3% CO_2-17.6% CO-1.96% H_2O at 593°C for 5 days. After the alloy sample was oxidized at 593ºC for 2 days, the sample was re-exposed to the carburizing atmosphere for (b) 2 days and (c) 4 days.

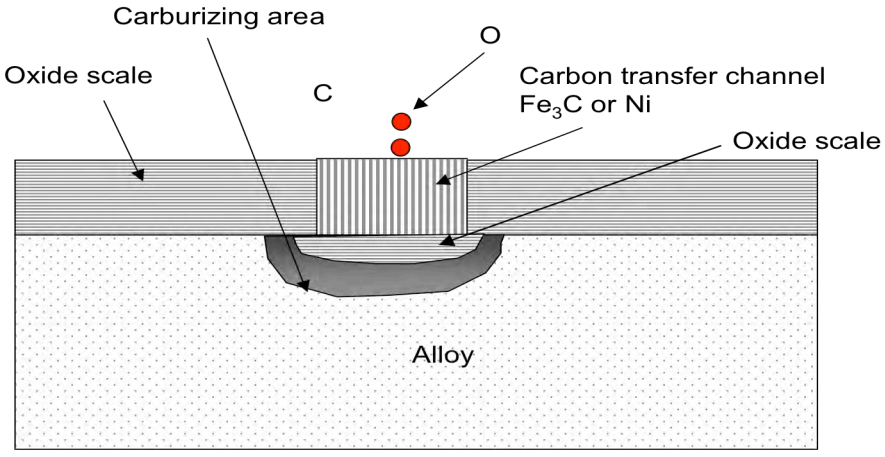

Figure 5.8. Schematic of a model for the blocking action of oxide layer after intermediate oxidation of metal dusted alloy.

The beneficial effect of intermediate oxidation depends on the integrity of the oxide that develops in the pit region and the protective capacity (from the standpoint of stability, phases present, etc.) of the oxide against metal dusting initiation when subsequently exposed to the process atmosphere. A continuous protective oxide scale, to stop the continued growth of the pit, could not form since carbon could transfer faster than oxygen through the channels in the oxide scale.

When the carbonaceous gases CO and CO_2 are removed during the intermediate oxidation treatment, a continuous oxide scale could form underneath the channels without the interference of carbon. The newly formed oxide acts as a barrier to further transport of carbon when the specimen is exposed to the metal dusting environment. The incubation time for Alloy 800 is ≈100 h in the gas chemistry and temperature used in our study. Therefore, after the 4-day exposure to a carburizing atmosphere, carbon broke through the new oxide scale and a pit grew, as shown in Fig. 5.7(c).

Intermediate oxidation of the metal dusted specimens was developed as an approach to slow the pit propagation rate therby, extend the useful life of a metallic component. Several experiments were conducted to evaluate the role of exposure temperature and the gas chemistry on the stability and integrity of the scale that develops after intermediate oxidation and its protective capacity against continued metal dusting attack. Table 5.1 lists the test time and temperature and gas chemistry along with the pit characteristics on Alloy 800 that was used for developing the approach. Earlier, we proposed that channels are present in the oxide scale for carbon to diffuse through the scale and enable the growth of metal dusting pits. If the pits are oxidized by an intermediate exposure to an oxidizing environment, the channels may be blocked and carbon diffusion can be eliminated or minimized.

Table 5.1. Effect of intermediate oxidation on subsequent growth of pits in Alloy 800

Oxidizing atmosphere	Temperature (°C)	Time (h)	Pit growth status after exposure (time given below) in Gas 5			
			2 days	4 days	6 days	10 days
2%H_2O-98%H_2	593	48	No	Yes	Yes	Yes
2%H_2O-98%H_2	593	24	yes	Yes	Yes	Yes
2%H_2O-98%H_2	593	6	yes	Yes	Yes	Yes
95%H_2O-5%H_2	593	24	yes	Yes	Yes	Yes
95%H_2O-5%H_2	593	6	yes	Yes	Yes	Yes
100%H_2O	593	24	yes	Yes	Yes	Yes
100%H_2O	593	6	yes	Yes	Yes	Yes
2%H_2O-98%H_2	760	24	No	No	No	No
2%H_2O-98%H_2	760	6	No	No	No	No
95%H_2O-5%H_2	760	24	No	No	No	No
95%H_2O-5%H_2	760	6	No	No	No	No
100%H_2O	760	24	No	No	No	Grew again
100%H_2O	760	6	No	Grew again	Grew again	Grew again

Alloy 800 specimens that were initially metal dusted (with pits) were oxidized in a mixture of steam and hydrogen. The oxygen pressure in the exposure environment, the exposure temperature and time will dictate the oxide thickness. At 593°C, the pits on Alloy 800 were not sufficiently oxidized even after 48 h treatment. Therefore, carbon

transfer channels have not been totally blocked. Pits started to grow in 4 days after exposure to the carburizing gas. However, when alloys were oxidized at 760°C, pits did not grow even after 240-h exposure in Gas 5 (72.2% H_2-8.3% CO_2-17.6% CO-1.96% H_2O). Generally, the incubation time for Alloy 800 is ≈100 h in Gas 5. The observation that the pits did not grow even after 240 h indicates that the channels were blocked and carbon diffusion is slowed considerably.

When Alloy 800 was oxidized in 95% H_2O-5% H_2 mixture at 760°C, 6 h was sufficient to stop the pit growth. However, pure steam was not as good as the mixture of steam and hydrogen. Figure 5.9 shows that the pit in Alloy 800 did not grow even after 10 days of subsequent exposure to metal dusting environment when the pit was oxidized in 2% H_2O-98 %H_2 mixture at 760°C. However, the pit started to grow in 4 days if the pit was oxidized in 100% steam at the same temperature (see Fig. 5.10). Figure 5.11 shows that the major phase in the oxide scale on Alloy 800 was spinel, if the alloy was oxidized in 100% steam at 760°C. Spinel phase is susceptible to attack by carbon, which leads to continued metal dusting. However, the major phase was Cr_2O_3, if the alloy was oxidized in 2% H_2O-98% H_2 mixture at 760°C (see Fig. 5.11). Presence of Cr_2O_3 in the scale protected the alloy from continued metal dusting corrosion.

These results indicate the potential of intermediate oxidation treatment to delay the onset of metal dusting and continued wastage. This approach may not be useful for Alloy 800 because the incubation time of Alloy 800 is short. However, if we apply this method to some of the Fe- and Ni-base alloys with long incubation time, we may be able to greatly extend the life of these alloys and process components for service in a metal dusting environment.

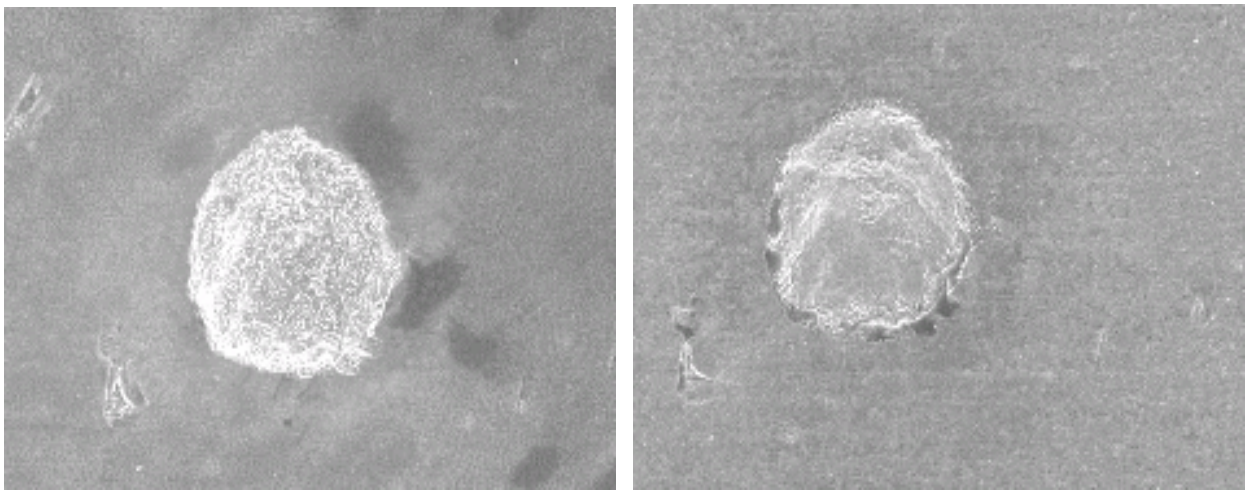

As oxidized After 10-day exposure

Fig. 5.9. (Left) metal dusting pit in Alloy 800 after 6-h exposure to 2% H_2O-98% H_2 at 760°C; (right) after subsequent 10-day exposure in Gas 5 at 593°C, indicating no change in size and shape of pit.

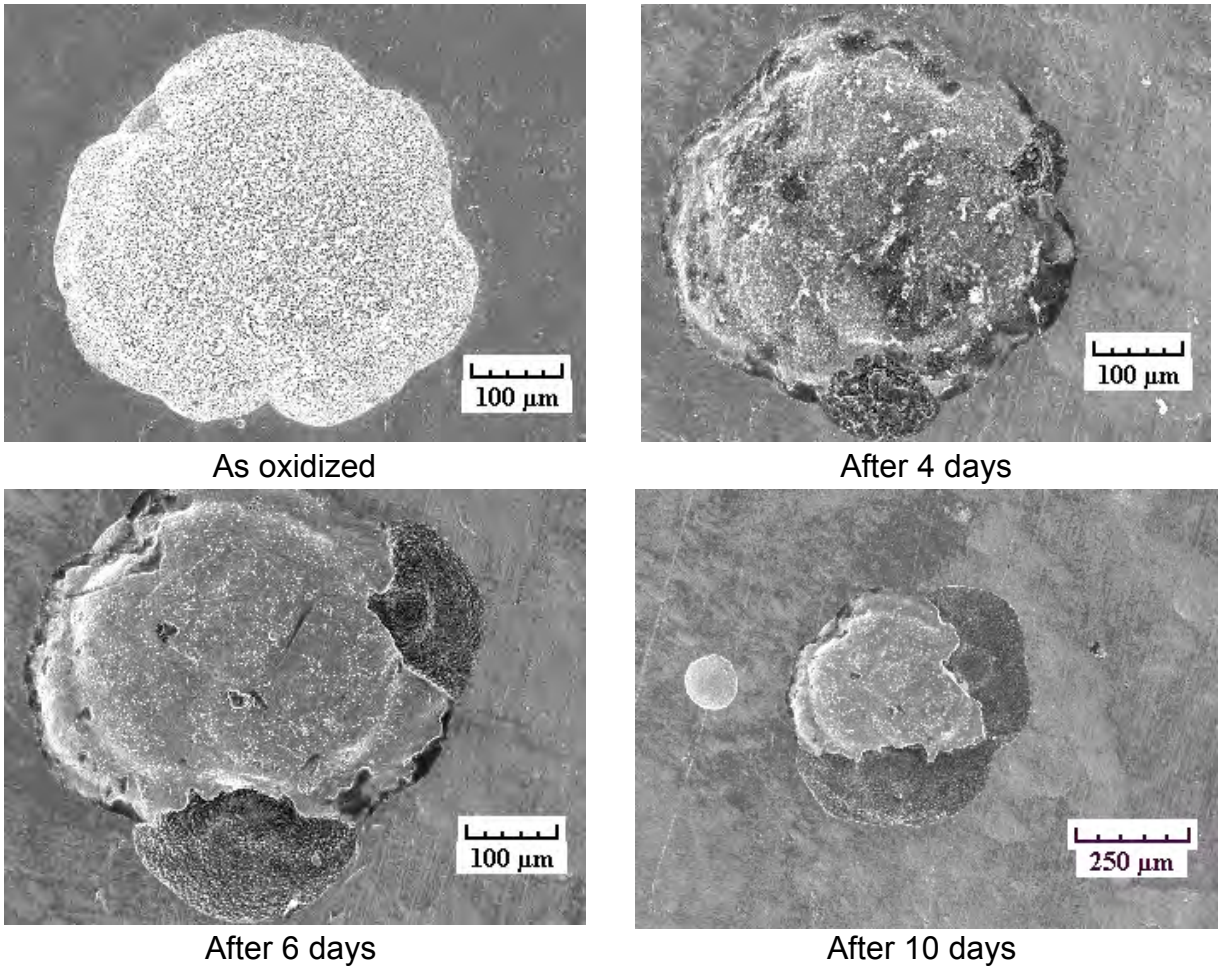

As oxidized | After 4 days

After 6 days | After 10 days

Figure 5.10. Time progression of a metal dusting pit in Alloy 800 after 6-h exposure to 2% H_2O-98% H_2 at 760°C and after subsequent 4-, 6-, and 10-day exposure in Gas 5 at 593°C.

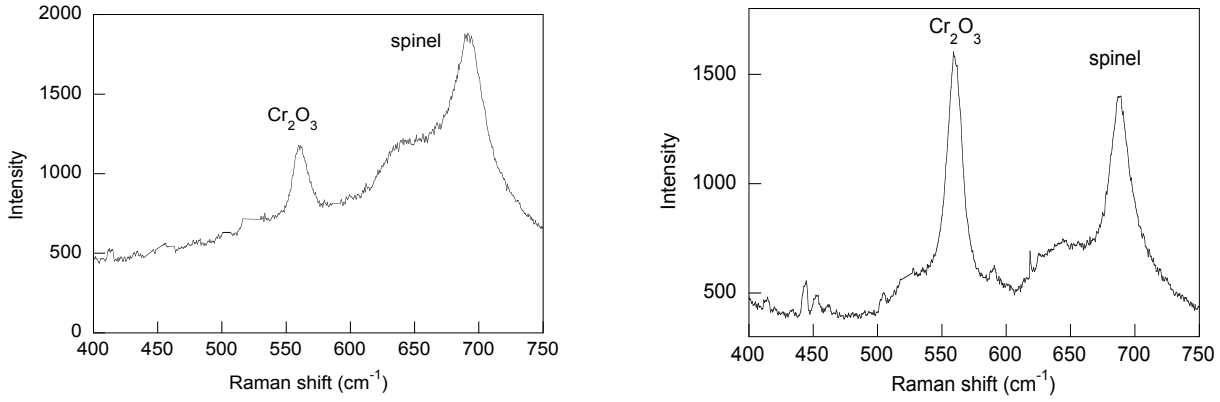

pure steam | 2% steam-hydrogen

Figure 5.11. Raman Spectra for Alloy 800 after oxidation at 760°C in pure steam and in 2% H_2O-98% H_2 mixture.

5.2 Mitigation of Metal Dusting in Ni-base Alloys

Alloy 800 specimens that were initially metal dusted (i.e., exhibited pits) were oxidized in a mixture of steam and hydrogen. The best oxidation condition for Alloy 800, based on results obtained from several experiments, was temperature of 760ºC and gas composition of 95% steam-5% hydrogen. The oxidation treatment stopped the growth of pits for as long as 240 h even though the incubation time for pitting in Alloy 800 is ≈100 h.

We applied the same method to several Ni-base alloys, which exhibit much longer incubation times than that of Alloy 800. If metal dusting corrosion can be mitigated by intermediate oxidation of the alloy surface by a relatively short exposure time, extension of component life is possible by alleviating the metal dusting problem by periodic oxidizing.

Several Ni-base alloys were pre-pitted by exposing them to 50% CO-50% H_2 at 593ºC. After pits were formed on these alloys, they were subsequently exposed to Gas 21 (65.1% H_2, 30% CO, 0.94% H_2O, 4% CO_2) at 593°C and 1 atm. The growth of pits on these alloys was evaluated by periodic measurements of the pit depth and size using the profiler. The pre-pitted specimens (after exposure to Gas 21 at 593°C for 1442 h) were cut into two parts. Figure 5.12 shows a photograph after the specimens were cut. One part was exposed to 95% steam-5% hydrogen at 760°C for 24 h to oxidize the surface of the alloys, and then subsequently exposed to Gas 21 at 593°C. The other part (without intermediate oxidation) was used for continued exposure in Gas 21 at 593°C.

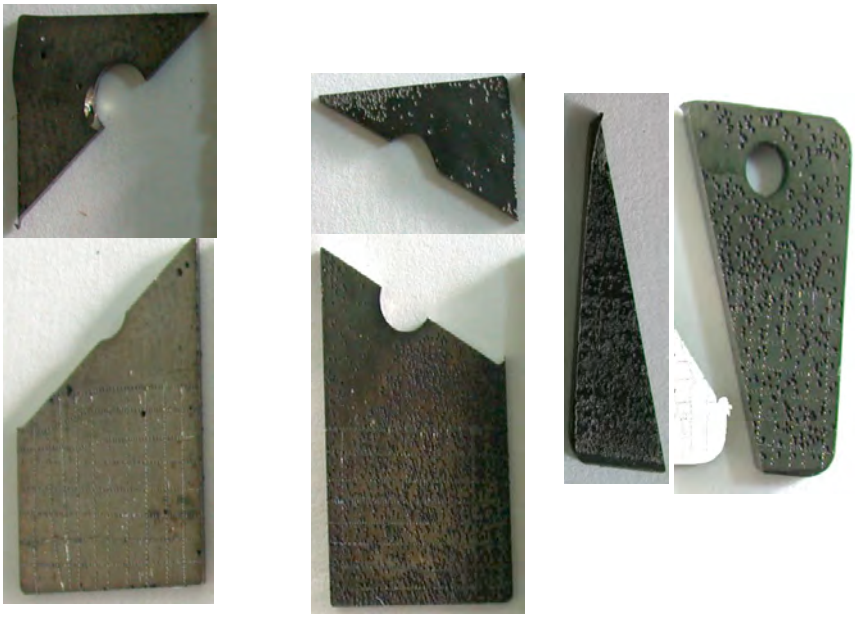

601 617 230

Figure 5.12. Macro-photographs of Alloy 601, 617, and 230. The specimens were cut into two parts after 1442-h exposure to a metal dusting environment (Gas 21) at 593ºC.

Figure 5.13 shows that pit sizes of Alloy 601 increase with time when specimens were exposed to Gas 21 at 593ºC. However, the pit sizes did not increase after the specimen was slightly oxidized by 95% steam-5% hydrogen mixture at 760ºC for 24 hours. Figures 5.14 and 5.15 show a similar trend for Alloys 617 and 230.

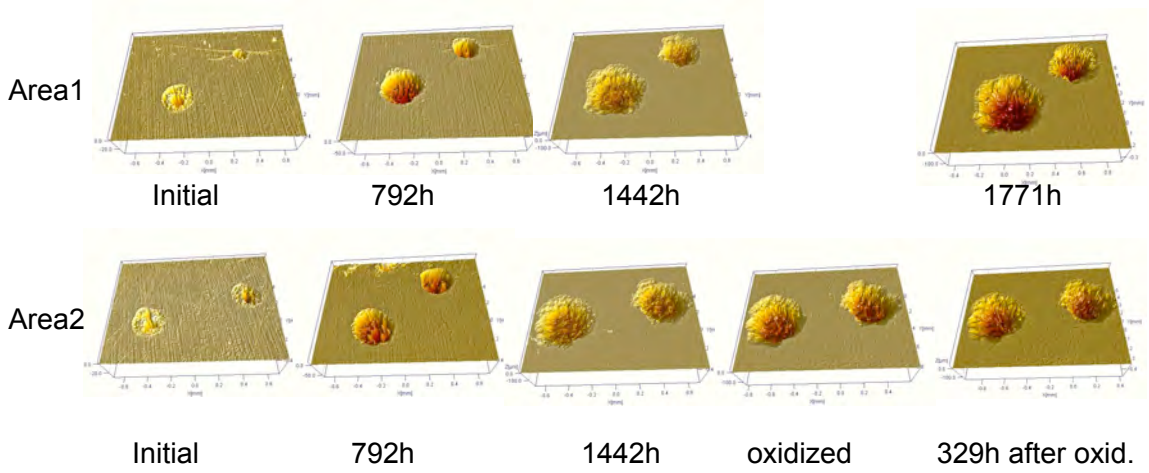

Figure 5.13. Pit morphology on Alloy 601. The Area 1 photographs show the pits without intermediate oxidation; Area 2 specimen was exposed to metal dusting environment for 1442 h and given an intermediate oxidation treatment and subsequently continued exposure for 329 h.

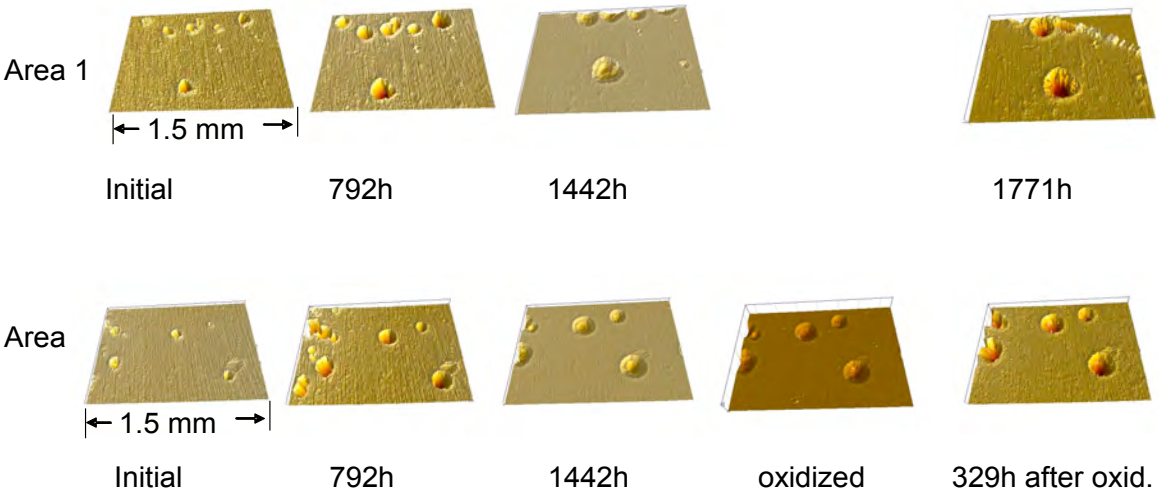

Figure 5.14. Pit morphology on Alloy 617. The Area 1 photographs show the pits without intermediate oxidation; Area 2 specimen was exposed to metal dusting environment for 1442 h and given an intermediate oxidation treatment and subsequently continued exposure for 329 h.

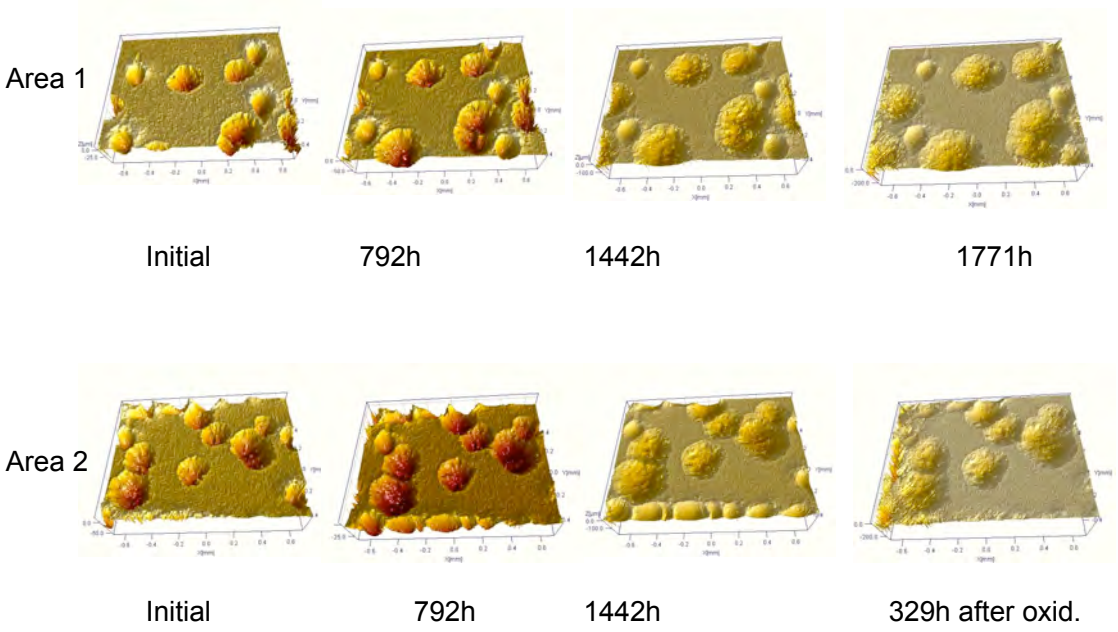

Figure 5.15. Pit morphology on Alloy 230. The Area 1 photographs show the pits without intermediate oxidation; Area 2 specimen was exposed to metal dusting environment for 1442 h and given an intermediate oxidation treatment and subsequently continued exposure for 329 h.

Figures 5.16 and 5.17 show the pit size as a function of exposure time for Alloys 617 and 602CA with and without intermediate oxidation. The specimens were exposed in a metal dusting environment with a carbon activity of 104 at 593°C and 1 atm. The results indicate that the pit growth can be arrested by intermediate oxidation that was conducted in 95% H_2O-5% H_2 at 760°C for 24 h. Without the oxidation step, the pits continued to grow in all the alloys tested. In the case of Alloys 617, the pit size was large prior to intermediate oxidation whereas the pit size was small for Alloy 602CA. The benefit of intermediate oxidation was observed irrespective of the pit size.

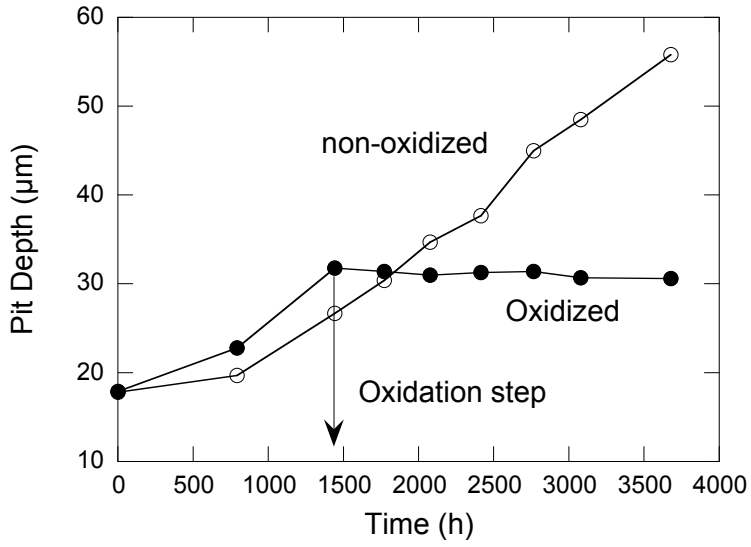

Figure 5.16. A comparison of pit-depth data for Alloy 617 with and without intermediate oxidation.

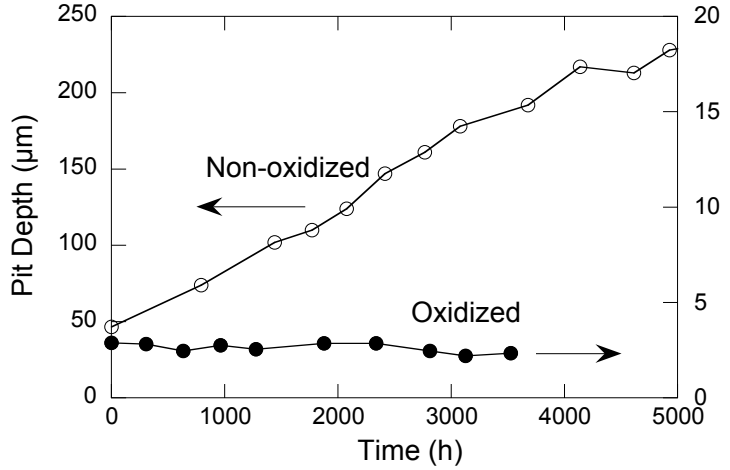

Figure 5.17. A comparison of pit-depth data for Alloy 602CA with and without intermediate oxidation.

This result indicates that carbon transfer channels at metal dusting pits in all four alloys were blocked after their surfaces were slightly oxidized. For the continuation of metal dusting corrosion, new channels have to develop for carbon to diffuse through the scale. This process can take as much or longer than the incubation period observed during the exposure of the virgin alloy. Figures 5.18 to 5.21 show the behavior of Alloys 214, 690, 230, and 601, with and without intermediate oxidation, when exposed to metal dusting environment at 593°C. In this case, the growth of the pit on Alloy 214 was only temporarily stopped for ≈600 h, beyond which it began to grow. However, the growth of the pits on Alloy 690 and 230 was stopped for 1900 h and 2700 h, respectively. The results indicate that the intermediate oxidation step need to be optimized based on the behavior of the alloy and also the time and environment need to be assessed to establish the threshold conditions for developing a protective oxide in the pitted region of the alloy. The pit on Alloy 601 started to grow within 600 h after the first oxidation. However, the growth of the pit was stopped for another 600 h when the surface was oxidized again. Therefore, the effect of intermediate oxidation is repeatable.

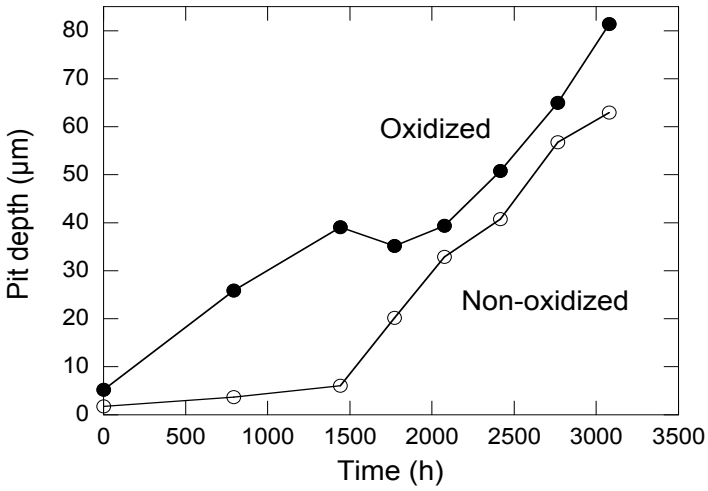

Figure 5.18. A comparison of pit-depth data for Alloy 214 with and without intermediate oxidation.

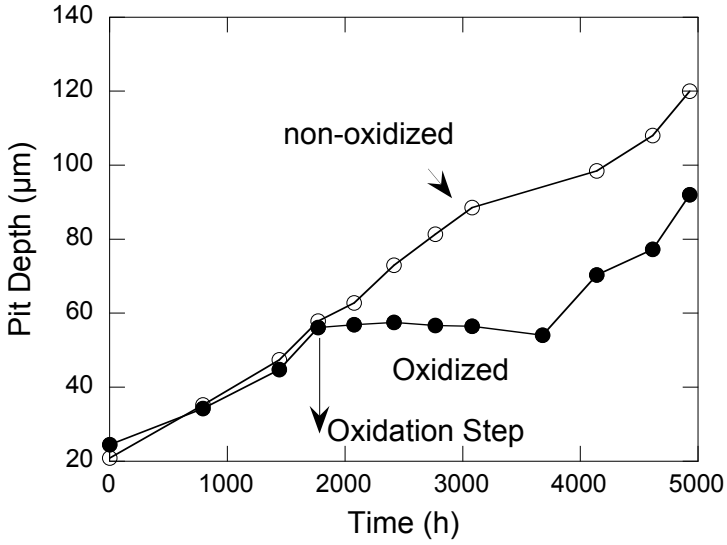

Figure 5.19. A comparison of pit-depth data for Alloy 690 with and without intermediate oxidation.

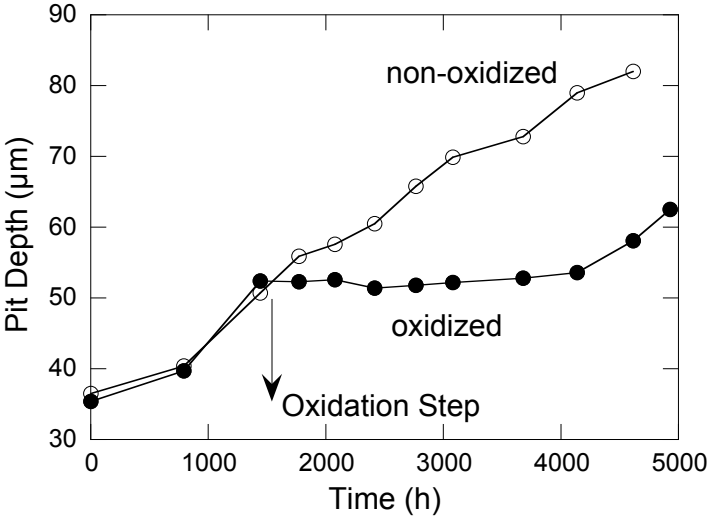

Figure 5.20. A comparison of pit-depth data for Alloy 230 with and without intermediate oxidation.

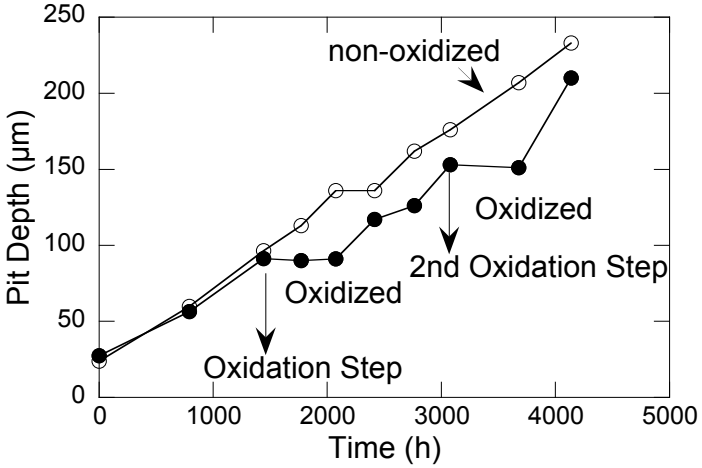

Figure 5.21. A comparison of pit-depth data for Alloy 601 with and without intermediate oxidation.

6. X-RAY NANO-BEAM STUDIES

Oxide scale is essential to protect the structural alloys from carbon-induced degradation and associated corrosion at elevated temperatures. We have shown in our studies that the oxide scale that develops in metal dusting environments can contain several phases, the protective capacity of which can be quite different.[17,18] The thermodynamic stability of different phases over long periods can influence the protectiveness of the oxide scale and on the overall performance of the alloy. It is necessary to understand the relationship between the phase composition of oxide scale and the capability of the scale to resist against further degradation. X-ray diffraction (XRD) is the best tool to determine the phase composition in oxide scale. However, some alloys develop oxide scales with several sub-layers. Regular X-ray beam cannot be focused on each sub-layer in the cross section of the alloys because the sublayers, in general, are only a few micrometers in thickness. Some alloys show pitting corrosion with micron-size pits that cannot be analyzed by regular XRD either. The 2ID-D beamline of the advanced photon source (APS) at Argonne National Laboratory produces a monochromatic X-ray beam of size ≈200 nm. The nano-size X-ray beam provides an excellent approach to study the local structure and chemistry of oxide scales and sublayers on alloys. Not only the phase composition but also the oxidation state of each ion in the oxide scale can be determined at sub-micrometer range using this nano-beam X-ray. Recently, we used this approach to study the oxide scale on alloys that were exposed to metal dusting environment. The results reveal important information which can aid in the development of new alloys with potential to extend the service life of metallic components used in metal dusting environment.

Figure 6.1 shows the photomicrograph of the cross section of a failed tube of Alloy 800H from a hydrogen reformer. The specimen was scanned by X-ray nanobeam in both the pit and non-pit areas as indicated in Fig. 6.1. The thickness of oxide scale in the pit region is thinner than that in the non-pit area (see Fig. 6.2). Spinel was identified as the major phase in the oxide scale. The spinel structure is named after the mineral $MgAl_2O_4$ and the general composition is AB_2O_4. It is essentially cubic, with the O ions forming a face-centered-cubic (fcc) lattice. The cations occupy 1/8 of the tetrahedral sites and 1/2 of the octahedral sites and there are 32 O ions in the unit cell. There are two types of cubic building units inside the fcc O-ion lattice, filling all 8 octants as shown in Fig. 6.3. The spinel structure is very flexible with respect to incorporation of cations and there are over 100 known compounds. In particular, the A and B cations can mix in several ways leading to compounds such as $(A_8)(B_{16})O_{32}$, or $A_8(B_8A_8)O_{32} = A(AB)O_4$, or $(A_{8/3}B_{16/3})(A_{16/3}B_{32/3})O_{32}$ and so on, with the atoms in the parentheses occupying the respective site at random.

Fe-Cr-O spinel can form a solid solution of $Fe_{1+x}Cr_{2-x}O_4$ ($0 \le x \le 2$). The oxidation of iron in $Fe_{1+x}Cr_{2-x}O_4$ has to change with x to keep charge balance in the lattice. Iron is +2 in $FeCr_2O_4$, the end member of $Fe_{1+x}Cr_{2-x}O_4$ (x = 0), and iron is +2.67 in Fe_3O_4, another end member of $Fe_{1+x}Cr_{2-x}O_4$ (x = 2). X-ray near edge absorption spectra (XNEAS) of iron, nickel, and chromium were obtained in the study. Figure 6.4 shows that the absorption coefficient changes dramatically at the interface between the oxide

scale and the alloy. The pre-edge a-feature of iron in Figure 6.5 is associated with transitions into d/d-p-hybridized final states; and has been shown to increase in strength with increasing Fe-valence (or d-hole population). Only a1 feature was observed for Fe^{2+}. The a2 feature appears when the compound contains Fe^{3+}. The oxidation state of iron in Fe_3O_4 is the highest in the solid solution of $Fe_{1+x}Cr_{2-x}O_4$ spinel. The intensity of the pre-edge a-feature of iron in oxide scale is between $Fe_{1.2}Cr_{1.8}O_4$ and $Fe_{1.8}Cr_{1.2}O_4$. The oxidation states of iron in $Fe_{1.2}Cr_{1.8}O_4$ and $Fe_{1.8}Cr_{1.2}O_4$ are 2.17 and 2.44, respectively. Therefore, iron in oxide scale is in a mixed valence between +2 and +3. Since the Fe^{3+} in spinel could be reduced in a metal dusting environment, the protective capacity of the oxide scale is destroyed. This result clearly explains the cause for easier pitting and significant attack of Alloy 800 in metal dusting environment.

Table 6.1. The spinel compositions of interest in metal dusting.

A	B	Formula	Mineral
Mg	Al	$MgAl_2O_4$	Spinel
Fe^{+2}	Fe^{+3}	$Fe^{+2}O.Fe^{+3}{}_2O_3=Fe_3O_4$	Magnetite
Fe^{+2}	Cr	$FeCr_2O_4$	Chromite

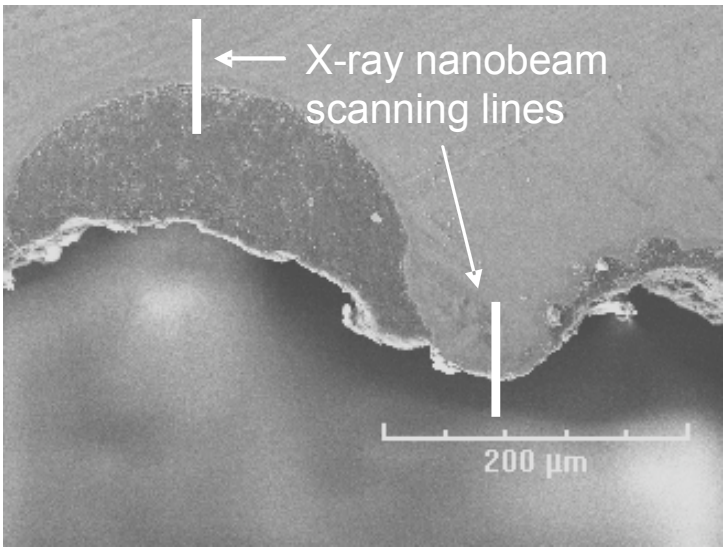

Figure 6.1. Photomicrograph of the cross section of an Alloy 800H specimen showing the regions that were scanned using X-ray nanobeam.

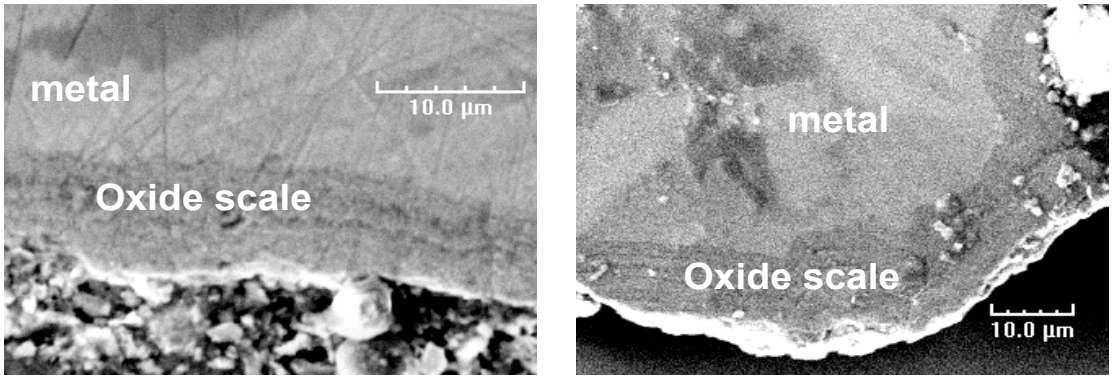

Pit area non-pit area

Figure 6.2. Scanning electron photomicrographs of cross section of Alloy 800H at the pit and non-pit areas.

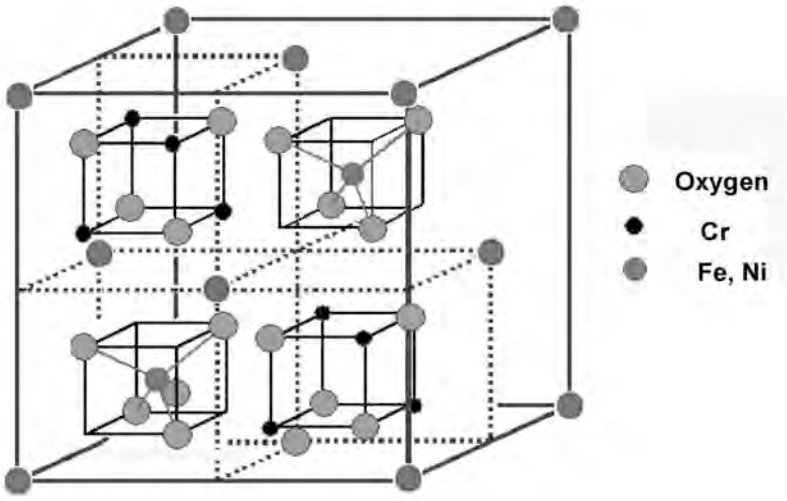

Figure 6.3. Structure of spinel.

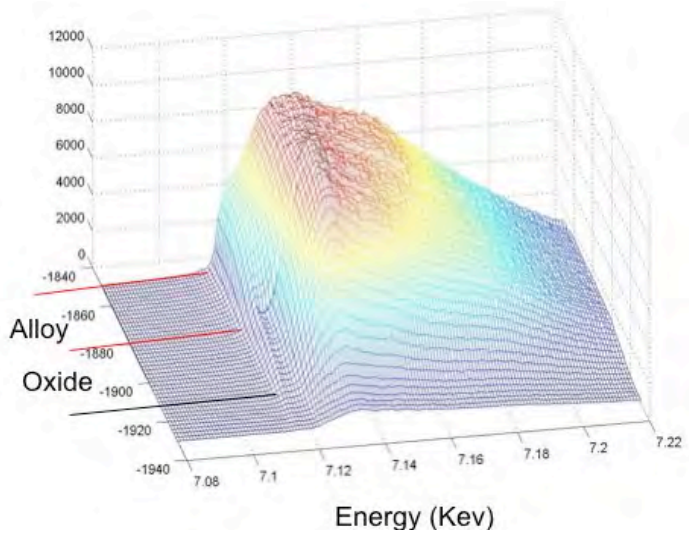

Figure 6.4. X-ray near edge absorption spectra (XNEAS) of iron. The X-ray nanobeam scanned across the oxide scale to the metal.

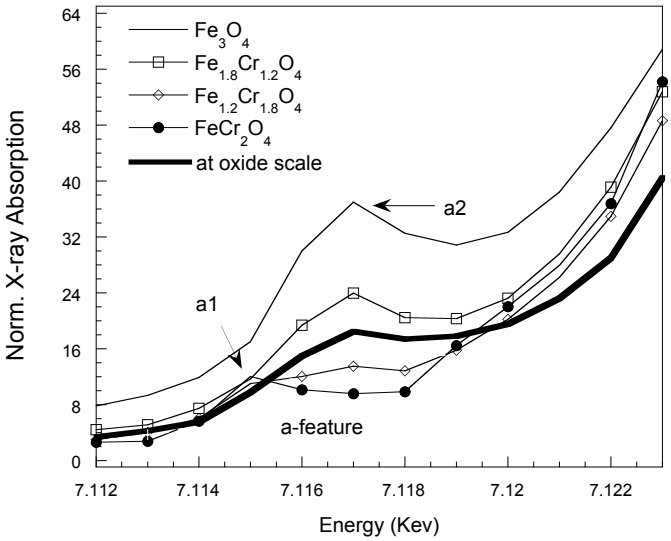

Figure 6.5. Pre-edge feature of X-ray near edge absorption spectra of iron in the oxide scale and for several standards with various valances.

Alloy 321 was also examined using the APS X-ray nanobeam. The sample was exposed for 1130 h in a simulated environment of a reformer outlet with a gas composition of 53.4%H_2-5.7%CO_2-18.4%CO-22.5%H_2O at 14.3 atm (210 psi) and 593°C. The carbon activity of the gas was ≈31 based on Reaction 1 at 14.3 atm and 593°C. Figure 6.6 shows the cross section of the Alloy 321 at the edge of a pit. EDX analysis was performed prior to analysis by X-ray beam. The thickness of the oxide scale at non-pit area is only a few micrometers. However, the thickness of the oxide scale at the pit area is ≈50 μm. Two layers were observed in the oxide scale in the pit area. The EDX analysis indicates more oxygen and iron in the outer layer than in the inner layer, but chromium and nickel concentrations in the outer layer are much less than in the inner layer (see Fig. 6.7). X-ray nanobeam was scanned across the cross section at the pit area from surface into the substrate region of Alloy 321. X-ray fluorescence analysis shows result similar to that observed by EDX. There is more iron in the outer layer of the oxide and more chromium in the inner layer (see Fig. 6.8). Only spinel phase was observed in both layers of the oxide scale, and Cr_2O_3 was not detected in the pit area (seeFig. 6.9). This result is consistent with previously reported Raman scattering results.

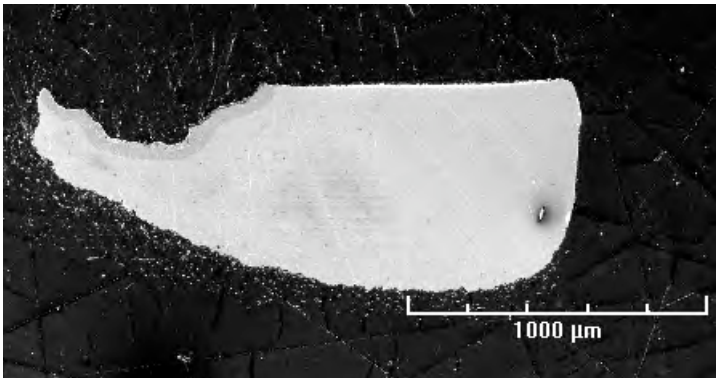

Figure 6.6. Scanning electron photomicrograph of cross section of Alloy 321 that was used for the X-ray nanobeam analysis.

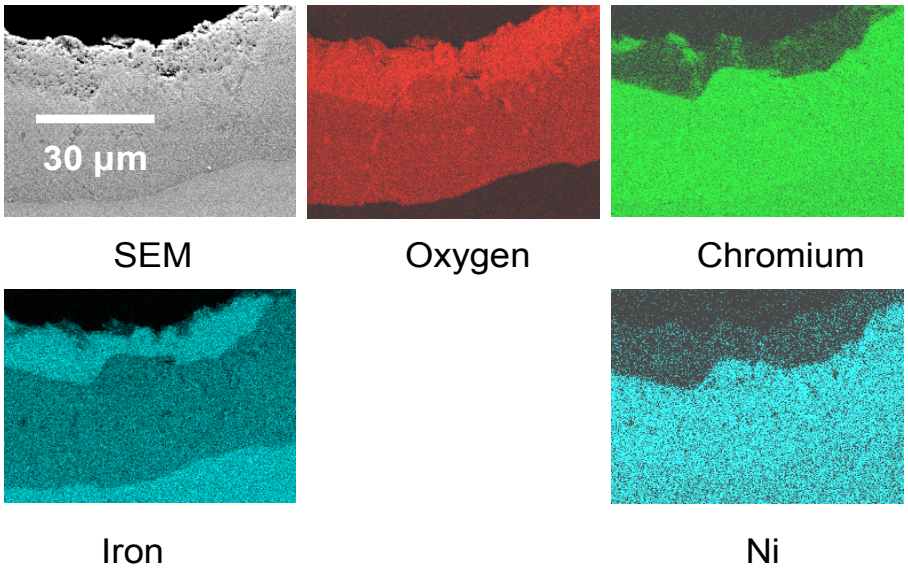

Figure 6.7. EDX analysis of cross section of Alloy 321 at the edge of a pit.

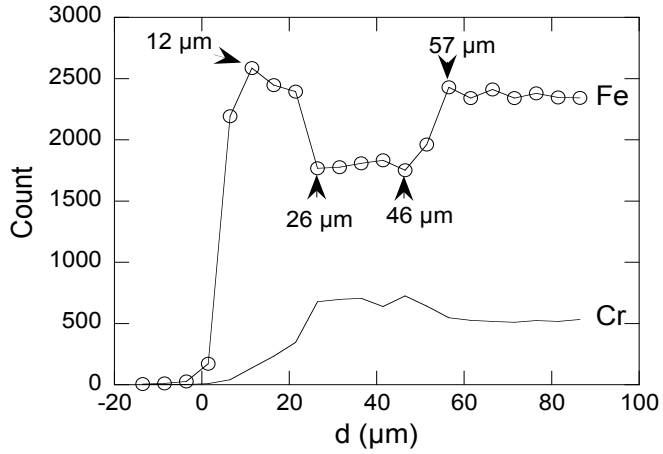

Figure 6.8. Nanobeam X-ray fluorescence analysis of oxide scale as a function of scale depth.

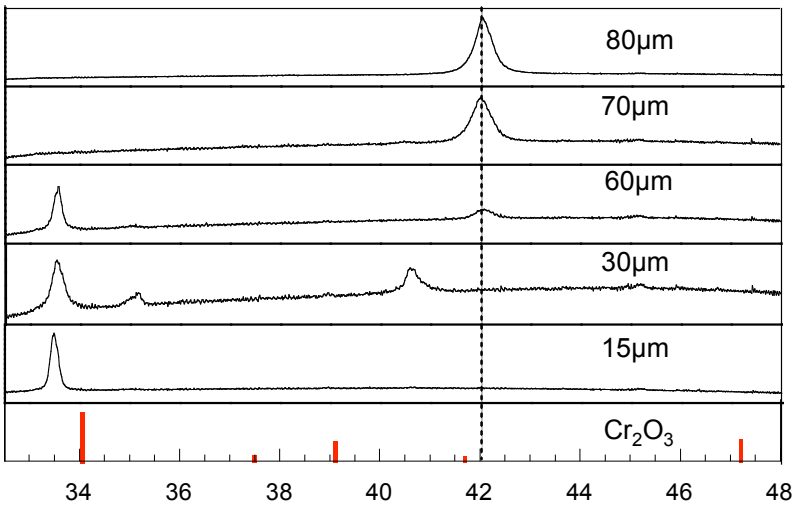

Figure 6.9. X-ray diffraction pattern at the pit area of Alloy 321 exposed in a metal dusting environment for 1130 h.

Although both inner and outer layers in the scale consist of spinel phase, the intensities of diffraction peaks are different as shown in Fig. 6.10a and b. This may be due to the difference in the concentration of iron in spinel at outer and inner layers. The CCD image of X-ray diffraction patterns show that the diffraction spots at outer layer are bright but isolated, but the spots at inner layer form even lines (see Fig. 6.11). This indicates the grain size of spinel at outer layer is larger than that at inner layer.

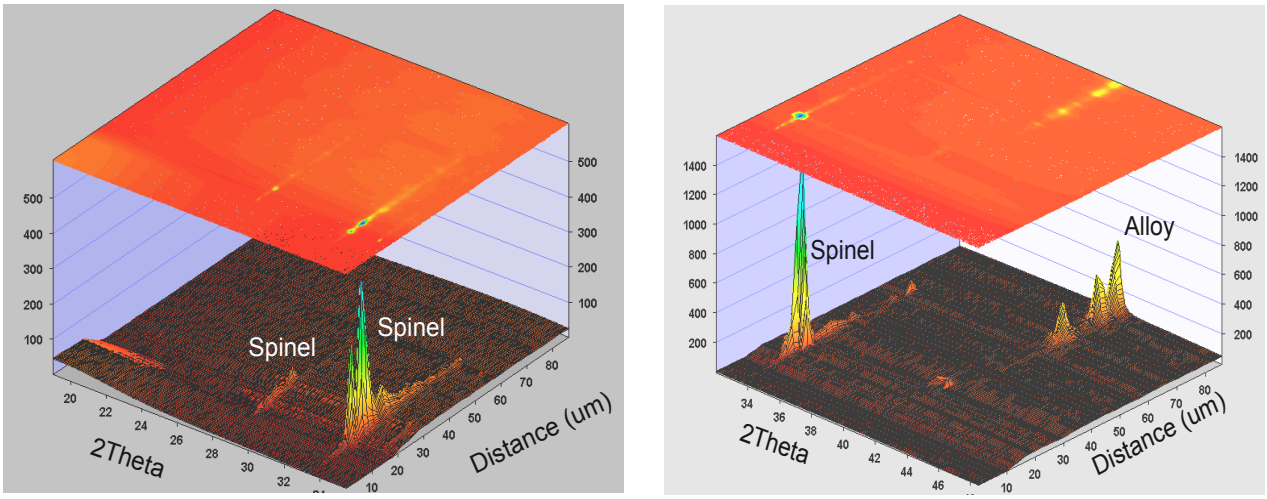

Outer layer Inner layer

Figure 6.10. X-ray diffraction patterns at the outer and inner layers in the pit region of Alloy 321 after 1130-h exposure in a metal dusting environment.

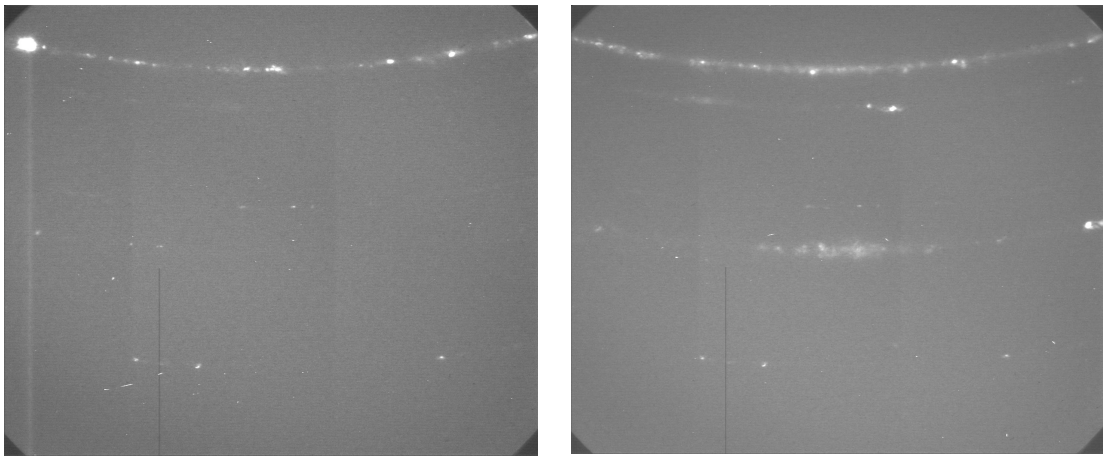

15 μm – outer layer 30 μm – inner layer

Figure 6.11. CCD images of X-ray nano-beam diffraction of oxide scale on Alloy 321 in the pit region.

The major phase in the oxide scale at non-pit area is chromium oxide (see Fig. 6.12). This result is consistent with the results of Raman scattering. Chromium oxide is stable and can protect the alloy from metal dusting corrosion. Similar to Alloy 800H, the intensity of the pre-edge of iron in oxide scale in Alloy 312 is between $Fe_{1.2}Cr_{1.8}O_4$ and $Fe_{1.8}Cr_{1.2}O_4$ (see Fig. 6.13). The oxidation states of iron in $Fe_{1.2}Cr_{1.8}O_4$ and $Fe_{1.8}Cr_{1.2}O_4$

are 2.17 and 2.44, respectively. Therefore, iron in oxide scales is in a mixed valence between +2 and +3 and the spinel is not perfect $FeCr_2O_4$, but a solid solution of $Fe_{1+x}Cr_{2-x}O_4$ with x > 0. Since the Fe^{3+} in spinel could be reduced in metal dusting environment,[1,19] the protective capacity of the oxide scale is easy to be destroyed.

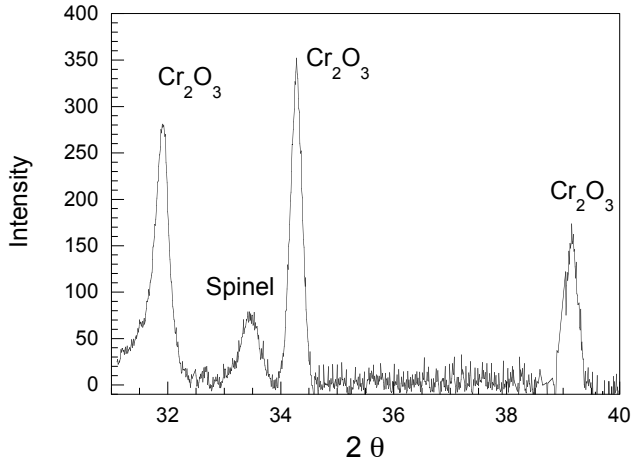

Figure 6.12. . X-ray diffraction pattern for the oxide scale at non-pit area of Alloy 321 after 1130-h exposure in a metal dusting environment.

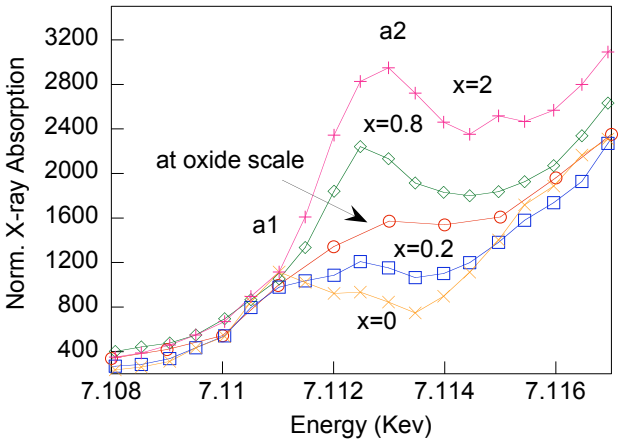

Figure 6.13. . Pre-edge feature of X-ray near edge absorption spectra of iron in the oxide scale at pit area on Alloy 321 and for several standards of $Fe_{1+x}Cr_{2-x}O_4$ with various valances.

Figure 6.14 shows that the excitation energy from 1S to 4P increases, when the X-ray nanobeam was scanned from inner to outer layer. The 1S electrons require more energy to excite to orbits with higher energy when the oxidation state of iron increases. Therefore, the XNEAS results indicate that the oxidation state of iron in outer layer is higher than in the inner layer, although both layers consisted of only spinel phase. Iron diffuses out from substrate alloy and accumulates in oxide scale. Spinel with a higher iron content forms in oxide scale after long time exposure at high temperature. The unstable spinel phase reacts with deposited carbon (from the gas environment) leading to breakdown in the protective capacity of the scale.

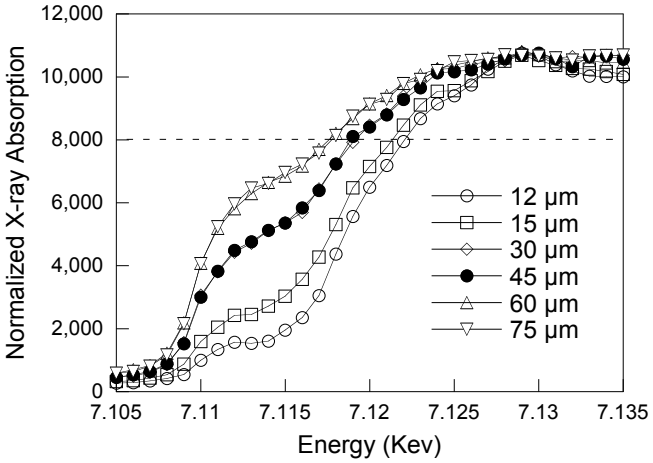

Figure 6.14. . X-ray near edge absorption spectra of iron. The X-ray nanobeam was scanned across the oxide scale to the metal. The positions of 12 and 15 µm are at the outer layer of the oxide scale; the positions of 30 and 45 µm are at the inner layer of the oxide scale; and the positions of 60 and 75 µm are in the alloy.

Chromium has four valence states 0, +2, +3, and +6. Generally, Cr^{+6} is not stable in a reducing environment. X-ray nanobeam was scanned across the oxide scale of ≈50 µm in thickness. Figure 6.15 shows the chemical shifts of chromium in oxide scale at 15 and 45 µm are very close to Cr^{+3} (similar to Cr in $NiCr_2O_4$ standard). Therefore, chromium is present in +3 valence state in both layers of oxide scale in the pit region of Alloy 321. The positions at 55 and 75 µm correspond to the scans in the substrate alloy in which the chromium has a neutral valence of 0.

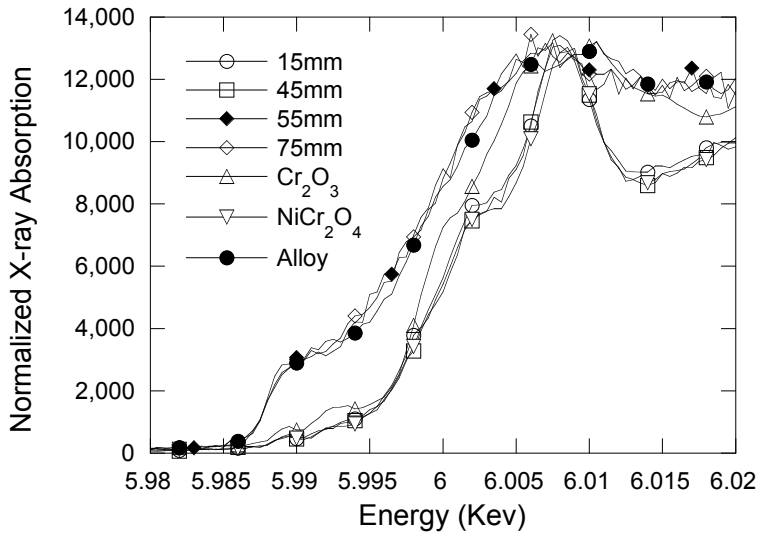

Figure 6.15. . X-ray near edge absorption spectra of chromium. The positions of 15 and 45 µm are at the outer and inner layers, respectively, of the oxide scale; and the positions of 55 and 75 µm are in the substrate alloy.

EDX line scanning results indicate that there is Ni in oxide scale (see Fig. 6.16). The EDX spot analysis results in Table 6.2 also show that the nickel content in oxide scale of Alloy 321 is close or even slightly higher than that in alloy. However, EDX cannot analyze the valence of the nickel in oxide scale. Nanobeam X-ray near edge absorption spectra show that the chemical shift of nickel in most locations of the oxide scale is close to zero valence nickel (see Fig. 6.17). This indicates that nickel is present as metal particles in the oxide scale. These particles seem to act as channels for the transport of carbon into the alloy.

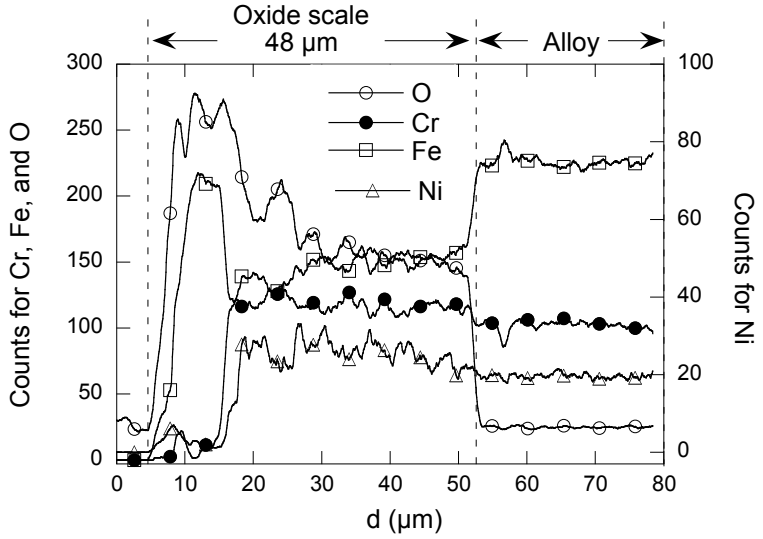

Figure 6.16. . EDX line scanning at the oxide scale on Alloy 321 after exposure to a metal dusting environment.

Table 6.2. EDX spot analysis at various locations near the surface of Alloy 321 after exposure in a metal dusting environment.

Spot position	Nickel (at.%)	Chromium (at.%)	Iron (at.%)	Oxygen (at.%)
Alloy	11.0	18.4	64.2	7.6
Inner layer of oxide scale	11.7	16.4	34.5	37.5
Outer layer of oxide scale	1.2	1.5	44.0	53.3

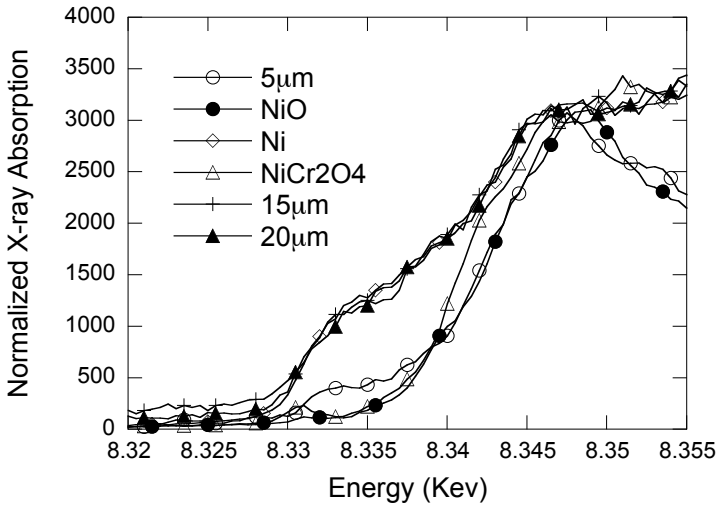

Figure 6.17. . X-ray near edge absorption spectra of nickel. The X-ray nanobeam was scanned across the oxide scale to the metal. The positions of 5 μm and 15 μm are at the outer layer of the oxide scale.

Nickel 2+ was observed at the outer layer of the oxide scale at the position close to surface. Although pure $NiCr_2O_4$ is not stale in the reducing environment, small amount of Ni^{2+} may enter the site of Fe^{2+} in $FeCr_2O_4$ to form $(Fe,Ni)Cr_2O_4$ solid solution. The maximum concentration of Ni^{2+} in the solid solution could be calculated from thermochemical data. Using ΔH and ΔS values of -5.309 kJ/mole and 16.7J/mole K,[30]

respectively, for the formation of $NiCr_2O_4$ from NiO and Cr_2O_3 phases and the oxygen partial pressure of 4×10^{-24} atm in Gas 10 at 14.3 atm and 593°C, the calculated value for the maximum concentration of Ni^{2+} in spinel phase is 15.2%. The oxygen partial pressure at the oxide/substrate interface, based on Cr/Cr_2O_3 equilibrium for an alloy with 18 wt.% Cr, is 2.5×10^{-36} atm which is much less than in the bulk gas. Therefore, the calculated value for the minimum concentration of Ni^{2+} (corresponding to the pO_2 established by $Cr\text{-}Cr_2O_3$ equilibrium) is only 1.2×10^{-5}%. These results indicate that the concentration of Ni^{2+} in spinel should be high at the gas side of the oxide scale, and it should be low at the alloy side of the oxide scale.

In the early stage of oxide scale formation, nickel could be oxidized to +2 at the gas-oxide surface and dope into the solid solution of $(Fe,Ni)Cr_2O_4$. The Ni^{2+} in the solid solution could be as high as 15.2%. When cations continue to diffuse out, the nickel contained spinel gets buried inside. The pO_2 in the inner layer of oxide scale decreases with the increase in thickness of the oxide scale (schematically shown in Fig. 6.18), and Ni^{2+} will be reduced to nickel metal when the pO_2 drops below the critical value. Such a process leads to the formation of nickel particles in oxide scale.

The X-ray nanobeam analysis results indicate that the oxide scale in the pit region is actually a mixture of oxide and metal particles. These metal particles can lead to preferential channels for the inward diffusion of carbon. The evidence for these channels is also confirmed by the preferential deposition of copper in the pit region (due to increased electrical conductivity) that was discussed in Section 3 of this report. However, the nickel oxidation and reduction process will occur if iron is present in alloys because pure $NiCr_2O_4$ spinel will not form in the reducing environment. Only when $FeCr_2O_4$ forms, Ni^{2+} can dope into iron-containing spinel to form $(Fe,Ni)Cr_2O_4$ solid solution. In the absence of iron, nickel will not be subjected to the oxidation-reduction process. Therefore, the spinel phases in oxide scale cause problems by forming unstable iron-rich phase and act as a solvent for the formation of Ni^{2+}, and the Ni^{2+} will be reduced to nickel metal (over long time) enabling formation of carbon transfer channels.

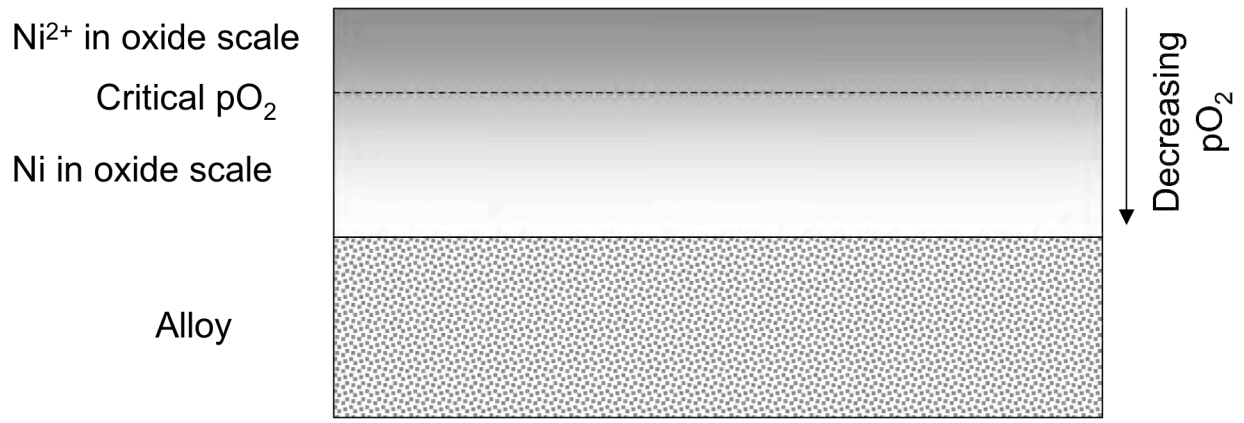

Figure 6.18. Oxygen partial pressure variation from oxide surface to substrate alloy.

7. DEVELOPMENT OF NEW ALLOYS TO RESIST METAL DUSTING

7.1 Development of Ni-base Alloys

Although the weight loss rate of Alloy 600 is much faster than that of Alloy 601, the growth rate of pit depth of Alloy 600 is slower than that of Alloy 601. This is due to the high pit density on Alloy 600. Figure 7.1 shows that pits covered most surface area of Alloy 600, but only a few pits were observed on Alloy 601. The content of chromium in Alloy 601 (21.9 wt.%) is higher than that in Alloy 600 (15.4 wt.%). However, The iron content in Alloy 601 (14.5 wt.%) is also higher than that in Alloy 600 (9.7 wt.%). The high chromium content in Alloy 601 decreases the pit density on surface of Alloy 601, but pit depth growth rate was not suppressed by increasing chromium content in the alloy. It may be more important to decrease the iron content of the alloy for decreasing the pit growth rate.

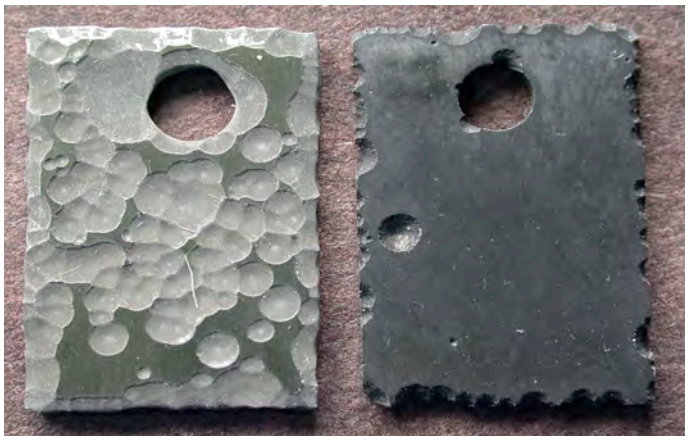

Figure 7.1. Alloy 600 (left) and Alloy 601 (Right) after 12,858-h exposure at 593°C, 1 atm in a gas mixture with a carbon activity of 104.

Figure 7.2 shows that the pit depth on Alloy 45TM is the deepest although its chromium content is the highest in these alloys. The maximum pit depth decreases with decreasing iron content. Therefore, the metal dusting rate is not necessarily determined by chromium content (beyond a certain amount) of the alloy, as can be seen from data in Figure 7.3. However, it is a function of iron content (see Fig. 7.4). The less iron content in alloys, the slower the metal dusting corrosion.

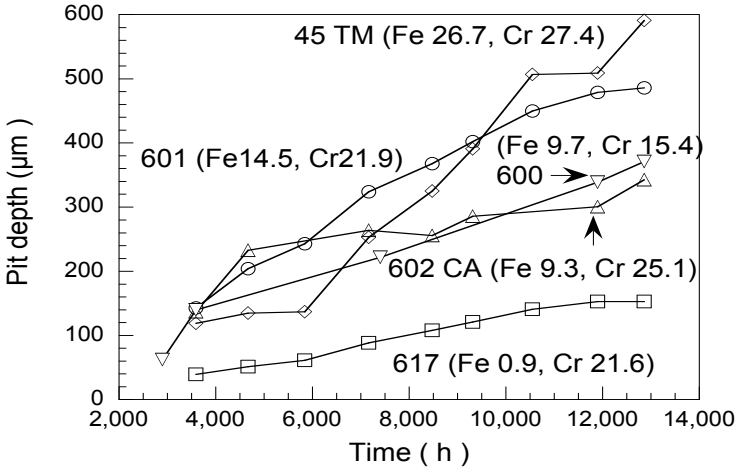

Figure 7.2. . Pit depth as a function of time for several Ni-base alloys exposed to a gas mixture with a carbon activity of 104 at 593°C and 1 atm.

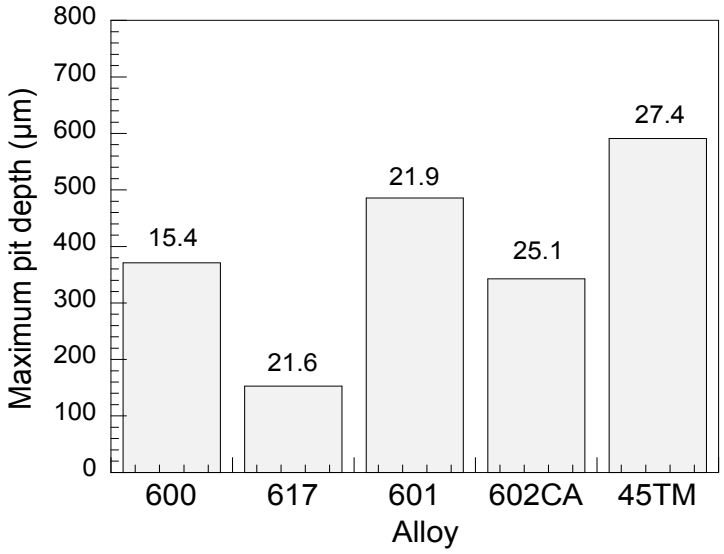

Figure 7.3. . Maximum pit depth for several Ni-base alloys exposed to a gas mixture with a carbon activity of 104 at 593°C and 1 atm. The numbers above the bars indicate the Cr content in the alloy in weight percent.

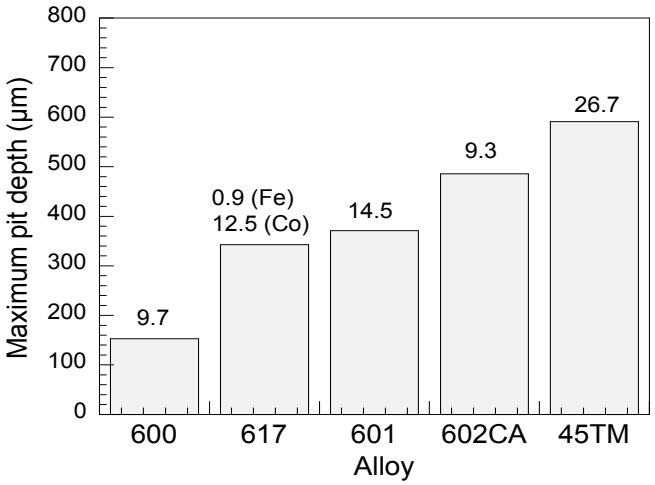

Figure 7.4. . Maximum pit depth for several Ni-base alloys exposed to a gas mixture with a carbon activity of 104 at 593°C and 1 atm. The numbers above the bars indicate the Fe content in the alloy in weight percent.

Figure 7.5 shows the thermodynamic stability of several oxide and spinel phases as a function of temperature. Chromium oxide is the most stable phase and cannot be reduced in the metal dusting environment identified as Gas 21. Nickel oxide and nickel spinel ($NiCr_2O_4$) are unstable and would not form in metal dusting environment. Therefore, nickel by itself would not cause problem for the protectiveness of the oxide layer. On the other hand, iron can form spinel in metal dusting environment. If only the spinel phase $FeCr_2O_4$ formed in the oxide scale, it should be stable in metal dusting environment, based on the thermochemical analysis. However, iron spinel can form solid solution of $Fe_{1+x}Cr_{2-x}O_4$ ($0 \le x \le 2$). Unfortunately, the oxygen partial pressure of metal dusting environment is within the range of the stability of $Fe_{1+x}Cr_{2-x}O_4$ solid solution. If the iron content in spinel is larger than a certain value, the spinel could be reduced. The XNEAS results have indicated that the spinel in oxide scale is not perfect $FeCr_2O_4$, but is generally iron-rich spinel. Therefore, presence of iron in the alloy can lead to formation of an unstable spinel phase in oxide scale and eventually degrade its protective capacity.

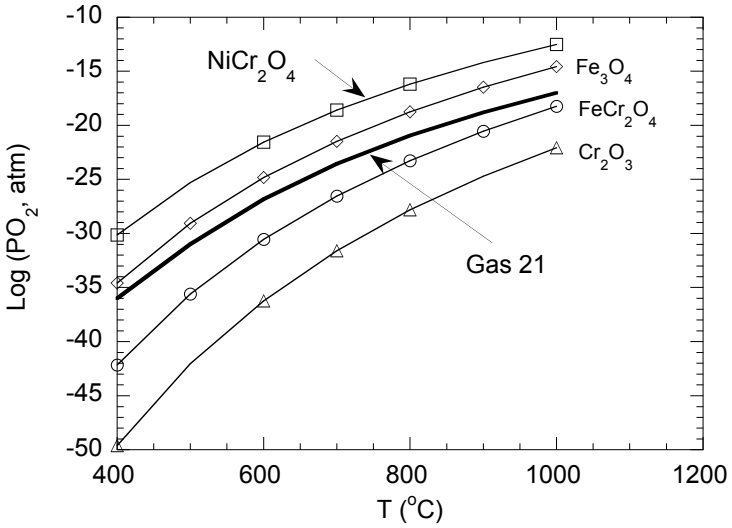

Figure 7.5. . Thermal stability of oxides in metal dusting environment.

According to above analysis, metal dusting would be greatly retarded if alloys can develop an oxide scale that consists of only chromium oxide. In the absence of iron in the alloy, the scale would not contain an iron-containing spinel and $NiCr_2O_4$ would not form in the reducing environment of the metal dusting. Therefore, several alloys were designed with minimal iron content, whose compositions are listed Table 7.1. Alloys ANL-1 to -3 and ANL-7 have chromium content similar to that of commercial Alloy 601, and ANL-4 and -5 have chromium content similar to the commercial Alloy 602CA. These newly-developed alloys formed only stable chromium oxide scale (see Fig. 7.6) after exposure in metal dusting environment. Raman scattering peaks at ≈550 and 680 cm^{-1} correspond to chromium oxide and spinel, respectively. Spinel phase was observed on Alloy 601 but not in ANL-developed alloys, after exposure in metal dusting environment.

Table 7.1. Composition (in wt.%) of alloys selected for metal dusting experiments.

Alloy designation	Elemental composition (in wt.%)								
	Ni	Cr	Al	Fe	Ti	Zr	C	Y	Cu
AGZ1	74.5	22.0	2.3	0.7	0.3	0.2	0.1	-	-
AGZ2	75.2	22.0	2.3	<0.1	0.3	0.2	0.1	-	-
AGZ3	73.5	22.0	3.3	0.7	0.3	0.2	0.1	-	-
AGZ4	71.4	25.0	2.3	0.7	0.3	0.2	0.2	0.1	-
AGZ5	71.1	25.0	3.3	<0.1	0.3	0.2	0.2	0.1	-
AGZ6	67.2	29.0	3.3	<0.1	0.3	0.1	-	0.1	-
AGZ7	65.2	22.0	2.3	<0.1	0.3	0.2	0.1	-	10

Several commercial and ANL-developed nickel-base alloys were exposed for 12,858 h at 593°C, 1 atm in Gas 21 with a composition of 65.1% H_2, 30% CO, 0.94% H_2O, and 4% CO_2 (carbon activity ≈30). Figure 7.6 shows that Alloys 600 and 601

developed deep pits, whereas the surfaces of all ANL-developed alloys exhibited virtually no attack. Metal dusting pits on Alloy 601 were observed within 1000-h exposure. Although the composition of ANL-1 is similar to that of Alloy 601, the low concentration of iron in ANL alloy extended the time for initiation of metal dusting in the ANL alloy.

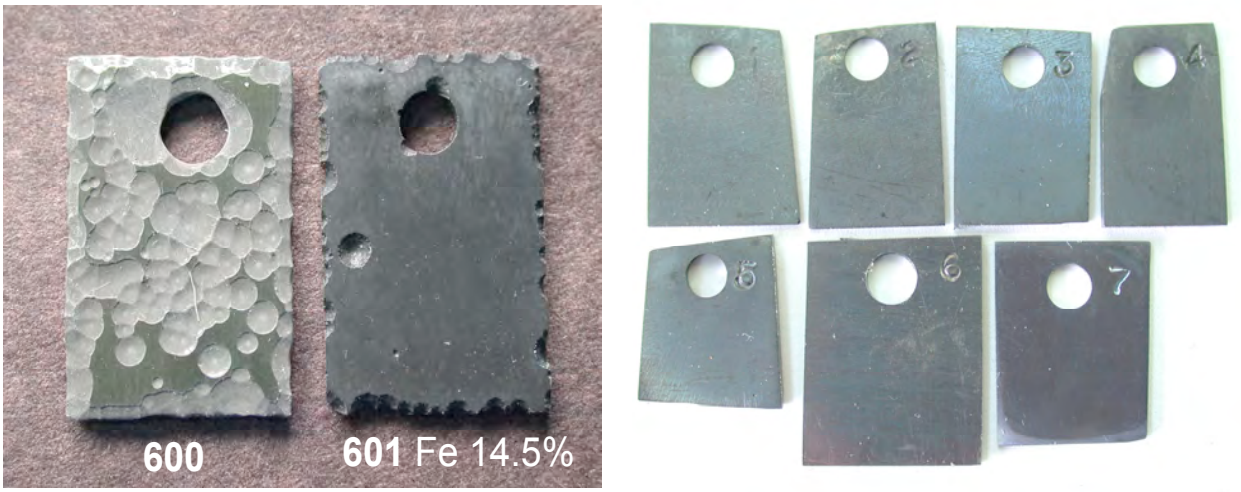

Figure 7.6. Macrophotographs of Alloys 600, 601 and ANL-developed Alloys 1-7 after 12,858-h exposure to the same metal dusting environment (Gas 21) at 593°C and 1 atm.

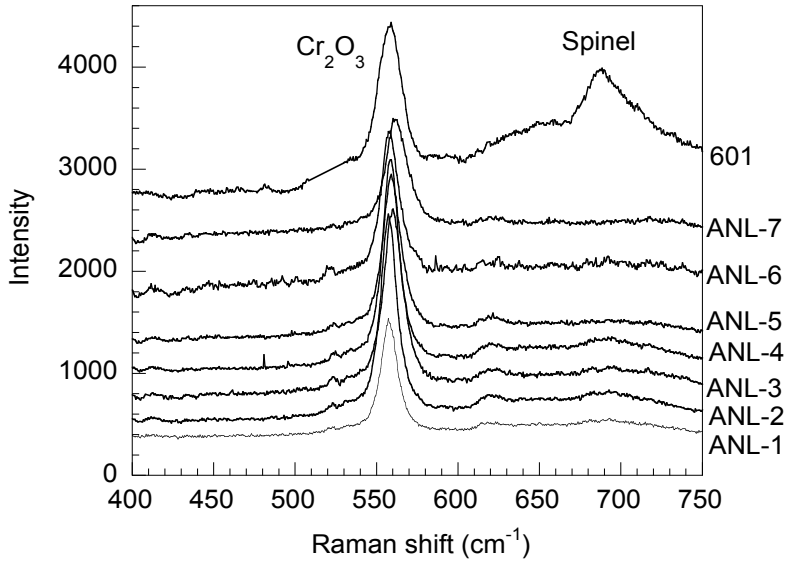

Figure 7.7. Raman spectra for Alloy 601 and ANL-developed alloys after 12,858-h exposure at 593°C to Gas 21 consisting of 65.1% H_2, 30% CO, 0.94% H_2O, and 4% CO_2.

7.2 Development of Cu-base Alloys

There are three steps in metal dusting degradation of metallic materials: (1) carbon deposition on alloy surface, (2) carbon transport into alloy, (3) alloy becomes powder by interaction with carbon. If any of the three steps can be

controlled/minimized, the metal dusting corrosion can be slowed. Usually, three reactions are responsible for the first step of carbon deposition.

$CO + H_2 = C + H_2O$

$2CO = C + CO_2$

$CH_4 = C + 2H_2$

Since the activation energy for all three reactions is high, a catalyst is generally needed to accelerate the reaction. Unfortunately, Fe, Co, and Ni (that are present in the metallic structural components) and some of their oxides can act as catalysts to initiate carbon deposition. Copper and copper-base alloys have several advantages: (1) copper does not catalyze the coking reactions and therefore coke deposition is almost completely avoided, (2) copper has very little solubility for carbon and therefore the dissolution of carbon and eventual transport of carbon can be minimized, and (3) copper can be applied as a clad or a coating onto the structural material to minimize direct contact of the metallic component from the metal dusting environment. As a result, we examined copper as a means to minimize the metal dusting attack. In addition, we also developed several cooper-base alloys with emphasis on both the metal dusting resistance and improvement (compared to that of pure copper) in elevated temperature mechanical properties to use them as monolithic structural materials in high hydrocarbon-containing environments.

7.2.1 Metal Dusting Tests on Copper and Copper-base Alloys

We tested pure copper specimens in different forms by exposing them in a metal dusting environment at various temperatures. Copper was found to be noncatalytic, as evidenced by absence of coke deposit in these experiments. The results are consistent with reports from other researchers.[31-33] The solubility and diffusion rate of carbon in copper are low. However, the strength of copper at elevated temperature is too low for its use as a structural material. Therefore, we also evaluated copper as a coating or a cladding on several Fe-, Co- and Ni-base alloys in resisting metal dusting corrosion in these alloys. In addition, we also developed several copper-base alloys with potential for higher strength and capability for use at elevated temperatures.

Copper was coated on alloys by electrolysis plating method and a minimum coating thickness of 25 μm seemed necessary based on preliminary screening studies. Alloys were also clad with copper by cold pressing copper onto the structural alloy. In addition, we prepared four copper-base alloys (see Table 7.2) that contained various amounts of nickel and aluminum.

Experiments were conducted in gas mixtures with several compositions and system pressures. Some of the specimens were exposed for >10,000 h. Results listed in Table 7.3 shows that copper, copper alloys, and copper-clad specimens do not degrade by metal dusting. However, uncoated and un-clad alloys are attacked in the same environment. Figure 7.8 shows photographs of the bare and Cu-coated Alloy 800 specimens after testing. Heavy deposit of carbon was noted on the uncoated specimen

Table 7.2. Composition of copper-base alloys evaluated in the study.

Alloy designation	Cu (w%)	Ni (w%)	Al (w%)	Others (w%)
Cu-Ni-Al2	90	8	2	---
Cu-Ni-Al4	88	8	4	---
Cu-Ni-Al12	48	40	12	---
Cu-Ni-Al20	40	40	20	---
Glidcop*	98.9	---	---	Al_2O_3 1.1%

*Commercial dispersion-strengthened alloy

whereas, no carbon was seen on the coated specimen, indicating lack of coke-catalyzing reactions on the coated surface. Figure 7.9 show SEM photomicrographs of Cu-coated and bare specimens of Alloys 800 after testing. Pits were observed only on the uncoated alloy surface. Figure 7.10 shows macrophotographs of Cu-clad and bare iron specimens after testing in a metal dusting environment. The Cu-clad specimen had no carbon deposit and did not lose weight, whereas the bare sample exhibited significant carbon deposit and substantial weight loss. Iron was consumed at a rate of 0.55 $mg/cm^2 \cdot h$. Figure 7.11 shows SEM images of the difference in iron surface before and after exposure in the metal dusting environment.

Table 7.3. Metal dusting results on copper and copper-base alloys

Run Number	Materials	Gas Mixture	Time (h)	Pressure (atm)	Results
33	Cu-coated Fe and alloys	4	163	1	Clean surface
35	Cu-clad Fe plate	4	784	1	Clean surface
36	Glidcop	4	144	1	Clean surface
37	Cu-coated iron andalloys	4	792	1	Clean surface
41	Cu	8	100	27	Clean surface
42	Cu	8	100	14	Clean surface
43	Cu	13	100	41	Clean surface
45	Glidcop	4	300	1	Clean surface
49	Cu	10	1131	14	Clean surface
50	Cu	10	100	14	Clean surface
51	Cu	10	113	41	Clean surface
52	Cu	10	680	41	Clean surface
53	Cu	11	8348	1	Clean surface
54	Cu	11	7589	1	Clean surface
56	Cu-Ni-Al2	14	3381	1	No weight loss
	Cu-Ni-Al4	14	3381	1	No weight loss
	Cu-Ni-Al12	14	3381	1	No weight loss
	Cu-Ni-Al20	14	3381	1	No weight loss
59	Cu-Ni-Al4	10	5200	14	No weight loss
60	Cu	10	246	1	Clean surface
61	Cu	21	13,842	1	Clean surface

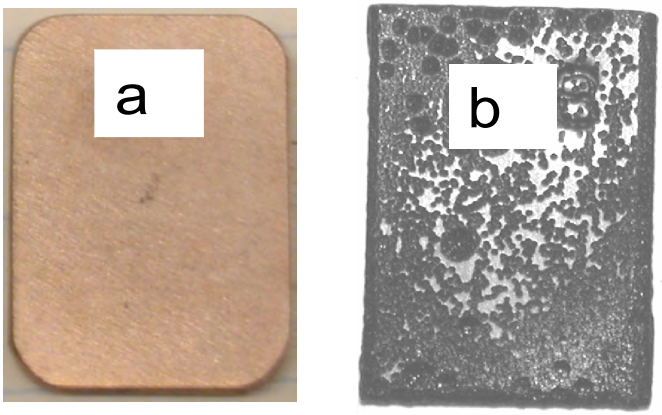

Figure 7.8. Alloy 800 tested in a metal dusting environment at 593°C for 600 h. (a) Cu coated and (b) bare.

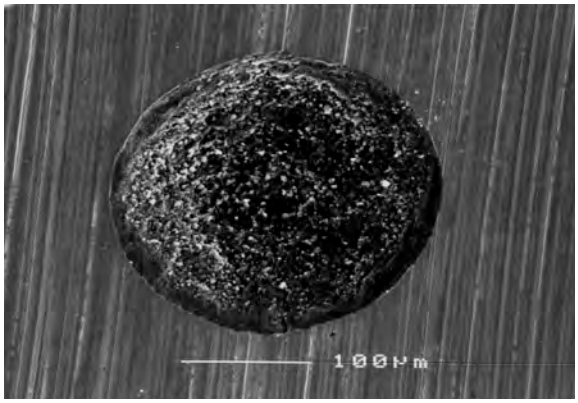

Figure 7.9. SEM image of a pit on Alloy 800 tested in a metal dusting environment at 593°C for 100 h.

Figure 7.10. Iron specimens tested in a metal dusting environment for 600 h at 593°C. (a) 0.8-mm thick Cu-clad iron and (b) bare iron coupon.

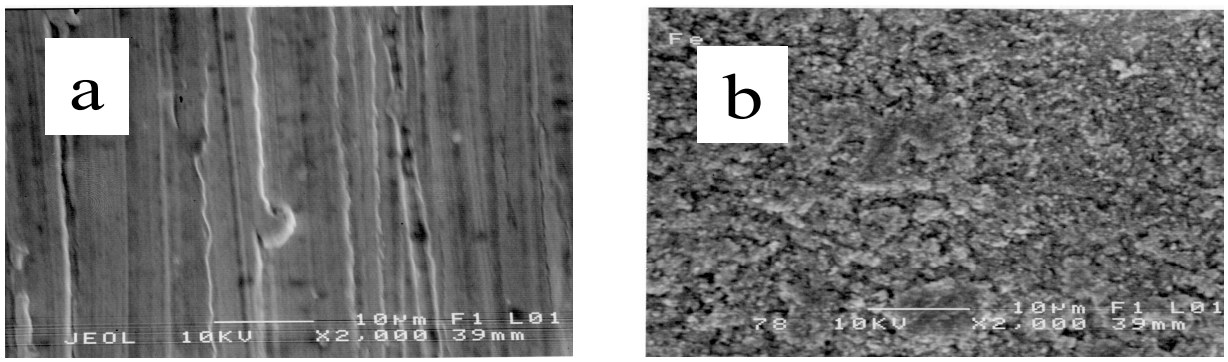

Figure 7.11. SEM photomicrographs of bare iron specimen (a) before and (b) after exposure in a metal dusting environment for 100 h at 593°C.

Although the Cu-coated specimens performed better than the uncoated alloy, the coated layer degraded after 792-h exposure (see Fig. 7.12). The carbon-containing gases seem to diffuse through the micropores that are generally present in the electrodeposited coatings and eventually react with the underlying substrate alloy constituents to initiate metal dusting attack. However, the Cu-clad iron specimen did not lose weight even after 1576 h exposure, due to lack of porosity in the clad copper layer and larger thickness of the clad layer. Figure 7.13 shows a comparison of the weight change data for several commercial alloys and copper after testing at 593°C and 1 atm. Results show that copper was not attacked by metal dusting for over 7,000 h. However, other Fe-base alloys lost weight severely during the same period. Figure 7.14 shows the change in weight loss for copper after exposure in gas mixtures with carbon activities of 31 and 104 at 593°C. The weight loss seems to accelerate at the higher carbon activity, but still relatively small when compared with those of commercial alloys (see Fig. 7.13).

Figure 7.12. Cu-coated Alloy 800 specimen after 792-h exposure in a metal dusting environment at 593°C.

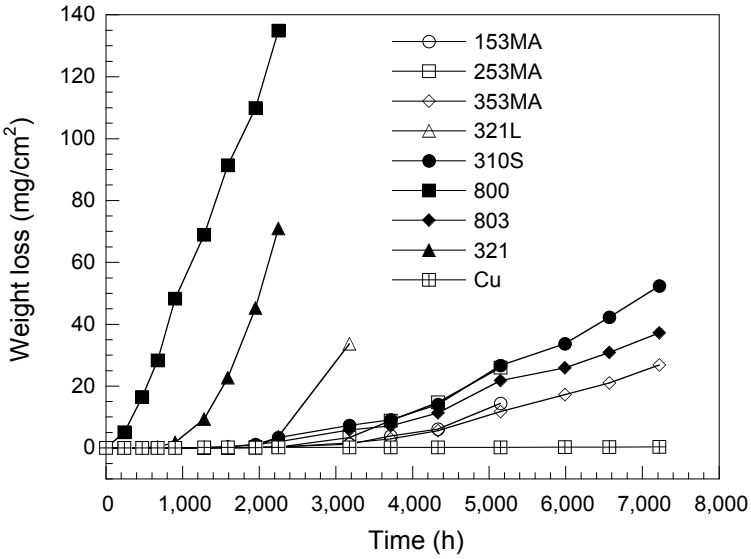

Figure 7.13. Weight loss data for several commercial Fe-base alloys and copper after exposure in a metal dusting environment (Gas 11, a_C=31) at 593°C and 1 atm.

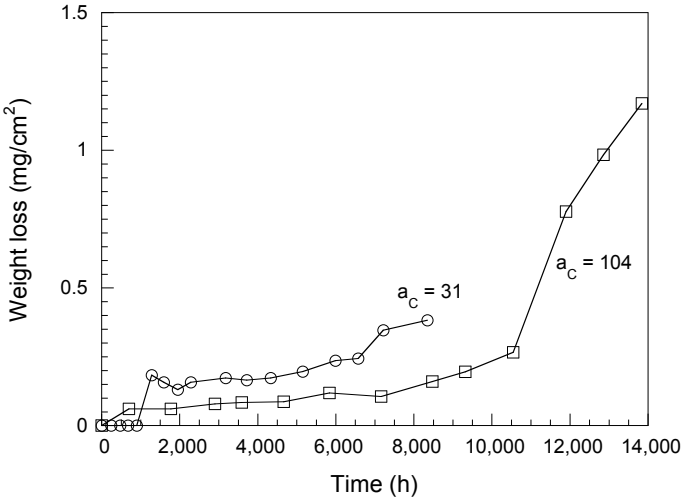

Figure 7.14. Weight loss data for copper after exposure in metal dusting environments, with carbon activities of 31 and 104, at 593°C and 1 atm.

Copper alloys also showed good resistance to metal dusting. No weight loss was observed for these alloys after 3000-h exposure to carburizing gas. In fact, the specimens gained small weight primarily due the internal oxidation of Al in the alloy. Meanwhile, Ni-base Alloy 214 severely lost weight (see Fig. 7.15). The copper alloys also showed excellent oxidation resistance as shown for the Cu40-Ni40-Al20 alloy at 800ºC (Fig. 7.16). Only Al_2O_3 phase was observed in the oxide scale (see the XRD spectra in Fig. 7.17) and as expected, no spinel phase is present.

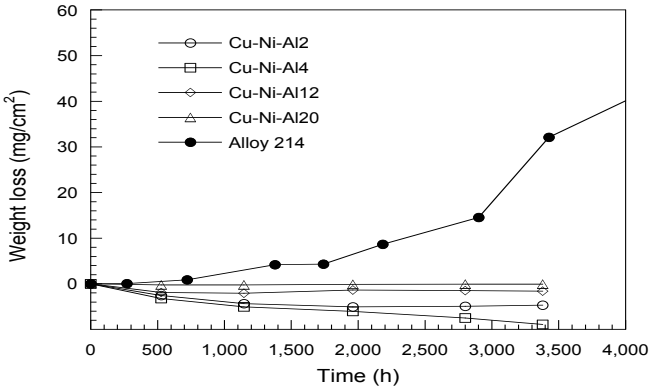

Figure 7.15. Weight loss data for ANL-developed Cu-base alloys and Alloy 214 after exposure in a metal dusting environment (Gas 14, a_C=10) at 593°C and 1 atm.

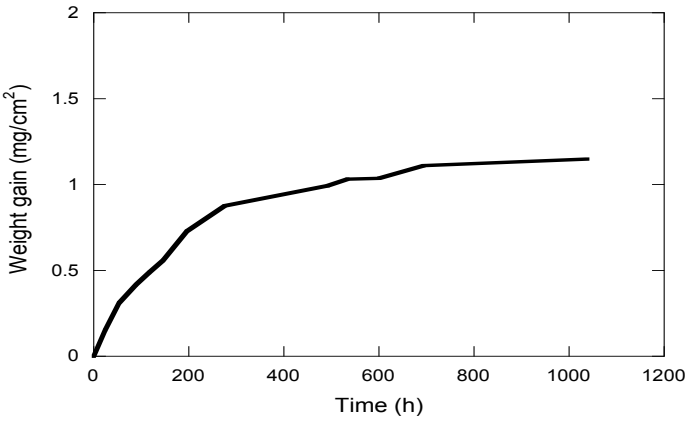

Figure 7.16. Weight gain data for Cu40-Ni40-Al20 alloy after oxidation in air at 800°C.

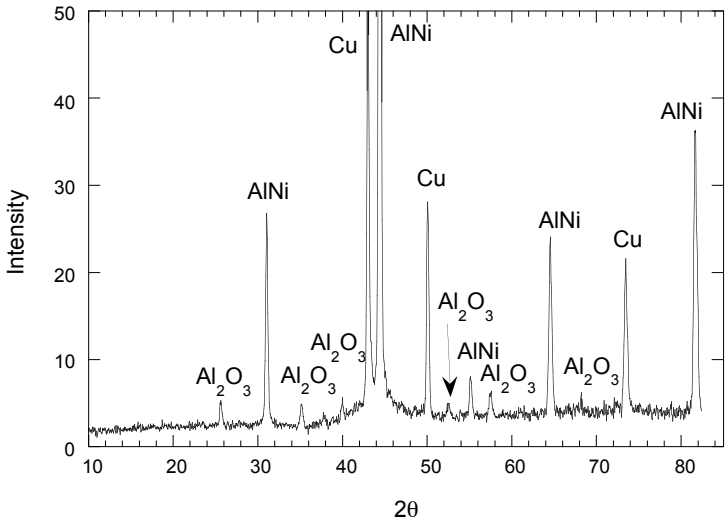

Figure 7.17. XRD analysis of Cu40-Ni40-Al20 alloy after 1100-h oxidation in air at 800°C.

7.2.2 Tensile Properties of Copper-base Alloys

Uniaxial tensile tests were conducted on two of the alloys at a strain rate of 1.8×10^{-4} s^{-1} in air at room temperature, 400, 600, and 800°C. The alloys tested contained 2 and 4 wt.% Al. Tensile properties such as 0.2% yield strength, ultimate tensile strength, uniform strain, and total strain were obtained and the values for various test conditions are listed in Table 7.4. The last column in the table also gives the fracture location in various specimens. It is evident that the fracture was not always in the center of the gage section but sometimes it is at the top of the gage section or at the shoulder. The screening study indicates the potential for Cu-base alloys but substantial additional effort is needed to quantify the data and commercialize the alloys. Figures 7.18 and 7.19 show the strength and strain data for various specimens tested at several temperatures. Figures 7.20 and 7.21 show the SEM photomicrographs of the fracture surfaces of the two alloys after testing at various temperatures. Figures 7.22 and 7.23 show SEM photomicrographs of cross sections of specimens near the vicinity of fracture surfaces.

Table 7.4. Tensile data for Cu-base alloys at several temperatures

Alloy	Test temperature (°C)	0.2% yield strength (ksi)	Ultimate tensile strength (ksi)	Uniform strain (%)	Total strain (%)	Comments
Cu90-Ni8-Al2	25	88.3	99.0	5.7	9.1	ok
Cu90-Ni8-Al2	400	40.0	51.6	6.4	8.1	shoulder fracture
Cu90-Ni8-Al2	600	8.7	12.6	4.3	18.9	top fracture
Cu90-Ni8-Al2	800	2.3	3.4	20.5	96.1	mid fracture, grip area deform
Cu88-Ni8-Al4	25	111.9	129.3	6.0	8.8	ok
Cu88-Ni8-Al4	400	44.7	51.0	3.9	3.9	shoulder fracture
Cu88-Ni8-Al4	600	4.9	6.2	3.7	78.4	top fracture
Cu88-Ni8-Al4	800	1.9	2.7	14.6	77.6	mid fracture, grip area deform

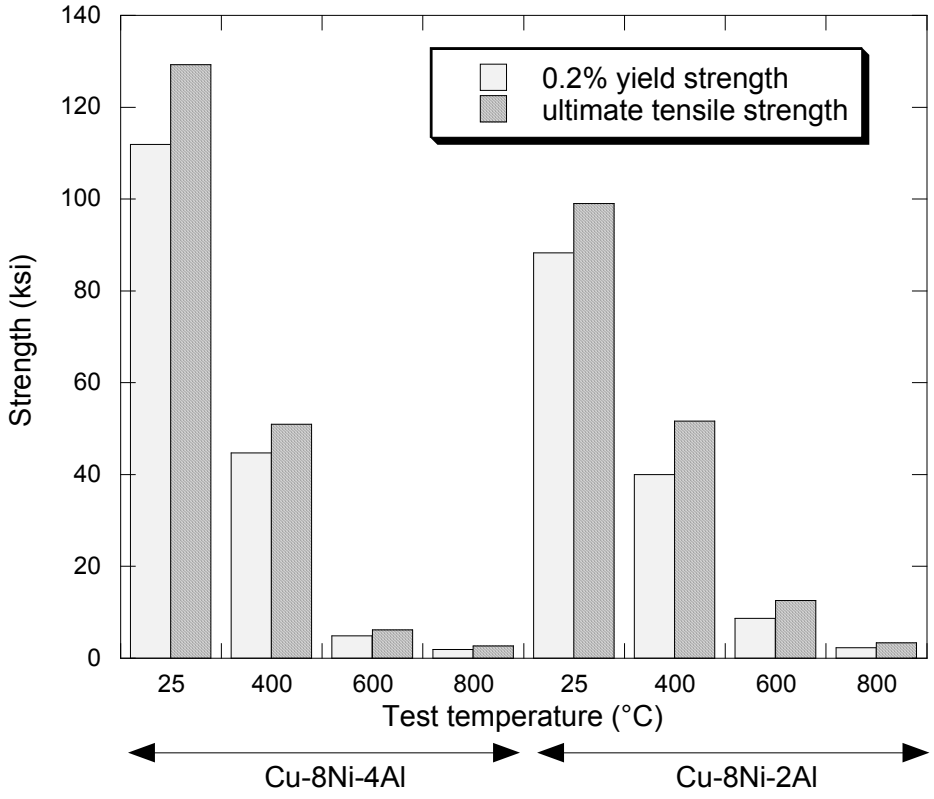

Figure 7.18. Strength data for Cu-Ni-Al alloys in air at a strain rate of 1.8 x 10^{-4} s^{-1}.

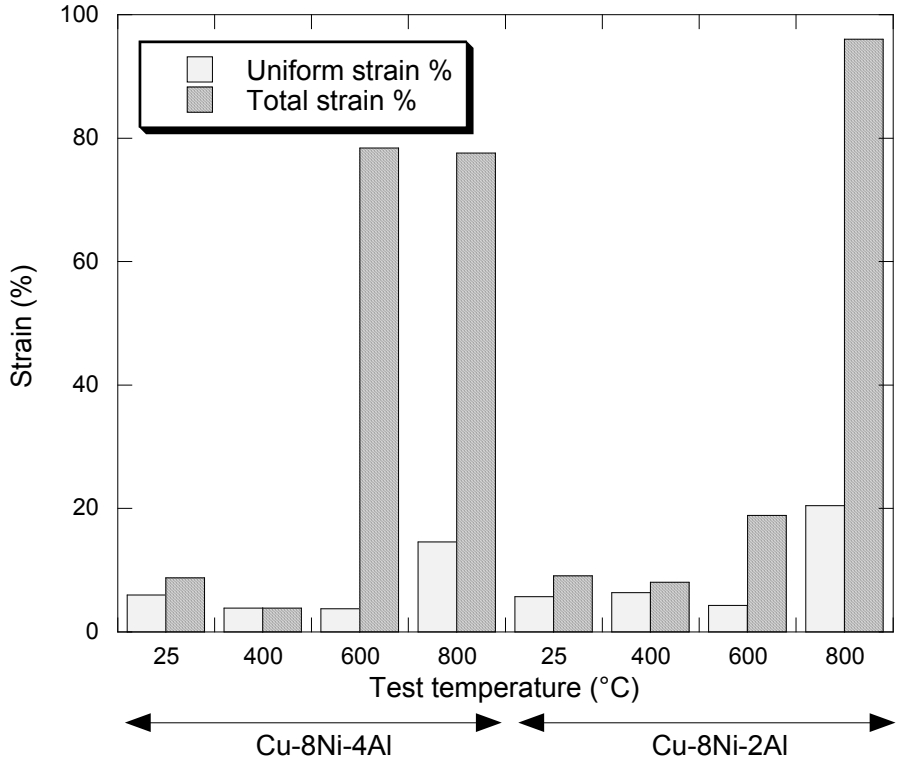

Figure 7.19. Stain data for Cu-Ni-Al alloys in air at a strain rate of 1.8 x 10^{-4} s^{-1}.

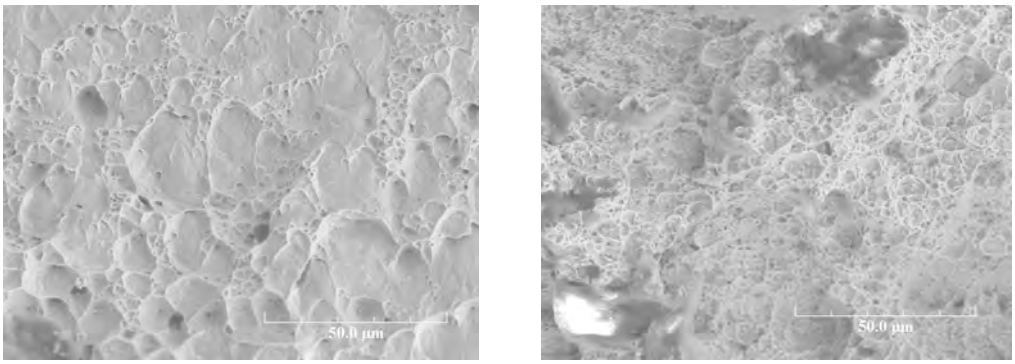

Room temperature 400°C

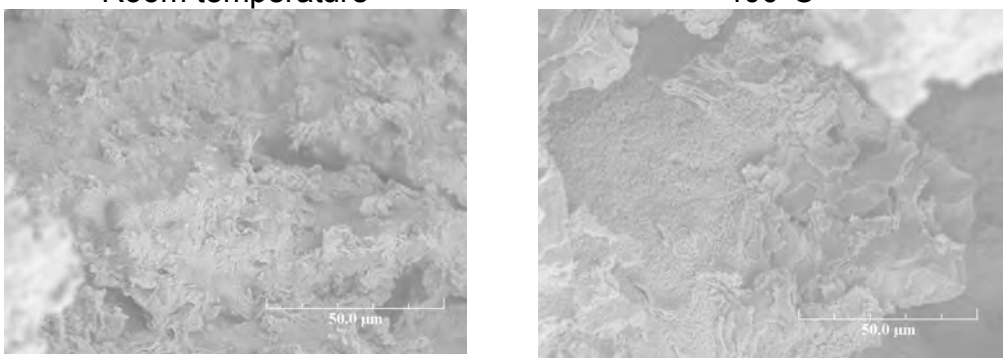

600°C 800°C

Figure 7.20. SEM photomicrographs of cross sections of fracture surfaces of 90Cu-8Ni-2Al alloy after tensile testing at various temperatures.

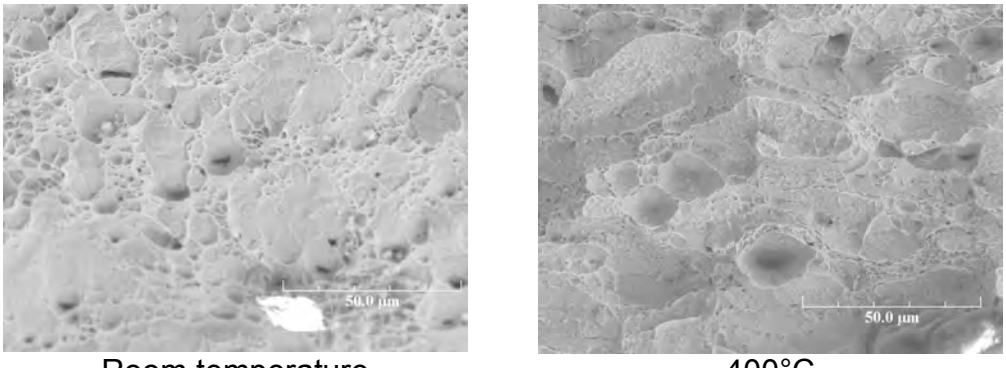

Room temperature 400°C

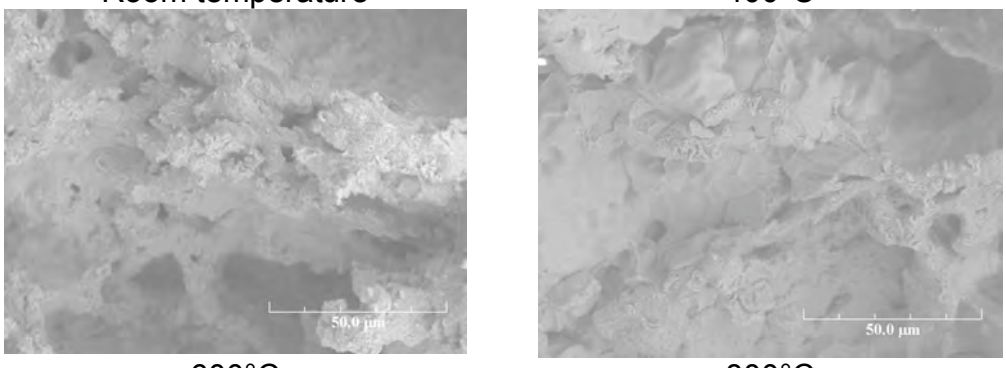

600°C 800°C

Figure 7.21. SEM photomicrographs of cross sections of fracture surfaces of 88Cu-8Ni-4Al alloy after tensile testing at various temperatures.

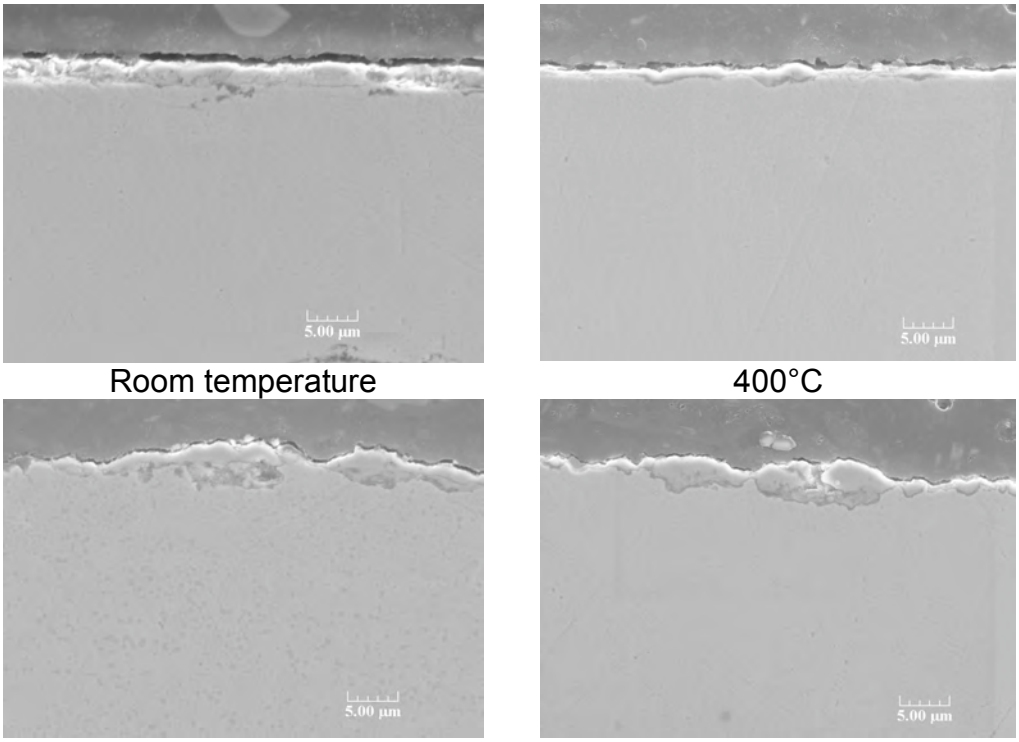

Room temperature 400°C

600°C 800°C

Figure 7.22. SEM photomicrographs of cross sections of 88Cu-8Ni-4Al alloy after tensile testing at various temperatures.

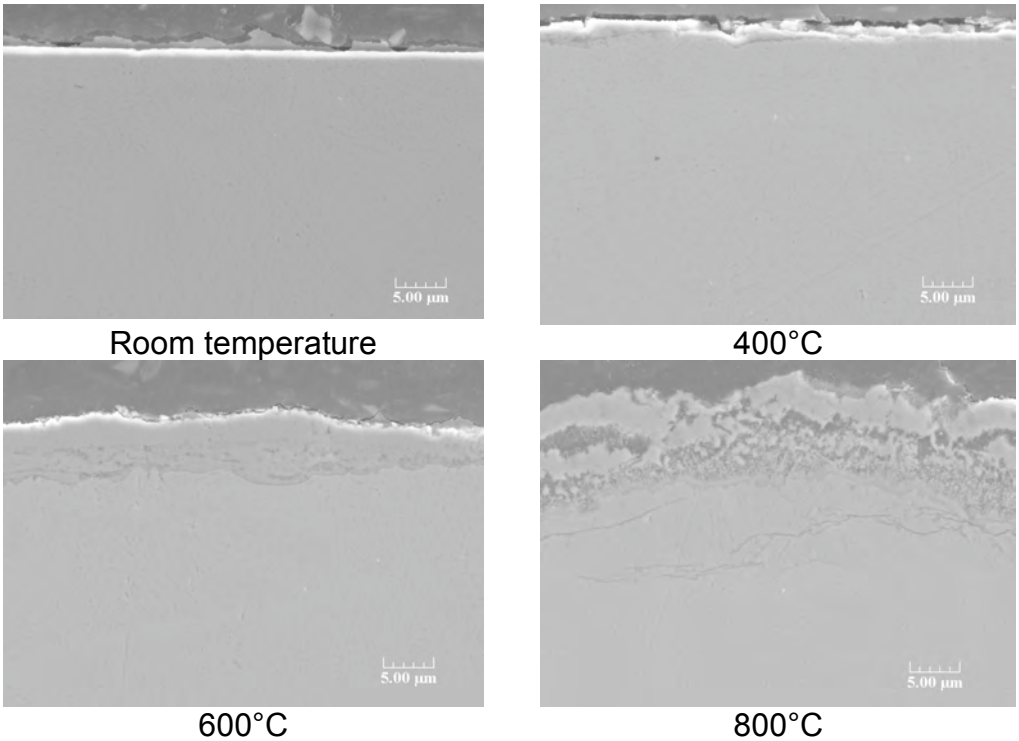

Room temperature 400°C

600°C 800°C

Figure 7.23. SEM photomicrographs of cross sections of 90Cu-8Ni-2Al alloy after tensile testing at various temperatures.

8. PERFORMANCE OF WELDMENTS IN METAL DUSTING ENVIRONMENTS

8.1 Weldments of Ni-base alloys

Table 8.1 lists the weldment specimens selected for the study. The chemical compositions of weld materials are similar to those of corresponding base alloys. However, the solidification structure in the weld zone (being different from those of base alloys) can behave differently when exposed in metal dusting environments. The metallurgical structures of the specimens in as-welded condition were determined by etching the specimens in a 5% HNO_3-methanol solution at 5V for 30 seconds.

Table 8.1. Weldments of Ni- and Fe-base alloys used in the study

Weldment designation	Base alloy	Filler metal/Welding procedure	Supplier organization
Ni-base alloy weldments			
W1	602CA	S 6025/GTAW	Krupp VDM
W2	230	230W/GTAW	Haynes International
W3	HR160	HR160/GTAW	Haynes International
W5	690	FM52/GTAW	Special Metals
W6	693	53MD/GTAW	Special Metals
W7	601	601/GTAW	Special Metals
Fe-base alloy weldments			
W4	803	617/GTAW	Special Metals
W8	347	No filler, e-beam	Argonne National Laboratory
W9	310	No filler, e-beam	Argonne National Laboratory
W10	353MA	353MA/GTAW	Outokumpu
W11	310	ER310/ GTAW	Allegheny Ludlum
W12	347	347/GTAW	Allegheny Ludlum

Dendrites could be observed in almost all the etched specimens (see Figs. 8.1-8.6). The weldment specimens have three distinct parts namely, base metal, Weld metal, and a heat-affected zone, the thickness of which can be alloy dependent. The process of welding an alloy can create metallurgical structures in the weld zone with several differences when compared with the base metal. For example, the grains can be oriented differently, preferential segregation of alloying elements, microporosity, and generally a non-homogeneous structure can result. Figure 8.1 shows that the boundary between weld and base metal of W3 is not as uniform as in other weld specimens. Only W5 shows less dendrites and the grain size of the weld area of W5 is larger than that of the base alloy.

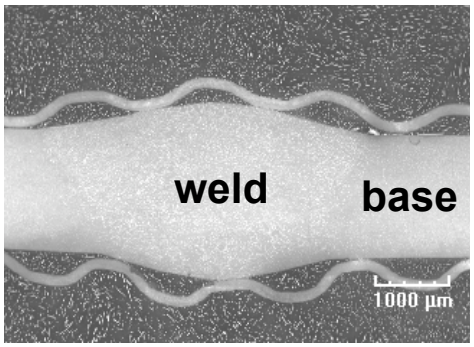

20X

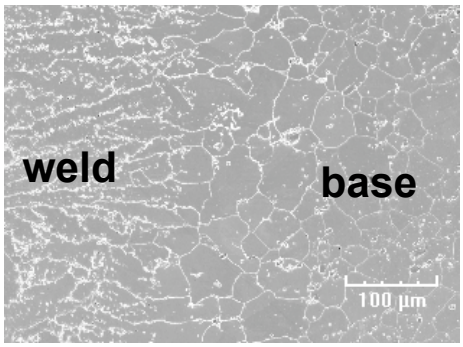

250X

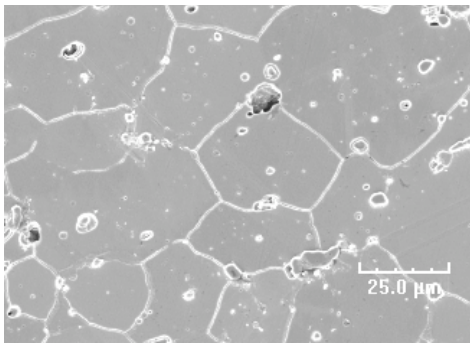

1000X at base metal

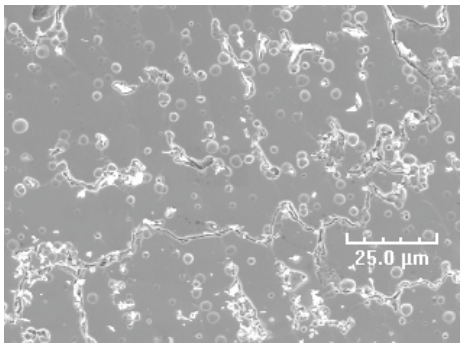

1000X at weld

Figure 8.1. SEM photomicrographs of cross sections of weldment W1.

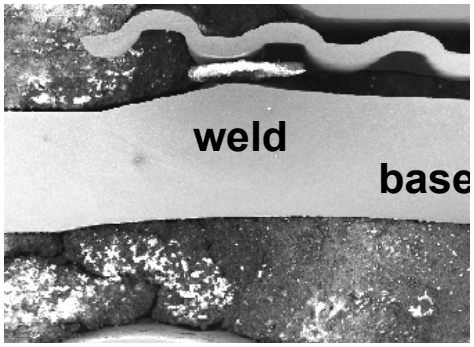

20X

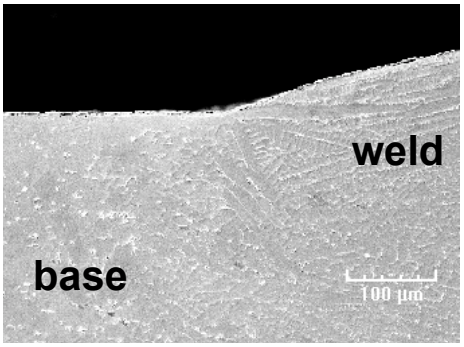

250X

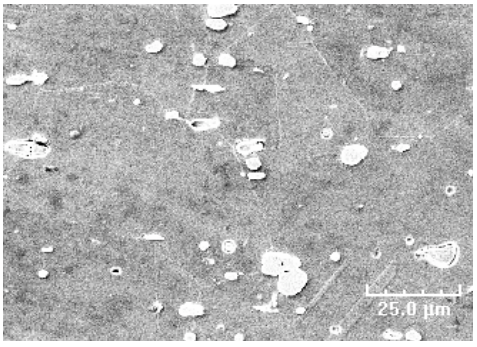

1000X at base metal

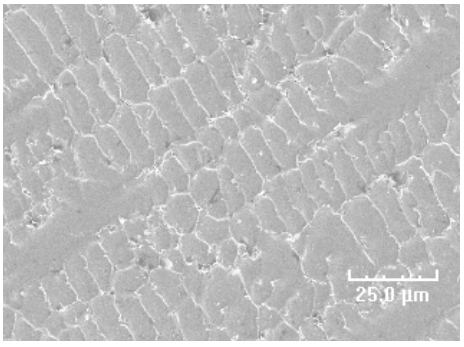

1000X at weld

Figure 8.2. SEM photomicrographs of cross sections of weldment W2.

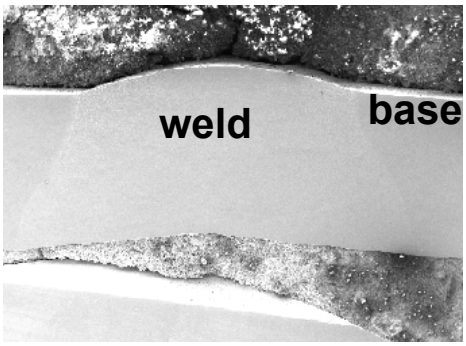

20X

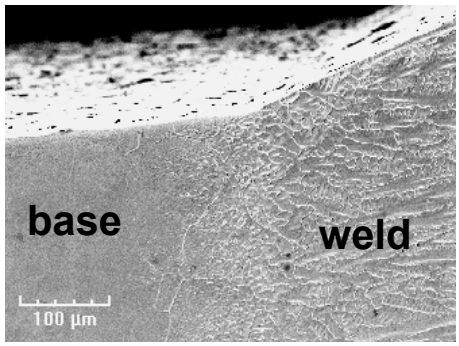

250X

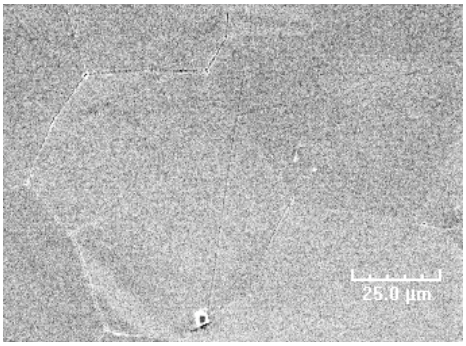

1000X at base metal

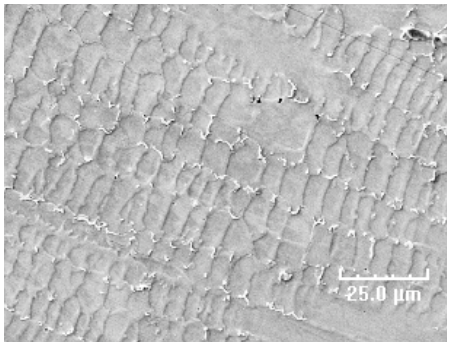

1000X at weld

Figure 8.3. SEM photomicrographs of cross sections of weldment W3.

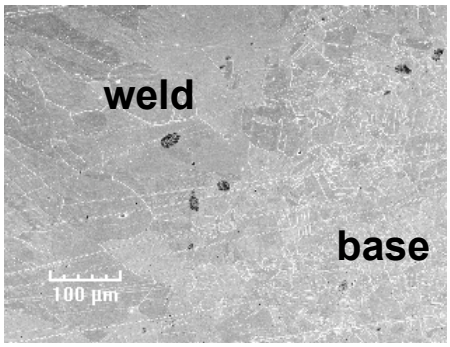

20X

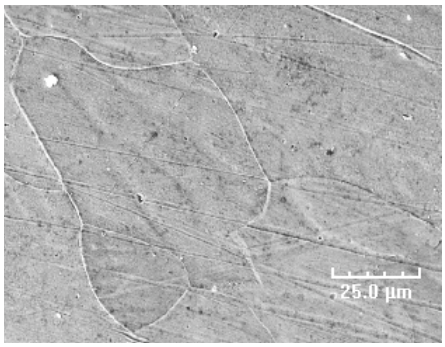

250X

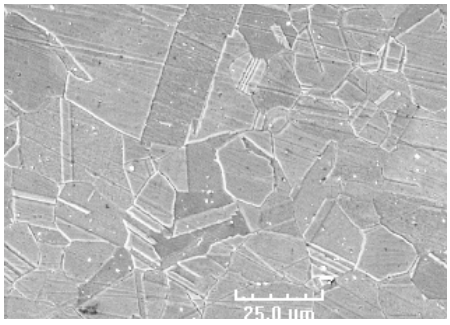

1000X at base metal

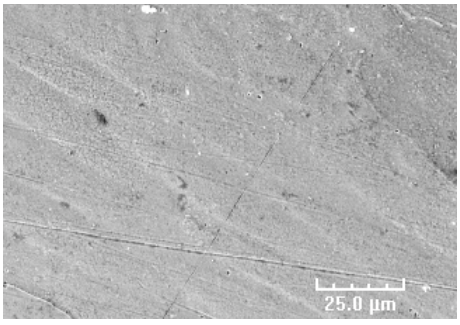

1000X at weld

Figure 8.4. SEM photomicrographs of cross sections of weldment W5.

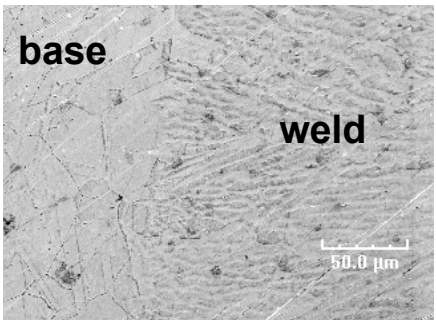

500X

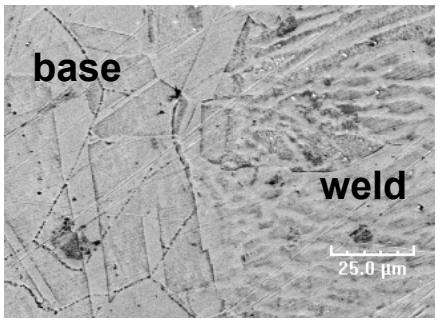

1000X

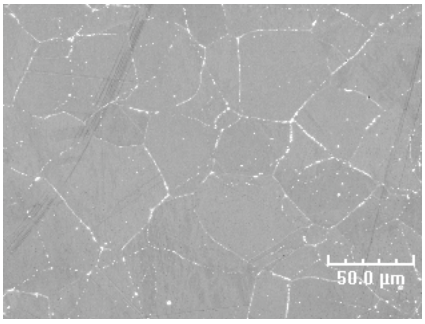

500X at base metal

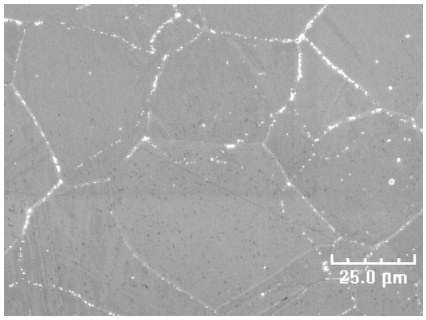

1000X at base

Figure 8.5. SEM photomicrographs of cross sections of weldment W6.

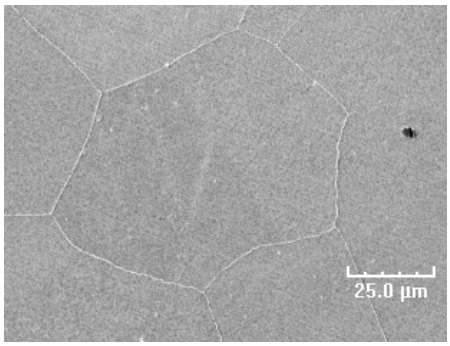

1000X at base metal

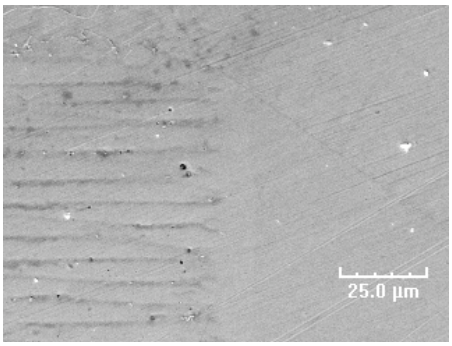

1000X

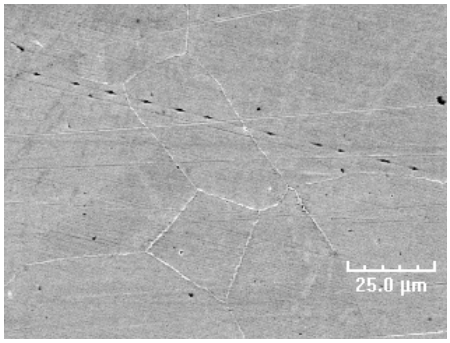

1000X at base metal

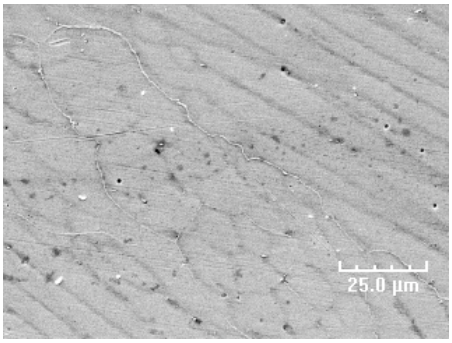

1000X at weld

Figure 8.6. SEM photomicrographs of cross sections of weldment W7.

Weldments listed in Table 8.1 were exposed at 593°C and 1 atm in Gas 21 at a carbon activity of ≈104. Figure 8.7 shows a macrophotograph of the weldments and corresponding base metals after 3114-h exposure. Figure 8.8 shows the 3D-profile map of W3 across the weld area. Pits had coalesced along the boundary of the weld and base alloy. Weldment W7 showed pits predominantly in the weld area (see Fig. 8.9), although the composition of both the base and filler metals is the same. Figure 8.10 shows a photomicrograph of weldment W7, indicating pit development in the weld zone. Weldment exposures and analysis of the size, depth, and distribution of pits were performed as and when the specimens are retrieved from the exposure runs.

Figure 8.7. Macrophotograph of weldment and corresponding base metal specimens after 3114-h exposure at 593°C and 1 atm in a gas mixture with a carbon activity of 104.

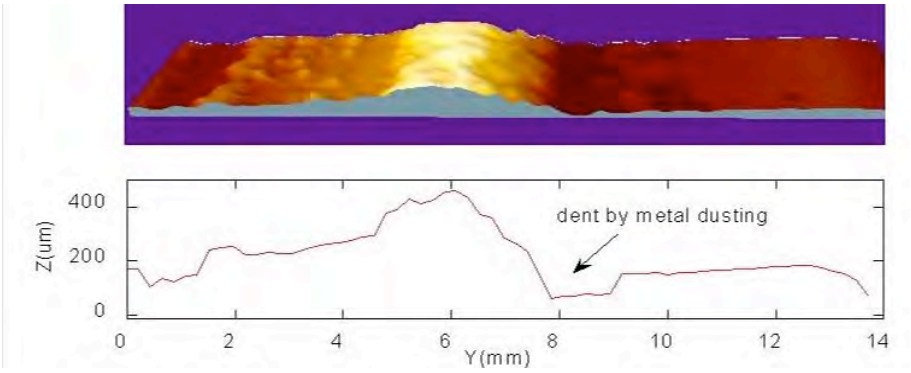

Figure 8.8. 3D-profile map of W3 weldment. Metal dusting pits had coalesced into a belt in the boundary between the weld and base alloy.

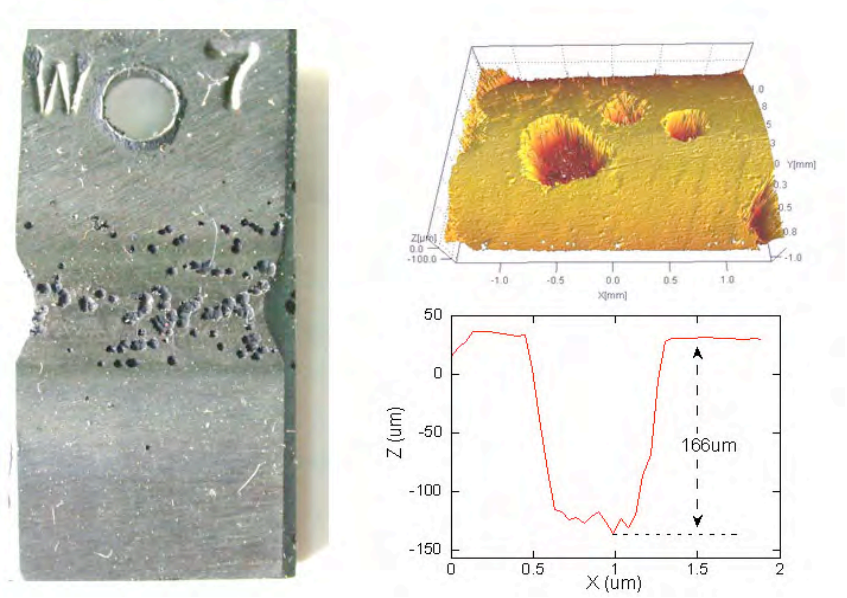

Figure 8.9. Macrophotograph of weldment W7. (left) pits in the weld area, (right top) profile of metal dusting pits in weld area, and (right bottom) depth of a metal dusting pit.

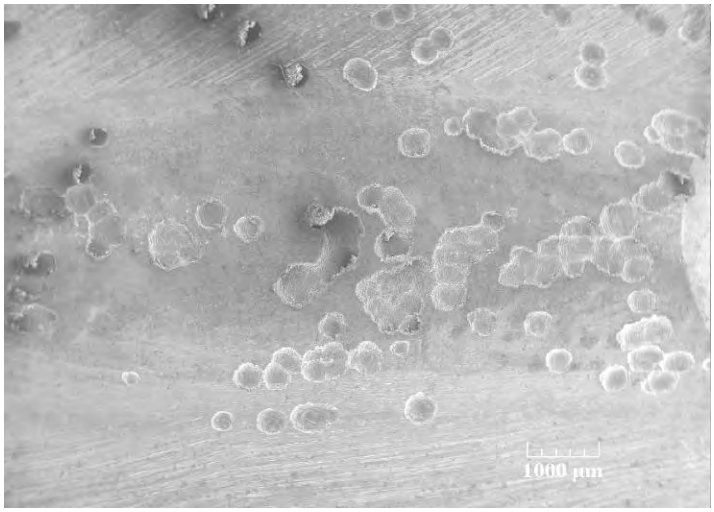

Figure 8.10. Photomicrograph of weldment W7 showing pits in the weld zone.

Weldments W5 and W6 were not attacked by metal dusting even after 9108-h exposure in high carbon activity gas. Only a few pits were observed in the weld area of W1. Pits in W7 were concentrated in the weld and heat-affected zones of the specimen. Pits on W2 and W3 were almost uniformly distributed in both weld and base metal regions.

Figure 8.11 shows weight loss data for the weldments and the corresponding base alloys. Weight loss and pitting were observed on weldments W2, W3, and W7. Weight loss rate for W3 was highest among the weldments and its base alloy (HR160) was also subjected to metal dusting, although the weight loss rate of HR160 is less than that of Alloy 601.

Weight loss and pitting were observed on weldments W1, W2, W3, and W7. Although the onset of metal dusting starts early in W3, the weight loss for W7 exceeded that of W3 after 9109-h exposure in the metal dusting environment. The weight loss rates of W1 and W2 in steady growth state are faster than that of W3. The surface treatment of the W3 specimen, performed by the supplier, seems to result in a shorter initiation time and faster growth at the beginning. However, after the surface material was removed by the pitting process, metal dusting corrosion reaches a steady growth rate and the weight loss rate slowed.

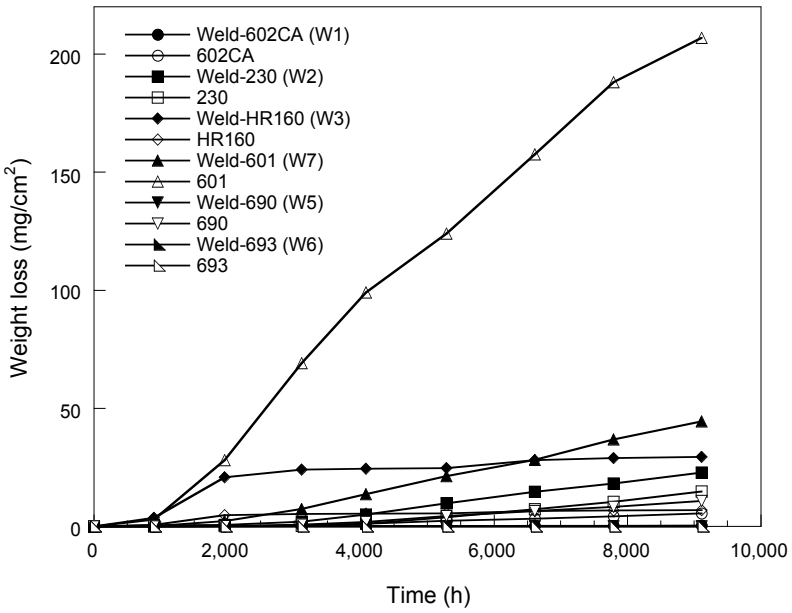

Figure 8.11. Weight loss data for weldment specimens and corresponding base alloys exposed at 593°C and 1 atm in a gas mixture with a carbon activity of 104.

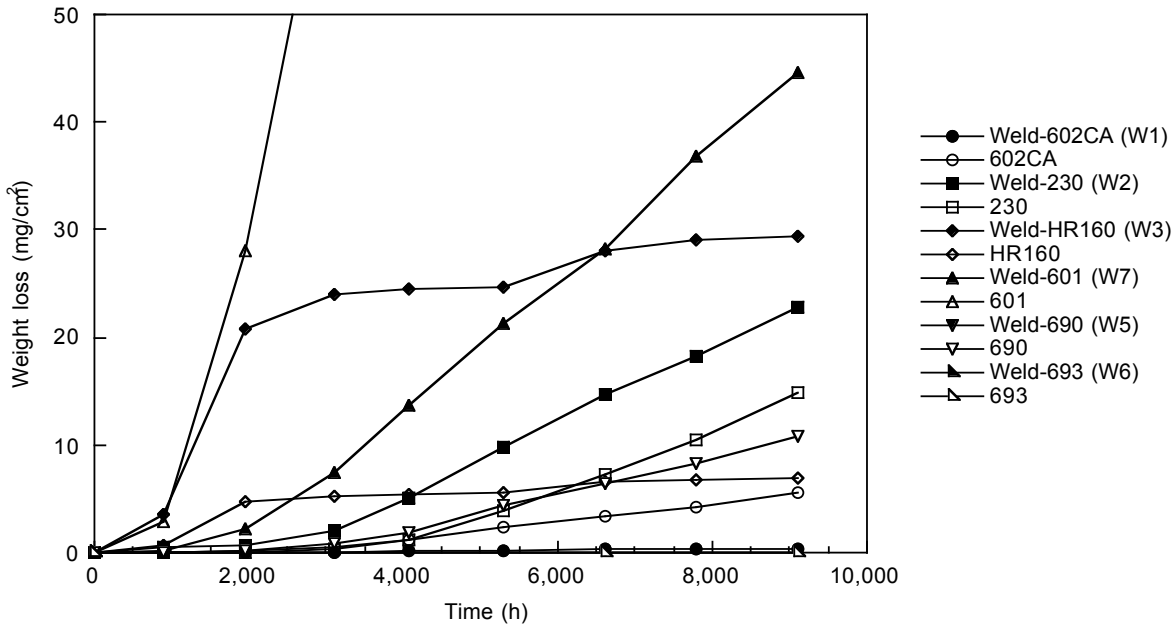

Figure 8.12. Expanded view of data in Figure 8.11.

Pits in the weld area of W7 grew much faster than in other weldment specimens (see Fig. 8.13). Its base alloy 601 is attacked easier by metal dusting. The base alloy of W3 was uniformly corroded, but the pits on W3 had coalesced along the boundary of weld and base alloy. SEM cross section image shows that the boundary between weld and base metal of W3 is not as uniform as other weld specimens, which may lead to severe attack on this area. W1 also developed deep pits at the weld area. The pits on W2 were shallow, but a lot of pits were almost uniformly distributed on both weld and base alloy. Figure 8.14 shows a comparison of the pit growth rate for Alloy 601 in polished condition and W7 (a weldment of Alloy 601). The pitting rate is faster in the weldment when compared to that in the base alloy.

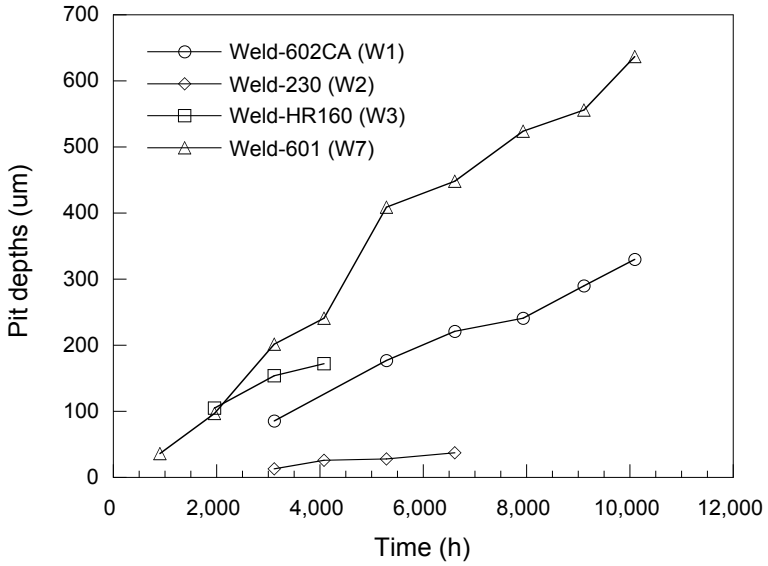

Fig. 8.13. Pit depth as a function of time for weldment specimens exposed to a gas mixture with a carbon activity of 104 at 593°C and 1 atm.

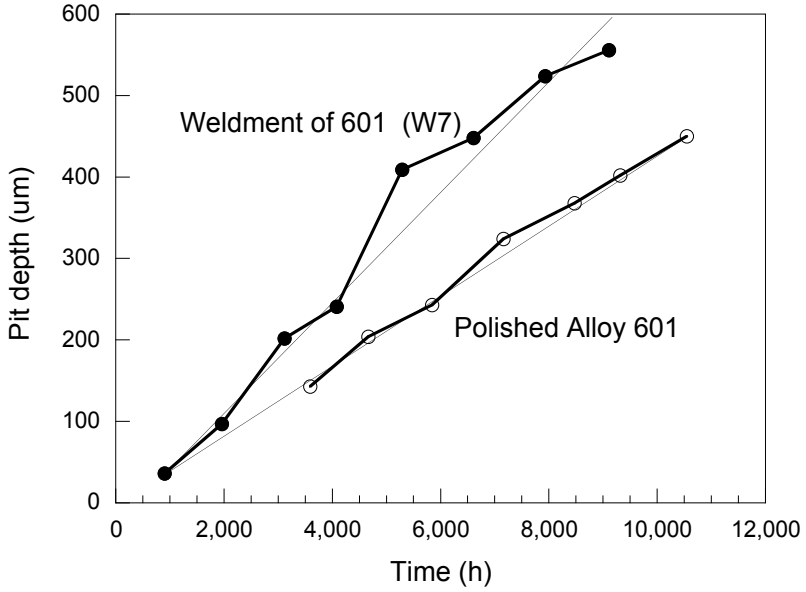

Figure 8.14. Pit depth as a function of time for base metal and weldment specimens of Alloy 601 exposed to the same metal dusting environment.

8.2 Weldments of Fe-base alloys

Table 8.1 also lists the Fe-base alloy weldments used in the study. Figures 8.15-8.20 show the microstructures of various weldments after etching to delineate the dendritic structures and heat-affected zones.

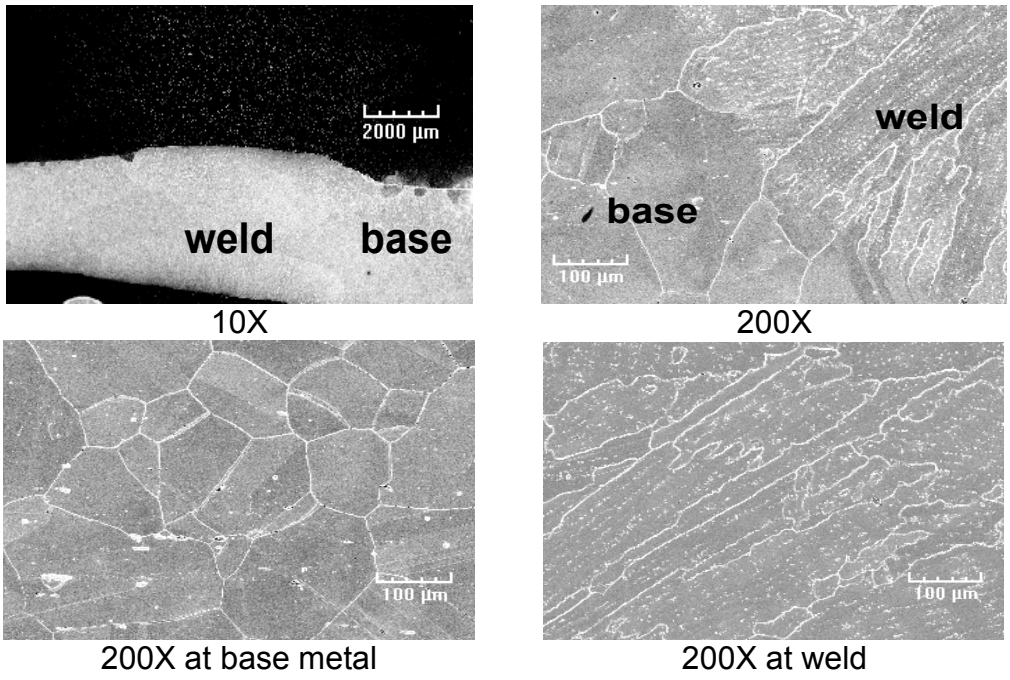

10X 200X

200X at base metal 200X at weld

Figure 8.15. SEM photomicrographs of cross sections of weldment W4.

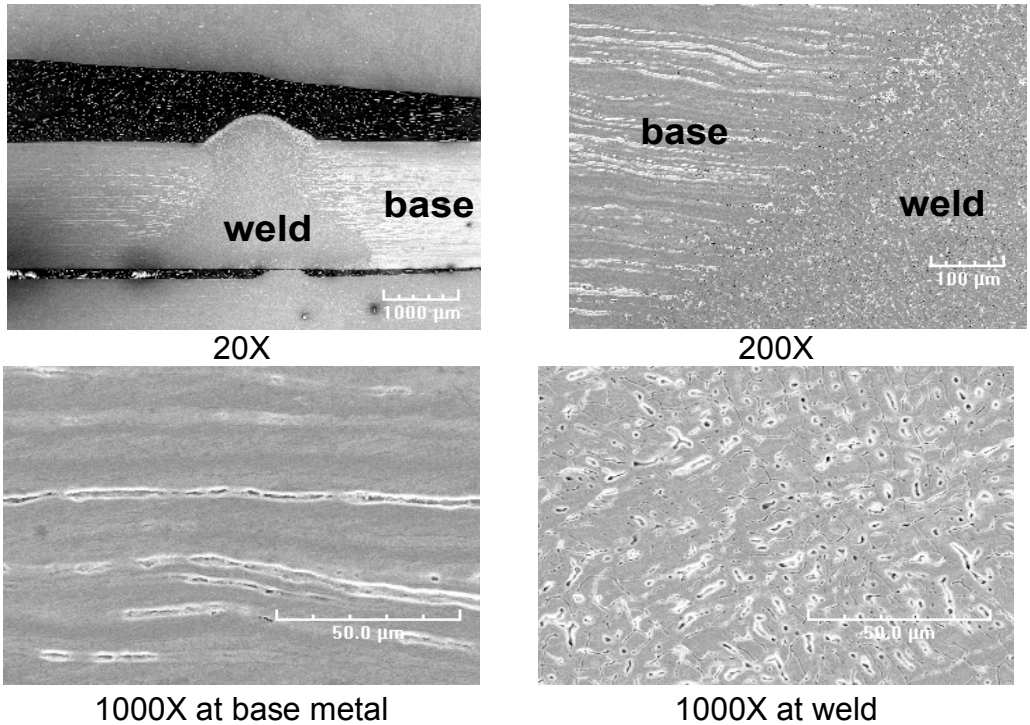

20X 200X

1000X at base metal 1000X at weld

Figure 8.16. SEM photomicrographs of cross sections of weldment W8.

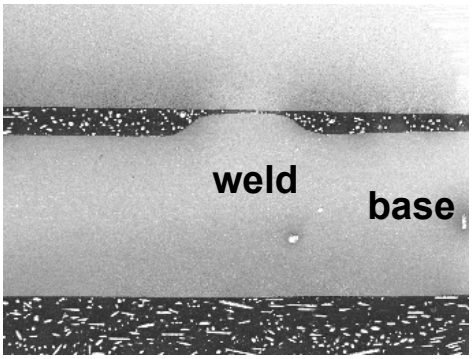

50X

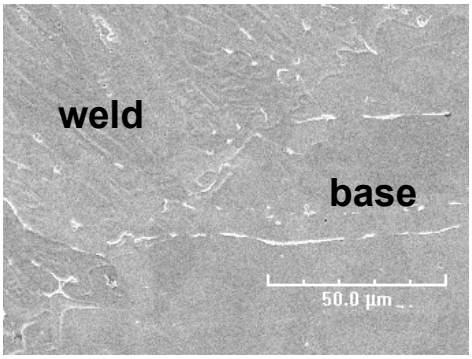

1000X

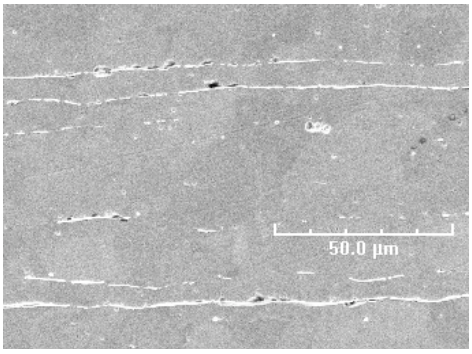

1000X at base metal

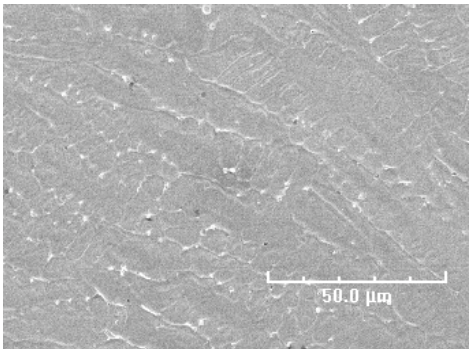

1000X at weld

Figure 8.17. SEM photomicrographs of cross sections of weldment W9.

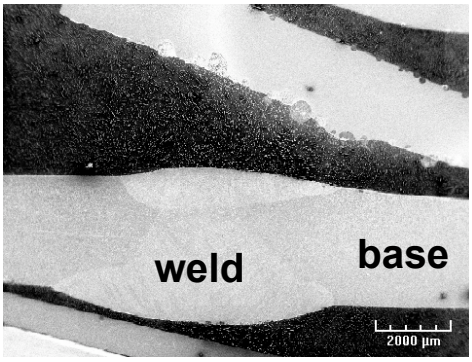

10X

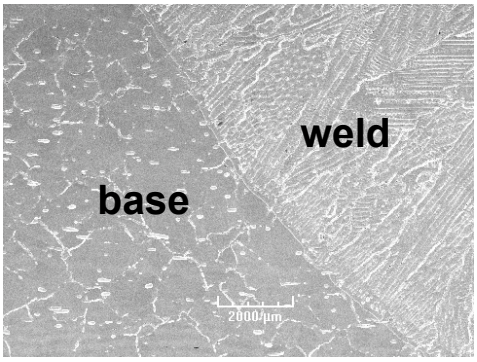

200X

Figure 8.18. SEM photomicrographs of cross sections of weldment W10.

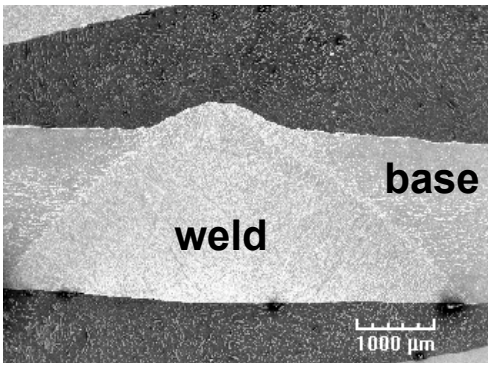

20X

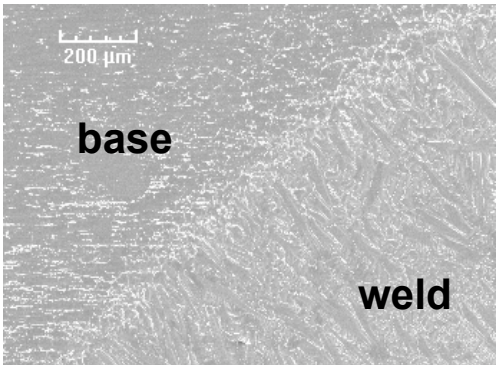

100X

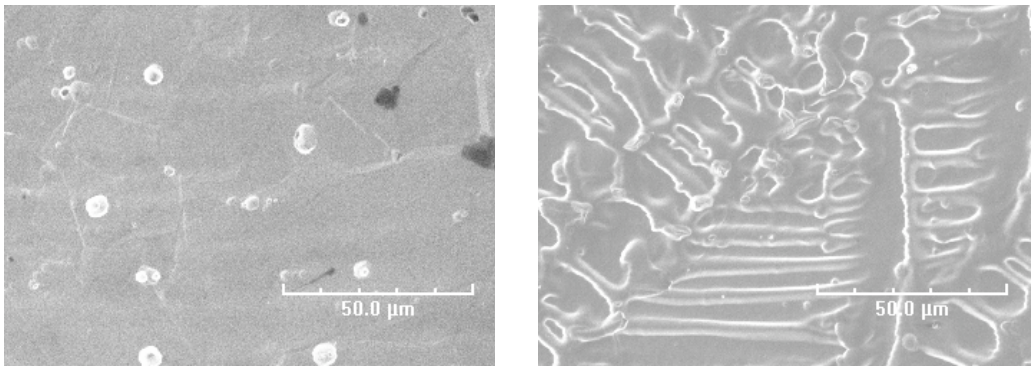

1000X at base metal 1000X at weld

Figure 8.19. SEM photomicrographs of cross sections of weldment W11.

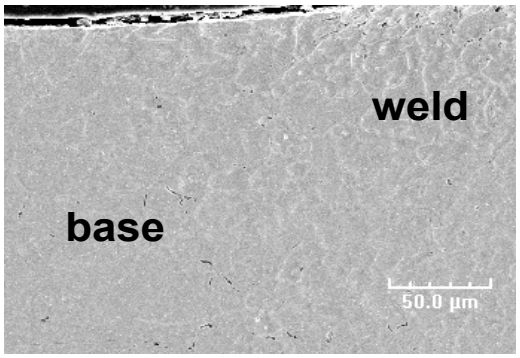

500X

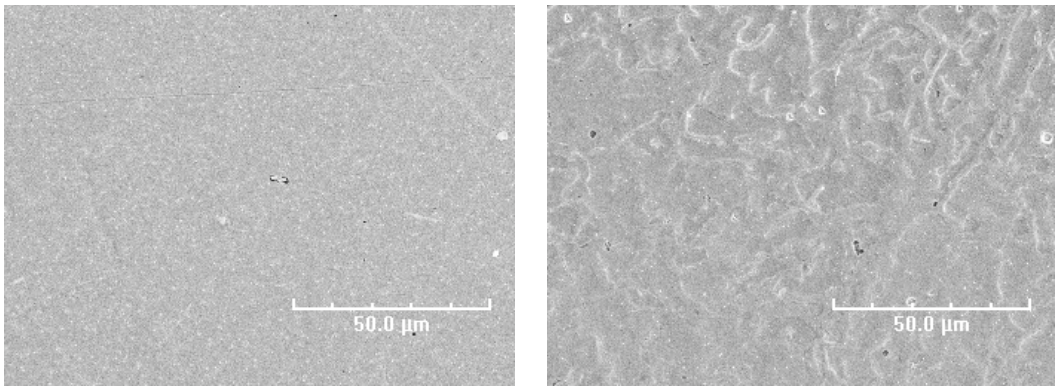

1000X at base metal 1000X at weld

Figure 8.20. SEM photomicrographs of cross sections of weldment W12.

The base alloy of W4 is Alloy 803 with 25.6 wt.% Cr and the filler metal is Ni-base Alloy 617. Many pits were observed on the base alloy (see Fig. 8.21). However, only a few pits were observed in the weld area. Although the pit diameter in the weld region is small, the depth of the pit is much larger in the weld region compared to that in the base alloy region (see Fig. 8.22). W8 was welded by electron beam without filler metal. Both weld and base metal regions of W8 were almost uniformly corroded.

The low Cr content in Alloy 347 made the alloy susceptible to metal dusting corrosion. W12 was also made of Alloy 347. The weld area was severely attacked by metal dusting. Pits as deep as 205 µm were also observed in the heat-affected zone.

Both W9 and W11 were made of Alloy 310 with 25 wt.%Cr. W9 was welded by electron beam without filler metal, but W11 was joined using GTAW method, with 0.125" dia. 2%-thoriated tungsten electrode using filler metal ER310. The resistance to metal dusting of Alloy 310 is better than that of Alloy 347. Both W9 and W11 did not lose weight after 1136-h exposure to Gas 21 at 593°C. However, the surface on W11 along the heat-affected zone becomes dark with several small metal dusting pits (see Fig. 8.23). Although the surface of W9 in the heat-affectted zone is rough, no pit was observed during the exposure period. Therefore, electron beam welding may be a better method for welding materials that are used in metal dusting environment. Some dark spots have been observed on W10, which is made of Alloy 353MA. However, no weight loss was observed after 1136-h test.

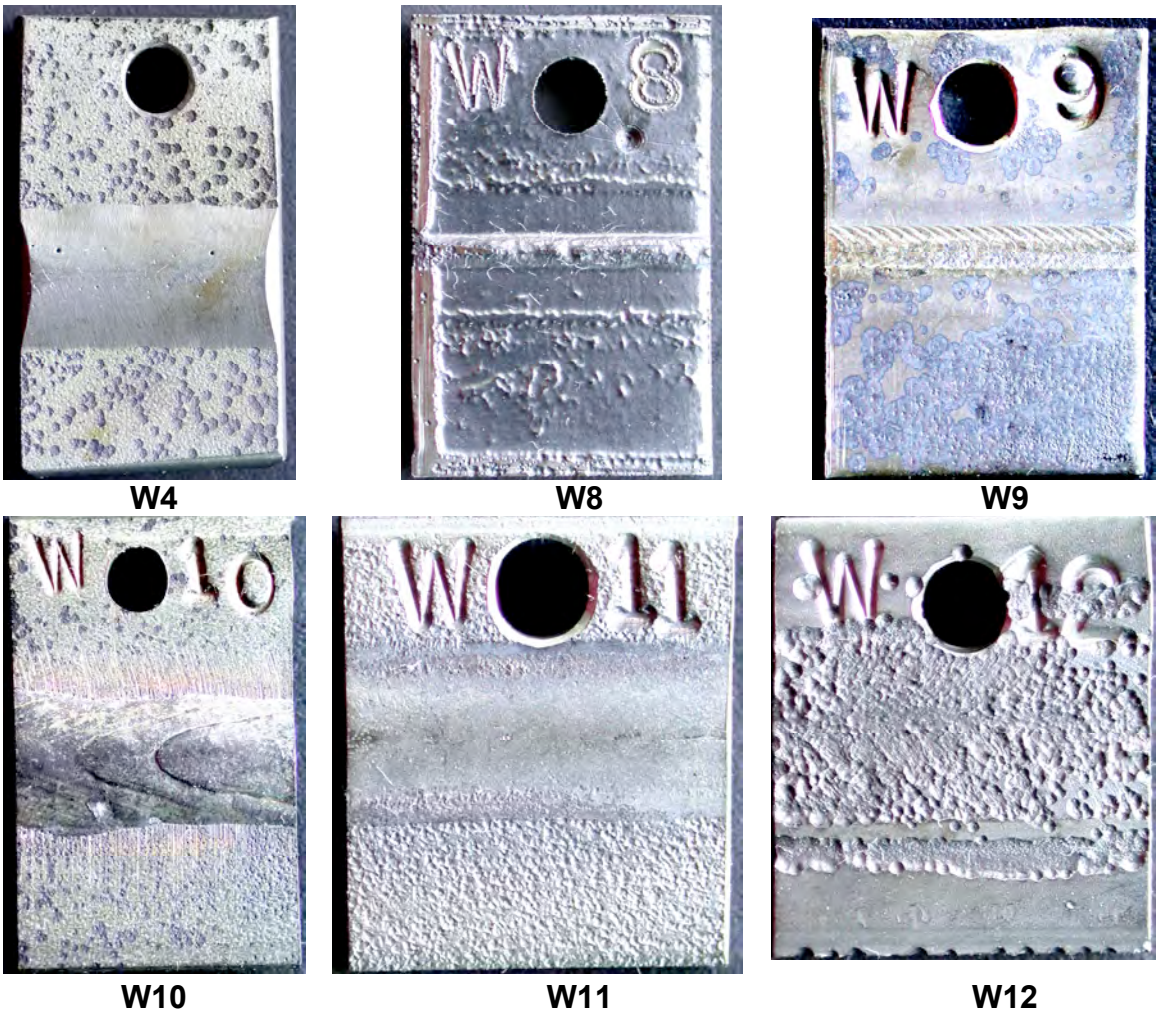

Figure 8.21. Photographs of Fe-base weldments after 1136-h exposure to Gas 21 at 593°C, 1 atm.

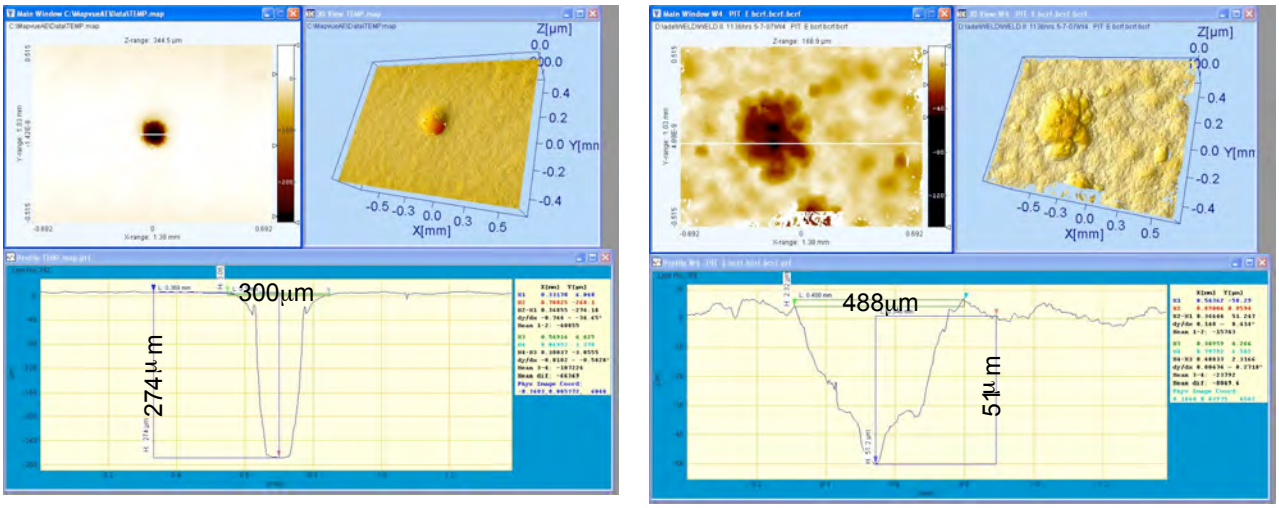

Figure 8.22. Metal dusting pit on weldment W4 after 1136-h exposure to Gas 21 at 593°C, 1 atm. (left) pit in weld area and (right) pit in base alloy.

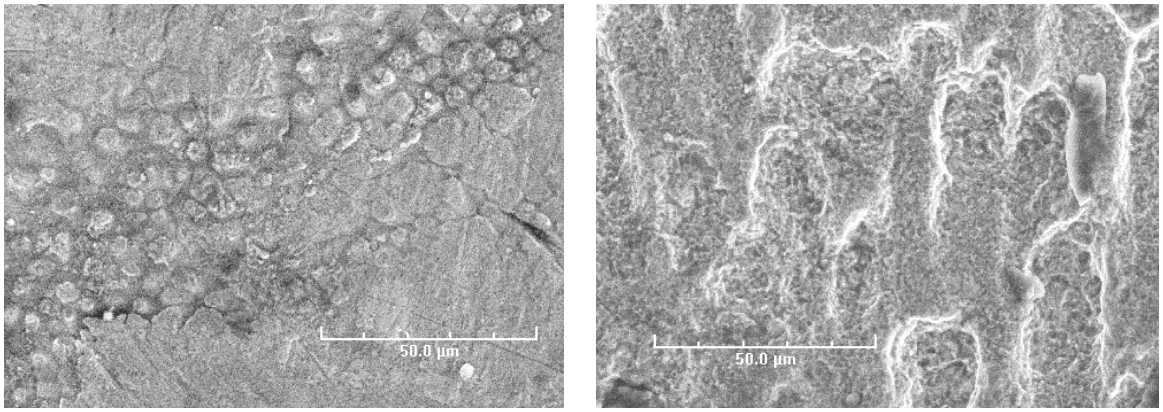

W9 **W11**

Figure 8.23. SEM images of heat-affected zones of W9 and W11 weldments.

9. FAILURE ANALYSIS IN INDUSTRY-SUPPLIED COMPONENTS

Metal dusting degradation of structural metallic materials has been observed in plants in the production of syngas, a step used in the manufacture of hydrogen, ammonia, methanol, and various liquid hydrocarbons. The failures are generally observed in the temperature range of 400-700°C in complex gas environments with high carbon activity (>>1). Further, these systems operate at elevated pressures, which also exacerbate metal dusting degradation, since carbon activity increases with an increase in system pressure. During the course of this project, we examined several failed components from a hydrogen-production plant and from a reformer plant.

9.1 Ni-base Alloys Tested in a Reformer Plant

Alloys 602CA and 693 were exposed in a reformer plant of Haldor Topsoe at 659°C and 25 atm. Two sets of samples were analyzed. One had been exposed to metal dusting environment for 1.5 years. The other had been exposed for 3 years. Figure 9.1 shows the macrophotograph of Alloy 693 that had been exposed for 1.5 years. Pit depths and pit diameters were determined by measuring the profile along lines that pass across the pit regions. The surface was automatically leveled using software to maintain the surface leveled during the scan. Generally, depths of four or five pits on the surface were measured. Their 3D mappings are shown in Figs. 9.2 and 9.3. Figure 9.4 shows the macrophotograph of the specimen that had been exposed for 3 years. To insert the specimen to surface profiler, it was cut into three pieces as shown in Fig. 9.4. Depths of eight pits were measured in this specimen. Their 3D mappings are shown in Figs. 9.5-9.8. Table 9.1 lists the pit depth and pit diameter data for specimens that were exposed for both time periods. The maximum pit depth is 72.5 μm for the specimen that was exposed for 1.5 years. The maximum pit depth increased to 341 μm for the specimen that was exposed for 3 years, and the depth/diameter ratio increased as the exposure time increased from 1.5 to 3 years. The pits in the bent region are not as deep as those at the flat region of the specimens.

Figure 9.1. Macrophotograph of Alloy 693 specimen, after 1.5-y exposure in metal dusting environment.

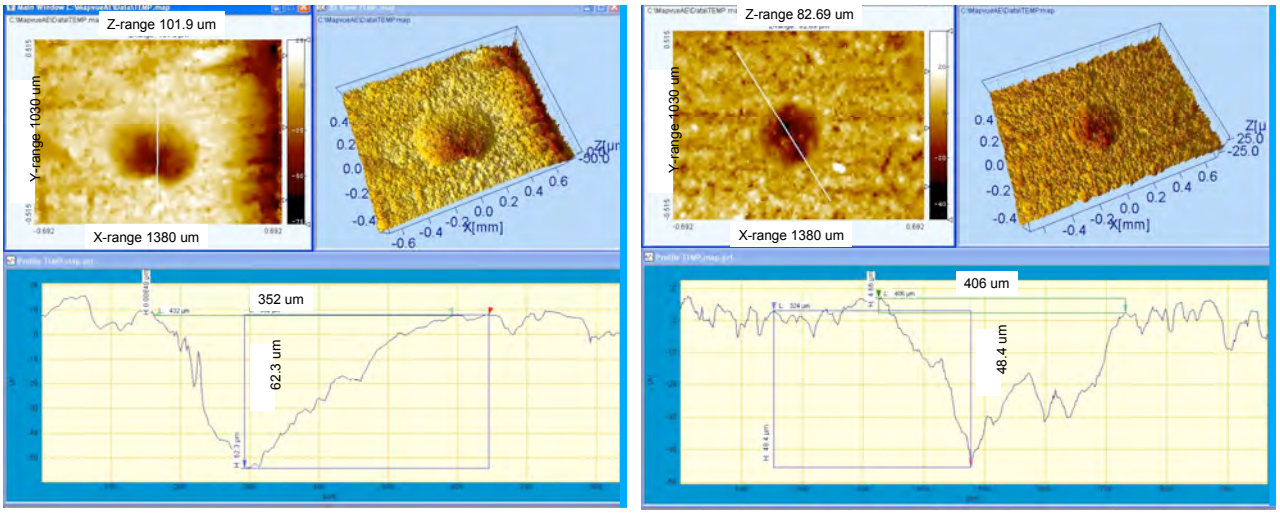

Figure 9.2. Profile mapping of pits 1 and 2 on Alloy 693 after exposure to metal dusting environment for 1.5 years.

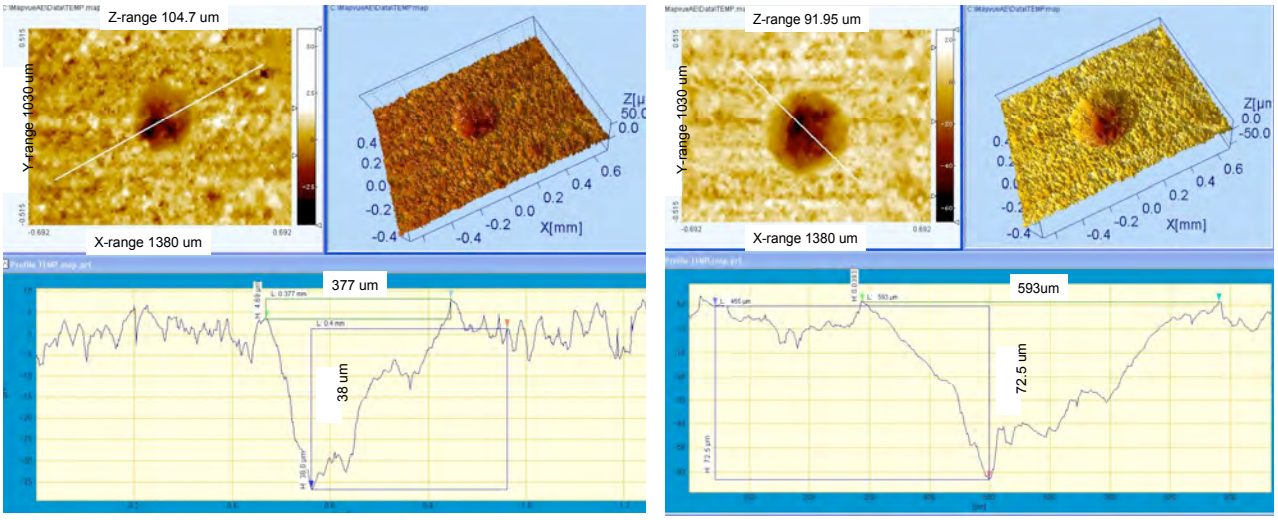

Figure 9.3. Profile mapping of pits 3 and 4 on Alloy 693 after exposure to metal dusting environment for 1.5 years.

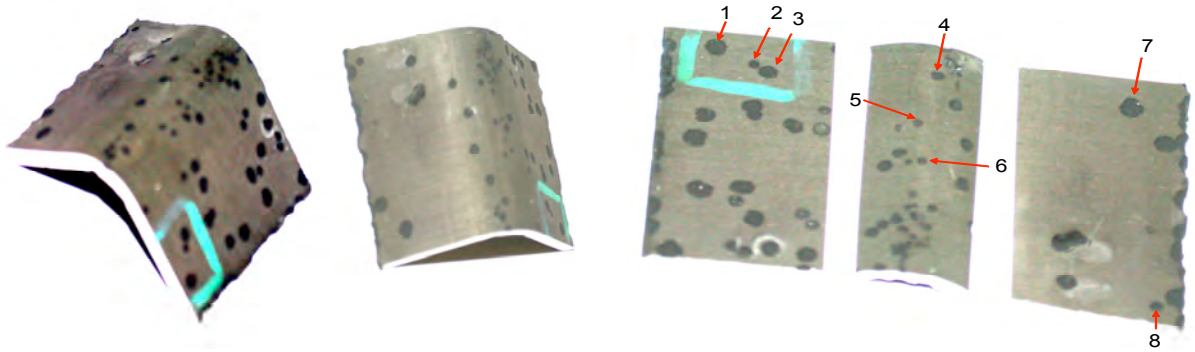

Before cutting After cutting

Figure 9.4. Macrophotographs of Alloy 693 specimen after exposure for 3 years.

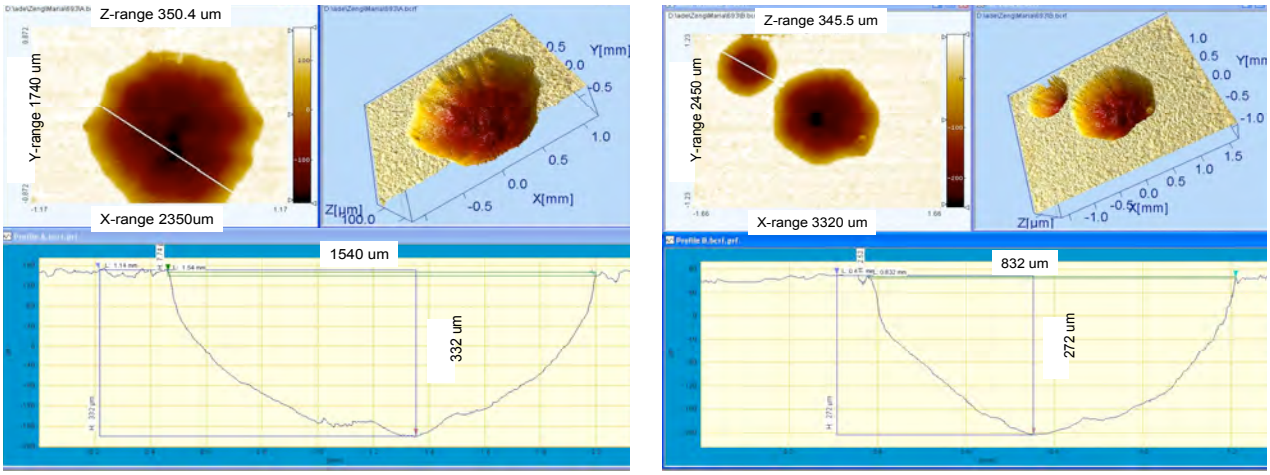

Figure 9.5. Profile mapping of pits 1 and 2 on Alloy 693 that had been exposed to metal dusting environment for 3 years.

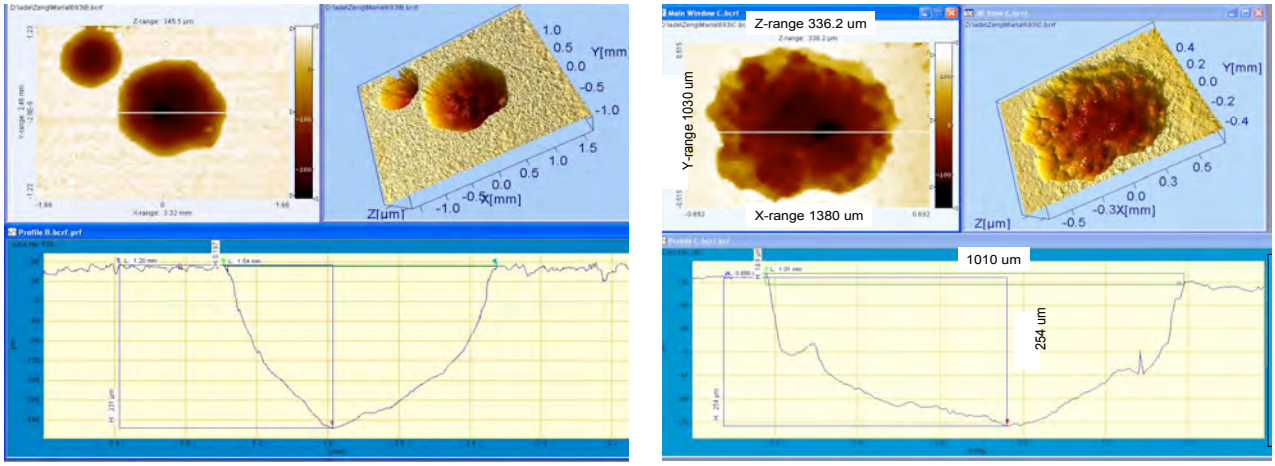

Figure 9.6. Profile mapping of pits 3 and 4 on Alloy 693 that had been exposed to metal dusting environment for 3 years.

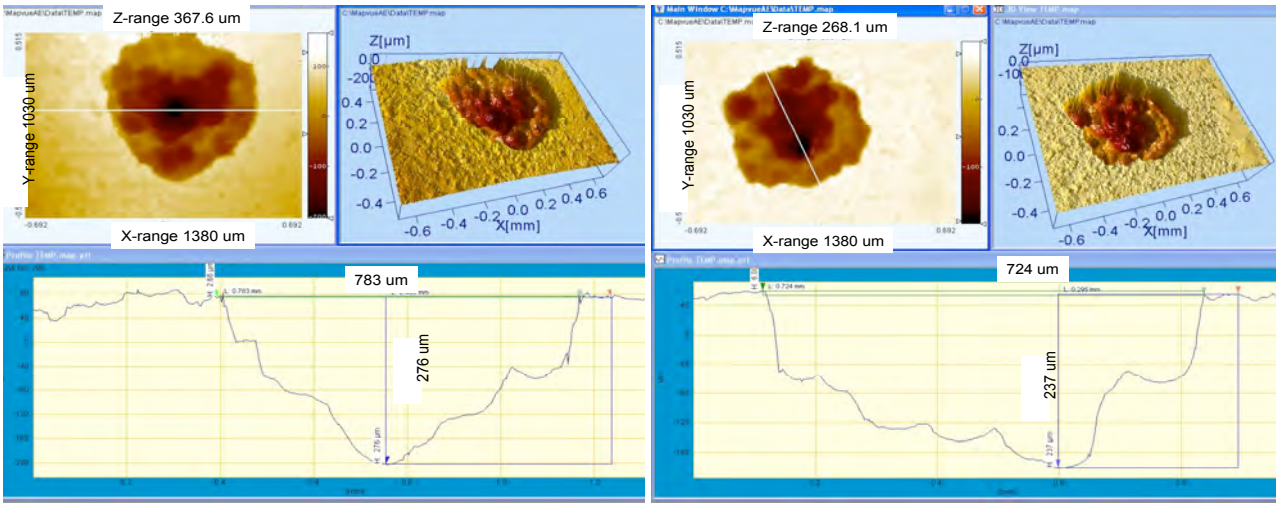

Figure 9.7. Profile mapping of pits 5 and 6 on Alloy 693 that had been exposed to metal dusting environment for 3 years.

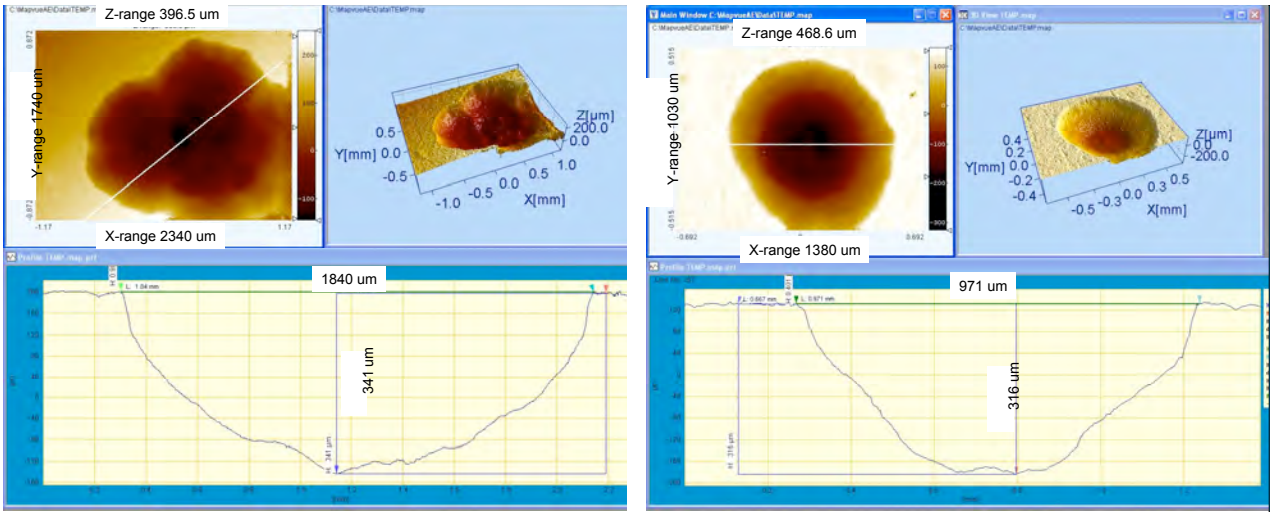

Figure 9.8. Profile mapping of pits 7 and 8 on Alloy 693 that had been exposed to metal dusting environment for 3 years.

Table 9.1. Pit depths and diameters in Alloy 693 after 1.5- and 3-y exposures in a metal dusting environment at 659°C and 25 atm.

Pit	Depth (μm)	Diameter (μm)	Depth/Diameter
Data for specimens exposed for 1.5 y			
1	62	432	0.14
2	48	406	0.12
3	38	377	0.10
4	73	593	0.12
5	38	547	0.07
Data for specimens exposed for 3 y			
1	332	1540	0.22
2	272	832	0.33
3	331	1540	0.21
4	254	1010	0.25
5	276	783	0.35
6	237	724	0.33
7	341	1840	0.19
8	316	971	0.33

Figure 9.9 shows the macrophotograph of Alloy 602CA that had been exposed for 1.5 years to metal dusting environment at 659°C and 25 atm. The depth and diameter of four pits were measured in this specimen. Their 3D mappings are shown in Figure 9.10-9.12. Figure 9.13 shows macrophotographs of the sample that had been exposed for 3 years. To insert the specimen to surface profiler, we have to cut it to three pieces as shown in Fig. 9.13. Eight pits were measured in this specimen. Their 3D mappings are shown in Figs. 9.14-9.16. Table 9.2 shows the pit depth and pit diameter

data for specimens that were exposed for both periods. The maximum pit depth is 307 µm for the specimen that was exposed for 1.5 years. The maximum pit depth increased to 645 µm for the specimen exposed for 3 years. The pits at the bent region are not as deep as in the flat region, similar to the observation in Alloy 693.

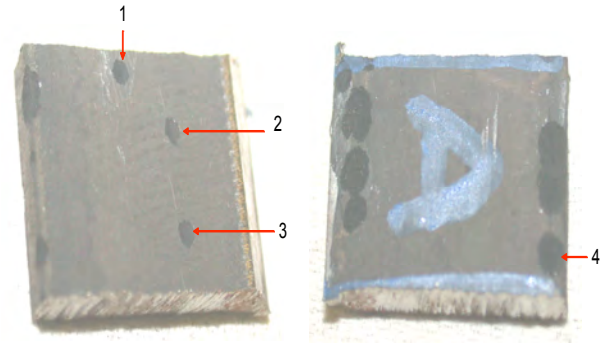

Figure 9.9. Macrophotograph of Alloy 602CA specimen, after 1.5-y exposure in metal dusting environment.

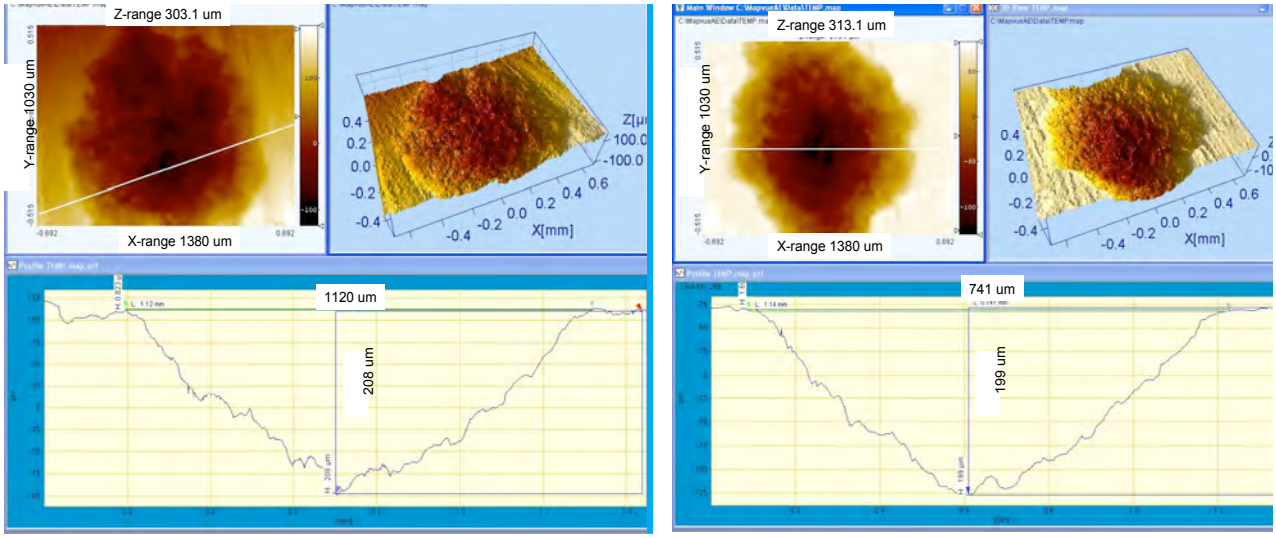

Figure 9.10. Profile mapping of pits 1 and 2 on Alloy 602CA that had been exposed to metal dusting environment for 1.5 years.

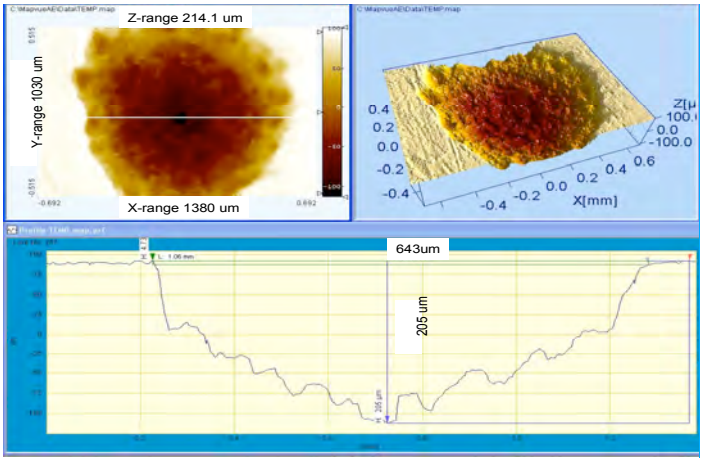

Figure 9.11. Profile mapping of pit 3 on Alloy 602CA that had been exposed to metal dusting environment for 1.5 years.

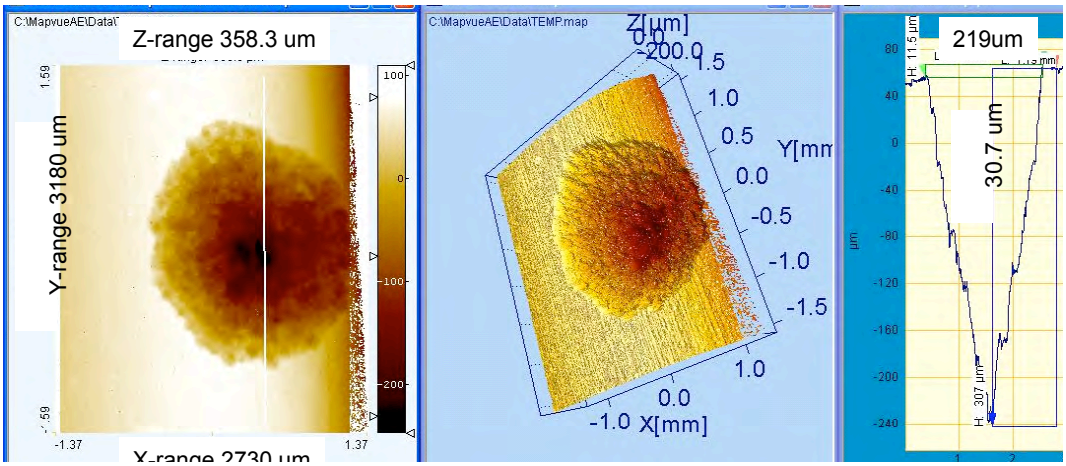

Figure 9.12. Profile mapping of pit 4 on Alloy 602CA that had been exposed to metal dusting environment for 1.5 years.

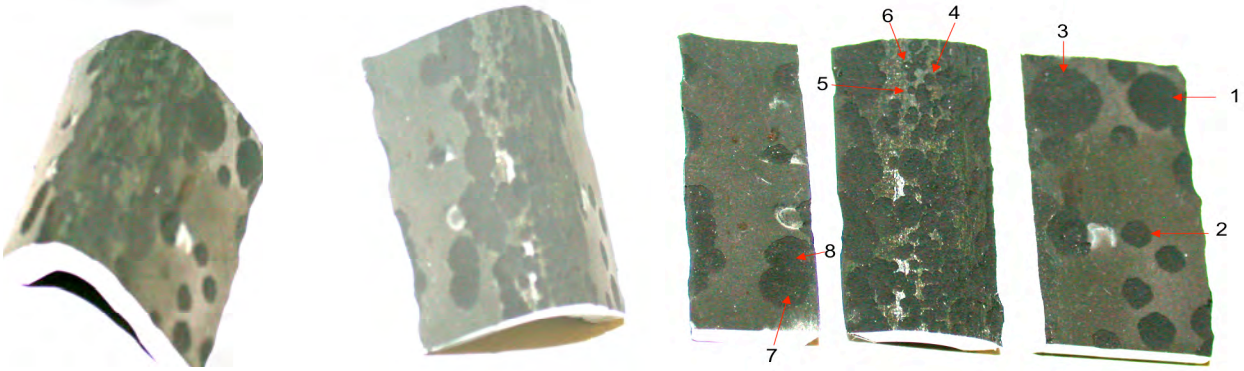

Before cutting After cutting

Figure 9.13. Photos of Alloy 602CA after exposure for three years. The two photos were taken from different angles.

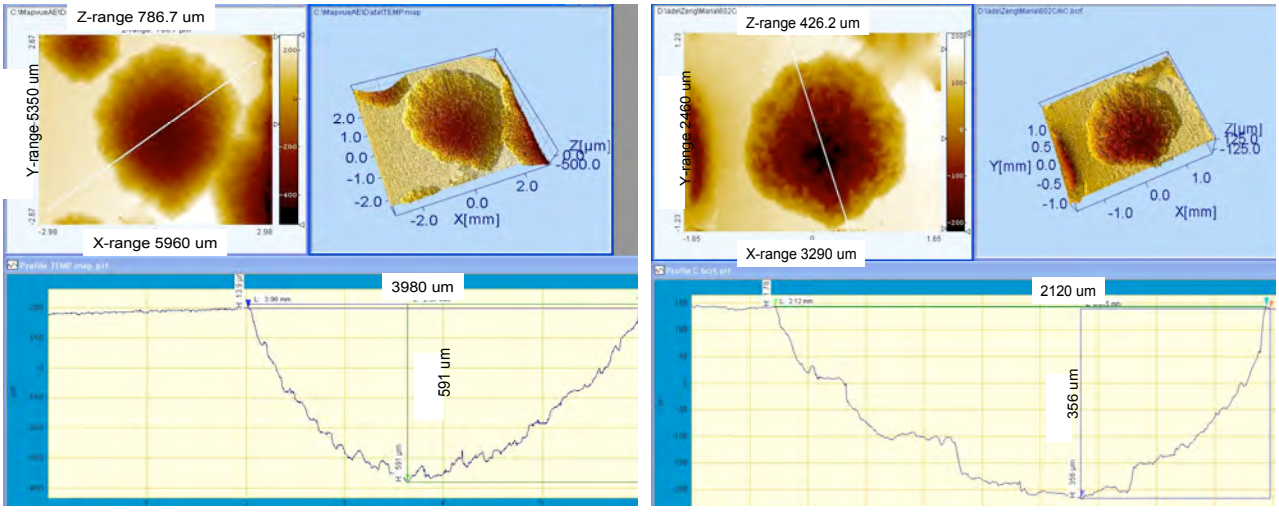

Figure 9.14. Profile mapping of pits 1 and 2 on Alloy 602CA that had been exposed to metal dusting environment for 3 years.

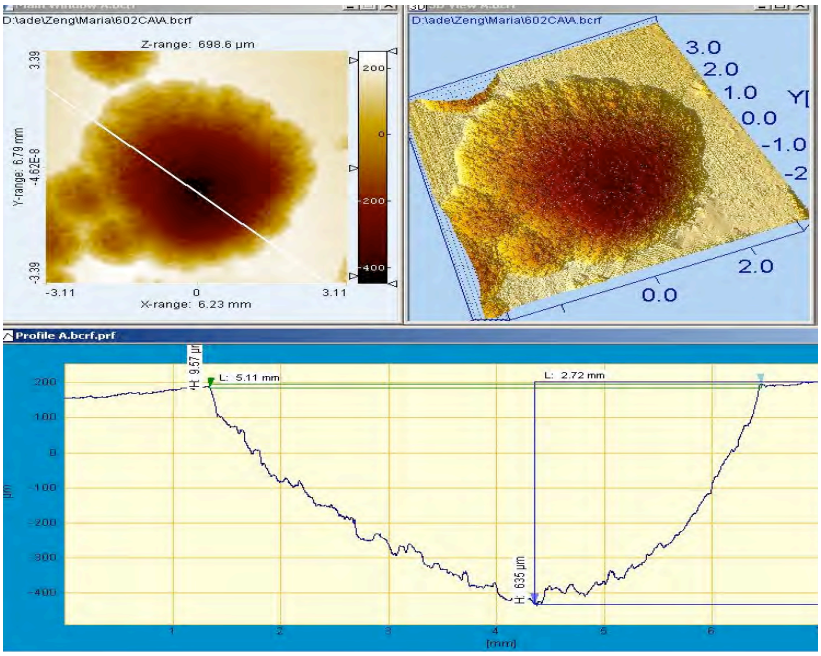

Figure 9.15. Profile mapping of pit 3 on Alloy 602CA that had been exposed to metal dusting environment for 3 years.

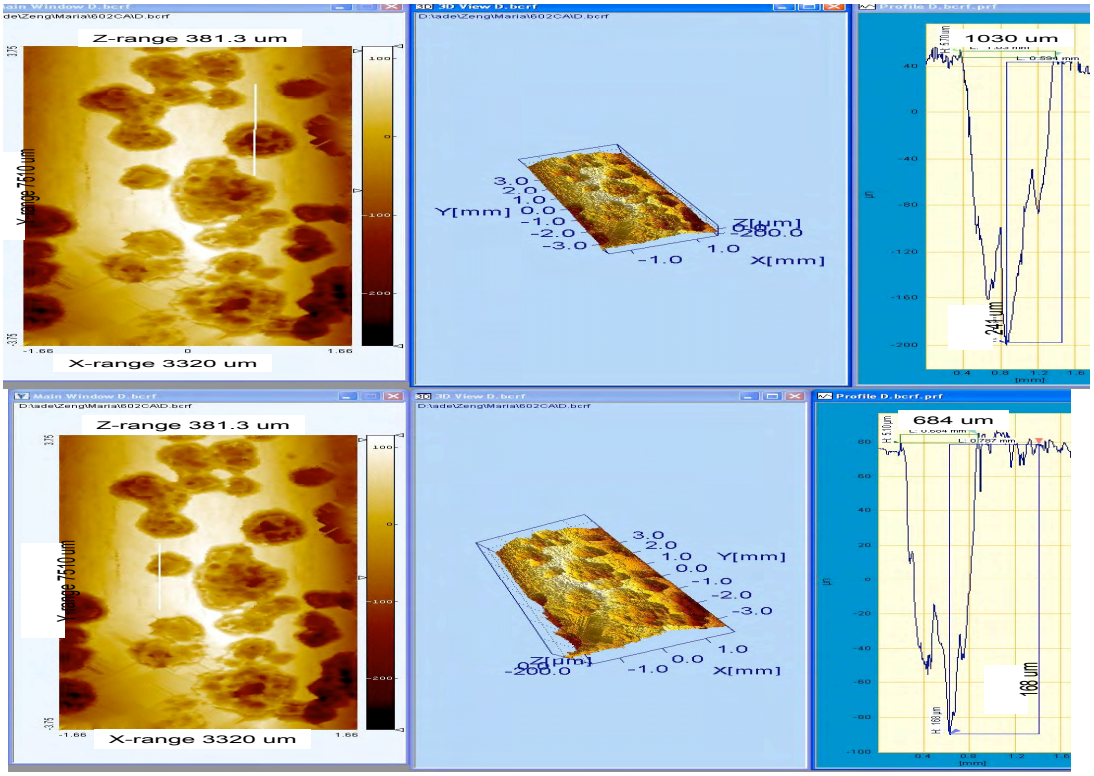

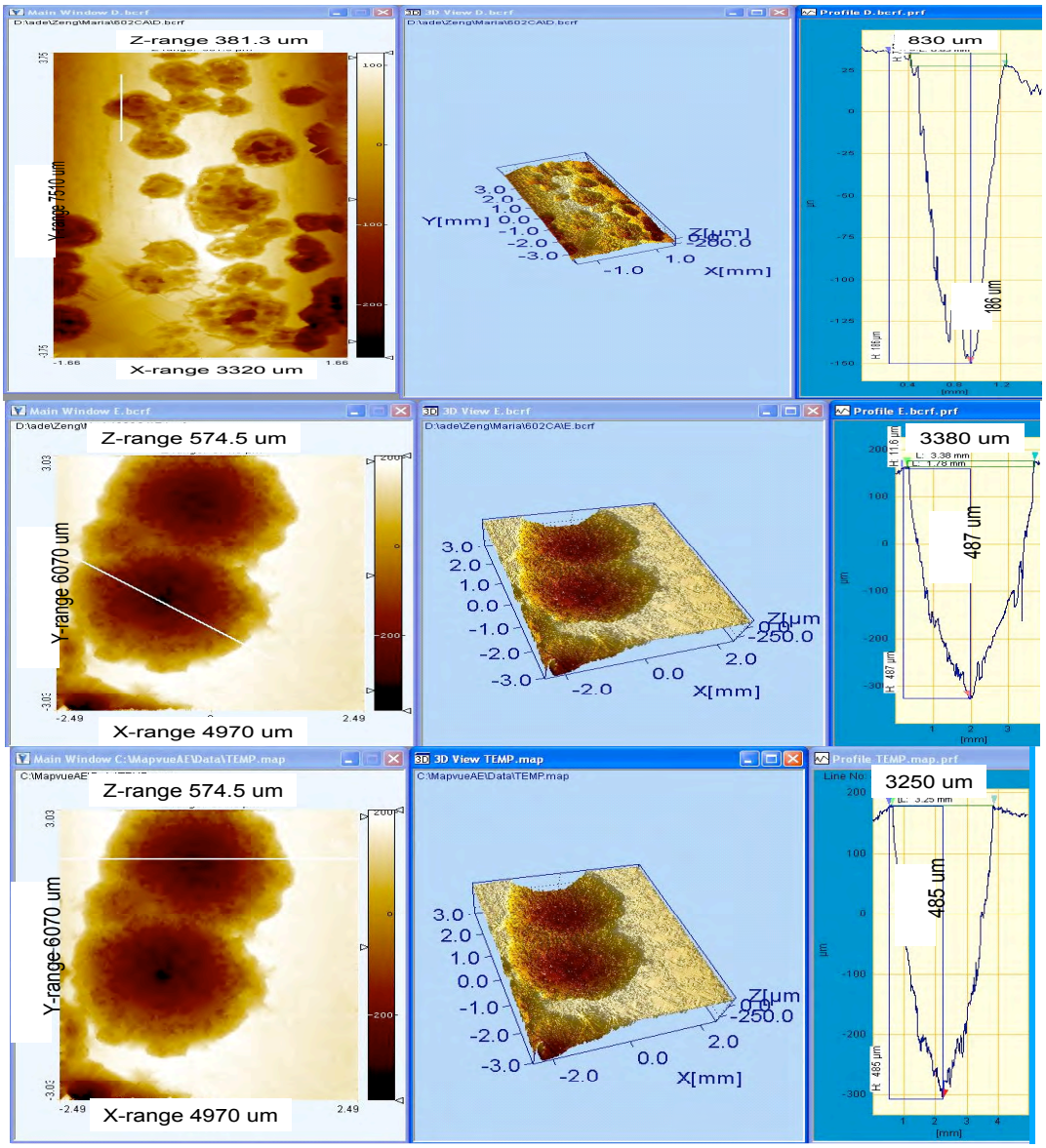

Figure 9.16. Profile mapping of pits 4-8 on Alloy 602CA that had been exposed to metal dusting environment for 3 years.

Figure 9.17 shows the pit depth data as a function of pit diameter for Alloys 693 and 602CA after 1.5- and 3-y exposure in a metal dusting environment at 659°C and 25 atm. If the pit diameters can be correlated with the pit depth as a function of key variables such as exposure time, carbon activity, system pressure, etc. then one may be able to assess the pit depth progression from the pit diameter measurements (in a non-destructive manner) and may be able to predict the remaining life of the component in service. All the data lines should pass through the origin since prior to initiation both pit depth and diameter will be zero. The data indicate that the pit depth increases at a faster rate when the pit diameter is small and stabilizes to a linear relationship when the pit diameter reaches ≈600-700 μm. The pit depth corresponding to this diameter is ≈150 and 250 μm for Alloys 602CA and 693, respectively, after 3-y exposure in the

Table 9.2. Pit depths and diameters in Alloy 602CA after 1.5- and 3-y exposures in a metal dusting environment at 659°C and 25 atm.

Pit	Depth (um)	Diameter (um)	Depth/Diameter
Data for specimens exposed for 1.5 y			
1	208	1120	0.19
2	199	1140	0.18
3	205	1060	0.19
4	31	219	0.14
Data for specimens exposed for 3 y			
1	591	3980	0.15
2	356	2120	0.17
3	635	5110	0.12
4	241	1030	0.23
5	168	684	0.25
6	186	830	0.22
7	487	3380	0.14
8	485	3250	0.15

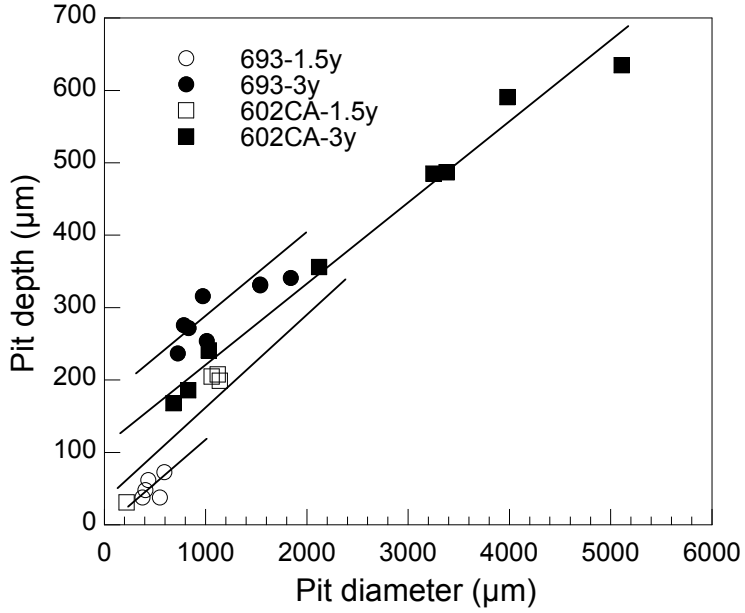

Figure 9.17. Relationship between pit diameter and pit depth for Alloys 693 and 602CA, after 1.5- and 3-y exposures in a metal dusting environment.

metal dusting environment. The results indicate that for 3-y exposure, the maximum pit diameters measured in Alloys 693 and 602CA are 1840 and 5110 µm, respectively, and the maximum pit depths measured for the two alloys are 341 and 635 µm. The data further indicate that for a given exposure time, the pits in Alloy 693 are smaller in diameter but deeper whereas the pits in Alloy 602CA are larger in diameter but shallower.

9.2. Analysis of Failed Components From a Hydrogen Plant

A pipe and a plate, that had metal dusted in a hydrogen-reformer plant, were analyzed in detail to establish the causes for failure and to compare the observations from the plant-exposed components with the laboratory-generated data. The pipe and the plate were made of Alloy 800HT. Figure 9.18 shows several large holes in the pipe and one large hole (≈10 cm in diameter) in the plate. Specimens were cut from the two components and analyzed using SEM and Raman scattering. Figure 9.19 shows SEM photomicrographs of cross sections of thick and thin parts of the Alloy 800HT pipe, that was subjected to metal dusting attack.

Figure 9.18. Macrophotographs of a pipe and a plate obtained from a hydrogen-reformer plant after failure by metal dusting attack.

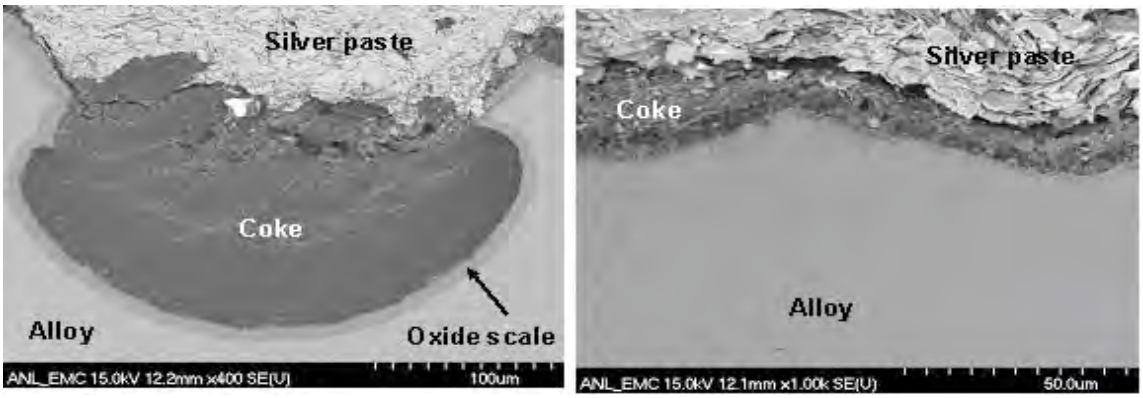

(a) Thick part of Alloy 800 pipe (b) Thin part of Alloy 800 pipe

Figure 9.19. SEM photomicrographs of cross sections of (a) thick and (b) thin parts of an Alloy 800HT pipe, subjected to metal dusting attack.

The pipe had a tightly adhering coke layer on the surface, which could not be easily removed by either ultrasonic cleaning or acetone washing with a cotton tip. A ≈9 μm oxide scale was observed on the surface of the thick part of the pipe. However, no such oxide scale was observed on the surface of the thinner part of the pipe, which was attacked severely by metal dusting. Therefore, the alloy in the thin part was directly exposed to high carbon activity gas without the protection of an oxide scale. Although

metal dusting pits appeared on the surface of the thick part of the pipe, its corrosion rate was much lower than that of the thinner section because it was protected by the oxide scale.

Figure 9.20 shows EDX mapping of the cross section of the pipe sections. The oxygen content in the scale on the surface of the thick part is obviously higher than that inside the alloy and in coke. However, the thin part did not have a continuous oxide scale on the surface. Therefore, carbon could readily diffuse into the alloy. EDX line scan results show that the Fe/Cr ratio in the 9-μm-thick oxide scale is higher than that in the alloy (see Fig. 9.21). A solid solution $Fe(Cr_{1-x}Fe_x)_2O_4$ can form in the range $0 \leq x \leq 1$. As shown in Fig. 9.22, $FeCr_2O_4$ is stable in the metal dusting environment, but $Fe_{1.8}Cr_{1.2}O_4$ can react with high carbon activity gases, and the carbon deposition rate in $Fe_{2.4}Cr_{0.6}O_4$ is much larger than that of $Fe_{1.8}Cr_{1.2}O_4$. Therefore, spinel with higher iron content is susceptible to attack by high carbon activity gases. The average Fe/Cr ratio for the oxide scale on the surface of Alloy 800 is 2.18, which is much higher than the 0.5 for $FeCr_2O_4$. Therefore, this oxide scale seems to be not protective in the metal dusting environment.

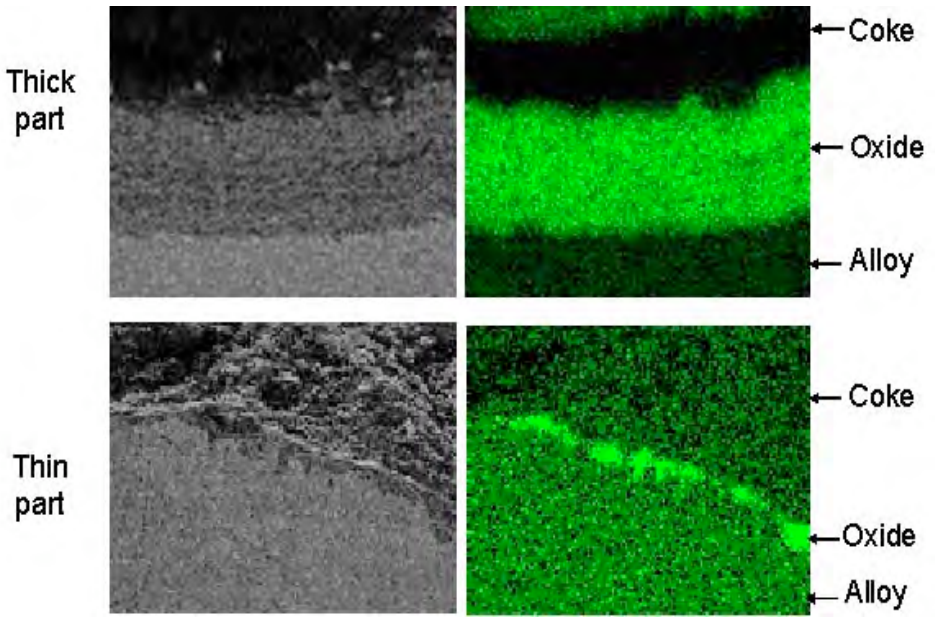

Figure 9.20. EDX map of cross sections of the pipe from a hydrogen-reformer plant.

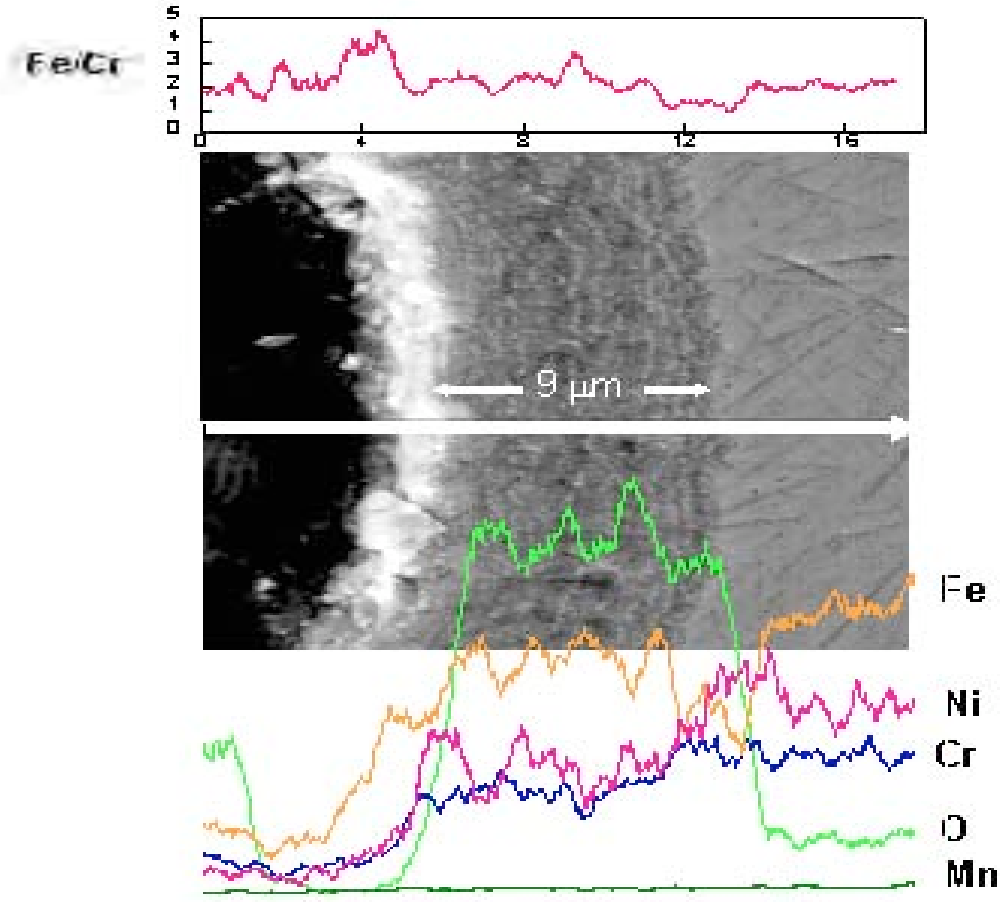

Figure 9.21. EDX linescan of the cross section of the thick part of the pipe. 9 µm oxide scale region indicated by arrows. Alloy is to the right of the scale.

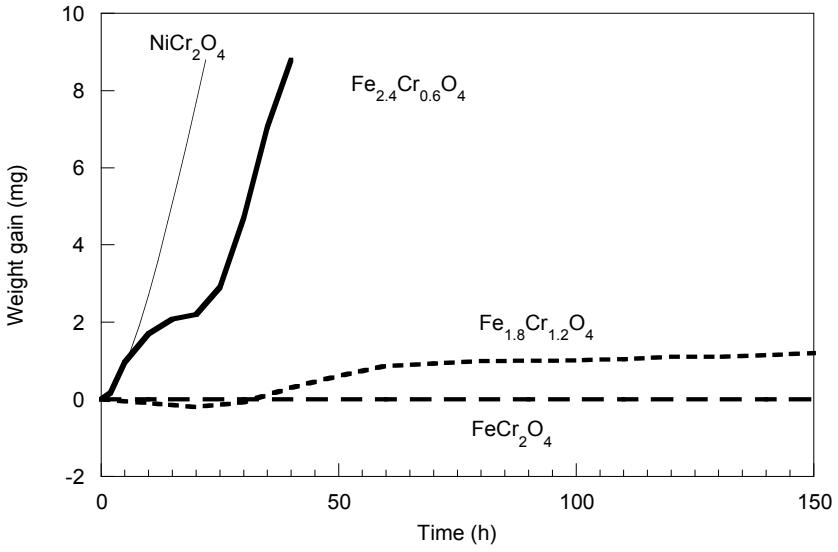

Figure 9.22. Weight change data for spinels with various Fe/Cr ratios, during exposure in Gas 2 (66.2% H_2-7.1% CO_2-23% CO-1.4% CH_4-2.3% H_2O) at 593°C.

Raman spectra show spinel as the primary phase in the oxide scale (see peaks in Fig. 9.23). There is almost no Cr_2O_3 phase in the scale. Previous study has shown that Cr_2O_3 is the desirable phase than spinel to resist metal dusting corrosion.[16,17] Figure 9.24 shows the carbon signal that was observed through the oxide scale on the Alloy 800 surface, indicating that carbon can penetrate even through the oxide scale. The results obtained from the SEM analysis of the cross section and Raman spectra of the plate surface are similar to those observed on the pipe. There was almost no oxide scale on the surface of the thin part of the plate. An oxide scale was observed on the surface of the thick part of the plate, but it contained a high Fe/Cr-ratio spinel and no Cr_2O_3.

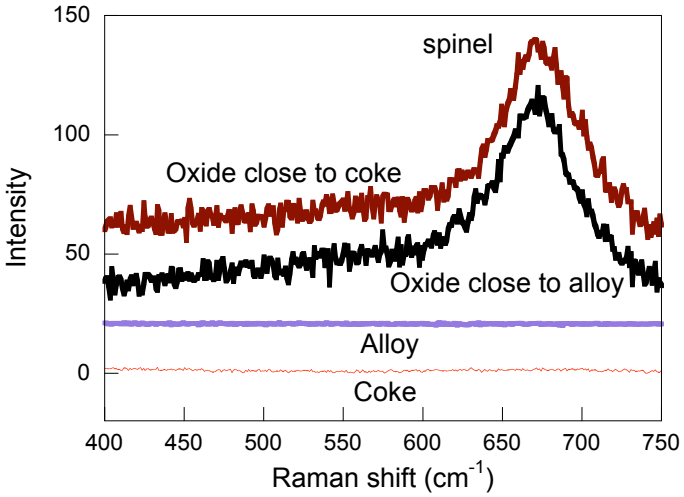

Figure 9.23. Spectra from the cross section of thick part of the pipe for Raman shift of 400-750 cm^{-1}.

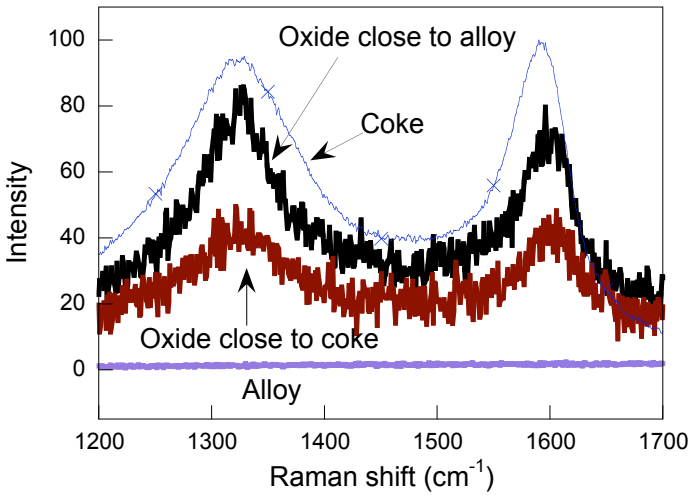

Figure 9.24. Spectra from the cross section of thick part of the pipe for Raman shift of 1200-1700 cm^{-1}.

The compositions of phases present in oxide scales in Ni-base alloys are generally different from those present in the Fe-base alloys. Figure 9.25 shows the EDX mapping of the cross section of Alloy 45TM after 3700-h exposure to Gas 10 at 14.3 atm (210 psi) and 593ºC. This alloy is not as good as other Ni-base alloys at resisting metal dusting corrosion. However, the Fe content in the oxide scale on the

surface of Alloy 45TM is much lower (Fe/Cr = 0.2) than that in the oxide scale on the surface of Alloy 800 (Fe/Cr = 2.15). Therefore, the corrosion resistance of even a higher-iron containing Ni-base alloy (Alloy 45TM) is somewhat better than Alloy 800.

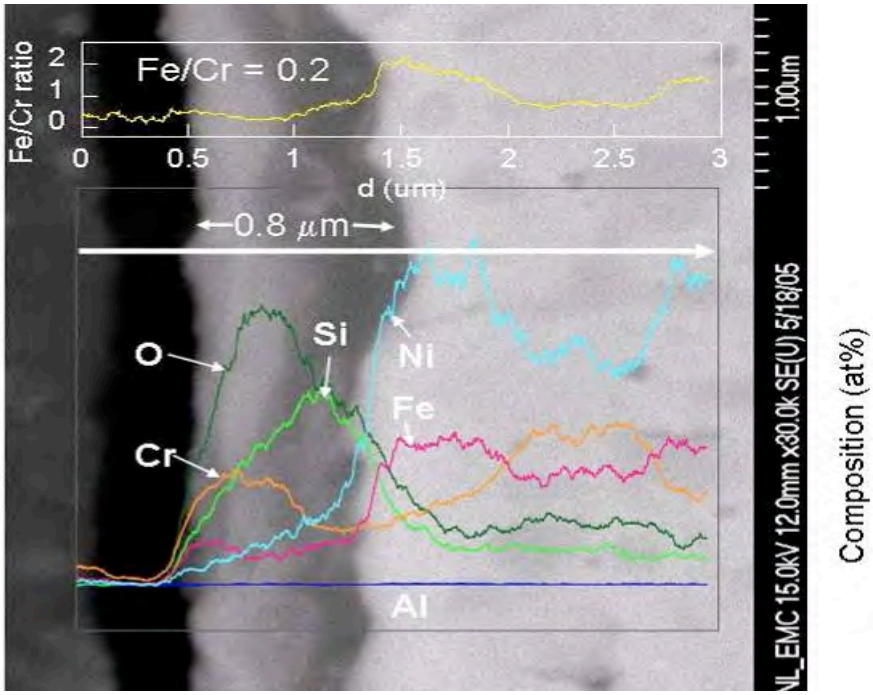

Figure 9.25. EDX line scanning of the cross section of Alloy 45TM after 3700-h exposure to Gas 10 at 593°C and 14.3 atm (210 psi). Oxide scale indicated by 0.8 μm and arrows.

9.3 Analysis of a Metal Dusted Sample From a Gas Boiler

A tube in a gas boiler that had been exposed for 21 months to a gas consisting of 52.31% H_2, 0.08% N_2, 10.9% CO, 5.01% CO_2, 29.08% H_2O and 2.63 CH_4 at 17.7 atm (260 psi), failed due to metal dusting attack. The tube was made of Alloy RA333 (in wt.%: 25Cr, 45Ni, 18Fe, 3Mo, 3Co, 3W, 1Si, 1.5Mn, and 0.05C). The incoming gas temperature was 920ºC and the temperature of the gas leaving the boiler was 340ºC. About two third of the length of the tube was attacked by metal dusting. The worst attack occurred in the vicinity of the outlet where temperature was low. Figure 9.26 shows a ring that was obtained from the worst area of the tube. Numerous pits were present on both outside and inside surfaces of the tube. The pit diameter was larger on the inner surface of tube.

Figure 9.26. Macrophotograph of Alloy RA333 tube after 21-month exposure in a metal dusting environment.

Oxide scale (≈6 μm in thickness) was observed in the non-pit area of the tube (see Fig. 9.27). Figure 9.28 shows cracking of the oxide scale into two layers. EDX mapping indicates that the oxide scale consists of Cr, Mn, and oxygen. EDX linescan further shows that Mn content in the outer layer of the oxide scale is high and its content in the inner layer is low (Fig. 9.29). This result indicates that the outside oxide scale may primarily consist of $Mn_{(1+x)}Cr_{(2-x)}O_4$ spinel and the inner layer predominantly consist of Cr_2O_3. The area indicated by the circle in Figure 9.28 shows that the particle in the region consists primarily of Ni and Fe. Chromium was depleted from the particle. The EDX analysis of the RA333 further validates the presence of carbon channels in the oxide scale and that the channels consist of metallic Fe and Ni particles.

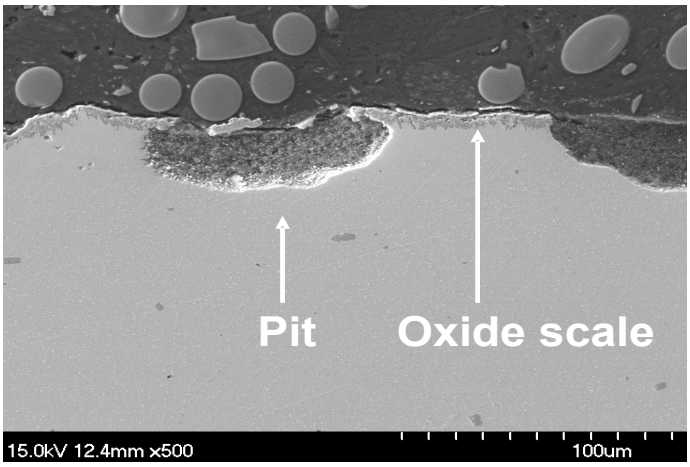

Figure 9.27. SEM cross section image of Alloy RA333 tube after 21-month exposure in a metal dusting environment.

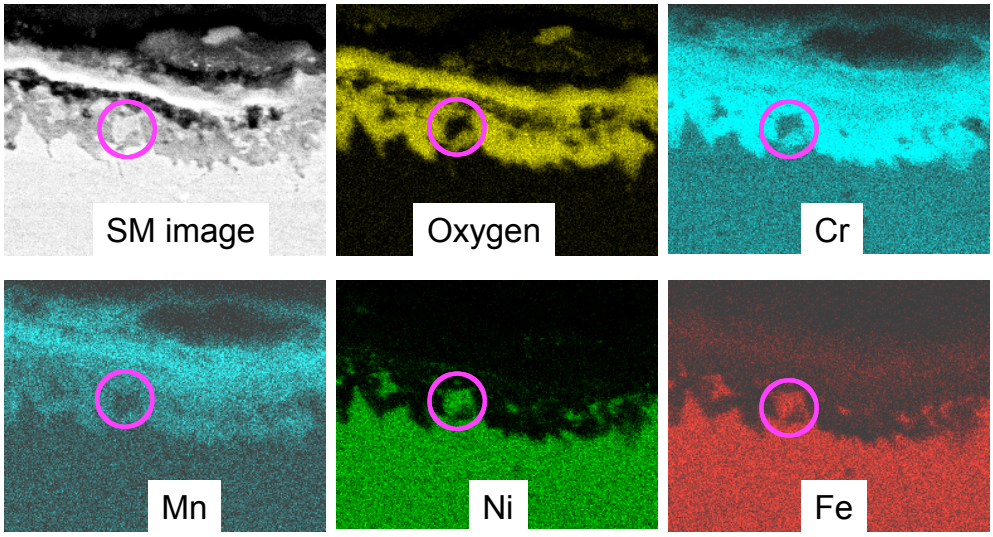

Figure 9.28. Energy dispersive X-ray mapping of the cross section of the non-pit area of Alloy RA333 after 21-month exposure in a metal dusting environment.

Figure 9.29 shows the EDX mapping of the pit area in the Alloy RA333. The chromium distribution near the surface area is not uniform. The area with iron and nickel has less chromium. This indicates that chromium was depleted leaving iron and nickel which act as channels for carbon diffusion into the alloy.

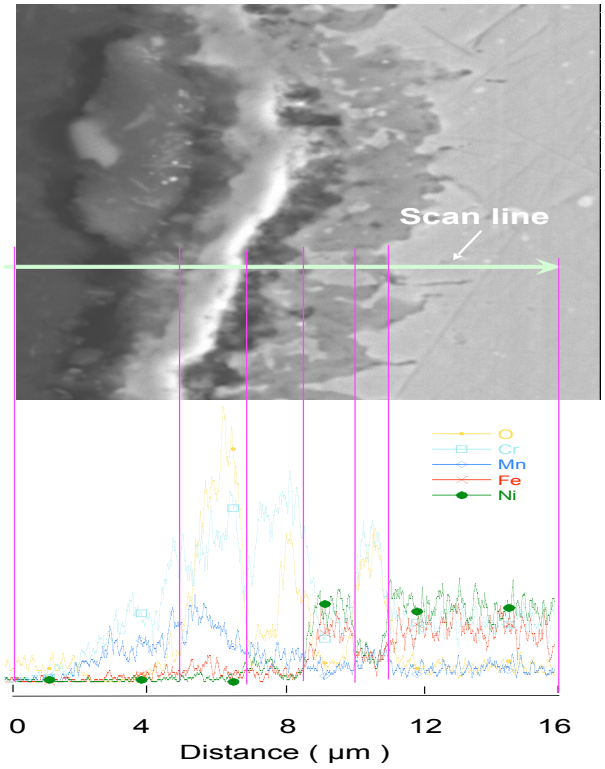

Figure 9.29. EDX linescan through the oxide scale developed on surface of Alloy RA333 after 21-month exposure in a metal dusting environment.

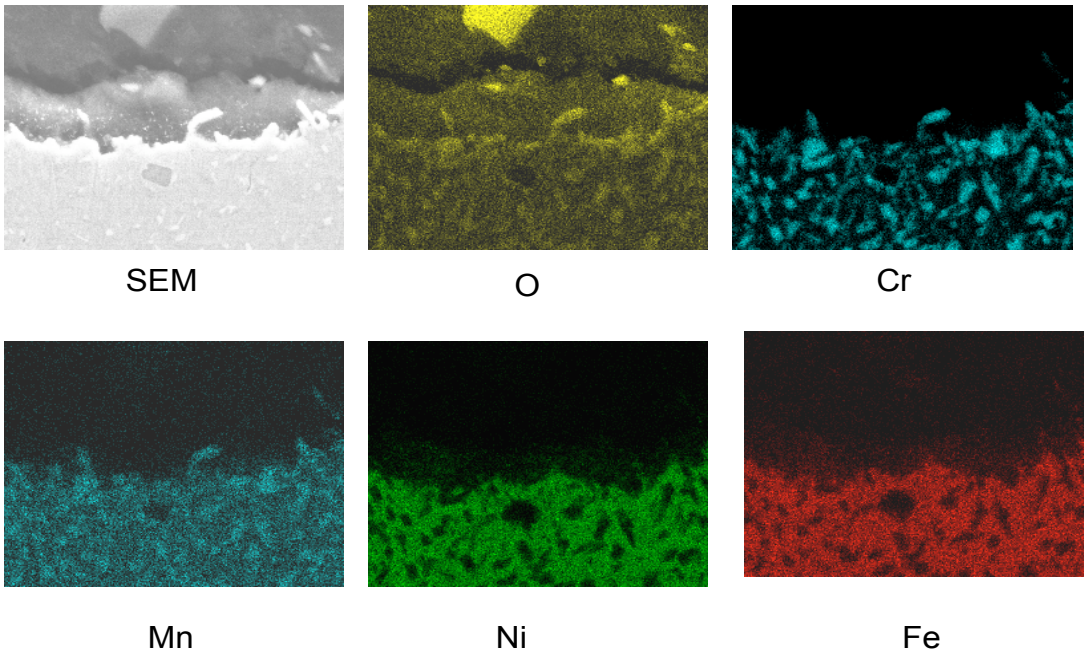

Figure 9.30. Energy dispersive X-ray mapping of the cross section of the pit area of Alloy RA333 after 21-month exposure in a metal dusting environment.

10. SUMMARY

The deposition of carbon from carbonaceous gaseous environments is a problem in many chemical and petrochemical processes, such as reforming systems and syngas production systems, iron ore reduction plants, heat treatment, and others. One of the major consequences of carbon deposition is the degradation of structural materials by a phenomenon known as "metal dusting." In recent years, an extensive program has been conducted at Argonne National Laboratory to establish the mechanisms for metal dusting degradation in metallic materials exposed to carbon-bearing gaseous environments, to identify the key parameters that influence the onset of metal dusting and propagation of degradation, to establish the metal wastage under a variety of exposure conditions, to characterize the morphology of degradation using a wide variety of analytical techniques, and to assess the effect of alloy chemistry, carbon activity, and system pressure on the extent of metal dusting.

We have conducted extensive studies on the coke deposit and metal-dusted alloys using Raman scattering, XRD, and SEM/EDX analysis to develop a fundamental understanding of the metal dusting process and the key variables that influence the initiation and propagation of the degradation. Based on these studies, we concluded that there exists a strong relationship between metal dusting and degree of crystallization of the coke and proposed a mechanism for the initiation and propagation of metal dusting attack. We found that the coke that has experienced metal dusting exhibits much better crystallinity than the coke deposits in the absence of metal dusting. Both metal dusting and carbon filament growth are related to the catalytic crystallization of carbon. Carbon does not crystallize well at low temperatures because of the strong C-C bond and its special layered structure. Carbon must dissolve and diffuse into a metal or a carbide particle. This particle acts as a catalyst to aid in the crystallization of carbon. In this catalytic crystallization process, metals are liberated as small particles which further contribute to metal dusting corrosion. The catalytic growth of carbon filaments is due to the transport of carbon from one facet of a metal or carbide particle that favors carbon deposition (but not carbon precipitation) to another facet that favors precipitation. The decrease in free energy from highly disordered carbon to well-crystallized carbon is the driving force for both catalytic growth of carbon filaments and for metal dusting.[9,11,12]

Based on the above studies, we conclude that the metal dusting mechanism for both iron and nickel are similar, which is due to the carbon catalytic crystallization process. The only difference is that iron carbide is thermodynamically stable and can form and can serve as a catalyst for the carbon catalytic crystallization, but nickel carbide is thermodynamically not stable. In the case of nickel, carbon dissolves and directly diffuses through nickel and uses nickel lattice as a template for its catalytic crystallization. Since the rate of the lattice mismatch of nickel and carbon is larger than that between carbon and Fe_3C, the energy barrier is larger for carbon precipitating from nickel lattice than that for carbon precipitating from Fe_3C lattice. Therefore, the metal dusting rate for nickel and its alloys is smaller than that of iron and its alloys.

In the current project, substantial progress was made in evaluating the performance of metallic materials subjected to simulated metal dusting environments at 1 atm and at high pressures. Surface profiler has been successfully introduced into metal dusting research for quantitative measurements on pit characteristics, in particular, pit depth. Several accomplishments can be identified from the study as:

- There are two major issues of importance in metal dusting. First is the formation of carbon/coke and subsequent deposition of carbon on metallic materials. Second is the initiation of metal dusting in the alloy and subsequent propagation of the degradation. The first is influenced by the a_C in the gas mixture and the availability of the catalytic surface for carbon-producing reactions to proceed. There may be a threshold in a_C (>>1) for carbon deposition. Metal dusting of the alloy in the reformer environments is determined by a competition between the oxide scale development and access to the virgin metal surface for the carbon deposit. In several long-term metal dusting experiments, we conducted extensive post-exposure analysis of the specimens to establish the time for initiation of metal dusting and propagation rates as a function of alloy chemistry, gas chemistry, and system pressure.

- By conducting long-term tests at 1 and 14.3 atm, while maintaining a carbon activity of ≈31, we established that the time for initiation of metal dusting is substantially reduced at the higher pressure, even for Ni-base alloys. Similar results were obtained when comparing the surface morphology of specimens tested at 1 and 30 atm at a carbon activity of 104.

- Surface profiler was introduced by the first time into metal dusting research to measure the depth of pits associated with metal dusting attack. We also measured the pit density in several Ni-base alloys using scanning electron microscopy. Pit density for each alloy was found to be different. The results indicated higher pit density in Alloys 601 and 45TM when compared to that in Alloys 602CA and 693.

- Based on a detailed analysis of pits (in several Ni-base alloys) as a function of exposure time, we correlated the growth in diameter of a single pit with the weight change observed for the alloys. We established that the alloys tested, except Alloy 214, lose weight by localized pitting when exposed in metal dusting environments. Alloy 214 developed numerous shallow pits leading to more uniform attack.

- Generally, the time for initiation of pits in Ni-base alloys is of the order of thousands of hours. However, the pit propagation rate is of major importance in assessing the viability of an alloy for any chemical process application. To expedite the initiation step and thereby emphasize pit propagation, we developed a pre-pitting approach. We used Alloy 800 and 9Cr-1Mo steel, as surrogate alloys, to develop the pre-pitting approach, since these alloys have a short initiation time for pitting. Subsequently, we applied the same approach to several Ni-base alloys. The method has led to development of multiple specimens of each alloy with pits for further study on propagation as a function of process variables such as temperature, system pressure, and gas chemistry.

- We have also developed an approach to identify the locations of pits and potential pitting areas by an electrochemical copper deposition approach since the pit locations exhibit low resistance, leading to enhanced deposition of copper. Copper indicator experiments showed that there may be channels in the oxide scales for transfer of carbon into alloy substrates. These channels could be located because their electrical resistance is much lower than that of the oxide scale.

- We have tested several Ni-base alloys at a carbon activity of 104 at system pressures of 1 and 30 atm. The environment in these tests being more aggressive, the time for pit initiation is short. The emphasis in these tests is to quantify the pit propagation rates and correlate the data with alloy chemistry.

- Synchrotron X-ray nanobeam was used to analyze the thin oxide scale and oxide sublayers on the surface of alloys after exposure in simulated metal dusting environment. Results showed spinel with enhanced iron content as the major phase in the oxide scale at the metal dusting pit region. The oxidation state of Iron in spinel in the oxide scale on alloy surface is greater than +2, which diminishes the stability of oxide scale in the reducing condition prevalent in the reformer environments. Nickel metal particles were also identified in oxide scale which may join to form continuous channels for transport of carbon into the alloys.

- Increasing the Cr content (from 20 to 29 wt.%) in alloys had less effect in decreasing the pit growth rate when compared with the benefit of decreasing the Fe content in the alloy on the growth rate. The presence of Fe in the alloy leads to formation of (Fe,Cr) spinel phase in the scale. Over time, the Fe/Cr ratio in the spinel increases to essentially make it unstable in the high-carbon environments and eventual breakdown of the protective capacity of the scale. Therefore, we designed and prepared several alloys with low concentration of Fe and tested in metal dusting environments. Results showed that the ANL-developed alloys formed predominantly Cr oxide in the scale and the incubation time (for metal dusting) was extended ten times more than that of the commercial alloys with similar chromium contents.

- We developed a process-control approach to mitigate metal dusting, in which the metal-dusted alloys (i.e., with pits on the surface) were given an intermediate oxidation treatment in an atmosphere without carbon. Subsequent exposure of these oxidized specimens to metal dusting environments showed substantial drop in pit-progression rate leading to possibility of extended service life for the metallic components.

- We also evaluated Cu, Cu-coated, and Cu-clad materials for their susceptibility and pitting degradation in metal dusting environments. Copper and Cu-coated materials did not exhibit adequate resistance to metal dusting, especially after thousands of hours of exposure. The performance of Cu-clad alloys is dependent on the thickness and mechanical integrity of the clad layer. Additional long-term tests are needed to establish the adequacy of their performance in metal dusting environments.

- We also developed several Cu-Ni-Al alloys and evaluated their resistance in metal dusting environments and their tensile properties in air. Cu-Ni-Al alloys were resistant to metal dusting attack and they need to be evaluated further in a systematic manner for commercializing them for structural applications.

- We have evaluated weldment specimens of several Fe- and Ni-base alloys in metal dusting environments at a system pressure of 1 atm. In general, Ni-base alloy weldments exhibited superior performance than the Fe-base alloy weldments when tested in the same environment. The study focused on the relative performance of the weld metal, heat affected zone, and base metal upon exposure to metal dusting environments. The pit growth rates at the weld area are generally higher than those of the corresponding base alloys. Severe corrosion at the heat-affected zones was also observed.

- We have evaluated the pit progression in Alloys 602CA and 693 that were exposed at 659°C for 1.5 and 3 years in a metal dusting environment of a reformer plant. Both alloys exhibited several pits on the surface. Maximum size of the pit in Alloy 602CA was larger than that in Alloy 693. The average pit depth/diameter ratio for Alloy 693 is higher than that for Alloy 602CA. The size of pits in the bent regions (probably cold worked) of both Alloys 602CA and 693 are smaller than that in the flat regions.

- We conducted a detailed analysis of two Alloy 800HT components that failed in a hydrogen reformer service. Results showed that the oxide scale on the alloy surface was predominantly $Fe_{1+x}Cr_{2-x}O_4$ spinel phase with high Fe content, which has been shown to offer little resistance to metal dusting attack.

- We examined a failed component made of Alloy RA333 that was exposed to a metal dusting environment in a gas boiler. The analysis showed evidence for Cr depletion in the surface region and accumulation of Fe and Ni which can act as channels for transport of carbon and continued metal dusting degradation of the substrate alloy.

ACKNOWLEDGMENTS

This work was sponsored by the U.S. Department of Energy, Office of Industrial Technologies, and Dr. Sara Dillich is the Program Manager for the project. D. L. Rink assisted with the experimental program, pit depth analysis, scanning electron microscopy, and EDX analysis. W. K. Soppet assisted in the tensile testing of copper-base alloys. The authors acknowledge the members of the steering committee for valuable discussions during the course of this research. Haynes International, Sandvik Steel, Special Metals, Allegheny Ludlum, Krupp VDM, Rolled Alloys, and Outokumpu supplied alloy and weldment specimens of various alloys. The SEM analysis was performed in the Electron Microscopy Center, Materials Science Division, Argonne National Laboratory, Argonne, IL.

PUBLICATIONS ON METAL DUSTING PROJECTS

K. Natesan, Z. Zeng, V. A. Maroni, W. K. Soppet, and D. L. Rink, “Metal dusting Research at Argonne National Laboratory,” International Workshop on Metal dusting, Argonne National Laboratory, Sep. 26-28, 2001, p. 19.

V. A. Maroni, “Applications of Molecular Spectroscopy Methods to the study of Metal Dusting Corrosion,” International Workshop on Metal dusting, Argonne National Laboratory, Sep. 26-28, 2001, p. 41.

Z. Zeng, K. Natesan, and V. A. Maroni, “Study of Metal Dusting Mechanism in Iron Using Raman Spectroscopy and X-ray Diffraction,” International Workshop on Metal dusting, Argonne National Laboratory, Sep. 26-28, 2001, p. 93.

K. Natesan, Z. Zeng, V. A. Maroni, W. K. Soppet, and D. L. Rink, “Metal dusting Behavior of Coatings,” International Workshop on Metal dusting,” Argonne National Laboratory, Sep. 26-28, 2001, p. 191.

K. Natesan, A. Purohit, D. L. Rink, and W. Salot, “Analysis of Metal Dusting in a Waste Heat Boiler,” International Workshop on Metal dusting, Argonne National Laboratory, Sep. 26-28, 2001, p. 233.

K. Natesan, “Study of Metal Dusting Phenomenon and Development of Materials Resistant to Metal Dusting: Annual Report,” Argonne National Laboratory Report, ANL-02/05, February 2002.

Z. Zeng and K. Natesan, “Metal Dusting Mechanism of Fe and Ni Base Alloys,” ASM International Materials Solutions Conference, Indianapolis, USA, November 5-8, 2001.

Z. Zeng, K. Natesan, and V. A. Maroni, “Investigation of Metal Dusting Mechanism in Iron Using Raman Spectroscopy, X-ray Diffraction, and Electron Microscopy,” Oxidation of Metals, 58, 147, 2002.

Z. Zeng and K. Natesan, “A New Mechanism for the Catalytic Growth of Carbon Filaments and Metal Dusting Phenomenon,” Mat. Res. Soc. Symp. Proc. 755, DD5.1, 2002.

K. Natesan and Z. Zeng, “Study of Metal Dusting Phenomenon and Development of Materials Resistant to Metal Dusting: Final Report,” Argonne National Laboratory Report, ANL-03/33, 2003.

Z. Zeng and K. Natesan, “Relationship of Carbon Crystallization to the Metal Dusting Mechanism of Nickel,” Chemistry of Materials, 15, 872, 2003.

Z. Zeng and K. Natesan, “Metal Dusting Problem with Metallic Interconnects for Solid Oxide Fuel Cell,” Mat. Res. Soc. Symp. Proc. 756, FF4.2, 2003.

Z. Zeng, K. Natesan, and M. Grimsditch, “Effect of phase compositions of oxide scale on metal dusting corrosion of Fe-base alloys,” Corrosion, 60, 632, 2004.

Z. Zeng and K. Natesan, “Corrosion of Metallic Interconnects for SOFC in Fuel Gases,” Solid State Ionics, 167, 10, 2004.

K. Natesan and Z. Zeng, “Metal Dusting Performance of Structural Alloys,” Corrosion, Paper # 05409, published by NACE International, Houston, TX. 2005.

Z. Zeng and K. Natesan, “Relationship between the Growth of Carbon nanofilaments and Metal Dusting Corrosion,” Chemistry of Materials, 17, 3794, 2005.

Z. Zeng and K. Natesan, “Initiation of metal-dusting pits and a method to mitigate metal-dusting corrosion,” Oxidation of Metals. 66, 1, 2006.

Z. Zeng and K. Natesan, “Control of Metal Dusting Corrosion in Ni-Base Alloys,” International Journal of Hydrogen Energy, 32, 3640, 2007.

Z. Zeng, K. Natesan, and S. B. Cai, “Characterization of the Oxide Scale on Alloy 446 by X-ray Nanobeam Analysis,” Electrochem. Solid-State Letters Volume 11, Number 1, 2007.

REFERENCES

1. E. Q. Camp, C. Phillips, and L. Gross, Corrosion 1, 149 (1945), 15, 627t (1959).
2. P. A. Lefrancois and W. B. Hoyt, Corrosion 19 (10), 360t (1963).
3. R. F. Hochman, Proc. of the 4th Int. Congress on Metallic Corrosion, N. E. Hamner, ed., National Assn. of Corrosion Engineers, pp. 258-263 (1972).
4. R. C. Schueler, Hydrocarbon Processing 51, 73 (1972).
5. R. F. Hochman, Proc. Symp. on Properties of High-Temperature Alloys with Emphasis on Environmental Effects, Z. A. Foroulis and F. S. Pettit, eds., The Electrochemical Society, pp. 715-732 (1977).
6. H. J. Grabke, Materials and Corrosion, 49, 303 (1998)
7. H. J. Grabke and G. Tauber, Arch. Eisenhuttenwes, 46, 215 (1975).
8. S. R. Shatynski, H. J. Grabke, and S. Strauss, Arch. Eisenhuttenwes, 49, 129 (1978).
9. Z. Zeng, K. Natesan, and V. A. Maroni, Oxidation of Metals, 58, 147 (2002).
10. C. H. Toh, P. R. Munroe, and D. J. Young, Oxidation of Metals, 58, 1 (2002).
11. Z. Zeng, K. Natesan, and V. A. Maroni, 2001, Proc. Intl. Workshop on Metal Dusting, Sept. 26-28, 2001, Argonne National Laboratory, Argonne, IL, p. 93.
12. Z. Zeng and K. Natesan, Chemistry of Materials, 15, 872 (2003).
13. Z. Zeng and K. Natesan, Chemistry of Materials, 17, 3794 (2005).
14. K. Natesan, “Study of Metal Dusting Phenomenon and Development of Materials Resistant to Metal Dusting: Annual Report,” Argonne National Laboratory Report, ANL-02/05 (2002).
15. K. Natesan and Z. Zeng, “Study of Metal Dusting Phenomenon and Development of Materials Resistant to Metal Dusting: Final Report,” Argonne National Laboratory Report, ANL-03/33 (2003).
16. K. Natesan, Z. Zeng, V. A. Maroni, W. K. Soppet, and D. L. Rink, “Metal Dusting Research at Argonne National Laboratory,” Proc. Intl. Workshop on Metal Dusting, Sept. 26-28, 2001, Argonne National Laboratory, Argonne, IL, p. 19 (2001).
17. Z. Zeng and K. Natesan, Effect of Oxide Scale Compositions on Metal Dusting Corrosion of Fe-Base Alloys, Corrosion, 60, 632 (2004).
18. Z. Zeng and K. Natesan, Corrosion of Metallic Interconnects for SOFC in Fuel Gases, Solid State Ionics, 167, 10 (2004).
19. Z. Zeng and K. Natesan, Initiation of metal-dusting pits and a method to mitigate metal dusting corrosion, Oxidation of Metals, 66, 1 (2006).
20. M. Maier and J. F. Norton, Materials and Corrosion, 50, 640 (1999).
21. S. Strauss and H. J. Grabke, Materials and Corrosion, 49, 321 (1998).
22. H. J. Grabke and E. M. Muller-Lorenz, Materials and Corrosion, 49, 317 (1998).
23. H. J. Grabke, R. Krajak, and E. M. Muller-Lorenz, Werkst. Korros. 44, 89 (1993).
24. P. Szakalos, M. Lundberg, and R. Pettersson, Corrosion Science 48, 1679 (2006).
25. A. Schneider and J. Zhang, Materials and Corrosion, 54, 778 (2003).
26. Y. Nishiyama, N. Otsuka, and T. Kudo, Corrosion Science 48, 2064 (2006).
27. R. Bernst, A. Schneider, and M. Spiegel, Materials and Corrosion, 57, 724 (2006).
28. C. Rosado, and M. Schutze, Materials and Corrosion, 54, 831 (2003).
29. B. A. Baker, V. W. Hartmann, L. E. Shoemaker, S. A. McCoy, and S. Rajendran, Transactions of the India Institute of Metals, 56, 327 (2003).
30. F. Muller and O. J. Kleppa, J. Inorg. Chem., 35, 2673 (1973).

31. J. Zhang, D. M. I. Cole, and D. J. Young, Materials and Corrosion, 56, 756 (2005).
32. Y. Nishiyama and N. Otsuka, High-temperature Oxidation and Corrosion, 2005 Materials Science Forum, 522-523: 581-588 (2005).
33. D. J. Young, High-temperature Oxidation and Corrosion, 2005 Materials Science Forum, 522-523: 15-26 (2005).

Nuclear Engineering Division
Argonne National Laboratory
9700 South Cass Avenue, Bldg. 212
Argonne, IL 60439-4838

www.anl.gov

UChicago ▶ Argonne LLC

A U.S. Department of Energy laboratory
managed by UChicago Argonne, LLC